Probing the X-ray Binary Populations of Star-Forming Galaxies

by

Qiana M. Hunt

A dissertation submitted in partial fulfillment
of the requirements for the degree of
Doctor of Philosophy
(Astronomy and Astrophysics)
in the University of Michigan
2024

Doctoral Committee:

Professor Elena Gallo (Co-chair)
Professor Rupali Chandar (Co-chair), University of Toledo
Assistant Professor Lia Corrales
Professor August Evrard
Professor Jon Miller
Dr. Andrea Prestwich, NSF/SAO

"Whilst this planet has gone circling on according to the fixed law of gravity, from so simple a beginning endless forms most beautiful and most wonderful have been, and are being evolved."
— Charles Darwin

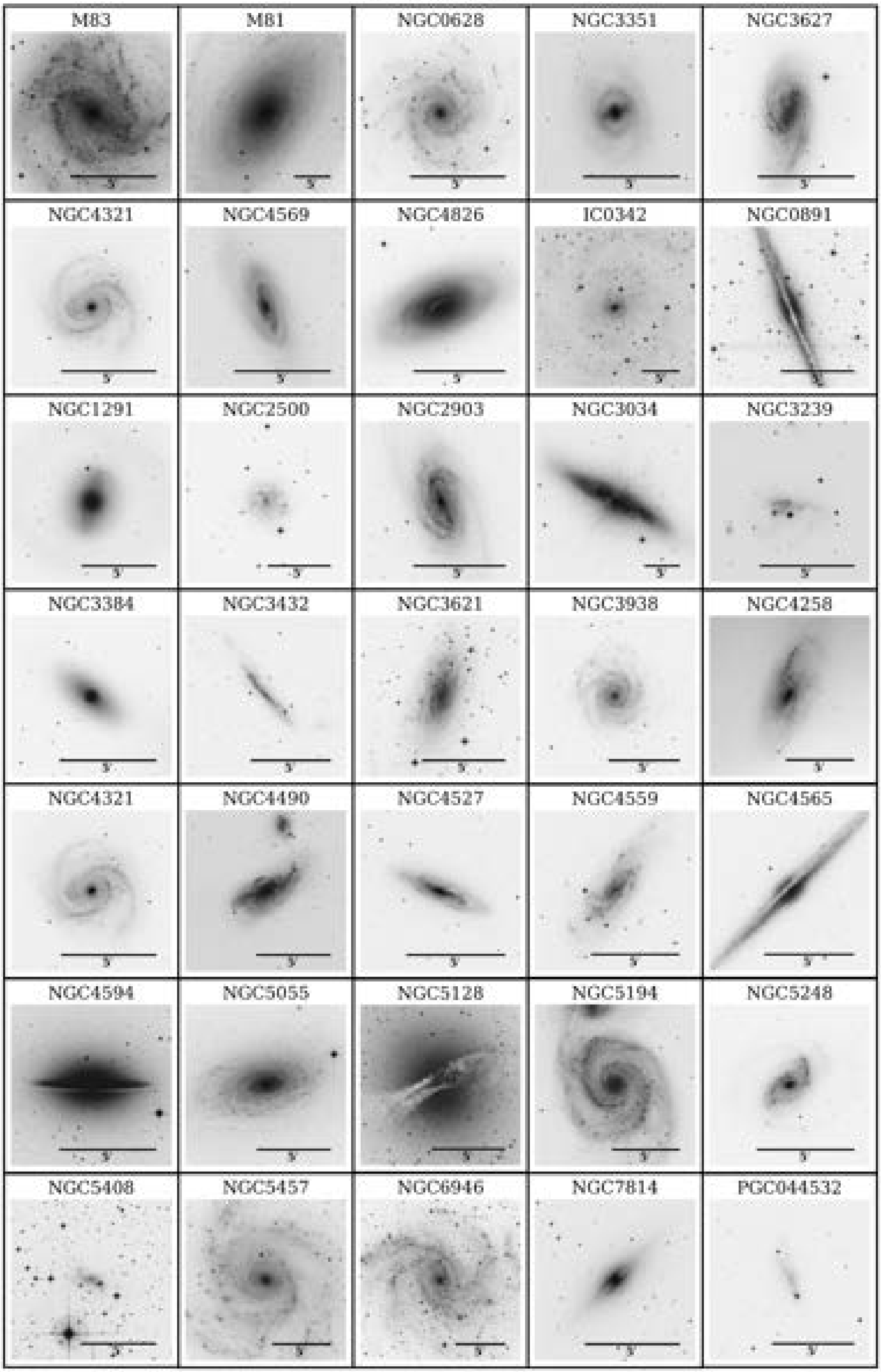

Qiana M. Hunt

qiana@umich.edu

ORCID iD: 0000-0002-4669-0209

DEDICATION

This thesis is dedicated to my parents, who have always believed I could do anything. Thank you, Mom, for making sure I had every opportunity to pursue my dreams wherever they took me. And thank you, Dad, for all the brain power you lent me over the years. I hope you agree I've made good use of it.

ACKNOWLEDGEMENTS

I would like to thank all of those who have been endlessly supportive of me throughout this incredible journey. I cannot possibly name every single person who have touched my life in immeasurable ways, but there are a few I would like to take the opportunity to shout out.

I must first thank the educators who have made a difference in my life: those who inspired me, like my my 7th grade science teacher, Mrs. Hill, and the legendary Carl Sagan; those who advised me, like Drs. Elena Gallo, Rupali Chandar, Jenny Greene, Rachel Bezanson, Ken-ichi Nishikawa, Jack Hewitt, and Bernard Kelly; those who guided me, like the entirety of my thesis committee, and others in the department (including staff!); and the countless other teachers and professors who have instructed me over the decades. My gratitude is infinite.

I would also like to give a special thanks to my graduate cohort, the greatest to ever grace West Hall — Kate, Irene, Hayley, Jenny, Felipe, and Cam. Even though most of our time together was spent in lockdown, I still have the fondest memories of our adventures. And thank you to all the other grads, past (shout out to Tom!) and present, who have made this journey enjoyable. You are the reason I came to Michigan, and the reason I managed to survive the ups and downs of it all.

Finally, I wish to thank my family, as well as my external support systems and the communities I've been a part of throughout the past several years. This includes (but is not limited to): the Rackham graduate school, which funded me through the Rackham Merit Fellowship and the Predoctoral Fellowship; the LSST Discovery Alliance and the amazing Data Science Fellows I've come to know; the National Astronomy Consortium (shout out to the OG OC!); Black in Astro, the best thing to ever come out of Twitter; and the good people at the Ann Arbor District Library. And, of course, an astronomical thanks to my most steadfast source of support, Chris and the cats. Much love, and thank you for being there for me!

TABLE OF CONTENTS

CHAPTER

LIST OF FIGURES

FIGURE

LIST OF TABLES

TABLE

LIST OF APPENDICES

LIST OF ACRONYMS

AGN Active Galactic Nucleus

CMD Color-Magnitude Diagram

FWHM Full Width at Half Maximum

GC Globular Cluster

HMXB High-mass X-ray Binary

HST Hubble Space Telescope

IMXB Intermediate-mass X-ray Binary

LMXB Low-mass X-ray Binary

ML Maximum Likelihood

MW Milky Way

PL Power-Law

PSF Point Spread Function

SED Spectral Energy Distribution

SNR Supernova Remnant

SFR Star Formation Rate

sSFR Specific Star Formation Rate

ULX Ultraluminous X-ray source

XLF X-ray Luminosity Function

XRB X-ray Binary

ABSTRACT

X-ray binaries (XRBs) represent a subset of compact objects (e.g. neutron stars and black holes) made visible by their accretion-driven X-ray emission. Approximately 20% of all stellar-mass black holes and neutron stars are expected to pass through an XRB stage at some point in their evolution, making XRBs a crucial evolutionary step for a population gravitational waves progenitors. XRBs with low-mass vs. high-mass donor stars have different formation channels, formation rates, and distributions that are correlated with their environmental properties. In this thesis, I classify the populations of XRBs in nearby, late-type galaxies in M83 and M81 on a source-by-source basis, allowing us to directly test the accuracy of modern XRB models for the first time. Through this work, I find a possible disconnect between the modeled XRB distributions in spiral galaxies and their actual distributions, which appears to fuel a mismatch between the expected number of high-mass vs. low-mass XRBs and the populations I identify through this work. I also conduct the first comprehensive study of XRBs and their relation to both young and old compact star clusters in a broader sample of spiral galaxies, identifying a similar correlation between denser, more massive clusters and XRB formation as is seen in elliptical galaxies. This work yields, for the first time, a statistically significant correlation between X-ray luminosity and cluster mass for young XRB–hosting clusters and an *anticorrelation* for ancient clusters. Finally, I identify the optical counterparts of 46 ultraluminous X-ray sources across 28 late-type galaxies, contributing 8 new sources to the ongoing effort to classify the donor stars in these extreme X-ray systems.

CHAPTER 1

Introduction

Since the first detection of gravitational waves from colliding black holes in 2015 (Abbott et al., 2016) and, more recently, the 2020 Astronomy & Astrophysics Decadal Survey (National Academies of Sciences & Medicine, 2023), the study of compact objects (e.g. black holes and neutron stars) has become a top science priority for the astronomy community. X-ray binaries (XRBs) represent a subset of compact objects made detectable when matter from a closely-orbiting companion star is accreted onto a black hole or neutron star. The release of gravitational potential energy as matter falls onto the compact object generates some of the most luminous X-ray emission in the Galaxy. An estimated 20% of all stellar-mass compact objects are expected to be in an XRB at some point in their evolution, based on the estimated birthrate of compact objects, the observed number of luminous XRBs, and the typical duration of their X-ray active phase (Mineo et al., 2012). Since some of the compact objects within XRBs are bound to become the progenitors of gravitational waves, the abundance and evolution of XRBs inform gravitational wave predictions for instruments such as LIGO/VIRGO/KAGRA or the future LISA mission (e.g. Belczynski et al., 2008; Marchant et al., 2017). Futhermore, the radiation from XRBs dominates the total X-ray output of their host galaxy in the absence of a central supermassive black hole, so accurate modeling of XRB populations is also necessary for X-ray studies of supermassive black holes in distant galaxies (e.g. Lehmer et al., 2010; Bykov et al., 2024). At higher redshifts, XRBs are even believed to play a vital role in the reionization of the early Universe and may be used to place observational constraints on primordial black holes (Fragos et al., 2013; Inoue & Kusenko, 2017; Montero-Camacho et al., 2024).

There are several ways to subdivide XRB populations based on the nature of the compact object (i.e. whether the compact object is a black hole or neutron star), the accretion mechanism through which X-rays are produced, and/or the mass and spectral type of the donor star. This dissertation focuses on the latter. The nature of the donor star is a crucial factor in the measurable properties of the XRB, such as mass transfer rate, luminosity, and duty cycles. Since many of these characteristics are influenced by the mass of the donor star, XRBs are typically divided into two mass classes: low-mass X-ray binaries, and high-mass X-ray binaries.

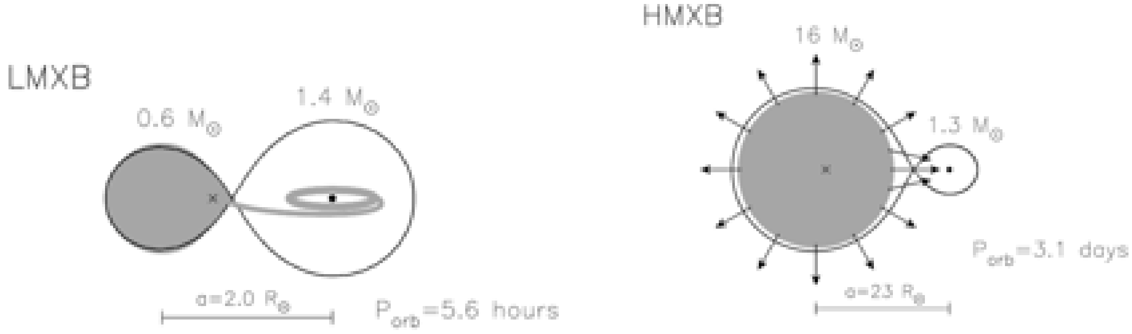

Figure 1.1 Typical accretion mechanisms of LMXBs (Roche Lobe overflow, left) and HMXBs (stellar winds, right). *Source: Tauris & van den Heuvel (2006)*

1.1 Low-mass X-ray Binaries

Low-mass X-ray binaries (LMXBs) are XRBs in which the donor star is less massive than the compact component (Bahramian & Degenaar, 2023). While there is no universally-accepted upper mass limit for LMXB donors stars, the typical delimiting mass is roughly a solar mass or lower. Some studies (including those presented here) set the upper mass limit as high as 3 $\mathrm{M}_\odot$, corresponding to the approximate lower mass limit of a stellar-mass black hole formed by a core-collapse supernova (Grimm et al., 2006; Lattimer, 2012; Chandar et al., 2020; Avdan et al., 2022). The vast majority of XRBs in this mass regime are powered through Roche lobe overflow, which occurs when the outer layers of a "donor" star expands beyond the gravitational equipotential surface between the star and compact object and forms an accretion disk around the compact object (e.g. Figure 1.1). Since accretion from a disk occurs in phases due to thermal-viscous instabilities (Lasota, 2001; Carbone & Wijnands, 2019), LMXBs that accrete via Roche lobe overflow are transient X-ray sources that undergo days- to months-long periods of strong X-ray outbursts followed by periods of quiescence. During outbursts, the luminosity of the star is overpowered in all wavelengths by the luminosity of the accretion disk, making it impossible to conduct direct observations of the donor star. However, the observed duty cycle of LMXBs is low, with an average of 2.5% of their time actively spent in outburst (Yan & Yu, 2015).

LMXBs are found both in the diffuse stellar field of their host galaxy and within compact star clusters. Field LMXBs may either be formed in situ following the supernova collapse of the more massive companion in a close binary system (van den Heuvel & van Paradijs, 1997), or may form first within compact star clusters before being released into the field via ejection from or the evaporation of the parent cluster (Grindlay, 1984; Grindlay & Hertz, 1985; Hut et al., 1992; Kremer et al., 2018). LMXBs that form within clusters form through dynamical interactions: either a compact object tidally captures a nearby star (Fabian et al., 1975), the lower-mass companion

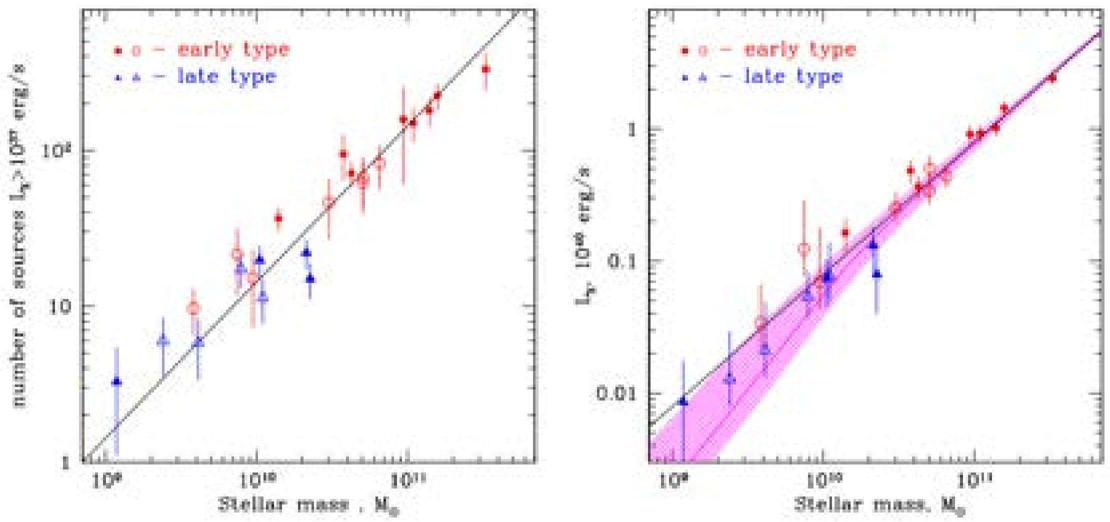

Figure 1.2 (Left) The relation between the total stellar mass and the total number of bright X-ray sources (LMXBs) in elliptical galaxies (red) and the red bulges of spiral galaxies (blue), with a best-fit slope of 1.00 ± 0.07. (Right) The relation between galaxy stellar mass and the total X-ray luminosity. The black line shows a power-law relation with a best-fit slope of 1.01 ± 0.06. The magenta line is the relation between the stellar mass and the estimated total luminosity given by the average X-ray luminosity function, with the shaded region indicating the 67% intrinsic uncertainty. *Source: Gilfanov (2004).*

of an existing binary is exchanged for a compact object via three-body scattering (Hills, 1976), or a neutron star physically collides with and becomes gravitationally bound to an evolved star (Sutantyo, 1975; Ivanova, 2013).

LMXBs are thought to form hundreds of times more efficiently in globular clusters (GCs) — massive spherical clusters composed of old, red stars — than in the stellar field of their host galaxy (Clark & Parkinson, 1975; Katz, 1975). Observations of elliptical galaxies with the *Chandra X-ray Observatory* and the *Hubble Space Telescope* (*HST*) have shown that between 20% to 70% of bright LMXBs currently reside in GCs (Angelini et al., 2001; Kundu et al., 2002; Jordán et al., 2004; Kundu et al., 2007; Humphrey & Buote, 2008; Peacock & Zepf, 2016), and that a near constant 4–6.5% of GCs in elliptical galaxies host bright LMXBs. Observational evidence suggests the dense environments within GCs facilitate the formation of LMXBs, with LMXBs preferentially appearing in brighter (i.e. more massive) and more compact (i.e. denser with a greater stellar encounter rate) clusters (e.g. Kundu et al., 2002; Sivakoff et al., 2007; Brassington et al., 2010; Fabbiano et al., 2010; Peacock & Zepf, 2016; Lehmer et al., 2020; Riccio et al., 2022). It is these reasons, as well as the observed correlation between the total X-ray luminosity (L_X) of LMXBs and the specific frequency of GCs in a galaxy, that indicate the field population of LMXBs may be seeded by GCs (Grindlay, 1984; Grindlay & Hertz, 1985; Hut et al., 1992; Zhang et al., 2013;

Kremer et al., 2018; Ferrell et al., 2021). However, the degree to which seeding by clusters contributes to the field XRB population is still an open question; recent work by Lehmer et al. (2020), for example, finds evidence that the X-ray luminosity function (XLF) of LMXBs requires a term that scales with galactic stellar mass ($\mathrm{M}_{\star}$) and that dominates in galaxies with fewer GCs for a given galactic V-band magnitude. This suggests that a non-negligible fraction of the field LMXB population in elliptical galaxies form in situ.

The bulk of our knowledge of LMXBs comes from observations of the Milky Way and early-type (elliptical) galaxies. Within the Milky Way, over 300 of the nearly 500 Galactic XRBs are LMXBs (Fortin et al., 2023, 2024). The primary formation mechanism for Galactic LMXBs is believed to be in situ formation, though as much as 20% of Galactic LMXBs are found within GCs. Since the birth of the compact object component of an XRB imparts a natal kick on the system that displaces it from its original birth environment, and since the lifespan of an LMXB is defined by nuclear timescale of a low-mass star (in excess of 1 Gyr), LMXBs may travel far over the course of their lifetime. This contributes to both their broad distribution throughout their host galaxies, and the fact that they are found out to scale heights of over 400 kpc in the Milky Way (Grimm et al., 2002).

Studies of extragalactic LMXBs have been mostly confined to early-type galaxies, which have much older stellar populations that yield a “pure” sample of LMXBs. Following this logic, a foundational study by Gilfanov (2004) considered the XRBs in the old stellar populations of 11 nearby early-type galaxies and found that the number of X-ray sources with $\mathrm{L_X} > 10^{37}$ erg s^{-1} (i.e. the number of presumed LMXBs), is proportional to the total stellar mass ($\mathrm{M}_{\star,\mathrm{tot}}$) of the galaxy (Figure 1.2). The integrated $\mathrm{L_X}$ is proportional to galactic stellar mass in a similar fashion, insinuating a universal XLF for LMXBs that scales with $\mathrm{M}_{\star,\mathrm{tot}}$ of the host galaxy (see also Kim & Fabbiano 2004). Thus, it is asserted that LMXBs may be a good proxy for stellar mass within old stellar populations, such as elliptical galaxies or the cores of spiral galaxies.

1.2 High-mass X-ray Binaries

The standard definition of a high-mass X-ray binary sets the mass of the donor star to 8 $\mathrm{M}_{\odot}$ or greater. At these masses, stars exhibit extreme stellar winds which may accrete directly onto the compact object (e.g. Figure 1.1). An HMXB may also experience disk-fed accretion via Roche lobe overflow, though such a configuration is unstable and extinguishes within $\sim 10^4$ years (Kretschmar et al., 2019). Unlike LMXBs, which are usually transient, HMXBs that experience direct accretion via stellar winds are persistent X-ray sources with optical and UV emission that is dominated by light from the donor star (e.g. Lutovinov et al., 2013; Bahramian & Degenaar, 2023). The typical formation mechanism of an HMXB is through the in situ evolution of massive stellar

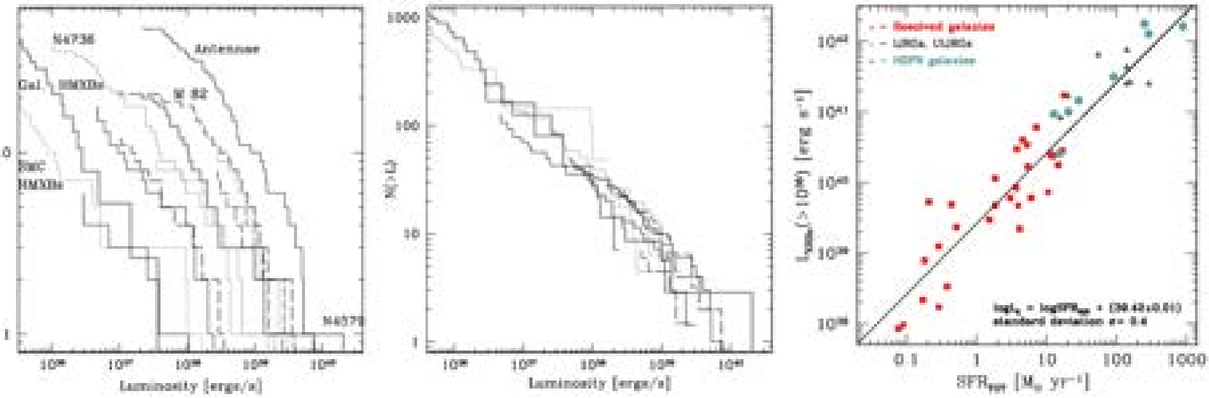

Figure 1.3 (Left) The XLFs of 14 local late-type galaxies. When normalized by the ratio of their star-formation rates (SFR) to the SFR of Antennae (Center), the XLFs align within a narrow band, indicating a strong correlation between the XLFs of HMXBs and galactic SFR. (Right) The observed correlation between the $\mathrm{L_X}$ of HMXBs and SFR of galaxies with high specific SFR. The standard deviation on this relation is roughly 0.4 dex, which may be either physical in nature or pointing to contamination in the HMXB XLF. *Source: Grimm et al. (2003a, left/center); Mineo et al. (2012, right)*

binaries, in which the transfer of mass onto the more massive companion triggers a supernova explosion and produces a tighter binary between the resulting compact object and the surviving companion (Postnov & Yungelson, 2014). If the separation between the binary objects is especially small and the accretion rate is high, this may produce X-ray luminosities up to 10^{40} erg s^{-1}.

While most HMXBs form in the galactic disk, there is also a correlation between HMXBs and nearby young clusters (within ~ 200 pc, on average) that suggests at least some field HMXBs may have originated from within compact star clusters (Kaaret et al., 2004; Zuo & Li, 2010; Rangelov et al., 2011; Poutanen et al., 2013; Fortin et al., 2022). In such cases, HMXBs may be deposited in the disk by natal kicks, ejection via dynamical interactions, or the evaporation of the parent cluster, similar to LMXBs (McSwain et al., 2007; Portegies Zwart et al., 2007; Sippel & Hurley, 2013). About 2–19% of HMXBs reside within their parent clusters in the galaxies studied thus far (Rangelov et al., 2012; Chandar et al., 2020), and there is an apparent preference for denser, more massive clusters among XRBs in clusters younger than 400 Myr (Mulia et al., 2019).

Because the lifespan of a massive star is brief — on the order of 10 Myrs or shorter (Crowther, 2012; Postnov & Yungelson, 2014) — HMXBs are only found in galaxies with relatively recent star formation and typically do not achieve significant displacement from their birth places (Fornasini et al., 2023). As such, HMXBs within the Milky Way are found at low scale heights compared to LMXBs (Grimm et al., 2002; Lutovinov et al., 2013). This has made local HMXBs difficult to observe, due to significant obscuration through the disk of the Milky Way. Nevertheless, a foundational study by Grimm et al. (2003a), based in part on *ASCA* and early *Chandra* observations of nearby starburst galaxies and *RXTE/ASM*, *ASCA* and *MIR-KVANT/TTM* studies of the Milky Way Galaxy and the Magellanic Clouds (see also Ranalli et al. 2003), first established a quantitative scaling between the integrated $\mathrm{L_X}$ of HMXBs with the star formation rate (SFR) of the host galaxy (Figure 1.3). In a follow-up study, Gilfanov et al. (2004) crystallized the notion of a "universal" HMXB XLF for star-forming galaxies, the normalization of which is proportional to the host galaxy SFR. The spatial distribution of HMXBs in the Milky Way (e.g. Coleiro & Chaty, 2013; Lutovinov et al., 2013) and other late-type (spiral) galaxies indicate that they are indeed strongly associated with regions of high star formation, such as the spiral arms or starburst cores (Shtykovskiy & Gilfanov, 2007; Politakis et al., 2020). This means the total $\mathrm{L_X}$ from HMXBs may be taken as a somewhat reliable SFR proxy in distant star-forming galaxies — with an estimated normalization factor of roughly 2.61×10^{39} erg s^{-1} per unit SFR — if one is able to determine the $\mathrm{L_X}$ contribution from LMXBs and the central AGN (Mineo et al., 2012, 2014, Figure 1.3).

1.3 Intermediate-mass X-ray Binaries

XRBs with donor star masses between the thresholds of LMXBs and HMXBs are known as intermediate-mass XRBs (IMXBs). Despite forming at least 5 times as readily as LMXBs (Pfahl et al., 2003), it is exceedingly rare to observe an X-ray luminous IMXB; intermediate-mass donor stars aren't massive enough to drive stellar winds, but are too massive to readily achieve stable mass transfer via Roche lobe overflow, since the rate of accretion onto the compact object is proportional to $\mathrm{M}_{\star}{}^{3}$ (van den Heuvel, 1975). Instead, XRBs with intermediate initial donor masses experience a very rapid thermal mass transfer phase, losing in excess of 10^{-6} $\mathrm{M}_{\odot}$ per year. Within a few thousand years, X-ray emission is extinguished, and the donor becomes a low-mass star (van den Heuvel, 1975; Kalogera & Webbink, 1996; Podsiadlowski et al., 2002). This results in a population of abnormally hot and luminous LMXBs (Podsiadlowski & Rappaport, 2000). In fact, Pfahl et al. (2003) finds that the majority of LMXBs must come from IMXB progenitors in order to explain the discrepancy between the observationally inferred vs. expected Galactic LMXB birthrates (see also Kiel & Hurley, 2006).

1.4 Ultraluminous X-ray Sources

Ultraluminous X-ray sources (ULXs) are a subset of XRBs that produce X-rays exceeding $\mathrm{L_X} \approx 10^{39}$ erg s^{-1}, the maximum expected luminosity from accretion onto a 10 $\mathrm{M}_{\odot}$ black hole. Because these mysterious objects surpass the standard Eddington limit ($\mathrm{L_{Edd}}$) of a stellar-mass compact object — above which the outward pressure from radiation overpowers the inbound gravitational force of the compact object and prevents further accretion — the nature of these sources have been a matter of great concern. Historically, there have been a few competing theories to explain these extreme luminosities: the compact object in these systems may be an intermediate-mass black hole, which would have a much higher $\mathrm{L_{Edd}}$ (e.g. Maccarone et al., 2007); they may be HMXBs that exhibit short bursts of super-Eddington accretion during periods of rapid mass transfer (Rappaport et al., 2005; Sutton et al., 2013; Fabrika et al., 2015); or they may be HMXBs with bright, anisotropically beamed X-ray emission (e.g. a microblazar; King et al., 2001; Körding et al., 2002). The discovery of a pulsating ULX in M82 (and the subsequent discovery of at least 7 more in other galaxies; Chen et al. 2021) implies that at least some ULXs are produced by a fourth channel, in which the accretor is a rapidly spinning neutron star with a strong magnetic field (i.e. a pulsar; Bachetti et al., 2014). In this model, because material is funneled along the magnetic field lines directly onto the solid surface of the neutron star, the maximum luminosity is not bound by the standard $\mathrm{L_{Edd}}$ prescription. To date, disc-wind beaming and pulsar accretion are the leading models for explaining ULX behavior, though this is still a hotly debated issue (King & Lasota, 2020; Mushtukov et al., 2020; Lasota & King, 2023).

Though the first ULX was discovered in the 1980's by the *Einstein Observatory* (see Fabbiano, 1989), the past 20 years of *Chandra* and *XMM-Newton* observations have led to the discovery of over 1000 ULX candidates throughout the Universe (Walton et al., 2022). Several multi-wavelength studies have sought to identify the counterparts to these ULXs in UV, optical, IR, and radio wavebands (e.g. Heida et al., 2014; Avdan et al., 2019; López et al., 2020; Allak, 2023). For example, some ULXs observed in optical and radio bandpasses have been shown to be coincident with ionized nebulae up to hundreds of parsecs in radii (Pakull & Mirioni, 2003; Russell et al., 2011). Such systems can be used to exclude beaming along our line of sight if the nebulae are X-ray ionized. On the other hand, some ULXs appear to have point-like counterparts, and their SEDs suggest many are photometrically consistent with giant or supergiant stellar companions (e.g. Gladstone et al., 2013; Heida et al., 2014; Lau et al., 2019). These candidate donor stars represent a promising sample of targets for radial velocity measurements, which could then be used to place constraints on the masses of the compact component (e.g. Motch et al., 2014; Kaaret et al., 2017). However, some ULXs have been shown to exhibit X-ray to optical flux ratios similar to that of LMXBs, which may suggest their optical emission is dominated by X-ray reprocessing within the accretion disk (Tao et al., 2011). If this is the case for the typical ULX, then direct observation of the donor star may be impossible for extragalactic ULXs. Complicating matters further, a growing number of ULXs are found to be associated with compact clusters, including a rare subset of ULXs within GCs that appear to have peculiar properties compared to the general cluster population (Heida et al., 2014; Lau et al., 2019; Dage et al., 2021; Dage et al., 2024). Given the variety of configurations ULXs can take, multi-wavelength studies remain a crucial avenue for understanding the nature of these enigmatic objects.

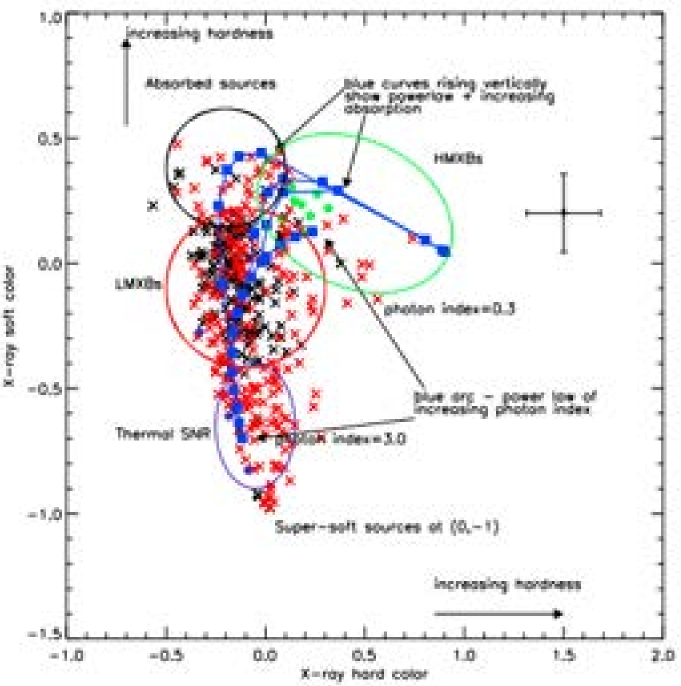

Figure 1.4 The X-ray color distribution of X-ray sources in a sample of 5 nearby galaxies, with ellipses representing the proposed color classifications. *Source: Prestwich et al. (2003)*

1.5 Disentangling XRB Populations

While the XRB population in early-type galaxies is exclusively comprised of LMXBs, both LMXBs *and* HMXBs must be present in star-forming, late-type galaxies. These populations differ in formation methods, evolutionary paths, lifespans, and abundances, so distinguishing between LMXBs and HMXBs is key to modeling their impact on the overall population. Disentangling these XRBs has proven difficult over the past 20 years. In the Milky Way, it is possible to directly observe the donor stars of XRBs and derive the LMXB and HMXB populations. A study of *Rossi X-ray Timing Explorer* all-sky data by Grimm et al. (2002) found that XRBs in the Milky Way are distributed such that HMXBs tend to avoid the central few kpc of the Galaxy, while LMXBs are more densely distributed within the Galactic Bulge. Furthermore, the association between HMXBs and the spiral arms of the Galaxy reveals a connection between the HMXB XLF (and total $\mathrm{L_X}$) and SFR (Grimm et al., 2003b), setting up SFR as a means for probing the HMXB population.

Outside of the Milky Way, studies of XRB populations in spiral galaxies were (until recently) primarily X-ray based. Prestwich et al. (2003), for example, proposed that sources with hard X-ray colors found in galactic disks are likely HMXBs, while sources in the bulges of galaxies exhibit spectral properties consistent with LMXBs. However, this study also cautions that classifying sources based on X-ray colors alone is impossible, largely due to intrinsic overlap among different

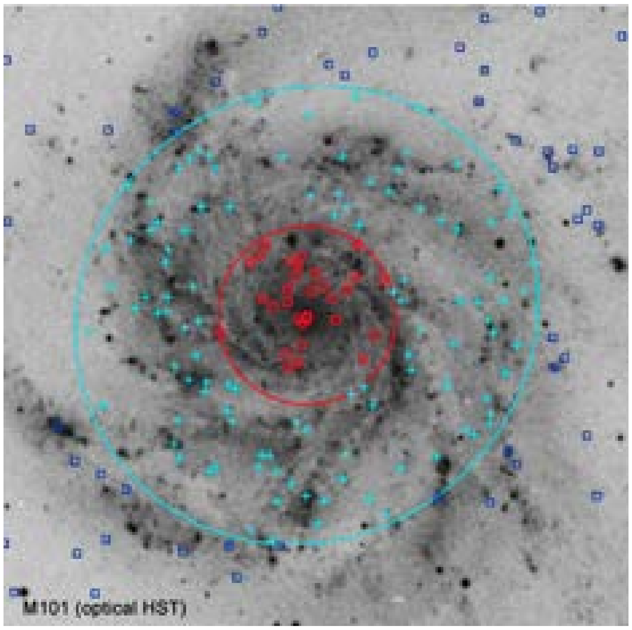

Figure 1.5 The division of XRBs by their spatial distributions. In studies of late-type galaxies that use this technique, the bulge of the galaxy (red) is considered to be dominated by LMXBs, while the disk (cyan) is dominated by HMXBs. *Source: Mineo et al. (2012)*

classes of X-ray emitters and the effects of absorption (Figure 1.4). Nevertheless, this division of XRBs by their spatial distribution proved useful for early investigations; because HMXBs are not expected to stray far from regions of recent star formation and have much higher formation efficiencies than LMXBs (Mineo et al., 2012; Antoniou et al., 2019), HMXBs were assumed to dominate the disks of spiral galaxies, while LMXBs dominate the central bulges (Figure 1.5). By relating the X-ray luminosities in these regions to SFR or $\mathrm{M}_\star$ tracers in other wavelengths (Fabbiano et al., 1982; David et al., 1992; Kennicutt et al., 1994; Kennicutt, 1998; Fabbiano & Shapley, 2002; Tzanavaris et al., 2013; Lower et al., 2020), HMXB-SFR and LMXB-$\mathrm{M}_\star$ relations were established for external spiral galaxies. These relations have progressively improved with the growing archive of deep *Chandra* observations of spiral galaxies (e.g. Grimm et al., 2003a; Ranalli et al., 2003; Gilfanov et al., 2004; Gilfanov, 2004; Mineo et al., 2012).

Decades of progress in XRB research culminated in the recent work by Lehmer et al. (2019). This study made a crucial advancement in modeling XRBs using sub-galactic maps of the $\mathrm{M}_\star$ and SFR of 38 nearby spiral galaxies (e.g. Figure 1.6) to generate a new global XLF for XRBs. By tying XRB classification to local galactic properties, Lehmer et al. (2019) created a $\mathrm{M}_\star$- and SFR-dependent XLF that simultaneously fits for the contribution from LMXBs, HMXBs, and background X-ray sources, allowing us to decompose the total XLF into its component parts with only a few inputs. This powerful approach reveals a smooth, progressive decline in the XLF normalization per unit SFR, accompanied by a decrease in normalization at the bright-end with

Figure 1.6 Examples of the sub-galactic property maps from Lehmer et al. (2019). Displayed here are the $\mathrm{M}_{\star}$, SFR, and sSFR (SFR/$\mathrm{M}_{\star}$) maps of M81, where lighter regions correspond to higher values of the respective physical property.

increasing specific SFR (sSFR, defined as the ratio SFR/$\mathrm{M}_{\star}$) as the dominant contribution to the XRB population shifts from LMXBs to HMXBs (Figure 1.7). The study also unveils interesting subtleties in the XLFs, such as a flattening of the HMXB XLF between $10^{38} - 10^{40}$ erg s^{-1} and a possible disagreement in the LMXB XLF slopes below 10^{38} and above 10^{39} erg s^{-1} compared to the results obtained for elliptical galaxies only (Zhang et al., 2012). This further emphasizes the need to move beyond a one-size-fits-all XLF.

1.6 Scientific Motivation

Due to the complicated mix of LMXBs and HMXBs within late-type galaxies, most modern analyses are only able to approximate the contributions of each to the total X-ray emission of their host galaxies, either by their spatial distributions or by relating L_{X} to $\mathrm{M}_{\star}$ and SFR. Early LMXB studies, for example, select massive elliptical galaxies with negligible SFRs to ensure no HMXB contamination, while HMXB studies focus on galaxies with high sSFR to minimize the contribution from LMXBs (e.g. Grimm et al., 2003a; Gilfanov et al., 2004; Mineo et al., 2012). While practical, these selection strategies may introduce biases in the inferred XLFs. Lehmer et al. (2019), on the other hand, took a different approach by incorporating both the local $\mathrm{M}_{\star}$ and SFR (measured at the sub-arcminute level via spatially-resolved multiwavelength observations) directly into the models, resulting in the most comprehensive XLFs to date.

Nevertheless, environmental nuances may impact the XLF scaling relations in ways that are difficult to account for. From a theoretical standpoint, large variations in the normalization of the LMXB XLFs are to be expected with stellar age (Zhang et al., 2012), while metallicity effects are

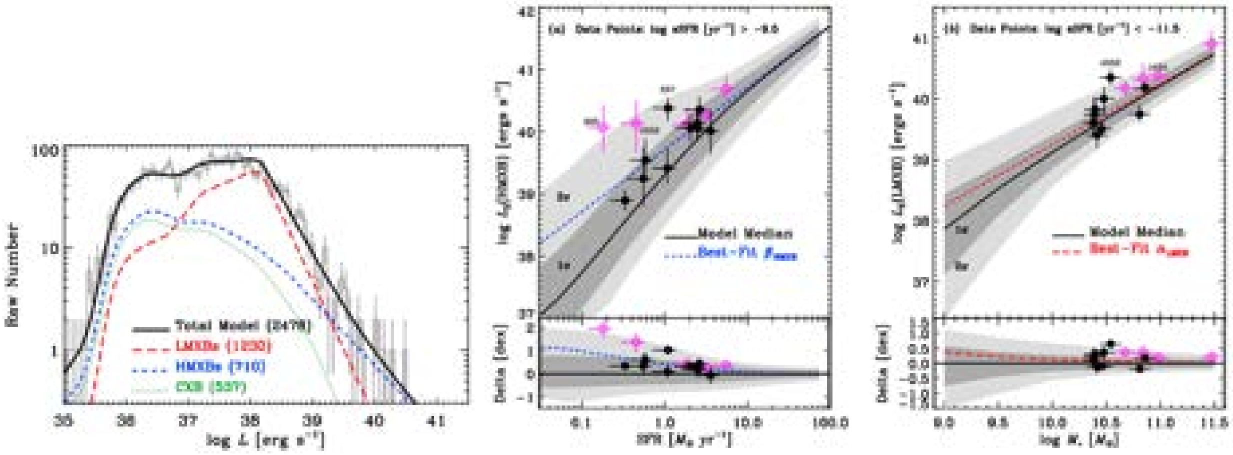

Figure 1.7 (Left) The modeled contribution from LMXBs, HMXBs, and cosmic X-ray background (CXB) sources using sub-galactic $\mathrm{M}_\star$/SFR maps. (Center/right) The best-fit (a) HMXB-SFR and (b) LMXB-$\mathrm{M}_\star$ correlations resulting from the global broken power-law (black) and single power-law (magenta) XLF models. *Source: Lehmer et al. (2019)*

expected to drive variations in the HMXB XLF of roughly an order of magnitude (Fragos et al., 2013). Metallicity can also affect the XLF of GC XRBs, as red GCs are more often associated with bright LMXBs (Jordán et al., 2004; Kim et al., 2006; Sivakoff et al., 2007; Peacock et al., 2017a; Kim et al., 2013; Luan et al., 2018). The notion that both age and metallicity have sizable effects on the XRB XLFs is consistent with the apparent redshift evolution of $\mathrm{L_X}/\mathrm{M}_\star$ and $\mathrm{L_X}$/SFR, whereby the cosmic decline in mean stellar age and metallicity would be responsible for the inferred increase of both ratios with z (Lehmer et al. 2016; Aird et al. 2017, and references therein). Deep, high-statistics XLFs have only been assembled for nearby galaxies spanning a relatively limited range in both age and metallicity (see, e.g., Irwin et al. 2004; Colbert et al. 2004; Kaaret et al. 2011; Prestwich et al. 2013; Plotkin et al. 2014; Basu-Zych et al. 2016; Tzanavaris et al. 2016; Wang et al. 2016), so it is difficult to determine to what effect these correlations may have on the accuracy of XLF-derived XRB population models. Moreover, the XRB XLFs could contain significant contamination from unidentified supernova remnants (Long et al. 2014), which could comprise a large fraction of the total X-ray source population in a galaxy at increasing SFRs.

One way to prevent these complicating factors from affecting our observations of LMXBs and HMXBs is to directly identify their donor stars. While this would have been impossible 30 years ago, the exquisite angular resolution now provided by both the *Chandra* and *HST* extends our ability to directly observe these populations beyond the Milky Way and into nearby galaxies. This was the motivation behind the recent study by Chandar et al. (2020): leveraging *HST* multi-band imaging data, they obtain photometric measurements of the optical counterparts to point-like, *Chandra*-detected sources in M101, which they then compare to stellar evolutionary models to estimate the donor star masses. The study demonstrated the ability of *HST* imaging to detect stars down to $\sim$3 $M_\odot$ at the distance of M101, enabling a source-by-source classification of LMXBs and HMXBs via observations of their donor stars. By construction, this procedure does not rely on underlying assumptions about the relationship between a galaxy's XRB populations and their local environments.

The work presented in this dissertation improves upon the techniques developed in Chandar et al. (2020) to explore the extragalactic XRB populations of nearby late-type galaxies through *direct* classification. In Chapters 2 and 3, I leverage the unmatched angular resolution of *Chandra* and high-resolution optical imaging and photometry from HST to infer the masses of the donor stars around a sample of spatially-resolved X-ray sources, thereby obtaining direct observations of the LMXB and HMXB populations in M83 and M81. Departing from population studies of the XRBs of single galaxies, Chapters 4 and Chapter 5 focus on populations of galaxies: in Chapter 4, I explore the correlation between XRBs and the properties of the clusters that host them using state-of-the-art PHANGS cluster catalogs in combination with *Chandra* observations of 6 spiral galaxies; and finally, in Chapter 5, I extend this methodology to examine the optical counterparts of 48 ULXs in 28 galaxies within 15 Mpc.

CHAPTER 2

XRBs in M83

The work in this chapter was originally published in the Astrophysical Journal (vol. 912, pg. 31) under the title "Calibrating X-Ray Binary Luminosity Functions via Optical Reconnaissance. I. The Case of M83.". The results of that work — produced in collaboration with Elena Gallo, Rupali Chandar, Paula Johns Mulia, Angus Mok, Andrea Prestwich, and Shengchen Liu — are introduced here. For a complete reading, please see Hunt et al. (2021).

2.1 Abstract

In this chapter, I construct XLFs for different classes of XRB donor stars through a novel methodology: rather than classifying LMXBs vs. HMXBs based on the scaling of the number of X-ray sources with stellar mass and star formation rate, respectively, I utilize multi-band *HST* imaging data to classify each *Chandra*-detected compact X-ray source as a low-mass (i.e. donor mass $\lesssim 3$ $\mathrm{M}_\odot$), high-mass (donor mass $\gtrsim 8$ $\mathrm{M}_\odot$) or intermediate-mass XRB based on either the location of its candidate counterpart on an optical color-magnitude diagram or the age of its host star cluster. In addition to the the standard (single and/or truncated) power-law functional shape, I approximate the resulting XLFs with a Schechter function. I identify a marginally significant exponential downturn for the high-mass XRB XLF, at $\log\mathrm{L}_\mathrm{X} \simeq 38.56^{+0.64}_{-0.36}$ in log CGS units. In contrast, the low- and intermediate-mass XRB XLFs, as well as the total XLF of M83, are formally consistent with sampling statistics from a single power-law. A comparison of our measured XLFs with predictions from state-of-the-art XRB XLF models shows good agreement for low-mass XRBs, but suggests that previous, X-ray data-based high-mass XRB XLFs likely encompass truly high-mass as well as intermediate-mass donor XRBs.

2.2 Introduction

In a recent endeavor to properly characterize the XLFs of both HMXBs and LMXBs in late-type galaxies, Lehmer et al. (2019, hereafter L19) fit the XLFs of 38 nearby galaxies spanning a broad range of SFR and $\mathrm{M}_\star$ with a global model which fits simultaneously for the contributions from HMXBs, LMXBs and background sources using sub-galactic SFR and stellar mass maps (see also Lehmer et al. 2017, and references therein, for other examples of sub-galactic modeling studies). This powerful approach reveals a decline in the XLF normalization per unit SFR, accompanied by a decrease in normalization at the bright-end with increasing sSFR, revealing a shift in the dominant XRB population from LMXBs to HMXBs. The study also unveils a flattening of the HMXB XLF between $10^{38} - 10^{40}$ erg s^{-1} and slopes for the LMXB XLF that differ from those observed in elliptical galaxies (Zhang et al., 2012). This emphasizes the need to move beyond a one-size-fits-all XLF modeling concept.

Motivated by similar considerations, this chapter follows a very different approach to disentangling the LMXB and HMXB XLFs: by leveraging *HST* multi-band imaging data, I directly classify the optical counterparts to *Chandra*-detected point-like X-ray sources in the field of view of the target galaxy. This technique, which was developed for and tested on the nearby spiral galaxy M101 by Chandar et al. (2020, hereafter C20), hinges on the notion that, on average, *HST* imaging enables the direct detection of XRB donor stars down to a given distance-dependent mass limit (e.g., down to ~3 M$_\odot$ at the distance of M101). By construction, this procedure does not rely on underlying assumptions about the relationship between a galaxy's XRB populations and their local environments. It also enables us, for the first time, to elucidate the role of intermediate-mass XRBs, i.e. with donors in the $\sim$ 3–8 $\mathrm{M}_\odot$ range.

Here, I introduce a number of improvements upon C20 and apply this revised methodology to M83 (NGC 5236). M83 is a face-on (i = 24°; Talbot et al. 1979) spiral galaxy with $\mathrm{M}_\star \sim 2 \times 10^{10}\ \mathrm{M}_\odot$, a moderate SFR of $\approx 2.5\ \mathrm{M}_\odot$ yr^{-1} (L19), and no significant contribution in the nuclear region from an active galactic nucleus (AGN). At a distance of 4.66 Mpc (Saha et al., 2006), yielding a distance modulus of 28.32 and a physical scale of $1''\approx$ 22 pc, it is closer than M101 (6.4 ± 0.2 Mpc, with $1'' \approx$ 31 pc). Furthermore, the Galactic absorption is low along the line of sight to M83 ($\mathrm{N_H} = 4 \times 10^{20}\mathrm{cm}^{-2}$; Kalberla et al. 2005), making it ideal for an optical photometric study of X-ray source populations.

In this chapter, I present a fully classified catalog of X-ray sources in M83 that builds upon that published in L19. Each source is classified on a source-by-source basis as either a low-, intermediate-, or high-mass XRB, a background galaxy, or a supernova remnant (SNR). We then use these classifications to construct uncontaminated XLFs for each XRB population. The main goal is to assess the shape of the XLFs and establish whether or not there is evidence for a statistically significant cut-off at the bright end, the presence of which has been widely debated (e.g. Zhang et al. 2012; Mineo et al. 2012; C20). We are also interested in the normalization of each XLF, and how well it matches predictions from the global model presented by L19. The rest of this work is organized as follows: in §2.3, I identify the optical counterparts to X-ray sources in M83, separating out contamination (AGN, foreground stars, and SNR, §2.3.4) from the XRBs, which may appear as an individual donor star or existing within a parent cluster; in §2.4, I investigates the spatial distribution of the classified XRBs; in §2.5, I present Schechter and power-law function fits to the the XRB XLFs and assess the presence of a downturn or cut-off; and finally in §2.6, I compare our optical data-based XLFs with the literature (namely, L19).

2.3 Source Classification

2.3.1 X-ray Source Catalogs

As our primary X-ray point-source list, I adopt the M83 catalog constructed from deep *Chandra* ACIS imaging data by L19. The L19 study includes a thorough estimate of the completeness of the detected X-ray point sources, which is crucial to our purposes. The *Chandra* data were reduced following the methods detailed in Lehmer et al. (2017): for each galaxy, the analysis was restricted to data sets with aim points within $5'$ of the nominal center position, ensuring a sharp point spread function for the nuclear regions, which tend to be the most crowded.

Out of a total of 456 point-like sources brighter than $\mathrm{L_X} = 10^{35}$ erg s^{-1}, I restrict my analysis to the 325 objects that fall within the M83 *HST* footprint, shown in Figure 2.1. For comparison, L19 restricts its XLF fitting to those 363 sources that are located within an ellipse that traces the $K_s \approx 20$ mag arcsec^{-2} galactic surface brightness (Jarrett et al., 2003), outlined in white.

Long et al. (2014) also published a catalog of X-ray point sources in M83 based on a partial set of the same data used in L19. The main focus of their work was to detect a sample of SNRs using multi-wavelength observations. In §2.3.4 I use classification information provided in this SNR catalog to eliminate SNRs and some background AGN from our initial X-ray point source catalog.

2.3.2 Combining X-ray and Optical Data

HST observations of M83 were taken with the WFC3/UVIS instrument, spanning seven fields that each cover approximately $162'' \times 162''$ for a total mosaic area of ~ 43 arcmin^2. All observations

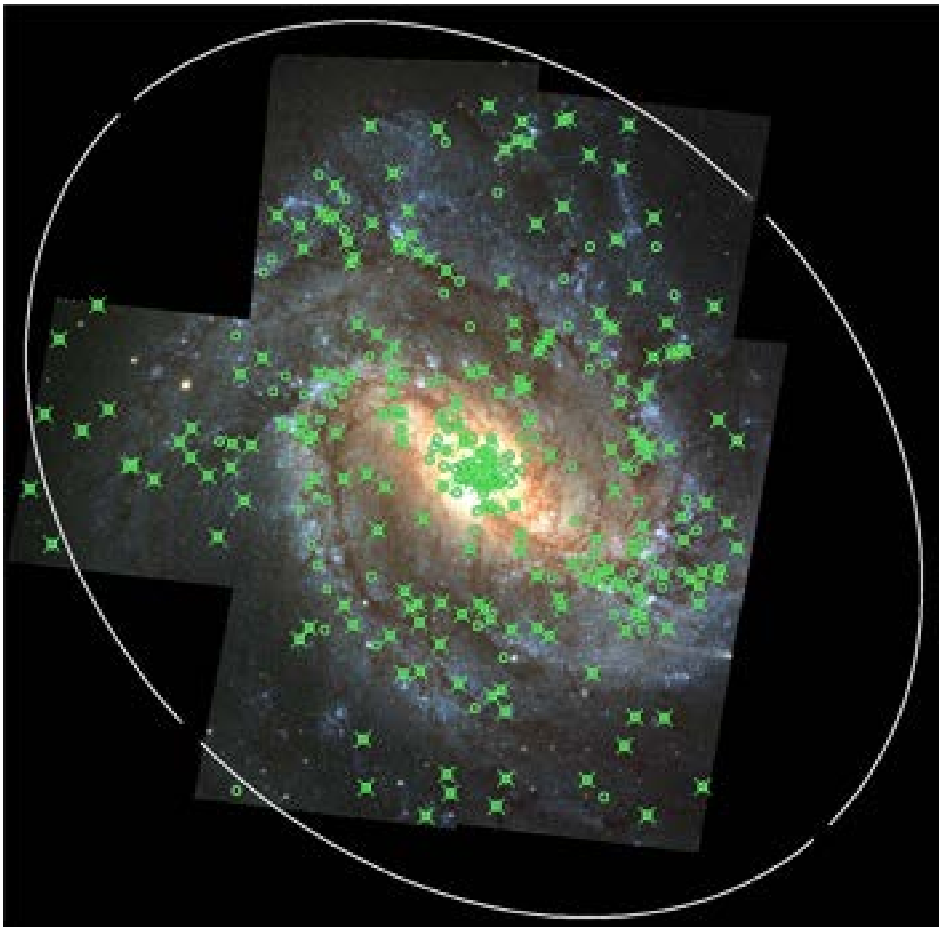

Figure 2.1 An optical image of M83 taken with by the WFC3/UVIS camera on *HST* (Blair et al., 2014, available at `https://archive.stsci.edu/prepds/m83mos`). The B-band is shown in blue, V-band in green, and I-band in red. The 7-pointing mosaic covers ≈ 43 arcmin^2 (75.2 Mpc^2) The locations of all X-ray sources from the L19 catalog (adopted here and shown as green circles) and those from the version 2.0 release of the Chandra Source Catalog (green X's) are shown. The galactic footprint adopted by L19 tracing the $\mathrm{K_s} \approx 20$ mag arcsec^{-2} galactic surface brightness (see Jarrett et al., 2003) is outlined in white for comparison.

were obtained between August 2009 and September 2012 by R. O'Connell (Prop ID. 11360) and W. Blair (Prop ID. 12513), with exposure times ranging from ~ 1.2–2.7 ks for each image. Images were downloaded from the Hubble Legacy Archive (HLA[1]). In general, BVI images are created using the F438W, F547M, and F814W filters. The central field, which includes the galaxy nucleus, uses the broader F555W rather than F547M V-band filter. I also use U-band images (F336W) to help calculate cluster ages (see §2.3.5).

Figure 2.1 shows a BVI mosaic of all seven M83 *HST* fields (available on the HLA; Blair et al. 2014). The mosaic combines the two different V-band filters used for the central field (F555W)

---

[1] `http://hla.stsci.edu/`

and the 6 remaining fields (F547M) by scaling the F555W data to match the scaling on F547M. I utilize this single, cohesive V-band image for correcting the relative astrometry between *Chandra* and *HST* observations. To perform the astrometric astrometric correction between the optical and X-ray coordinates, 6 X-ray sources whose *HST* counterparts are clearly background galaxies (as judged by morphology and color; see §2.3.4 for details) are identified as reference sources. For these objects, I calculate a median relative positional offset of $\sim 0.''079$ and $0.''229$ along the x- and y-axes of the *HST* image respectively, with standard deviations of $0.''177$ and $0.''182$. The X-ray centroid positions of all sources in our sample are shifted by these offsets to the positions indicated on Figure 2.1 in green.

2.3.3 Candidate Optical Counterparts

Optical counterparts to XRBs in M83 can be either donor stars or host stellar clusters. I use the IRAF DAOFIND task to detect all point-like sources, down to the faintest levels, on the composite V-band image. I perform aperture photometry with the IRAF PHOT task using a 3 pixel aperture radius for each detected source, with the local background level determined in an annulus with radii between 20 and 25 pixels. Due to the rescaling of the F555W field for the creation of the mosaic, which may have introduced calibration errors, photometry of all detected sources is performed on individual images rather than on the mosaic. Aperture corrections of -0.48 mag (V) and -0.61 mag (I) were determined by taking the median difference between the magnitude in 3 and 20 pixel apertures of several relatively bright, isolated stars with smooth radial profiles that flatten towards the background sky magnitude with increasing aperture radius.

An additional correction term of -0.06 mag is added to each filter to correct for the small amount of flux missing from a 20 pixel aperture (see Encircled Energy Fractions from 20 pixels to infinity in Deustua et al. 2017). These instrumental magnitudes are converted to the VEGAMAG system by applying the zero-point magnitude for each filter as reported in Table 2 of Deustua et al. (2017).

Candidate optical counterparts to each X-ray source are initially selected by applying a proximity criterion to the X-ray source positions. I define 1- and 2-σ positional uncertainty radii for each source by adding in quadrature the standard deviation in the *Chandra*-*HST* positional offsets and the X-ray positional uncertainty (see Figure A.1). The latter depends sensitively on the X-ray source distance from the observation aim-point, as well as the number of counts. I adopt Equations 14 and 12 in Kim et al. (2007) to calculate the 68% and 95% confidence positional uncertainty for each source, as a function of total counts (C) and off-axis angle (OAA) — both of which are available in the L19 catalog. An additional uncertainty term is added to the 1- and 2-σ radii calculated above, due to the slight rotations between the fields and the mosaic. This is an improvement on the method used in C20, where the 1- and 2-σ positional uncertainties in M101 were assumed to be circles with a radius of $0.3''$ and $0.6''$ for each X-ray point source. A final correction is made to the absolute optical magnitudes of each source to account for foreground extinction. Using the relation $\mathrm{N_H(cm^{-2})} = (2.21 \pm 0.09) \times 10^{21}\mathrm{A_V}$ (Güver & Özel, 2009) with the known Galactic absorption towards M83 (Long et al., 2014), I find an extinction of $\mathrm{A_V} \approx 0.174$ mag, corresponding to a reddening of $\mathrm{E(B-V)} \approx 0.054\ \mathrm{mag}$ (Mathis, 1990). I do not account for extinction intrinsic to each source, though I employ a confidence flag scheme (see Table A.1) to indicate sources that may be particularly susceptible to the effects of reddening and obscuration within M83.

2.3.4 Non-X-ray Binary Sources

Contributions from stellar sources such as coronally active binaries and cataclysmic variables are completely negligible above $L_X \simeq 10^{36}$ erg s^{-1} (Boroson et al., 2011), the completeness limit of this sample (L19). Hence, the main sources of contamination are background AGN and quasars, and bright SNRs within the host galaxy. I address them in turn below. My approach differs substantially from all other XLF investigations in that I aim to directly identify and reject all contaminants, whereas published works almost exclusively correct for AGN contamination statistically using the known Cosmic X-ray Background $\log N - \log S$.

In an extended, multi-wavelength spectral and temporal analysis of M83's X-ray point-source population, Long et al. (2014) classified a significant fraction of the point source population as SNR. These were classified based on variability, spectral hardness, [S II]:Hα line ratios or strong [O III] emission, and cross-referencing with earlier SNR catalogs using *Chandra*, *XMM-Newton*, Magellan, the Australia Telescope Compact Array, and the sites of historical supernovae (Wood & Andrews, 1974; Soria & Wu, 2003; Maddox et al., 2006; Dopita et al., 2010; Blair et al., 2012; Ducci et al., 2013).

Long's investigation provides us with the rare opportunity to construct a set of X-ray based diagnostic criteria that can be used to reject contaminants that have not been previously classified, and that are typically ignored in other studies. Out of the 87 X-ray sources identified by Long et al. (2014) as SNRs or SNR candidates, 76 are included in the *HST* footprint. Of these, 55 have available X-ray soft and hard counts (S and H, corresponding to the 2-7 keV and 0.5-1.2 keV bands, respectively) in the CSC R2. I obtain a hardness ratio — defined as the difference between H and S over the summed counts in both — for each source where available. I plot the measured X-ray luminosity, $\mathrm{L_X}$ (from L19), against the hardness ratio in Figure 2.2. The Long et al. (2014) SNR (red $+$'s), AGN (orange circles) and XRB (green X's) classifications are indicated where given.

I find that the majority of SNRs belong to a distinct parameter space that is well separated from

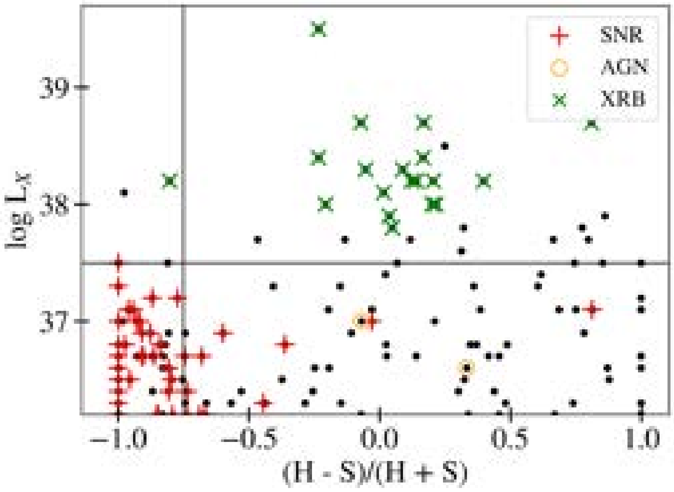

Figure 2.2 The measured X-ray luminosity vs. hardness ratio of sources in M83, with the subset classified as SNRs, AGN, and XRBs by Long et al. (2014) indicated. The hardness ratio is defined as the difference between the hard band (2–7 keV; H) and the soft band (0.5–1.2 keV; S) *Chandra* counts over their sum. I define a selection criteria that cuts sources with X-ray log luminosities below 37.5 and hardess ratios less than -0.75, the limit softer than which 60% of the sources are SNRs, to minimize contamination from unclassified SNRs in our sample.

other X-ray sources. Based on this phenomenological approach, I adopt minimum L_X and HR cuts to automatically select out candidate SNRs in our catalog. Our L_X cut is set to the highest L_X of the Long SNRs in our sample, or $\ell \leq 37.5$, where (hereafter) ℓ represents logarithmic X-ray luminosities in units of erg s^{-1}. The minimum HR is chosen such that 60% of all sources softer than this limit are Long-classified SNRs, which corresponds to HR ≤ -0.75. Excluding (76) X-ray sources classified by Long et al. (2014) as candidate SNRs, an additional 27 sources meet our criteria. All 27 X-ray sources with these properties are rejected from our catalog. I assess the impact of this on the XLFs in §2.6.2 and the Appendix.

After removing SNRs, the remaining population of contaminants consist of background AGN and quasars. The rest may be identified through catalog cross-referencing and an analysis of optical properties. Long et al. (2014) classify several foreground and background contaminants based on X-ray hardness, X-ray-to-optical flux ratios, color, and prior catalogs. I classify additional contaminants on the basis of their morphology and optical colors. Background galaxies can typically be identified by their distinct morphologies, including features such as nuclei, spiral arms and/or disks, with the exception of distant quasars, which appear in optical images as red point sources. I identify candidate quasars as point sources which have colors and magnitudes that fall red-ward of the theoretical evolutionary mass tracks for solar metallicity stars from the Padova models (Bertelli et al., 1994; Girardi et al., 2010; Marigo et al., 2017). These tracks are shown in Figure 2.4. In

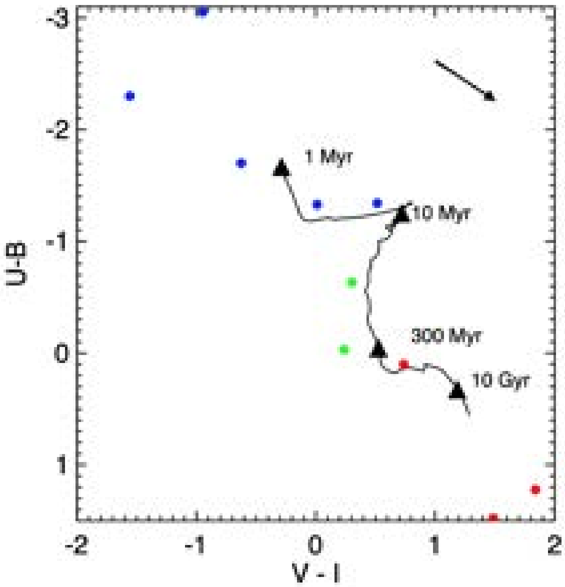

Figure 2.3 The measured $U - B$ vs $V - I$ colors of XRB host clusters compared with predictions for the color evolution of clusters from the Bruzual & Charlot (2003) models. Different model ages are marked. The arrow represents the direction of reddening expected from a Milky Way-type extinction curve with $A_V = 1$.

total, I remove 3 visually identifiable background AGN and 4 candidate quasars from our sample, as well as 2 sources identified as AGN in Long et al. (2014).

2.3.5 Classification of XRBs Based on Parent Cluster Age

We expect to find some XRBs in this sample still living within the stellar clusters in which they formed. In early-type galaxies, between 25–70% of LMXBs are found in ancient globular clusters (Angelini et al., 2001; Kundu et al., 2002; Jordán et al., 2004; Kundu et al., 2007; Humphrey & Buote, 2008; Peacock & Zepf, 2016). In star-forming late-type galaxies, however, the fraction of LMXBs found in globular clusters remains quite uncertain, albeit significantly lower: the dwarf starburst NGC 4449 and the spiral galaxy M101 each has only a single LMXB in a globular cluster (Rangelov et al. 2011; C20). The fraction of HMXBs which still reside in their parent clusters is also poorly known but tentatively higher, with $\approx 15\%$ of XRBs in M101 (C20) and $\approx 25\%$ in the Antennae (Rangelov et al., 2012) found in clusters younger than a few 100 Myr.

Because of the high stellar density within compact star clusters, the donor stars feeding XRBs that reside in clusters cannot be identified individually at the distance of M83. However, the ages of parent clusters can be used as a proxy for estimating the masses of the donor stars in XRBs, since the most massive surviving stars within a cluster are the most dynamically active, and hence the most likely to form tight binaries. High mass stars ($\geq 8\ M_{\odot}$) have hydrogen burning lifetimes of only ~ 10 Myr, and intermediate-mass ($\gtrsim 3\ M_{\odot}$) stars have lifetimes of ~ 400 Myr. This means that clusters older ~ 400 Myr only contain stars less massive than $3\ M_{\odot}$, and hence host LMXBs, while clusters younger than ~10 Myr are likely to host HMXBs. We assume that clusters with ages between 10 and 400 Myr host IMXBs, since the most massive stars remaining in clusters in this age range have intermediate mass.

To identify possible clusters among our candidates, I compare our optical matches for each XRB to a catalog of M83 clusters by Chandar et al. (2014). This catalog selected clusters by the full width at half maximum (FWHM) of their radial profiles, which are broader than the point spread function (PSF), as well as by their Concentration Index, defined as the difference in magnitudes measured for a 1 and 3 pixel aperture radius (see Chandar et al. 2014 for details about selection). I find that a total of 10 ($\sim 5\%$ of the total) XRBs in M83 are found within a compact stellar cluster. I compare the colors measured for the XRB host clusters with those predicted by the Bruzual & Charlot (2003) cluster color evolution models at solar metallicity in Figure 2.3. These models start at 1 Myr (upper left) and go through 13 Gyr (lower-right), with key ages marked along the model track. XRB cluster hosts have a range of colors and hence ages.

While the color-color diagram provides a good visual comparison of cluster colors with model predictions, the age of each cluster is actually estimated using a spectral energy distribution fitting method, where we fit for the best combination of age and reddening, as described in Chandar et al. (2014). Magnitudes measured in the UBVI and Hα filters for each cluster are fit to predictions from Bruzual & Charlot (2003) using a standard χ^2 minimization. The best fit age for each cluster is recorded in Table A.1 and used to classify each XRB: HMXBs have parent clusters < 10 Myr, IMXBs have parent clusters with best fit ages between 10–400 Myr and LMXBs have parent cluster ages > 400 Myr.

2.3.6 Classification of XRBs Based on Donor Star Mass

The majority of X-ray sources contain at least one optical point source within their 2-σ radius, with several coincident with multiple candidates. The most likely XRB donor is chosen on a case-by-case basis. Priority is given to brighter sources that fall within or closest to the 1σ radius. In most cases, it is not necessary to identify the exact donor of an XRB with several bright candidates, so long as the candidates fall within the same mass regime.

The masses of bright donor candidates may be estimated by comparing them to the Padova models on a color-magnitude diagram (CMD, Figure 2.4). Using the mass limits defined in §2.2 (LMXB $\leq 3\ \mathrm{M}_{\odot}$, HMXB $\geq 8\ \mathrm{M}_{\odot}$), I directly assign masses to each donor star based on where they fall with respect to the theoretical mass tracks. C20 find that archival *HST* images of M101

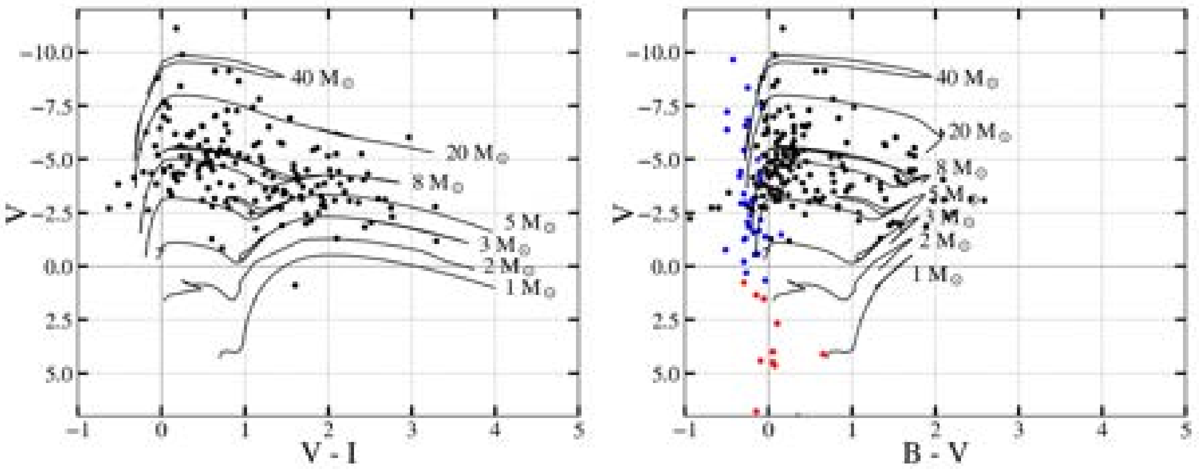

Figure 2.4 (Left) The $V - I$ vs. V CMD of XRB donor star candidates identified in M83 (black points). These are compared with theoretical evolutionary tracks modeled at solar metallicity (Bertelli et al., 1994; Girardi et al., 2010; Marigo et al., 2017). Overall, donor stars in M83 appear to be detectable with the *HST* down to $\gtrsim 3\ \mathrm{M}_\odot$. (Right) The $B - V$ vs. V CMD of candidate XRB donor stars. In addition, all X-ray bright Milky Way HMXBs and LMXBs having measured B and V magnitudes are shown as blue and red points, respectively, as identified by Liu et al. (2006) and Liu et al. (2007).

are deep enough to see stars down to 3 $\mathrm{M}_\odot$ at a distance of 6.4 ± 0.2 Mpc. Consistent with this, I find that the majority of the M83 XRB donors lie above the 3 $\mathrm{M}_\odot$ line, with a few sources falling below. This suggests that, indeed, we are able to detect sources down to the minimum threshold required to identify the donor stars of HMXBs within M83. On the other hand, X-ray sources that lack an optical counterpart likely have stellar components that fall beneath the 3 $\mathrm{M}_\odot$ threshold, suggesting the system is a LMXB.

The left and right panels of Figure 2.4 compare the V-I colors of each XRB to their B-V colors. Note, I am unable to extract B-band magnitudes from all of the point sources I detect in this sample due to the fact that the observations are not as deep in the B-band as they are in the V-band. Nevertheless, the absolute luminosities do not change relative to the evolutionary tracks, which is most important for estimating the masses of the donor stars.

In total, 212 of the 325 X-ray sources that fall within the *HST* footprint are classified as XRBs using the methods described, 10 of which exist within compact stellar clusters. I present these sources, their positions, X-ray luminosity, optical colors, and source classification in Table A.1 and Figure A.1 in the Appendix. For these X-ray sources, I find 68 are LMXBs, 79 are HMXBs, and 65 fall in the intermediate mass range between the two limits[2]. For each of the panels in Figure A.1,

---

[2] As discussed in §1.3, true IMXBs are exceedingly rare due to unstable mass transfer within this mass range. While I describe these sources simply as IMXBs in this chapter, the actual nature of these sources is uncertain and is a subject for future research. For a deeper discussion, see Chapter 3.

the 1- and 2-σ positional uncertainties are shown as yellow concentric circles, each detected optical source within the 2-σ radius is highlighted by smaller yellow circles, and the chosen donor is circled in red. In both Table A.1 and Figure A.1, italicized SNRs are those classified using our HR–L_X criterion described in §2.3.4 (as opposed to those identified directly in Long et al. 2014), italicized XRBs are those associated with clusters, and classifications in parentheses are objects with uncertain "candidate" classifications, as reported in Long et al. (2014) or as determined by the methods described in this work.

2.3.7 Assessing Misclassifications

While careful consideration is given to identifying LMXBs and HMXBs from each other and also from non-XRBs, misclassifications are still possible. Here, we discuss possible sources of misclassification, our methods for mitigating these occurrences, and the impact their inclusion could have on the final XLFs.

- A background AGN/quasar that is severely obscured by an optically thick portion of M83 could mimic an X-ray source with no detectable optical counterpart (LMXB). This type of misclassification will preferentially affect the inner and disk regions, a relatively small area of the total coverage. I estimate the dust obscured area within which we cannot see background galaxies to be roughly 20,000 arcsec^2 by inspecting the color mosaic image. Scaling the detected rate of 1,000 sources per square degree in the *Chandra*Deep Field down to similar flux levels as used here (Luo et al., 2017), we expect 1-2 background galaxies to fall within these optically thick regions and hence be misclassified as a LMXB. This is compared to a total expected count across the area covered by the full mosaic (155,402 arcsec^2) of 11-12 background galaxies; there are 9. At least one of the galaxies in our sample (L19X178) is totally obscured. Another (L19X181) is barely visible in a region with high background brightness and some dust extinction. In all, our observations match expectations.

- Distant quasars appear as red, point sources in optical images, and therefore could potentially be mistaken for a red giant donor star in a HMXB system. In fact, I identify 4 optical counterparts to X-ray point sources that have colors which are redder than the predicted stellar evolutionary tracks, which I classify as candidate quasars. Overall, the space density of quasars on the sky is quite low, with only $\sim$ 100 expected per square degree with X-ray fluxes in our catalog. This suggests we should expect 1-2 quasars in our field of view (155,402 arcsec^2), roughly consistent with our observations.

- A star in a dusty region can experience partial or total extinction, resulting in a lower mass estimate. Potentially, this could lead to HMXBs misidentified as IMXBs, particularly those that are near the 8 $M_\odot$ track. In §2.5, we construct XLFs of the XRB populations and find there is little difference in the shape of the HMXB XLF compared to the IMXB XLF. We conclude that any misclassification of HMXBs due to extinction will likely not cause major changes in the shape of the XLFs.

On the other hand, it is highly unlikely that a HMXB would be misidentified as a LMXB based on extinction in M83, because of the significant level required, which is not supported by a visual inspection of the optical color images.

- A high mass star may happen to lie coincident with an LMXB, causing the LMXB to be misidentified as an HMXB. However, massive stars are comparatively rare relative to lower mass stars within galaxies, and also highly concentrated spatially to regions of active star formation, such as the spiral arms (as is the case for M83 in §2.4). Similarly, XRBs themselves are uncommon. Statistical arguments therefore suggest that the chance superposition of these two relatively rare phenomena is unlikely[3].

  As a final precaution, I compare our maps of the XRB populations to the stellar mass and SFR maps of M83 published by L19. Since LMXBs and HMXBs are tracers of stellar mass and sSFR respectively, we expect a correlation between the locations of these populations and peaks in the stellar mass and sSFR maps. I examine these in §2.4.

- A parent cluster might be misidentified as a single donor star, leading to an improper mass estimate using its $V - I$ color and V magnitude rather than the age of the cluster. We expect very few, if any, misclassifications of this type, since clusters at the distance of M83 are more extended than the PSF. To minimize mis-identifications, I cross-reference these sources with the published M83 cluster catalog published by Chandar et al. (2014).

- An LMXB might potentially flare at the time of observation, causing its disk luminosity and color to mimic that of a high mass donor star. The probability of this occurring is statistically negligible, at the level of 1 object per Milky Way stellar mass or so (i.e. well above the inferred stellar mass content of M83).

2.4 X-ray source Spatial Distributions

In general, owing to the the short lifetimes of the donors, HMXBs trace regions of recent star formation, whereas LMXBs trace the integrated stellar mass content. Almost all previous works

---

[3] The statistical likelihood of such a superposition is further explored in §3.5.1

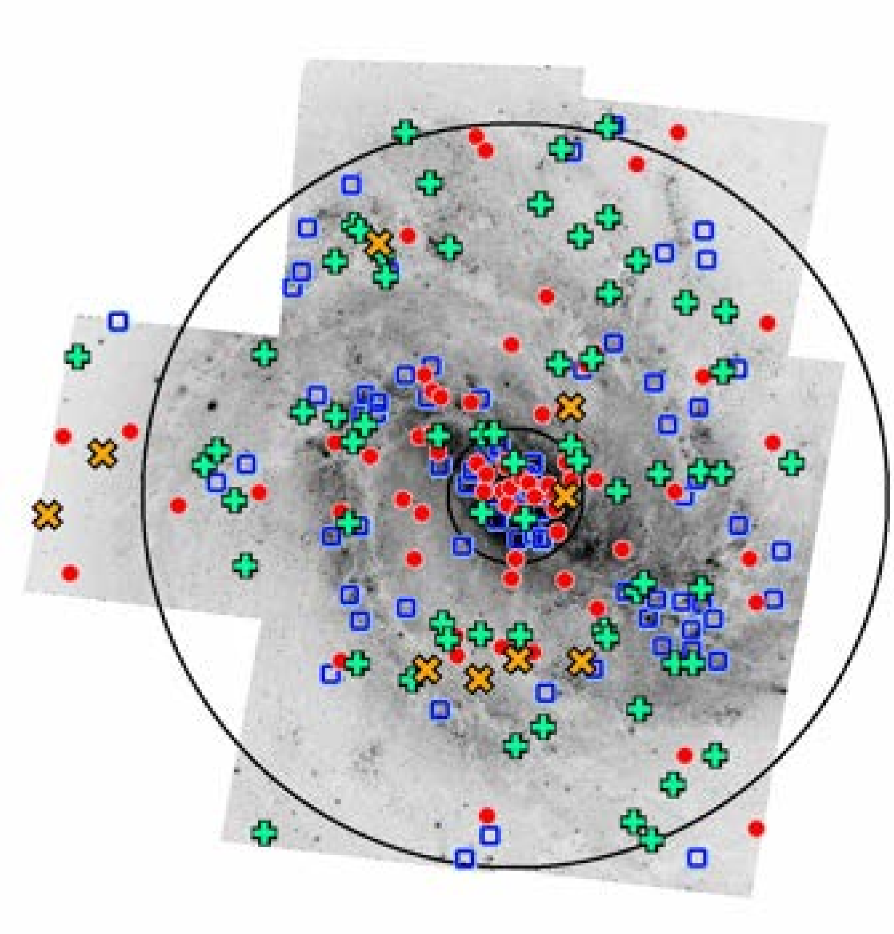

Figure 2.5 The spatial distribution of LMXBs (red points), IMXBs (green crosses), and HMXBs (blue boxes) in M83, as well as background galaxies (orange X's). Black outlines encircling the bulge and inner disk regions at $\sim 0.'66$ and $3.'66$ follow the prescription by Mineo et al. (2012), with the bulge radius from Dottori et al. (2008).

have taken a statistical approach to classifying and studying populations of HMXBs and LMXBs, typically based on their location relative to different galactic structures (e.g., bulge, disk or outer region, as identified by, e.g., Mineo et al. 2012) or based on the SFR or stellar mass at their location (L19). However, there are dynamical processes that can impart high spatial motions to XRBs, thereby moving them away from their sites of formation, and we would not expect a perfect spatial correlation in any case. This means that statistical and spatially-based classifications are likely to have at least a few erroneous classifications of individual sources. In this Section, we study the locations of HMXBs, IMXBs, and LMXBs based on our source-by-source classification method.

Figure 2.5 shows the spatial distribution of each class of XRB: HMXBs (blue diamonds), IMXBs (green crosses), and LMXBs (red points). I also find 9 AGN/quasars (orange X's). The

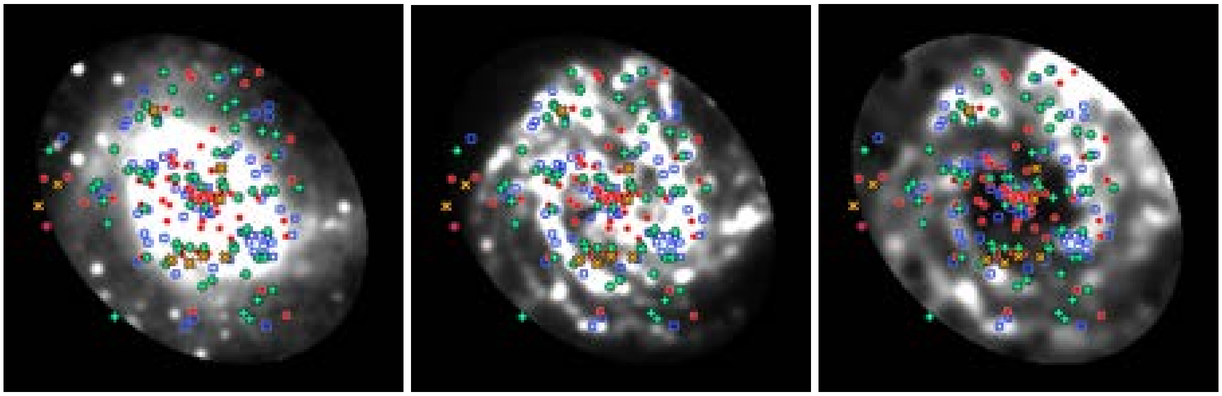

Figure 2.6 Overlays of LMXBs (red points), IMXBs (green crosses), HMXBs (blue squares), and background galaxies (orange X's) onto the (Left) stellar mass, (Center) star formation rate, and (Right) specific star formation rate maps for M83 generated by L19. All three maps are shown with a linear color scale.

classifications are over-plotted on three different maps of M83 constructed by L19: stellar mass ($M_\star$; top), SFR (middle), and specific star formation rate (sSFR=SFR$/M_\star$; bottom). These maps show both a high stellar mass *and* a high SFR in the central region, higher SFRs in the spiral arms, and significantly higher sSFR in the arms compared to the inter-arm regions.

In the central $0.'66$ or 894 pc of M83, there are a total of 45 XRBs; of these, 22 are HMXBs and 19 are LMXBs. This high fraction of HMXBs is perhaps not surprising, since M83 has a central starburst. However, it is different than the central region of M101, which is strongly dominated by LMXBs, even though it is a later-type galaxy with a smaller bulge.

Most HMXBs outside of the central region are found in regions of high sSFR. There are a few in 'dark' regions in the right-panel of Figure 2.6; these may be sources with high spatial motions that have moved from their birth-sites. HMXBs also tend to be preferentially found in the spiral arms, with a fairly 'clumpy' rather than even distribution.

LMXBs appear fairly centrally concentrated as expected from an old spheroidal (bulge/halo) population. There are however, sources distributed fairly evenly throughout M83, which may come from an old disk population. There are also a few LMXBs further away from the center and located in regions of high sSFR, i.e. where the SFR strongly dominates over the stellar mass. I checked the local background in these regions: extinction appears to be lower than closer to the center of M83, and the background level is sufficiently low that we would easily be able to detect donor stars down to 3 $\mathrm{M}_\odot$. These sources would be misclassified as HMXBs in studies that use a spatial approach, since they fall within a region of high sSFR (L19) and also within the 'disk' region, as defined by Mineo et al. (2012) and typically believed to be dominated by HMXBs. The distribution of IMXBs appears to be fairly evenly distributed throughout the disk of M83, like the LMXBs, although some what clumpier and more likely to be found in regions of sSFR.

2.5 X-ray Luminosity Functions

A key goal of characterizing the XLF(s) of XRBs is to ascertain whether a statistically significant downturn exists at high luminosities. Theoretically, a "cutoff" is expected near the Eddington luminosity for stellar-mass compact objects, but observations have yet to confirm this prediction with high confidence. Assessing the presence and robustness of such a downturn is inherently dependent upon the chosen functional shape of the XLFs. Virtually all investigations of XRB XLFs perform either single power-law (PL) or broken-power law (BPL) fits to the differential and/or cumulative XLFs, often with an assumed cutoff luminosity. To first order, most studies conclude that a single PL with a high-energy cutoff at or above the maximum measured XRB luminosity adequately describes the shape of the luminosity distribution of HMXBs in highly star forming galaxies (Mineo et al., 2012). For LMXBs, the XLF is modeled with either a single or a broken power-law (Kim & Fabbiano, 2004; Kim et al., 2009; Zhang et al., 2012; Lehmer et al., 2019), plus a high-luminosity cutoff.

There is, however, little physical motivation for adopting a BPL shape for the LMXB XLF; this approach dates back to the seminal work by Gilfanov (2004), who first noted that the XLF of LMXBs in external galaxies "is consistent with a power law with differential slope of $\simeq 1$ at low luminosities, gradually steepens above ℓ = 37.0–37.5 and has a rather abrupt cut-off at ℓ = 39.0–39.5." In later works, the best-fit values of the break and cutoff luminosities fall near $\ell \simeq 38$ and $\ell \simeq 40$, respectively. However, the lack of a unified approach (e.g., fitting cumulative vs. differential and/or binned vs un-binned distributions; fixing vs. fitting for the cutoff luminosity) makes it somewhat difficult to compare results across different studies. Furthermore, whether the presence of a break and/or a cutoff in the XLFs is required by the data with high statistical confidence remains an open, key question, whose answer is again intertwined with the choice of the XFL functional shape.

As shown by Mok et al. (2019) in their thorough exploration of the mass function of young star clusters (see also C20, and references therein), methods that bin the differential distribution in luminosity (or mass) intervals result in stable fits for the power-law indices, while fits to the un-binned distributions give the most robust detection of any downturn at higher luminosities.

Guided by the above considerations, we approximate the shape of the XRB XLF in M83 with two functional shapes: a single PL, and a Schechter function (Schechter, 1976). we fit the X-ray luminosity distribution of the (a) composite sample, i.e., all XRBs, as well as (b) HMXBs, (c) IMXBs, and (d) LMXBs, separately.

To assess the presence of a truncation – here defined as a luminosity above which no sources exist – we adapt the methodology developed by Rosolowsky (2005) to investigate the shape of the mass function of giant molecular clouds. To account for the presence of a maximum luminosity value (L_c) in the distribution, we approximate the cumulative distribution as:

$$N(>L) = N_0 \left[\left(\frac{L}{L_c} \right)^{\beta+1} - 1 \right], \tag{2.1}$$

where N_0 is the number of XRBs more luminous than $2^{1/(\beta+1)} L_c$, at which point the distribution shows a significant deviation from a single power law of index $(\beta + 1)$. In the case where $N_0 \simeq 1$, there is no significant deviation, and the distribution is consistent with sampling from a single power law (with this formalism, the cumulative mass distribution below L_c is proportional to $(L/L_c)^{\beta}$).

The (differential) Schechter luminosity distribution is proportional to $(L/L_\star)$ — where $L_\star$, known as the Schechter "knee", corresponds to a characteristic luminosity above which the distribution declines exponentially — as follows:

$$\frac{dN}{dL} = N_\star \left(\frac{L}{L_\star} \right)^{\beta} \exp^{-(L/L_\star)}, \tag{2.2}$$

where $N_\star \Gamma(1 + \beta, 1)$ is the number of galaxies with $L > L_\star$, and $\Gamma(-b, y)$ is the incomplete gamma function. This well-known functional shape provides a good analytical approximation to the measured luminosity (and/or mass) distribution of astronomical objects across a wide dynamic range.

We examine the shape of M83's XLFs with three methods:

1. We perform a single PL fit to the differential luminosity distributions, binned in intervals with an equal number of sources. This method yields the most stable and robust constraints to the power-law index of the distribution (Mok et al., 2019).

2. We utilize the IDL script `MSPECFIT` (Rosolowsky, 2005) to fit a single PL — with and without truncation — to the un-binned, cumulative luminosity distributions. This method is sensitive to the presence of a downturn at high luminosities, i.e., it serves to identify a characteristic luminosity above which the distribution declines sharply (if any).

3. We perform a Maximum Likelihood (ML) fit with a Schechter function to the un-binned differential luminosity distributions, following Mok et al. (2019). This method does not use binned data (which can hide weak features at the ends of the distribution), nor cumulative distributions (where the data points are not independent of one another). It thus gives the

most robust test for the presence of a statistically significant *exponential* decline at high luminosities.

The top, middle and bottom panels of Figure 2.7 illustrate the results of method (1), (2), and (3), respectively. Unless otherwise noted, fits are performed above the 90% completeness limit of $\ell = 36.2$ identified by L19.

Fitting the differential XLF of M83 (composite sample) with method (1), using bins by 10 sources each, yields a slope of $-\beta = 1.40 \pm 0.05$. The inferred slopes for the HMXB, IMXB, and LMXB XLFs are, respectively $-\beta = 1.35 \pm 0.10; 1.61 \pm 0.11; 1.49 \pm 0.08$, suggesting that the HMXBs are characterized by a somewhat shallower overall distribution (top panels of Figure 2.7; adopting bins of $3, 5$ and 7 sources yields consistent results, within the uncertainties).

With respect to the presence of a break, method (2) and (3) give consistent, and interesting, results. Fits to the cumulative XLF with a truncated power law (TPL) indicate that the HMXB XLF is the only distribution that shows any statistically significant evidence, at the $\sim 2.5\sigma$ level, for a high-energy cutoff (this is indicated by values of the N_0 parameter in excess of unity in the middle panels of Figure 2.7).

The ML fits with a Schechter function confirm this trend. The bottom panels in Figure 2.7 show the 1-, 2-, and 3-σ confidence contours for the best-fit values of the Schechter slope and knee luminosity. The best-fit values are indicated by the dashed black lines. The upper limit to the knee luminosity was set to be 100 times higher than that of the brightest XRB in each sample, ensuring convergence in all cases. A formally statistically significant detection of the exponential cutoff would be seen as closed 3σ contours in these diagrams. We find only marginally significant evidence (at the 1 to 2σ level) for an exponential cutoff at the bright end of the composite XLF, suggesting that M83's XLF is formally consistent with the expectations of sampling statistics from a single power-law. This is true for the composite XLF as well as individual donor classes. Interestingly though, in line with the conclusions from method (2), the presence of a (marginally significant) exponential cutoff is entirely driven by the HMXB population, which exhibits a knee at $\ell = 38.56^{+0.64}_{-0.36}$ (at the 1-2σ level), whereas the LMXB and IMXB XLFs show no evidence for a statistically significant dive (as indicated by the open 1σ contours in the third and fourth plots in the middle panel of Figure 2.7).

In summary, when approximated by a single PL, the composite XRB XLF of M83 has an index of -1.40 ± 0.05; the shapes of the XLFs for the HMXB, LMXB, and IMXB populations show marginal deviations, with HMXBs having a shallower slope than both LMXBs and IMXBs. Our maximum likelihood fits to the Schechter function do not find formally statistically significant

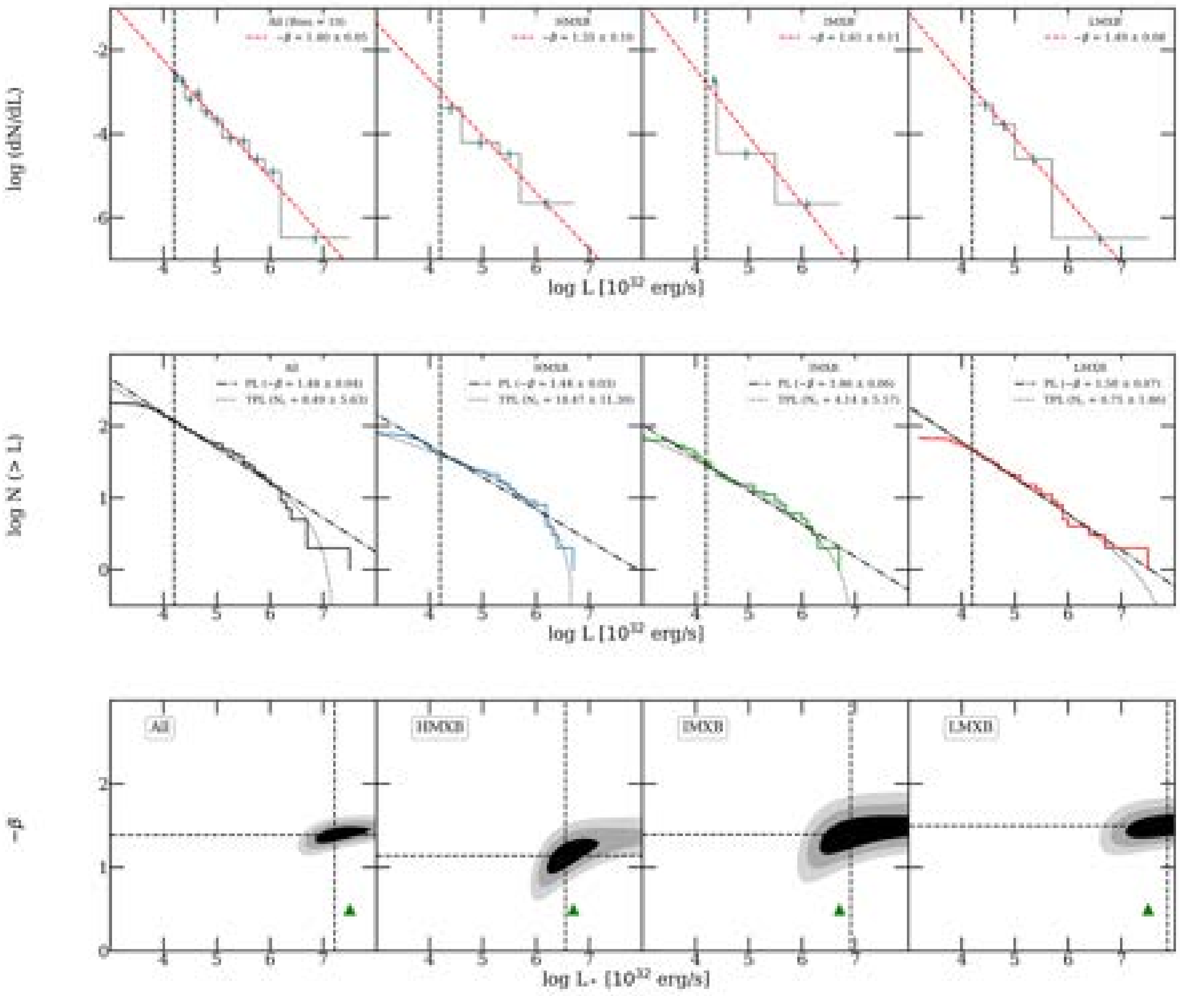

Figure 2.7 (Method 1, top): Fits to the differential XLFs, binned in intervals of $N = 10$ sources per bin (following Mok et al. 2019).
(Method 2, middle): Fits to the cumulative, un-binned XLFs with a single power law (PL) and a truncated power law (TPL Rosolowsky, 2005). For the top and middle panels, the dashed black vertical line indicates the 90% completeness limit of $\ell = 36.2$, above which the fits are performed.
(Method 3, bottom): Maximum Likelihood fits to the cumulative XLF with a Schechter function, following Mok et al. (2019). The dashed black lines indicate the best fit values for the slope and knee luminosity. Contours refer to the 1-, 2- and 3-σ confidence levels. The green triangles indicate the luminosity of the brightest object within each sample; if the best fit knee luminosity is greater than the maximum luminosity probed by the sample, the presence of an exponential downturn is not significant.

evidence for an exponential cutoff at the bright end of the luminosity functions. However, in combination with the results from the cumulative XLF fits, we find weak evidence (at the $\sim 2.5\sigma$ level) for a high-energy cutoff in the HMXB XLF, at $\ell \simeq 38.74 \pm 0.13$.

In §2.6.2, I compare our fit results for the XLFs of different populations in M83 with those from previously published results for M83, as well as average XLFs derived from large samples of (star forming) galaxies.

2.6 Discussion

2.6.1 The Nature of Donor Stars in HMXBs

The majority (144 out of 212) of M83's XRBs have candidate donors that I classified as either intermediate (3–8 $M_\odot$) or high-mass (> 8 $\mathrm{M}_\odot$) stars based on the evolutionary tracks in Figure 2.4. A few detected donors fall beneath the 3 $\mathrm{M}_\odot$ threshold and are considered LMXBs. One source falls well beneath the 1 $\mathrm{M}_\odot$ line; this is likely a spurious detection in a low-luminosity region, which is appropriately classified as low-mass.

Interestingly, we find that the majority of the intermediate and high-mass donor stars do not follow the blue main sequence ridge that runs along the left side of the models, but rather occupy the redder portion of the evolutionary tracks. While this is likely due to a combination of effects, the majority of these objects are likely truly evolved stars. To start with, HMXBs are typically wind-fed: the brightest of these will be those objects with more evolved donors, leading to lower surface gravity and thus higher wind loss rates.

Indeed, the brightest, persistent HMXBs in the Milky Way (MW) and Magellanic Clouds (Grimm et al., 2003a) have either evolved or peculiar main sequence donor stars; these include, e.g., a blue supergiant in Cygnus X-1 (MW); a (high-extinction) Wolf-Rayet star in Cygnus X-3 (MW); a blue supergiant in GX 301-2 (MW); a blue supergiant in SMC X-1; a main sequence B stars with highly distorted shape in LMC X-1; and an evolved O star in LMC X-3 (Liu et al., 2006). Generally speaking, about 60% of the MW HMXBs are known or suspected Be/XRBs, while 32% are supergiant/X-ray binaries Liu et al. (2006). Whereas Be/XRBs in very blue bands may be expected to be close to the main sequence, their decretion disks are extremely red, and can move the overall color off of the main sequence. At the same time, since bright Be/XRBs are predominantly *transients* rather than persistent, they are less likely to be represented in our investigation with respect to truly evolved stars.

The right panel of Figure 2.4 shows a comparison of M83's detected donors (in black), with all of the X-ray bright[4], MW XRBs listed in the Liu et al. (2006) and Liu et al. (2007) catalogues (blue points for HMXBs, red for LMXBs), and for which measured B and V magnitudes are available (i.e., these are intrinsically blue systems, for which extinction within the Galactic disk does not prevent a detection in the optical). Apparent magnitudes were converted to absolute

---

[4] Brighter than 0.2 μJy in the 2-10 keV range, as measured by the *Rossi X-ray Timing Explorer*; this corresponds to roughly $\ell \simeq 36$ erg s^{-1} at the distance of M83.

values using the formula $M = m + 5 - A_V - 5\log d$, where d is the distance of the source in pc and A_V is the interstellar extinction given by Liu et al. (2006) and Liu et al. (2007). The distance to each source was approximated by the relation $A_V \approx 2r$ mag for sources with a galactic latitude $b < 2^\circ$, where r is the distance in kpc. It is reassuring that, even based on this cursory conversion, the division between HMXBs and LMXBs among MW objects aligns nicely with the expected V magnitudes of each class as we define them in M83.

Lastly, contamination to M83's candidate HMXB population from exceptionally bright, disk-fed LMXBs, where the disk optical luminosity and colors can mimic a HMXB donor is technically possible but statistically negligible, at the level of roughly 1 object per MW stellar mass. The only persistent MW analog would be the black hole XRB GRS 1915+105; less than a handful of other Galactic systems, mainly long-period neutron stars, have comparable luminosities, but the associated outburst duty cycles make them statistically negligible, too.

2.6.2 M83 XRB XLFs: Comparison with previous results

A word of caution must be exercised when making direct comparisons with the published XLFs, for a number of reasons. First, our optical CMD-based approach enables us to *directly* differentiate between low- and high-mass XRB donors. In contrast, purely X-ray data-based XLF investigations indirectly differentiate between HMXBs and LMXBs by positing that the former population scales with star formation rate, and the latter with stellar mass. X-ray based studies do not explicitly differentiate between intermediate, vs. low or high-mass XRB donors. Rather, the assumption is made that the SFR-tracing XRB population maps into truly high-mass donors ($\gtrsim 8\ \mathrm{M}_\odot$). In turn, this hinges on the assumption that the adopted SFR tracer is sensitive to truly instantaneous, and hence very-short lived, star formation episodes. Our optical reconnaissance XRB classification enables us, for the first time, to test the above assumption. Since previous works have classified all XRBs into only high- or low-mass, it is not clear where the sources I classify as IMXBs end up in those studies. In particular I compare whether the inferred number of objects in each category agree with the expectations from the published XLFs, where HMXBs are allegedly truly high-mass donors.

Additionally, with the exception of L19 (which is discussed in detail below), all prior X-ray based investigations of high- vs. low-mass XRB XLFs rely on the assumption of little or no contamination to the compact X-ray population other than from cosmic background sources, which is typically minimized by limiting the search radius. While this is well justified, e.g., for massive elliptical galaxies, which are notoriously devoid of HMXBs, it is not necessarily valid for, e.g., star forming spirals, where a non-negligible fraction of the disk XRBs are likely LMXBs, particularly in mildly star forming galaxies. Furthermore, the contamination from SNRs has also been historically neglected.

The most recent and detailed analysis of XRB XLFs to date is presented by L19: they consider a sample of 38 nearby galaxies (including M83) spanning a vast range of morphologies and specific star formation rates. They use spatially resolved SFR and stellar mass maps to divide the ($\sim$2500) *Chandra*-detected X-ray sources into several sSFR bins, and derive a global model for the scaling of the HMXB XLF with SFR and of the LMXB XLF with $\mathrm{M}_\star$ (accounting for the cosmic background X-ray sources with a model that scales with sky area). In addition, they present 'standard' XLF fits for each of the target galaxies; these are computed following a forward-fitting approach where the XRB and cosmic X-ray background source contributions are fit for simultaneously, and convolved with a completeness function for each galaxy. For each galaxy, the XRB contribution to the (differential) XLFs is modeled as either a single or a broken PL (see equations 4 and 5 in L19 for the adopted functional shapes). For practical purposes, the break and high-energy cutoff luminosity for the individual galaxy fits are fixed to $\ell_\mathrm{b} = 38.0$ and $\ell_\mathrm{c} = 40.3$, respectively. A detailed comparison to those results, including broken power-law fits, is presented in the Appendix B. Here, I focus on the broad picture, and particularly on whether our classification hints at any high-level discrepancies with the literature.

For M83, L19 reports a slope of $-1.56^{+0.05}_{-0.04}$ for the single PL fit to the composite XLF. This value is slightly steeper than the value ($-\beta = 1.40 \pm 0.05$) inferred from our preferred method (1), as well as method (2) ($-\beta = 1.48 \pm 0.03$). We suspect that the reason for this mild discrepancy has to do with the issue of SNR contamination, which I further discuss below.

Perhaps more interesting is to assess whether the XLF is best described by a single PL or exhibits any evidence for a statistically significant deviation (in the form or a break, downturn, of cutoff). L19 concludes that, with the exception of one target, a single PL provides a statistically acceptable fit to the data of all 38 galaxies under examination, including M83. They note that, while broken power law fits typically provide improvements to the fit statistics, in very few cases are those improvements statistically significant. This is qualitatively consistent with our quantitative analysis results, where the composite XLF of M83 is consistent with being sampled from a single power law, with only marginal evidence for a (HMXB-driven) downturn.

Next, I compare the results obtained for the HMXB, LMXB, and IMXB populations to the global HMXB and LMXB XLFs derived by L19[5]. Starting with the slopes, the L19 HMXB XLF

---

[5] For the purpose of this comparison, I refer to the best-fitting parameters from their "Cleaned Sample" (which excludes from the sample five galaxies with low metallicity and three others with high specific number of globular

is best modeled as a single PL with slope -1.66 ± 0.02 (below a cutoff luminosity $\ell_c = 40.8^{+0.50}_{-0.20}$). For the LMXB XLF, the best-fit model is a broken PL with slopes $-1.31^{+0.05}_{-0.07}$ and $-2.57^{+0.54}_{-0.28}$, respectively below and above a break luminosity of $\ell_b = 38.33^{+0.21}_{-0.17}$, plus a high-energy cutoff at $\ell_c = 40.8^{+0.5}_{-0.2}$.

The fits to the HMXB XLF of M83 with a single PL model, with method (1), yield a shallower slope, with $-\beta = 1.35 \pm 0.10$. In terms of preferred functional shape, as discussed in §2.5, the cumulative XLF fit shows evidence (at the $\sim 2.5\sigma$ level) for a downturn in the HMXB population, at $\ell = 38.74 \pm 0.13$. This is confirmed by the ML fits with a Schechter function, which also find marginal evidence, at the 1-2σ level, for an exponential decline of the HMXB XLF at $\ell \simeq 38.56^{+0.64}_{-0.36}$.

A key finding in L19 indicates that the measured HMXB XLF has a more complex shape than previously reported, more so than even then single PL shape derived by the same authors; it exhibits a rapid declines between $\mathrm{L_X} \simeq 10^{36}$–$10^{38}$ erg s^{-1}, a 'bump' between 10^{38}-10^{40} erg s^{-1}, and an approximately exponential decline above 10^{40} erg s^{-1}. Not surprisingly, such level of complexity is not evident within M83's XLF. Similarly, our analysis does not indicate any significant deviation from a single PL for the LMXB XLF of M83, albeit this may again be due to small number statistics (the reader is referred to the Appendix for a direct comparison with L19 using a broken power-law approximation of the XLF).

Some of the above discrepancies, such as the steeper slope obtained by L19 when fitting M83's total XLF, are likely driven by the high degree of SNR contamination to the M83's X-ray source population (Long et al. 2014; this is less likely to affect our conclusions regarding the presence of a downturn, since all the sources I classified as SNRs are fainter than $\ell = 37.5$). As detailed in §2.3.4, based on the dedicated study by Long et al. (2014), I classified 103 of M83's X-ray sources as SNRs; 77 out of those 103 are brighter than the 90% completeness limit of $\ell = 36.2$, above which all fits are performed. While a detailed analysis of how this affects the measured XLF slopes for each XRB group is deferred to the Appendix, here I focus on comparing the *number* of sources that I classify as HMXBs, LMXBs and IMXBs against the expectations from the global HMXB and LMXB XLFs obtained by L19[6].

Starting with HMXBs, L19 quote a normalization value $K_{\mathrm{HMXB}} = 2.06^{+0.16}_{-0.15}$ per $M_{\odot}\mathrm{yr}^{-1}$ at $\ell = 38$. By convolving the *HST* footprint (155,403 arcsec^2) with M83's star formation rate map (shown in Figure 2.6), I estimate an enclosed SFR of 2.28 $M_{\odot}$ yr^{-1}. Adopting this value, M83 is then expected to have $\simeq 104$ HMXBs with $\ell \geq 36.2$. This is to be compared with 41 HMXBs

---

clusters).

[6] For this purpose, I adopt their best-fit values for the Cleaned sample and multiply the expected number of sources by the constant scaling factor $\omega = 0.95$, inferred by L19 specifically for M83.

identified by our optical reconnaissance analysis above the 90% completeness limit. If, for the sake of being thorough, I also consider those X-ray sources that were rejected as SNRs based on the cuts made in §2.3.4, I would gain an additional 34 high-mass objects, for a total of 75 HMXBs.

For LMXBs, I estimate that the *HST* footprint encloses 2.01×10^{10} $\mathrm{M}_{\odot}$ in stellar mass; with a LMXB XLF normalization value $K_{\mathrm{LMXB}} = 26.0^{+3.4}_{-2.4}$ per 10^{11} $\mathrm{M}_{\odot}$, the L19 XLF then predicts $\simeq$ 48 LMXBs above $\ell \geq 36.2$. I classify 48 sources as LMXBs above $\ell \geq 36.2$, totalling to 69 with the inclusion of rejected SNRs. Additionally, I identify 31 IMXBs above $\ell \geq 36.2$, plus an additional 22 SNRs, though the population of IMXBs remains necessarily ambiguous in term of which XLF they belong.

While the absolute numbers are less important (the global XLFs by L19 have a scatter of 0.4 dex; we might be missing a few sources that are local to M83 but are located outside of the *HST* footprint; additionally, candidate SNRs may be rejected too aggressively), this exercise shows that, for a galaxy with the mass and SFR of M83, based on state-of-the-art XLF models, *about 1/3 of the detected XRBs ought to be LMXBs*. For M83, our optical classification recovers this fraction remarkably well (regardless of SNR contamination). At the same time this implies that, for M83, the global HMXB XLF by L19 may encompass both truly high-mass as well as intermediate-mass donor XRBs.

In practice, whether X-ray based HMXB XLFs also include intermediate mass donors, with intermediate lifetimes between low- and high-mass stars, almost certainly depends on the star formation *history* of the host galaxy. Given the remarkably good agreement between our low-mass population and that predicted by L19's global LMXB XLF, and the fact that M83 has been forming stars at a fairly constant rate over at least the last several 100 Myr, I suggest that X-ray based models for HMXB XLFs may include both actual high-mass donors, but also a substantial number of these apparently intermediate-mass ones.

2.7 Summary and Conclusions

Building on the methodology developed by C20 for M101, I carry out an optical reconnaissance study of the XRB population in the nearby, star forming spiral galaxy M83. This method allows us to *directly* characterize the donor stars of each *Chandra*-detected compact X-ray source as low-, vs. intermediate- vs. high-mass stars by comparing their donor stars to stellar evolutionary models or by estimating the ages of their parent clusters using optical photometry from multi-band high-resolution *HST* imaging, while also enabling a direct identification of background contaminants. Similar to what was found by C20 for M101, I show that high-quality *HST* imaging of the star forming spiral M83 enables the direct detection of an optical counterpart down to about 3 $\mathrm{M}_{\odot}$.

After accounting for SNR contamination (which is especially severe in the case of M83), the differential XRB XLF of M83's is best fit by a single power law with slope $-\beta = 1.40 \pm 0.05$. At variance with previous studies, I also explore a Schechter function as a physically motivated alternative to the cutoff and/or broken power laws that are typically adopted to approximate XRB XLFs. Our Schechter modeling (the results of which are illustrated in the bottom panel of Figure 2.7) only identifies a marginally significant (at the 1-to-2σ level) exponential downturn for the HMXBs XLF in M83, at $\ell \simeq 38.56^{+0.64}_{-0.36}$. In contrast, the LMXB and IMXB distributions, as well as the total XLF, are formally consistent with sampling statistics from a single power-law.

That the HMXB XLF in M83 deviates somewhat from a single power-law is confirmed by our cumulative distribution analysis, for which we adopt a formalism that was developed for the mass function of giant molecular clouds (Rosolowsky, 2005). Through this method, we identify a marginally significant truncation at $\ell = 38.74 \pm 0.13$, at the 2.5σ level. Again, we find that no deviations from a single power-law are required for either the LMXB or IMXB population.

Lastly, our optical reconnaissance methodology enables us, for the first time, to make direct inferences on the role of IMXBs in the XRB XLFs. The assumption that the SFR-tracing XRB population maps into truly high-mass donors is typically predicated upon the notion that the adopted SFR tracer is sensitive to instantaneous, and hence very-short lived, star formation episodes. However, we note that whether the published, X-ray data-based "HMXB" XLF also includes (apparently) intermediate-mass donor XRBs is arguably dependent on the host galaxy star formation *history*. For spiral galaxies like M83, which had fairly constant (high) rates of star formation over at least the last Gyr (Chandar et al., 2010), IMXBs must contribute significantly to the measured XLF. This is tentatively confirmed by our analysis; comparing the relative fractions of X-ray sources that I directly classify as low-mass donors with the expectations from the global LMXB XLFs by L19, I find excellent agreement. This suggests that, for galaxies like M83, global, X-ray data-based HMXB XLFs may actually encompass both truly high-mass as well as lower-mass donor XRBs.

CHAPTER 3

XRBs in M81

The work in this chapter was originally published in the Astrophysical Journal (vol. 947, pg. 31) under the title "Calibrating X-Ray Binary Luminosity Functions via Optical Reconnaissance. II. The High-mass XLF and Globular Cluster Population of X-Ray Binaries in the Low Star-forming Spiral M81." The results of that work — produced in collaboration with Elena Gallo, Rupali Chandar, Angus Mok, and Andrea Prestwich — are introduced here. For a complete reading, please see Hunt et al. (2023b).

3.1 Abstract

Following the procedure developed in Hunt et al. (2021), I characterize the optical counterparts to the X-ray source population within the nearby spiral galaxy M81 using multi-band HST imaging data. By comparing the optical luminosities and colors measured for candidate donor stars and host clusters to stellar and cluster evolutionary models, respectively, I estimate the likely masses and upper age limits of the field and cluster XRBs. I identify 15 LMXBs within ancient globular clusters, as well as 42 candidate HMXBs. To estimate the likelihood of misclassifications, I inject 4,000 artificial sources into the HST mosaic image and conclude that our classifications of globular clusters and HMXBs are reliable at the $> 90\%$ level. Globular clusters (GCs) that host XRBs are on average more massive and more compact than GCs that do not. However, there is no apparent correlation between the X-ray brightness of the clusters and their masses or densities, nor are cluster XRBs more X-ray luminous than the general field population of LMXBs. This work represents one of the first in-depth analyses of the population of XRBs within GCs in a spiral galaxy.

3.2 Introduction

In this chapter, I continue my investigation into the XRB populations of late-type galaxies with Chandra and HST. We previously used the direct-classification technique outlined in Chapter 2 to identify LMXBs and HMXBs within M101 (Chandar et al., 2020) and M83 (Hunt et al., 2021). We found that within a distance of $\sim$10 Mpc, HST is able to detect stars down to $\sim 3\ \mathrm{M}_{\odot}$, thereby allowing us to identify the donor stars of HMXBs. By expanding our analysis to an additional galaxy, we hope to advance a step forward toward addressing the supposed "universality" of the LMXB and HMXB XLFs for late-type galaxies.

Here, I apply our methodology to M81 (NGC 3031, Figure 3.1). M81 is a spiral galaxy at an inclination of i = 58° (Okamoto et al., 2015) and a distance of $\sim$3.6 Mpc (Lehmer et al., 2019; Lomelí-Núñez et al., 2021), the nearest of the three galaxies sampled thus far. Compared to the previous galaxies we investigated, M81 has a low SFR of 0.25 $\mathrm{M}_{\odot}$ yr^{-1}, as opposed to 1.07 and 2.48 $\mathrm{M}_{\odot}$ yr^{-1} for M101 and M83 respectively. Based on the model XLFs from early-type galaxies and the global XLF by Lehmer et al. (2019), we should expect that LMXBs comprise a larger fraction of the total XRBs in this galaxy compared to M101 and M83.

What makes M81 a particularly interesting target for this study is that it exhibits a relatively high GC specific frequency (S_N) of 1.1 GC per unit galaxy luminosity, as opposed to 0.43 and 0.17 for M101 and M83, respectively (Harris et al., 2013). There is tentative evidence that the S_N may affect the shape and normalization of the LMXB XLF, since GC LMXBs and field LMXBs likely have different evolutionary paths. In that case, late-type spiral galaxies, which tend to have lower S_N, may yield a smaller normalization factor LMXB XLFs than elliptical galaxies, (Jordán et al., 2004; Kim et al., 2006; Sivakoff et al., 2007; Kim et al., 2013; Peacock et al., 2017b; Luan et al., 2018). Furthermore, the fraction of young HMXBs in clusters is also poorly known, though $\approx 15\%$ of XRBs in M101 (Chandar et al., 2020) and $\approx 25\%$ in the Antennae (Rangelov et al., 2012) are found in clusters younger than a few 100 Myr.

In this chapter, I present an optically classified catalog of X-ray sources within M81. Each source is identified as either an XRB (and tentatively classified by donor star mass), supernova remnant candidate, background galaxy, or foreground star. In §3.5.1, I quantify the likelihood of chance contamination using the results of an artificial source simulation. I also describe the results of our source-by-source classification with a special focus on the XRB spatial distribution (§3.4), the XLF of HXRBs (which we argue suffers from little contamination, §3.6.2), and the association between LMXBs and GCs in comparison to elliptical galaxies (§3.6.1).

3.3 Observations

3.3.1 X-ray Source Catalog

Following Hunt et al. (2021), we make use of the X-ray point source catalog constructed by Lehmer et al. (2019, hereafter L19), in which deep *Chandra* imaging data is examined for 38 nearby galaxies. This study includes thorough estimates of the X-ray completeness limits for each galaxy — crucial for our analysis. The *Chandra* data were reduced following the methods detailed in Lehmer et al. (2017): the analysis was restricted to imaging data within $5'$ of the nominal center position of each galaxy, ensuring a sharp point spread function across the field of view. The source detection and parameter extraction were performed within 0.5–7 keV, where ACIS is best calibrated, and fluxes were converted to between 0.5–8 keV for the purpose of comparing the XLF analysis to previous studies (see L19 for details).

Within M81, L19 identify 252 compact X-ray sources. The L19 study restricts its analysis of the sub-galactic properties of the galaxy, and ultimately the XRB population models that arise from them, to the ellipse that traces the $K_s \approx 20$ mag arcsec^{-2} surface brightness contour outlined in white in Figure 3.1 (see also Jarrett et al., 2003). The ellipse (hereafter referred to as the L19 ellipse) has semi-major and semi-minor axes of $8.'13$ and $4.'14$ respectively, covering a total area of $\sim$106 arcminute^2 (383,409 arcsec^2) and includes 199 X-ray sources, of which 150 are observed down to the 90% completeness limit of $\ell_X \geq 36.3$ (where ℓ_X represents logarithmic X-ray luminosities in units of erg s^{-1}). By comparison, the *HST* footprint shown in Figure 3.1 includes 240 of the 252 compact X-ray sources from L19 (see §3.3.2 below). These include 41 sources that fall outside of the L19 ellipse, 36 of which are above the completeness limit. I will use the full 240 sample in this analysis unless otherwise specified.

3.3.2 Optical Data

Archival *HST* imaging downloaded from the Hubble Legay Archive (HLA[1]) was used for the identification and classification of optical counterparts to the X-ray sources. For M81, a total of roughly 35 hours worth of ACS/WFC observations spanning 33 fields in three bands — F814W (I band), F606W (V band), and F435W for (B band) — were obtained between September 2004 and March 2006 by J. Huchra (Prop. ID 10250) and A. Zezas (Prop. ID 10584). Of these, 27 fields have sufficient observations for this work. Each field spans 3.4×3.4 arcminutes, yielding roughly 674,000 arcsec^2 of coverage over the entire galaxy (for comparison, the L19 ellipse covers roughly 380,000 arcsec^2 of the inner parts of the galaxy). The 33 fields were combined into a single mosaic using ASTRODRIZZLE from the STScI DrizzlePac software package[2]. The full BVI mosaic is shown in Figure 3.1. The mosaic was used to correct the astrometry between the *Chandra* and *HST* data and to identify the candidate counterparts, while the individual fields, which preserved more reliable photometry, were used to measure source magnitudes.

A visual inspection of the *HST* image reveals a bright central bulge and an outer disk. Unlike M83 and M101, the disk of M81 is marked by a region of exponential increase in brightness to-

---

[1] `http://hla.stsci.edu/`

[2] `https://www.stsci.edu/scientific-community/software/drizzlepac.html`

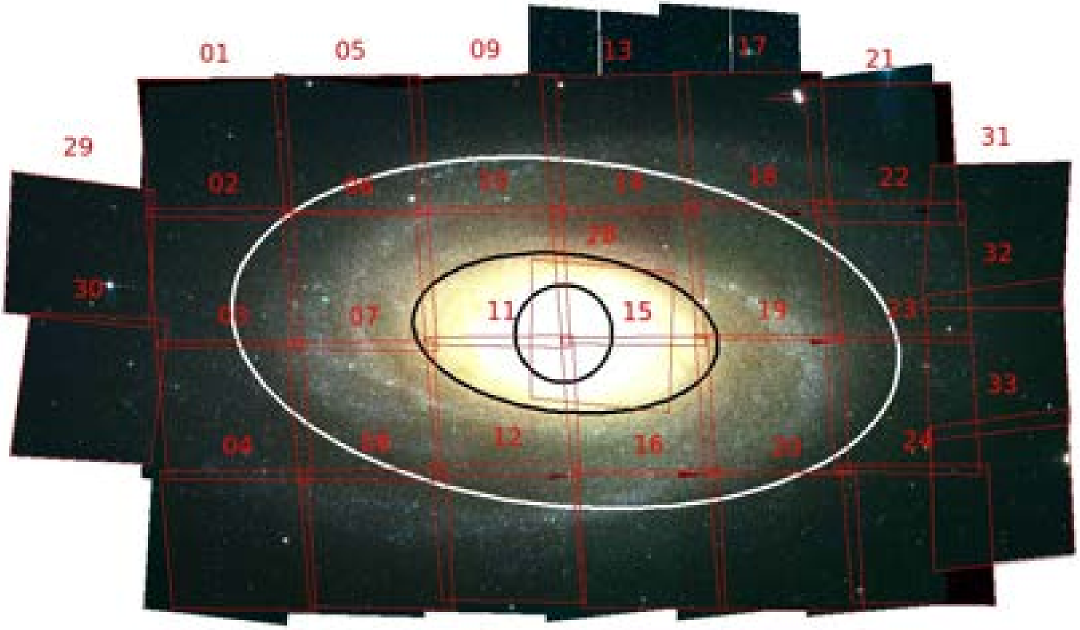

Figure 3.1 The *HST* ACS/WFC mosaic image of M81, composed of 33 individual fields numbered in red. The BVI color image is creating using F435W (B), F606W (V), and F814W (I) observations. The outer (white) ellipse traces the $K_s \approx 20$ mag arcsec^{-2} galactic surface brightness contour (see Jarrett et al., 2003). Within this region (which defines the chosen outer edge of the weak disk), L19 identify 199 compact X-ray sources, of which 150 are observed down to the 90% completeness limit of $\ell_X \geq 36.3$. The inner (black) ellipse and circle represent the chosen edges of the bright disk and the bulge, respectively.

wards the bulge. As such, we find it useful to approach the X-ray source populations as members of 4 distinct regions — bulge, bright disk, weak disk, and outskirts — since the background brightness can drastically affect our ability to reliably classify the optical counterparts of X-ray sources (see §3.5). The outer bounds of the weak disk is well-described by the L19 ellipse (white ellipse in Figure 3.1). The edge of the bright disk is defined by the smaller black ellipse in Figure 3.1, and has semi-major and minor axes radii of $3.'70$ and $1.'91$, respectively, so as to preserve the same aspect ratio as the L19 ellipse. The bulge (black circle in Figure 3.1) is enclosed by a $1.'18$ radius circle as defined by Fabricius et al. (2012).

3.3.3 Identifying Candidate Optical Counterparts

As described in Chapter 2, first step to identifying candidate optical counterparts to X-ray sources is to correct the astrometry between the *Chandra* and *HST* observations. 15 visually-identifiable background galaxies (i.e. those with clearly extended morphologies) and stellar clusters were selected as known reference points between the two data sets. I calculated a median relative positional offset between the X-ray coordinates of each source, as given by L19, and their *HST* optical counterparts to obtain a median shift of $0.''059$ and $-0.''016$ along the *HST* x- and y-axes, respectively, and standard deviations of $0.''207$ and $0.''413$. The X-ray centroid coordinates of all L19 sources in our sample were shifted by these offsets on the mosaic image.

1- and 2-σ uncertainty radii were calculated by adding in quadrature the standard deviation of the offsets with the positional uncertainties associated with the X-ray observation as given by Equations 14 and 12 in Kim et al. (2007), corresponding to the 68% and 95% confidence radii. These equations take into account the total X-ray counts and the off-axis angle of the X-ray observations, which is important given the degradation of the point spread function of *Chandra* observations with distance from the pointing. The resulting 1- and 2-σ radii, which are unique to each source, represent the regions within which one is most likely to detect an optical counterpart to a given X-ray source.

I then identify all potential optical counterparts within 2-σ using the IRAF DAOFIND task to detect point-like sources on the composite images. The IRAF IMEXAMINE task is used to plot the radial profile of each source, which enables us categorize candidate counterparts as AGN, star clusters, or single stars (see §3.4). To generate the magnitudes and colors needed for the analysis of each source, I perform aperture photometry on each detected source with IRAF PHOT. An aperture of 3 pixels is used on point sources, while an aperture of 10 pixels is used for sources with radii much larger than 3 pixels (i.e. clusters). The photometry is performed on individual field images rather than on the mosaic, due to the brightness rescaling that occurs during the mosaic building process. The local background levels are determined in an annulus with radii between 20 and 25 pixels and subtracted from the photometric measurements. Aperture corrections of 0.357 (V), 0.329 (B), and 0.413 (I) were calculated as the median difference between the 3 and 20 pixel aperture magnitudes of several bright, isolated stars with smooth radial profiles that flatten towards the background sky magnitude. Similarly, the 10 pixel aperture corrections were 0.154 (V), 0.128 (B), and 0.160 (I). In both cases, an additional correction term of 0.941 (B), 0.947 (V), and 0.949 (I) accounting for the flux missing within a 20 pixel aperture was also incorporated (see Encircled Energy Fractions from 20 pixels to infinity in Deustua et al. 2017). The magnitudes were converted to the VEGAMAG system by applying the zero-point magnitude for each filter as reported in Table 2 of Deustua et al. (2017). Finally, the optical photometry was converted to absolute magnitudes at 3.63 Mpc, and I applied a blanket correction for foreground extinction equal to $A_V \approx 0.255$ mag, assuming a galactic reddening of $E(B - V) = 0.08$ towards M81. As with M83 (Hunt et al., 2021), I do not account for extinction intrinsic to each source, though I employ a confidence flag scheme (see the table in Appendix C) to indicate sources that may be particularly susceptible to the effects of reddening and obscuration within M81.

3.4 X-ray Source Classification

X-ray sources may be classified as one of several objects on the basis of their detected optical counterparts: a foreground star, a background galaxy, a supernova remnant (SNR), or an XRB donor (either within a cluster or in the field). Foreground stars are identifiable by the bright diffraction spikes centered on the point source. Similarly, the majority of background galaxies that appear in the X-ray data can be identified by distinct morphological features, such as their extended radial profiles and the presence of a disk visible in the *HST* image. For reference, at the typical depth of the X-ray observations that formed the basis for the L19 X-ray source catalog (X-ray fluxes of roughly 10^{-15}–10^{-14} CGS), all optical counterparts of the X-ray sources in the sub-regions of the *Chandra* Deep Field-S that were targeted with *HST* are found and resolved at the resolution and depth corresponding to 1 orbit ACS exposure (Grogin et al., 2003, 2005).

When identifying the most likely optical counterpart to X-ray sources, priority is given first to foreground stars and second to background galaxies that fall within the 2-σ confidence regions of each X-ray source. These proximity-based classifications may be made with a high degree of confidence, as the probability of an unassociated chance superposition with either a foreground star or a background galaxy is low within M81 (see §3.5.1 for an in-depth analysis of chance superpositions with X-ray sources). I identify 5 foreground stars and 10 background galaxies in our sample. All other source classifications require a more in-depth analysis to ascertain.

3.4.1 Supernova Remnants

SNRs are a source of contamination that likely plagues many current XLFs. Recently, Galiullin & Gilfanov (2021) convincingly demonstrated that the vast majority of so-called soft and quasi-soft X-ray sources are indeed SNRs; these include soft X-ray sources both with and without an optical or radio counterpart SNR. As a confirmation, soft X-ray sources are a factor ~ 8 more abundant in star forming spiral galaxies compared to ellipticals.

In Hunt et al. (2021, Chapter 2), I devised a quantitative X-ray-based criterion by which to identify potential SNRs using the multi-wavelength SNR catalog compiled by Long et al. (2014) for M83 as the basis. I found that the majority of SNRs common between the Long et al. (2014) and L19 belong to a distinct parameter space on an $\mathrm{L_X}$–X-ray hardness ratio (HR, here defined as the ratio of the sum of the counts in the 2–7 keV and 0.5–1.2 keV bands to the difference of their counts) plot. Based on this phenomenological approach, I adopt a minimum $\mathrm{L_X}$ and HR cuts to automatically select out candidate SNRs in our catalog, which correspond to $\ell_X \leq 37.5$ and HR ≤ -0.75. In this X-ray source sample, these cuts yield 19 SNR candidates — roughly a factor 5 less than in M83. This is unsurprising, considering the large difference in SFR between M81 and M83. I exclude an additional 6 SNRs identified by Lee et al. (2015). Of the 25 total SNRs in our

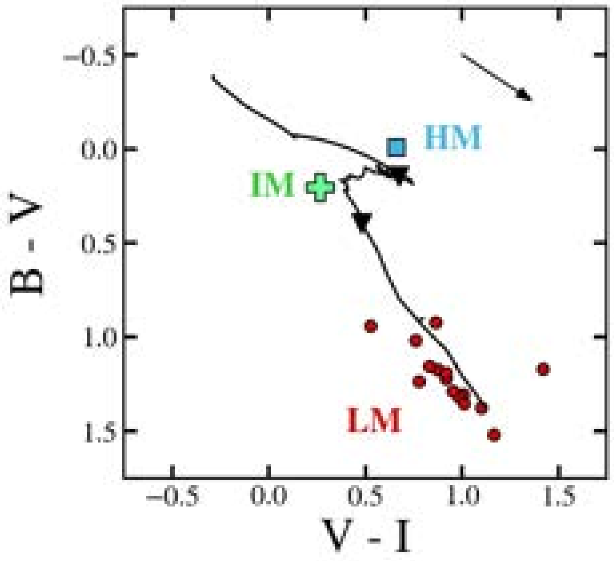

Figure 3.2 The measured $B - V$ vs $V - I$ colors of XRB host clusters compared with predictions for the color evolution of clusters from the Bruzual & Charlot (2003) models. The black triangles mark cluster ages of 10 Myr (top) and 400 Myr (bottom). The arrow represents the direction of reddening following the Milky Way extinction law with an example reddening of $E(B-V) = 0.2$.

sample, 15 have optical counterparts, and 2 of these appear to be associated with clusters.

3.4.2 Stellar Cluster Hosts

We expect to find some fraction of XRBs to exist within stellar clusters, due to the compact nature of clusters creating a higher likelihood of stellar interactions. These are identified as candidate sources with FWHMs that are broader than the point-spread function of a typical field star within the M81 *HST* image; I find that GCs in M81 have FWHMs greater than 4 pixels (0.″2), whereas typical stars have FWHMs less than 2 pixels (0.″1). As a final confirmation, I compare our selections with a number of catalogs that identify clusters and extended sources in M81 (Nantais et al., 2010, 2011; Nantais & Huchra, 2010; Santiago-Cortés et al., 2010), in which all but one of the sources I call a cluster are identified as clusters or extended sources. The only source that was not identified in any other catalog is found within the bulge region.

We assume that, unless identified as SNRs by our method outlined in §3.4.1, X-ray emitting clusters are indeed XRB hosts. In order to classify a cluster XRB by donor mass, we use the cluster age as a proxy; since high-mass stars have hydrogen burning lifetimes of only ~ 10 Myr and intermediate-mass stars have lifetimes of ~ 400 Myr, globular clusters that are older than 400 Myr are dominated by long-lived, low-mass stars, and their XRBs may be confidently classified as

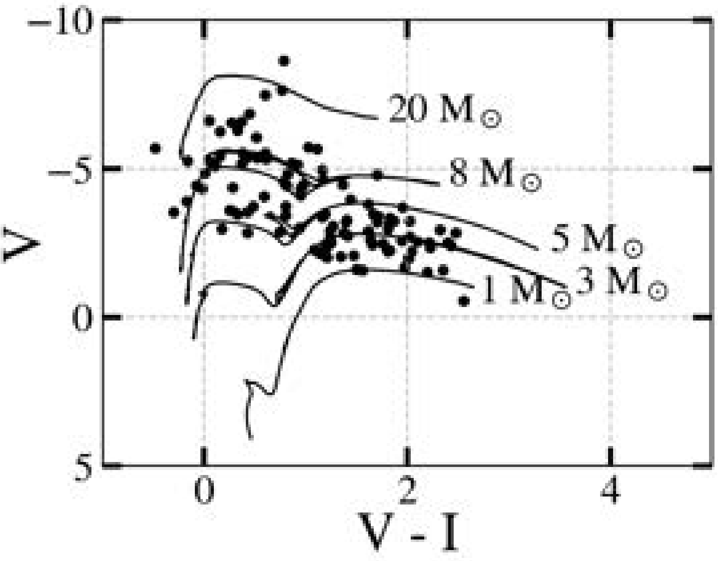

Figure 3.3 The $V - I$ vs. V color-magnitude diagram (CMD) of the donor stars of field XRBs in M81, compared to theoretical evolutionary tracks modeled at solar metallicity (Bertelli et al., 1994; Girardi et al., 2010; Marigo et al., 2017). Stars in M81 are detectable with the *HST* down to $\gtrsim 1$ $\mathrm{M}_{\odot}$.

LMXBs. Likewise, we classify clusters younger than 10 Myr as HMXB hosts and those falling between 10–400 Myr as IMXB hosts, since the most massive stars in a dense region are the most dynamically active and most likely to form stable binaries (Bonnell & Bate, 2005).

I approximate the ages of these clusters by comparing their colors to those predicted by the Bruzual & Charlot (2003) cluster evolution models at solar metallicity, as shown in Figure 3.2. The models span 1 Myr to 13 Gyr in cluster ages, moving from the upper left to the lower right. The black triangles demarcate the bounds of 10 Myr and 400 Myr, and the arrow shows the direction the colors would move due to reddening by dust. I find that 15 of the 17 clusters in our sample fall red-ward of the 400 Myr mark, distinguishing them as ancient globular clusters that host LMXBs. 1 cluster appears younger than 10 Myr, and 1 cluster falls between the two age ranges. I classify these as an HMXB and an IMXB respectively. By comparison, M83 had 4 HMXBs, 4 IMXBs, and 4 LMXBs found in clusters, while M101 had 2 HMXBs, 6 IMXBs, and 1 LMXBs. The difference between these three galaxies is as expected given the SFR/S_N of each.

3.4.3 Field X-ray Binaries

In the case where an X-ray source is neither a foreground star, background galaxy, SNR, nor a cluster, we assume the source is a field XRB with a donor star falling somewhere within the 2-σ radius of the source. For sources that contain multiple candidates, the most likely donor is chosen on a case-by-case basis. Priority is given to high-mass stars that fall within or nearest to the 1-σ radius, since high-mass stars are more likely to remain in a binary following a supernova kick (Kochanek et al., 2019). Low-mass stars are given second priority over intermediate-mass stars, since IMXBs are expected to be short-lived and are thus extremely rare (Podsiadlowski et al., 2002; Pfahl et al., 2003).

To estimate the masses of candidate donor stars, I compare them against Padova theoretical stellar evolutionary models on a color-magnitude diagram (CMD, Figure 3.3). Following our definitions of each category of XRBs and in the order of priority given, I classify sources with candidate donors above the 8 $\mathrm{M}_{\odot}$ model line as HMXBs, those with donors below the 3 $\mathrm{M}_{\odot}$ model line as LMXBs, and those falling between the two as IMXBs. The CMD demonstrates that at the distance of M81, the *HST* image is deep enough to detect stars down to 1 $\mathrm{M}_{\odot}$. Thus, sources that do not have visible donor stars are also categorized as LMXBs. These estimates implicitly assume there is no contamination from the X-ray-irradiated accretion disk to the optical band. This is further discussed in §3.5.

We note that M81 has regions of very intense star formation appearing as bright green HII regions in the *HST* image. In these regions, it is difficult to detect individual stars due to crowding and saturation. In these cases, the donor star is assumed to be high-mass.

3.4.4 Final Classifications

Concluding the source classification, I identify 199 XRBs out of the total 240 X-ray sources that fall within the M81 *HST* footprint: 122 LMXBs, 35 IMXBs, and 42 HMXBs. Of these, 17 exist within stellar clusters: 15 low-mass (within GCs), 1 intermediate-mass, and 1 high-mass. Taking only XRBs above the 90% completeness limit of $\ell_X \geq 36.3$ estimated by L19, there are 159 XRBs: 100 LMXBs (11 in clusters), 25 IMXBs (none in clusters), and 34 HMXBs (1 in a cluster). Of the remaining 41 sources, including the nucleus, 25 are SNRs, 10 are background galaxies, and 5 are foreground stars.

Restricting the sample to those sources that fall within the L19 ellipse, I find 88 LMXBs, 27 IMXBs, and 31 HMXBs in the field, with an additional 15 LMXBs, 1 IMXB, and 1 HMXB within clusters. Above the completeness limit, this comes to 71 LMXBs, 19 IMXBs, and 26 HMXBs, with an additional 11 LMXBs in GCs. The L19 ellipse also contains 22 SNRs, 9 background galaxies, and 4 foreground stars (14, 5, and 4 above the completeness limit, respectively).

A complete description of the positions, L_{X}, V-band magnitudes, optical colors, and classifications of all 240 sources within the *HST* footprint is given in Table C in the Appendix. Full-color optical images of all sources — with their 1- and 2-σ radii outlined in red, candidate sources highlighted with yellow dashed circles, and most likely counterpart/donor circled in red — are shown

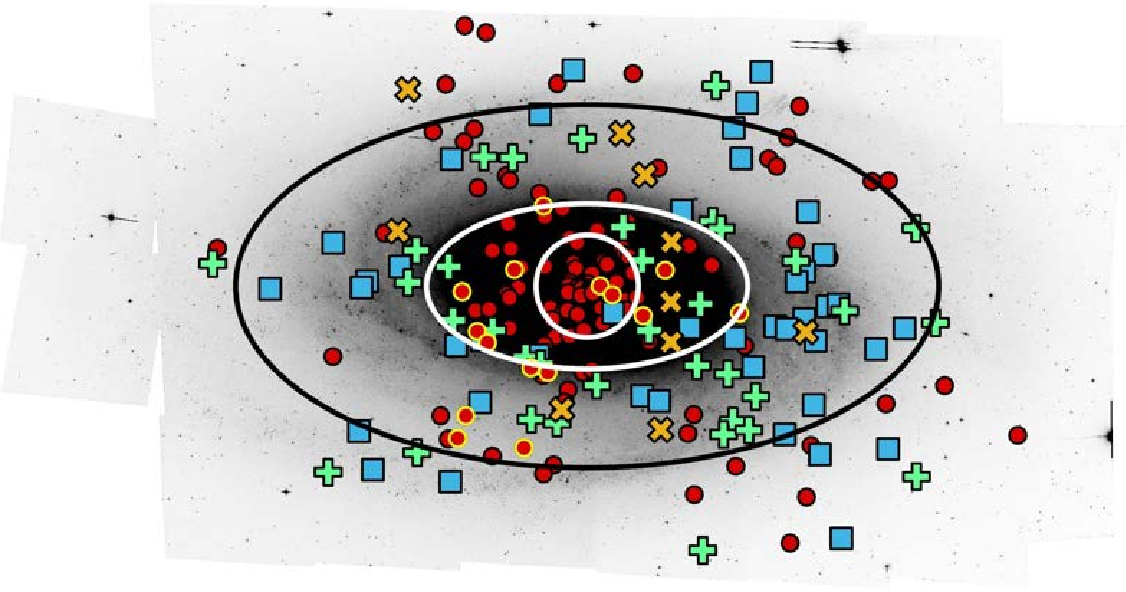

Figure 3.4 The spatial distribution of LMXBs (red points), with globular cluster hosts circled in yellow, IMXBs (green crosses), and HMXBs (blue boxes) on an inverted image of M81. Background galaxies are also shown (orange X's). The 4 regions (bulge, bright disk, weak disk, and outskirts) are marked by white and black ellipses.

in the Appendix, Figure C.1.

The overall spatial distribution of the candidate XRB counterparts is shown in Figure 3.4, where our classifications (not accounting for possible misclassifications; see §3.5.1) of low-, intermediate-, and high-mass donors are shown in red, green, and blue, respectively. The 15 cluster LMXBs are outlined in yellow. As expected, the bulge of M81 is dominated by LMXBs: 39 total LMXBs (2 of which are found in GCs) are found in the bulge compared to 1 HMXB. Above the completeness limit, there are 38 bulge LMXBs (1 in a cluster) compared to 1 HMXB. The majority of HMXBs (31 out of 42) are within the disk; however, roughly $\sim 52\%$ of all disk XRBs are LMXBs. When the disk is broken into a bright and weak component, 80% of the bright disk XRBs are low-mass, while nearly 40% of the weak disk XRBs are low-mass. The percentages may skew even higher, considering the possibility that some (or all) of the sources I classified as IMXBs may actually be LMXBs, as discussed in §3.5.1.

When compared with the stellar mass, SFR and specific SFR (sSFR) sub-galactic maps generated by L19 (Figure 3.5), HMXBs appear to be concentrated in high SFR regions, whereas most (albeit not all) LMXBs appear to follow the radial profile of the stellar mass. The IMXBs popula-

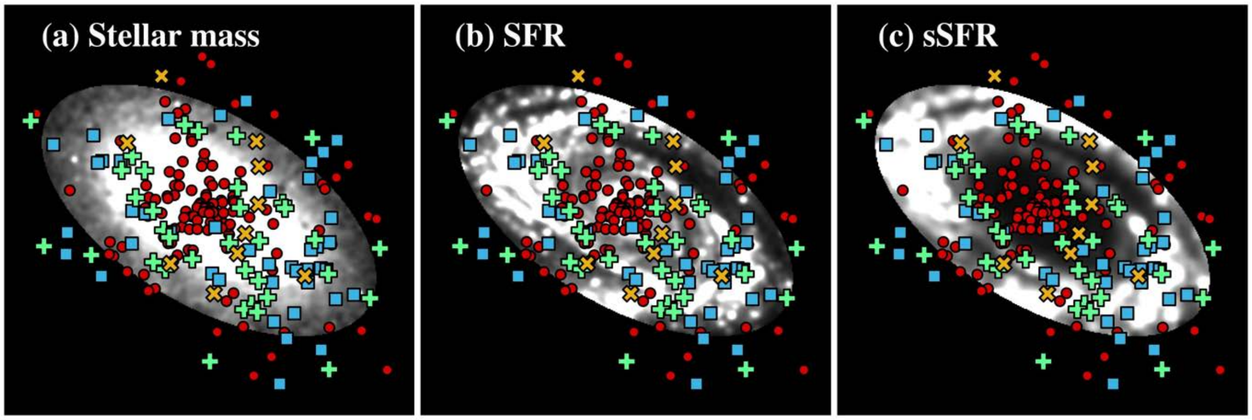

Figure 3.5 Overlays of LMXBs (red points), IMXBs (green crosses), HMXBs (blue squares), and background galaxies (orange X's) onto the (a) stellar mass, (b) star formation rate, and (c) specific star formation rate maps for M81 generated by L19 within the L19 ellipse. All three maps are shown with a linear color scale.

tion seems to be somewhat hybrid; whereas their spatial distribution resembles more closely that of HMXBs, they are found in larger proportions in the bright disk. As discussed in §3.5, however, this population is likely affected by a high degree of contamination, so we refrain from further speculating on their properties.

3.5 Assessing Misclassifications

Here, I discuss a few of the most pressing sources of misclassification of the optical counterparts in M81. For an additional discussion of potential sources of misclassification inherent to our method, see Chandar et al. (2020) and Hunt et al. (2021).

3.5.1 Quantifying Chance Superpositions

In this section I assess the likelihood that an X-ray source may have a chance superposition (rather than physical association) with a high- or intermediate-mass star, globular cluster, or background galaxy. Since low mass stars dominate the stellar population of a galaxy, I seek to quantify how certain can we be that, for any given region, the true donor is not an unseen low-mass star. While our prioritization scheme for sources with multiple point-source candidates places HMXBs above other classifications in any case (due to the higher chance of binary survival post-supernova, Kochanek et al. 2019), this becomes a greater issue for IMXBs, which we would naturally de-prioritize compared to LMXBs due to their rareness.

In order to quantify the frequency of chance superposition with a source that is *not* a low mass

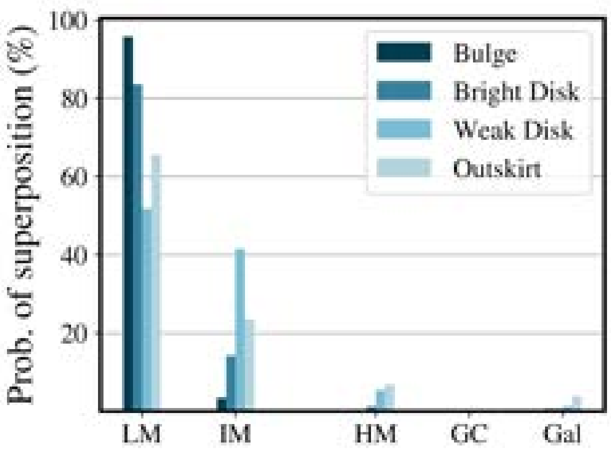

Figure 3.6 Results from our chance superposition simulation, in which 1,000 simulated sources were randomly distributed throughout each of our 4 regions — the bulge, the bright disk, the weak disk, and the outskirt, as defined in §3.3.2 — and their optical counterparts classified using the same methods as for the observed X-ray sources. These probabilities are also given in Table 3.1.

star, I randomly populate the 4 regions of the galaxy (bulge, bright disk, weak disk, and outskirts, as defined in § 3.3.2) with 1,000 artificial X-ray sources per region and classify each using the *HST* images and photometry, as done with our 'true' X-ray sources. The 2σ positional uncertainty used to search for an optical counterpart to each synthetic X-ray source is assumed to be the median of the 2σ positional uncertainties of the 'true' X-ray sources within that region; these values are compiled in Table 3.1. As expected, these increase as one moves further from the center of the galaxy, largely due to the degradation of the *Chandra* PSF farther from the pointing.

The results of our artificial source experiment are compiled in Table 3.1 and shown in Figure 3.6. For each region I estimate the probability of a chance superposition with a high-mass star, an intermediate-mass star, a globular cluster, and a background galaxy as a percentage.

In Table 3.2, I compile the number of observed XRBs that were classified as HMXBs, IMXBs, and LMXBs in the same four regions, as well as X-ray sources found in GCs and associated with background galaxies. The total number in each region is given as the first number in the table, and the number of sources above the completeness limit is given in parentheses.

One key result of the simulation is that the probability of finding a chance superposition with a high-mass star, a globular cluster, or a background galaxy is extremely low ($< 1\%$ in total) in the bulge region. There is a somewhat higher probability of a chance superposition with an intermediate-mass star (3.4%). Because the bulge region of M81 is bright, it is hypothetically possible for sources to be misclassified as an LMXB with no optical counterpart, as the background brightness could outshine any potential point source. However, the fact that we *do* see a handful of intermediate-mass stars within our simulation in this region indicates that we are still able to

Table 3.1 Probability of Chance Superposition (percentage)

Region	Median 2σ	HMXB	IMXB	GC	AGN
Bulge	$0.''54$	0.1	3.4	0.1	0.6
Bright disk	$0.''66$	1.2	14.2	0.2	0.7
Weak disk	$0.''78$	5.4	41.5	0.0	1.3
Outskirts	$1.''48$	6.8	23.6	0.1	3.8

Table 3.2 Observed Populations (Total & Completeness limited)

Region	Field LMXB	HMXB	IMXB	GC	AGN
Bulge	37 (32)	1 (1)	0 (0)	2 (1)	0 (0)
Bright disk	25 (14)	2 (2)	6 (2)	7 (5)	3 (1)
Weak disk	26 (25)	29 (23)	22 (17)	6 (5)	6 (4)
Outskirts	19 (18)	10 (7)	7 (6)	0 (0)	1 (1)

identify stars down to intermediate masses, though intermediate-mass stars closer to the 3 $\mathrm{M}_{\odot}$ limit may be lost. This, as well as the low probability of chance superposition with non-low-mass sources, suggests that our source classifications — particularly of any HMXBs — in the bulge are likely accurate and are not prohibitively sensitive to background brightness or chance superposition.

The bright disk also shows a low probability for a chance superposition with a high-mass star (1.2%), a globular cluster ($< 1\%$), or a background galaxy ($< 1\%$). There is however, a more significant probability that an X-ray source will have a chance superposition with an un-associated intermediate-mass star (14.2%). These probabilities increase in the weak disk, especially for high-mass (5.4%) and intermediate-mass stars (41.5%). The probability of overlapping with a background galaxy increased to 1.3%, while there is virtually no chance superposition with a cluster in the weak disk. Potential explanations for these increases is the inclusion of the spiral arms in these regions, which tend to harbor bright, massive stars, the decreasing background brightness, and (perhaps more importantly) the larger positional uncertainty of the X-ray observations in this portion of the galaxy.

The outskirts of the galaxy also show substantial contamination by intermediate-mass stars (23.6%) and — albeit to a lesser degree — high-mass stars (6.8%). The chance of overlapping with a background galaxies triples (3.8%). The increased frequency of background galaxies in our simulation with galactocentric distance is not surprising, as many more background galaxies are visible in the outskirts of M81, where the background brightness is lowest and the density is most diffuse (see also §3.5.2).

Taken together, these results lead to the following conclusions:

- The probability of finding a chance superposition with a globular cluster is negligible all 4 regions of M81. This indicates that any X-ray source-GC association is almost certainly physical.

- X-ray sources classified as HMXBs in the bulge (1 source) or bright disk (2 sources) are almost certain to be correctly classified. The weak disk and outskirts have relatively low probabilities of chance superposition with high-mass stars ($< 10\%$ each). There are 70 and 31 XRBs above the completeness limit in the respective regions, with 23 and 7 identified as HMXBs in each region, respectively. The artificial experiments suggest minor contamination, with at most 4 possible misclassifications in the weak disk and 3 in the outskirts.

  We note that high-mass stars are more likely to survive in an X-ray binary than those with lower masses, so in a galaxy with continuous star formation, it may be reasonable to assume a greater fraction of XRBs identified as having high-mass donors are *truly* HMXBs than this simple simulation suggests.

- At face value, intermediate-mass stars are, after low-mass stars, the most abundant potential counterparts within our simulation. This suggests a good number of our XRBs may overlap with intermediate-mass stars that are un-associated with the X-ray emission, simply by chance. In the bright and weak disks, I classified 9 and 17 X-ray sources above the completeness limit as IMXBs (there are only a handful of such sources in the outskirts and none in the bulge). In the weak disk where the probability of chance superposition is greatest, we may expect up to 30 of the 70 XRBs to be misclassified as IMXBs. This suggests that we cannot trust our classified IMXB population to be truly representative of the IMXB population of M81.

  Evolutionary arguments further strengthen our conclusion that a large fraction of XRBs with an associated intermediate-mass stars may not be reliable. Even though the probability of *forming* an XRB with an initial intermediate-mass donor is higher than that of a low-mass donor, population synthesis models show that most intermediate-mass donors (particularly those with neutron star accretor) evolve very quickly into low-mass stars through a short-lived thermal mass transfer phase (Podsiadlowski et al., 2002; Pfahl et al., 2003). This results into a population of abnormally hot and luminous LMXBs formed from IMXB progenitors, which may be misclassified through our method.

  I check whether X-ray irradiated disks may contribute significantly to our optical bands by comparing the colors of our HMXBs to other nearby, high-mass stars. I identify a sample

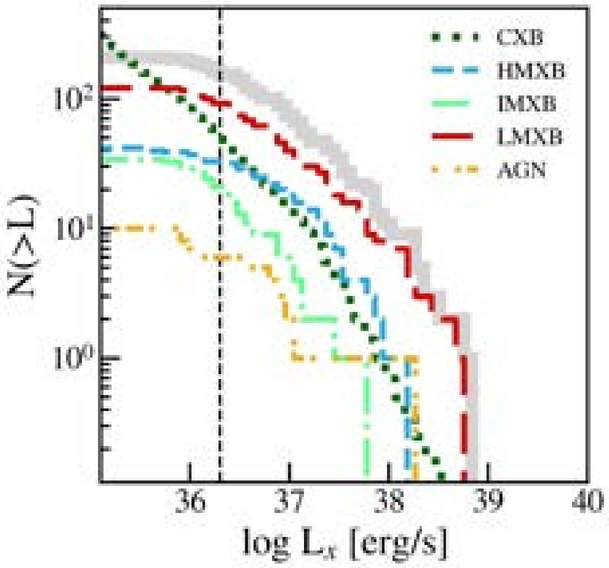

Figure 3.7 The contribution of X-ray sources to the total cumulative X-ray luminosity function of M81 (grey). LMXBs (red), IMXBs (light green), HMXBs (blue), and AGN (orange) are identified based on the radial profiles and photometry of the optical counterparts as described in §3.4. The expected cosmic X-ray background, derived from Kim et al. (2004) using the ChaMP survey fitting parameters, is shown in dark green. The M81 90% completeness limit of $\ell_X \gtrsim 36.3$ (from L19) is shown as a vertical dashed line.

of 115 high-mass comparison stars located within $\approx 3''$ of our 42 HMXBs, to account for potential environmental effects that could alter the colors of the donor stars. I find that the B-V and V-I colors of the candidate HMXB donor stars are entirely consistent with typical field stars of similar brightness. We note, however, the discrepancies arising from X-ray irradiated disks would become more prominent in the UV band (Tao et al., 2011).

- While remaining small, the probability of chance superposition with an optically identified background galaxy in our simulated sample increases radially towards the outskirts, as expected. In terms of our 'true' sample, I find 3 X-ray sources associated with background galaxies in the bright disk and 6 in the weak disk, and only a single such object in the outskirts. This is addressed specifically in §3.5.2.

3.5.2 The Cosmic X-ray Background

In Figure 3.7, I plot the cumulative XLFs of the M81 X-ray sources classified as low-, intermediate- and high-mass XRBs (based on their candidate optical counterparts) within the L19 ellipse, as well as the XLF of the optically identified AGN. These are compared with the expected XLF of Cosmic X-ray Background (CXB) sources, based on the log(N)-log(S) from the ChaMP *Chandra* survey using the 0.5–8 keV band fit, which has a limiting flux of 6.9×10^{-16} ergs cm^{-2} s^{-1} — intermediate between the Chandra Deep Fields and previous surveys (Kim et al., 2004). The ChaMP survey covers an area of 9.6 degrees^2, wider than many prior CXB studies, and detected ~ 6500 sources —the most detected in a single satellite survey. The wider field of view means that cosmic variance will have less an impact on observations than for smaller, deeper fields. At the same time, the flux limit of our X-ray data is shallower than ChaMP's.

Unlike in M83, where the contribution of the CXB is expected to be negligible outside of the $K_s \approx 20$ ellipse, the proximity and larger angular size of M81 imply that the CXB can be expected to contribute significantly to the detected X-ray source population (see also Figure 3 of L19). Specifically, 55 CXB sources (that is, AGN) are expected down to the completeness limit within the L19 ellipse (dark green line in Figure 3.7), whereas I directly identify the host galaxies of only 10 sources. This implies that optically obscured AGN are a non-negligible source of contamination to the compact X-ray source population within the field of view of M81. We expect those will be mostly associated with LMXB candidates with no detected optical counterparts.

To test this hypothesis, I conduct a thorough inspection of of 3 *HST* fields: one covering the outskirts of M81 (outside of the weak disk/L19 ellipse), one covering the weak disk, and one covering the bright disk and a portion of of the bulge. I identify any optical source falling within the 3 fields with a radial profile similar to a galaxy (i.e. non-point source, non-cluster, with extended or unusual shapes, excluding sources that are clearly crowded stars) as a potential galaxy. The aim of this exercise is to quantify the fraction of optically identified galaxies that have an associated X-ray emitting source (AGN), and to assess how that varies as a function of galactocentric distance. The result is a high-end estimate of the number of background galaxies captured within each field.

In the outskirt field, where background galaxies should be virtually unabsorbed and easily identifiable, I identify 545 background galaxies, none of which have an X-ray counterpart. For a field covering 37,913 arcsecs^2, this translates into a number density of less than 0.02 galaxies per arcsecs^2, or 1 galaxy for every 70 arcsecs^2. Across the same field there are 7 compact X-ray sources (4 of which are above the X-ray completeness limit); none are associated with an optical galaxy. Owing to increased absorption and crowding, the number of optical galaxies goes down to 349 and 104 for the weak disk and the bright disk/bulge HST fields, respectively; the number of compact X-ray sources in these regions is 7 and 10 (4 and 8 above the completeness limit), respectively. Again, none are identified as AGN.

This supports our hypothesis that the X-ray emitting AGN that make up the CXB over the field of view of M81 have no detectable optical counterparts, and are thus highly likely to be 'hidden' within the objects that I classify as LMXBs. This, combined with our chance superposition assessment analysis (§3.5.1) indicates that our HMXB population suffers from minimal (if any) CXB contamination, whereas the LMXB population is likely contaminated, particularly at the low luminosity end. Specifically, out of the 82 LMXBs that I identified down to the completeness limit (71 of which are field XRBs) within the regions mostly likely to be obscured (i.e. within the outer bounds of the weak disk), a large fraction (of the order of 50) are expected to be potential AGN.

3.6 Discussion

3.6.1 LMXB Production in Globular Clusters

Extensive research has been done into the population of LMXBs found within GCs in *elliptical galaxies*, in large part due to the abundance of GCs and the ease with which LMXBs can be isolated in galaxies with old stellar and cluster populations. Several early works found that GCs are especially efficient at forming LMXBs thanks to the increased likelihood of dynamical interactions within dense environments. Up to 70% of all LMXBs within any given early-type galaxy are found within old star clusters, and some particularly luminous GCs appear to harbor more than one LMXB (Angelini et al., 2001; Jordán et al., 2004; Kundu et al., 2007). Furthermore, a significant fraction of field LMXBs may have formed originally within GCs, only to be ejected later or deposited within the field when the parent GC dissolved (Kundu et al., 2003; Lehmer et al., 2020).

There is evidence to suggest metal-rich GCs form LMXBs 2–4 times more efficiently than their metal-poor counterparts (Jordán et al., 2004; Kundu et al., 2007; Humphrey & Buote, 2008). One explanation for this may be that, because they have larger radii, metal-rich stars are better able to facilitate both the formation of binaries and the Roche-lobe overflow that characterizes LMXBs (Bellazzini et al., 1995). Alternatively, this effect may be explained by the potentially longer lifetimes of metal-rich LMXBs due to stronger stellar winds (and therefore faster evolution) of lower-metallicity stars (Maccarone et al., 2004). On the other hand, metal-rich clusters tend to be more compact, with may lead to more dynamical interactions within the cluster environment (Peacock et al., 2010). Despite these hypotheses, a suitable explanation for this apparent dependence is still a subject of much debate.

For all the uncertainty regarding the role of GCs in XRB production in early-type galaxies, even less is known about their role in *late-type galaxies*. Spiral galaxies tend to host GC populations with a range of ages, which makes it difficult to pursue the effect of metallicity on XRB populations due to the degenerate effects of both age and metallicity on cluster colors (Kundu et al., 2003). In our previous work, we found only 1 LMXB in a GC in M101 (Chandar et al., 2020) and 4 within M83 (Hunt et al., 2021). These are much lower fractions of the total LMXB population than expected in early-type galaxies, since massive spiral galaxies like M83 and M101 are expected to have on the order of ~ 100 GCs. Given that M81 is a spiral galaxy with a low SFR (0.25 $\mathrm{M}_{\odot}$yr^{-1}) and relatively high S$_N$ (1.1), it is the ideal target for analyzing the production of XRBs within the

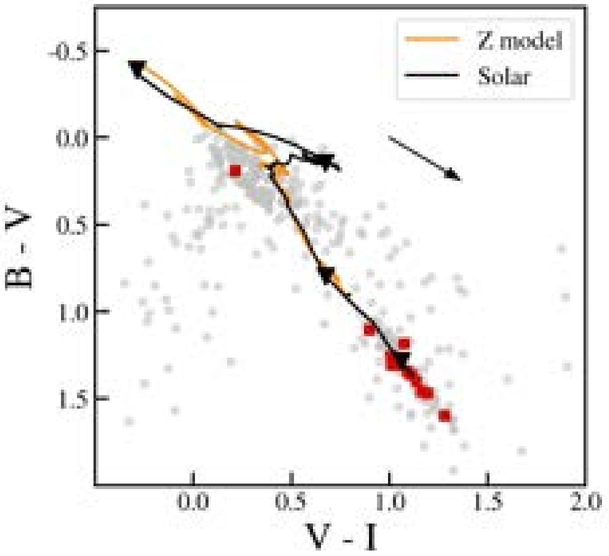

Figure 3.8 The color-color diagram of clusters from the SC10 catalog, compared to those that I determine are XRB hosts. The black and orange lines represent the Bruzual & Charlot (2003) cluster evolution models for solar and 20% solar metallicities, respectively. Cluster colors are taken from the SC10 measurements. The arrow represents the direction of reddening following the Milky Way extinction law with an example reddening of $E(B-V)=0.2$.

GCs of late-type galaxies. Furthermore, the clusters in M81 have been well-studied, allowing us to analyze the properties of XRB-hosting clusters compared to non-XRB clusters and, along the same lines, the differences between field XRBs and cluster XRBs using previously published works.

As a primary basis for this analysis, I use the M81 cluster catalog by Santiago-Cortés et al. (2010, hereafter SC10). Within this work, a total of 435 compact stellar clusters were identified using HST ACS/WFC F435W, F606W, and F814W data in combination with the source detection code Source Extractor (SE). They used bounds of $2.4 <$ FWHM < 10 ACS pixels (or $2.1-9$ pc) for their definition of a compact cluster. 10-pixel aperture magnitudes were also generated by SE, from which $B-V$ and $V-I$ colors are derived.

Of the 435 clusters in the SC10 catalog, 13 coincide with X-ray sources within our catalog. Of these, 12 are located in GCs, and 1 (located in a young cluster) is identified as a potential SNR by our methods outlined in §3.4.1, which I remove. I also find an additional 3 GC LMXBs not included in the SC10 catalog, which suggests that the SC10 catalog is not complete. To account for these 3 missing GCs in our analysis of the cluster population in M81, I compare the measured properties of the X-ray clusters in SC10, as measured by SE, to the values I measure by our methodology, as described in §3.3.3. I find that, between the two catalogs, the FWHM measurements for the clusters have a median difference of 0.33 pixels, and the V-band photometry has a median offset of approximately 0.09 mags, while our B-band photometry is fairly consistent with

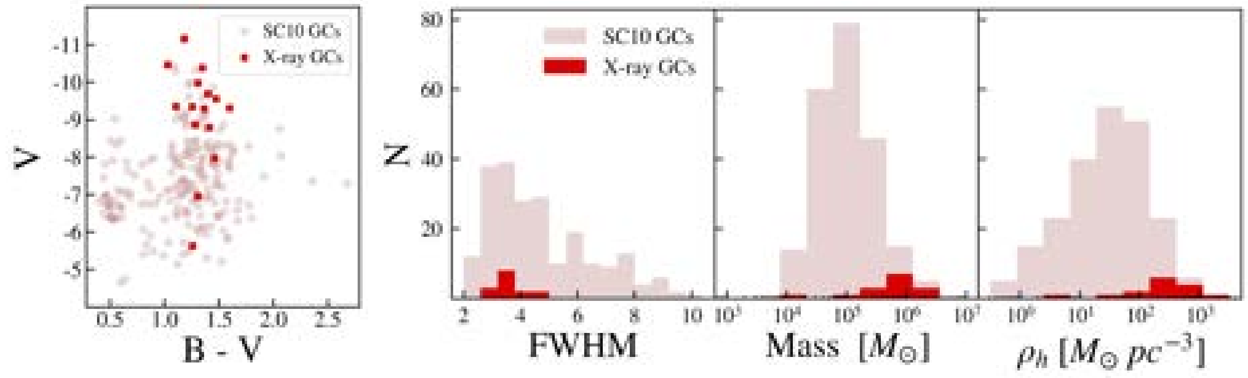

Figure 3.9 Comparing the properties of X-ray emitting SC10 clusters to all GCs in the SC10 catalog. (Left) The color magnitude diagram, with red squares representing GCs that are XRB hosts. The magnitudes are taken from the SC10 measurements. (Right) The radii and densities of the XRB-hosting GCs are compared to the total GC population.

the SC10 measurements. Thus, by applying these offsets to our 3 GCs that are missing in the SC10 catalog, I am able to calibrate our measured values to the SC10 system, which will enable us to include our full GC LMXB population in our analysis of M81 clusters.

Figure 3.8 shows all 435 SC10 clusters (grey points) compared to two models for cluster evolution from Bruzual & Charlot (2003): a solar metallicity model, and a model with metallicity $Z = 0.004$, or 20% solar. As is the case for Figure 3.2, cluster ages increase down and to the right, and the arrow represents the direction of reddening for M81. The red squares represent X-ray emitting clusters that appear in our source catalog, i.e. XRB hosts. All but one fall towards the lower-right end of the model track, where we expect GCs.

Since we are interested in understanding the population of LMXBs within GCs, I isolate the GCs in the SC10 sample by making a color cut corresponding to minimum cluster age of 400 Myrs, based on the Bruzual & Charlot (2003) models. 220 of the 435 clusters meet these requirements. This cut successfully selects the 12 clusters I classify as LMXB-hosts in our sample, which corresponds to roughly 4.4% of the total GC population in SC10. The additional 3 GCs not present in the SC10 catalog are also added to the total X-ray GCs population for the remainder of our analysis. I calculate the masses of the GCs by adopting a mass-luminosity ratio of 1.5 $\mathrm{M}_\odot/L_\odot$ as presented in Chandar et al. (2007). The mass of each cluster is estimated by converting their V-band magnitudes using an absolute Vega magnitude of 4.66 for the Sun, as viewed in the ACS F606W filter (Willmer, 2018). From these masses, I also calculate cluster densities following Chandar et al. (2007), converting FHWMs to effective radii using a pixel scale of 0.″05 pixel^{-1} and a conversion factor of 1.48 (Anders et al., 2006; Mulia et al., 2019).

In Figure 3.9, I compare the properties of GCs that host XRBs (red) with the properties of those that do not (pink) — that is, the 15 X-ray emitting GCs from our sample compared to the

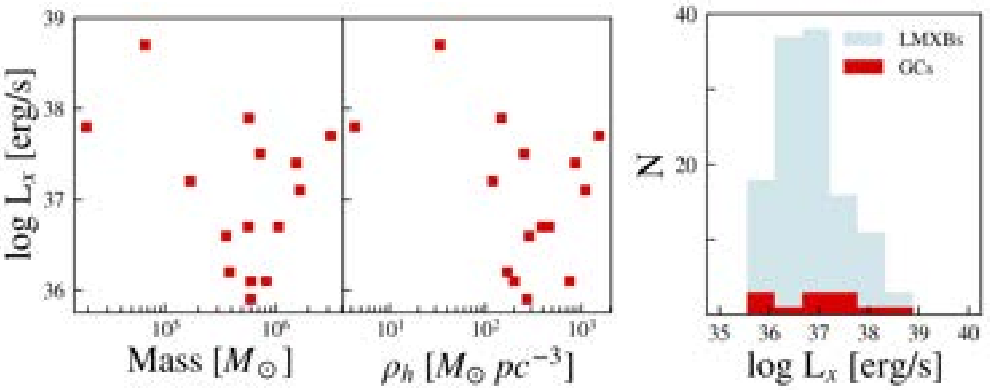

Figure 3.10 The X-ray properties of the SC10 XRB-hosting clusters. On the left, histograms of the densities and masses of the XRB-hosting GCs from the SC10 catalog are compared to their L19 X-ray luminosities. On the right, a histogram of the X-ray luminosities of the SC10 clusters is compared to our total M81 LMXB population, not accounting for possible misclassifications (see §3.5.1).

208 GCs from the SC10 catalog that do not have X-ray counterparts. I find that, within the spiral galaxy M81, GCs that host XRBs tend to have higher V-band magnitudes than non-XRB GCs, as demonstrated in the leftmost panel. Furthermore, when observing the sizes, masses, and densities of the clusters (right panels), I find that *GCs that host XRBs have smaller radii, are more massive, and hence are denser than GCs that do not*. Higher masses and densities may be more conducive for the formation of XRBs, since dense environments allow for more close interactions between stars, increasing the chances of capture. Similarly, higher masses correlate with more stars and, therefore, more opportunities for dynamical interactions (Peacock et al., 2010).

With only BVI photometry, it is hard to make definitive statements about the metallicities of GCs in spiral galaxies, since small amounts of reddening would significantly change the estimated metallicity. I do find however, that the majority of GCs which host LMXBs in M81 are more centrally concentrated than the full SC10 GC catalog. This is potentially indirect evidence that LMXBs may prefer to form in more metal-rich GCs in spiral galaxies as well, since metal-rich GCs tend to be associated with bulges (rather than halos), and more concentrated towards the centers of their host galaxies as a result.

When I analyze the properties of the 15 X-ray emitting GCs (Figure 3.10, left), I find no significant correlation between X-ray luminosity and the mass or density of the host cluster. That is, more massive XRB-hosting GCs are *not* more luminous in the X-rays, in line with what was found by Sivakoff et al. (2007) for GCs in Virgo cluster elliptical galaxies. It is also interesting to compare the population of LMXBs within GCs to the total number of XRBs and to field LMXBs specifically, although the latter is quite uncertain in M81. Of the 199 XRBs I identified within M81 (excluding SNR candidates), 15 are found in GCs. 159 XRBs, 11 of which in GCs, are above

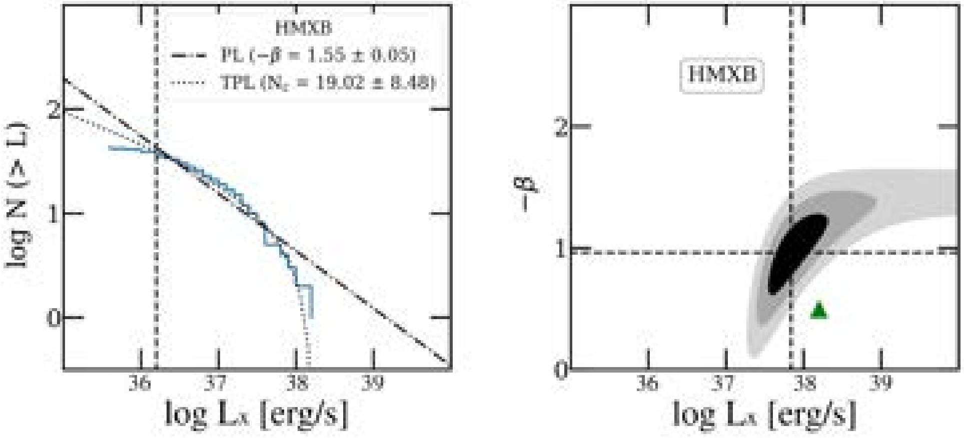

Figure 3.11 (Left) Fits to the HMXB XLF of M81 with a cumulative, un-binned power-law function, with and without a truncation at high luminosities (dotted-dashed and dotted lines, respectively). The functions are fitted down to the completeness limit, $\ell_X = 36.3$ (dashed line). (Right) The maximum likelihood fit to the cumulative HMXB XLF using a Schechter function. The green triangle marks the X-ray luminosity of the brightest HMXB. Contours represent the 1-, 2-, and 3σ confidence level. The dashed lines represent the 'best fit' at $-\beta = 0.96$ and a luminosity knee at $\ell_X = 37.84$ ($\ell_{\rm knee}$).

the completeness limit. Taken at face value, I classified 122 XRBs as low-mass (100 above the completeness limit). However, as discussed in §3.5.2, this population likely has significant contamination from CXB sources, and may be missing other sources classified as IMXBs (due to, e.g., intense X-ray irradiation). The X-ray luminosities of XRB-hosting GCs are consistent with field XRBs, independent of whether they are compared to *only* low-mass field XRBs (blue sources in the right panel of Figure 3.10) or to the *total* field XRB population. This may bolster the idea that GCs are "seeding" the field population of LMXBs (Lehmer et al., 2020).

Overall, our observations of XRB-hosting GCs in M81 is consistent with observations of those in early-type galaxies. However, as noted, a more complete sample of GCs in M81 is needed before any strong conclusions may be drawn as to what fraction of GCs may host XRBs in star-forming galaxies.

3.6.2 HMXB XLF in M81

In this section I will focus on the shape and normalization of the XLF of the HMXB population, which our experiments in §3.5.1 show have negligible chance superposition/background contamination. We are especially interested in how our method for classifying HMXBs compares to state-of-the-art X-ray based results (e.g., L19) both in terms of shape as well as normalization. Following the analysis conducted in Hunt et al. (2021), we examine the HMXB XLF via two methods: first, we fit the un-binned, cumulative XLF to a power-law (PL), with and without a high-luminosity truncation, using the IDL script `MSPECFIT` (Rosolowsky, 2005). Second, we perform a Maximum Likelihood (ML) fit of the differential XLF to a Schechter function. The former enables us to potentially detect a break (regardless of its functional shape) at high luminosities, which may be expected to be present near the Eddington luminosity for a stellar-mass compact object. The latter is a robust test for the presence of an *exponential* break (Mok et al., 2019).

Figure 3.11 shows the results of these fits. The left panel shows the PL fit to the cumulative HMXB XLF down to the 90% completeness limit (vertical dashed line). The index of the PL fit is given by $-\beta$, while a value $N_c > 1$ for the truncated PL indicates a statistically significant high-energy downturn. The right panel of Figure 3.11 shows the results of the ML fit, where the best-fit index ($-\beta$) is plotted against the best fit Schechter knee luminosity, with the contours representing the 1-, 2- and 3σ confidence levels, and the green triangle marking the luminosity of the brightest HMXB. The upper limit to the knee luminosity is set to be well in excess of the brightest HMXB to ensure convergence of the fit.

The results of both fitting methods suggest a marginal cutoff or downturn at a luminosity just below $\ell_X = 38$, as indicated by $N_c = 19.02 \pm 8.48$ (left) and a closed 2σ but an open 3σ ML contour (right) with a fit of $-\beta = 0.96$ and $\ell_{\rm knee} = 37.84$. This is similar to our results for M83, in which only the HMXB population shows marginal evidence of a downturn (at a $\sim 2.5\sigma$ level), albeit at a higher luminosity ($\ell_X \gtrsim 38$). In contrast, we found that none of the XRB populations in M101 (high-, intermediate-, or low-mass) required a truncation or Schechter-like cutoff (Chandar et al., 2020). We note, however, that we did not excise the SNR population using the X-ray luminosity and color cuts as for M81 and M83, so it is possible that the inclusion of a large population of low-luminosity SNRs in the XLFs of M101 washed out any PL deviation at high-luminosity.

I compare our PL fit for HMXBs to that found by L19. Using sub-galactic SFR and $\mathrm{M}_\star$ maps (Figure 3.5), they construct both a global HMXB XLF model that scales with enclosed SFR and a standard XLF fit for each individual galaxy in their sample (38 galaxies in total). These fits employ a forward-fitting model that fits both the XRB and CXB contributions simultaneously. They find that the individual galaxy HMXB XLFs are best fit with a single PL with a fixed high-energy cutoffs of $\ell_c = 40.3$. For M81, L19 reports a best fit PL index of -1.43 ± 0.06, which is consistent within the errors with our fitted value of $-\beta = 1.55 \pm 0.05$.

The L19 global HMXB XLF model gives a slightly steeper index of -1.66 ± 0.02. We can use the global model to estimate how many HMXBs are expected within the L19 ellipse, given the enclosed SFR provided by the maps. L19 gives a global HMXB normalization of $2.06^{+0.16}_{-0.15}$ per unit $M_\star \mathrm{yr}^{-1}$, with a galaxy-specific scaling factor of $\omega = 0.90$ for M81. I estimate a total SFR of 0.25 $\mathrm{M}_\star \mathrm{yr}^{-1}$ enclosed within the L19 ellipse (excluding the 0.01 $\mathrm{M}_\star \mathrm{yr}^{-1}$ within 12 arcsec of the bulge, which hosts a bright AGN). Based on these numbers and the functions given by Equation 4 in L19, 10 HMXBs with $\ell_X \geq 36.3$ are expected within the bounds of the L19 ellipse. This is to be compared with 26 HMXBs classified by our optical methods. As discussed in §3.5, these are highly likely to be genuine counterparts as the chance superposition with a high-mass star is negligible across the whole disk.

3.7 Summary and Conclusions

I make use of multi-wavelength *HST* imaging data to characterize the compact X-ray source population of M81 (using the X-ray source catalog by Lehmer et al. 2019), a nearby spiral galaxy with moderately low SFR. I directly characterize each X-ray source as a foreground star, a background galaxy/AGN, a SNR (based on the X-ray luminosity/hardness criterion developed by Hunt et al. 2021) or an XRB. In the latter case, I use color-magnitude diagrams to tentatively identify the most likely donor as a low-, intermediate- or high-mass star, or colors to estimate age in cases where the XRB is associated with a stellar cluster. In summary, I find the following:

- 199 out of 240 X-ray sources that are found over the HST footprint of M81 are classified as XRBs (Figures 3.1 and 3.4). Out of these, 159 are above the X-ray completeness limit of $\ell_X > 36.3$. Based on color-magnitude diagrams of the most likely counterpart(s), I identify 100 LMXBs (no visible counterpart), 25 IMXBs (donor mass between 3–8 $\mathrm{M}_{\odot}$), and 34 HMXBs (donor mass above 8 $\mathrm{M}_{\odot}$).

- After a thorough misclassification assessment using artificial sources to quantify chance superpositions, we conclude that the HMXBs population is robust, with a very low probability that a X-ray source will have a chance superposition with a massive star. In contrast, X-ray sources with no detectable counterparts likely harbor a significant population of background AGN with no visible optical host galaxy, whereas IMXBs suffer from a non-negligible likelihood of chance superposition. Moreover, intense X-ray irradiation may contribute to enhance the brightness and alter the colors of genuinely low-mass donors, adding further complexity to the LMXB/IMXB populations.

- 15 XRBs are found in old GCs, whereas 2 are associated with young star clusters (< 400 My old). GCs that host XRBs tend to be more massive and more compact than GCs that do not, similar to earlier findings in elliptical galaxies. These have X-ray luminosities consistent with the field population, and there is no obvious correlation between the X-ray luminosities of XRBs in GCs and the masses or densities of their host clusters.

- The XLF of HMXBs in M81 shows a marginal high-luminosity break at $\ell_X = 37.84$, similar to that found for M83 (Hunt et al., 2021). We note that the emergence of such a cut-off around the Eddington limit for a stellar-sized accretor may depend on whether the contamination from SNR at the low-luminosity end of the XLF is properly accounted for. While this effect may be negligible in a low star forming galaxy, it is likely to affect the XLFs of late types with high SFRs (such as M83).

CHAPTER 4

The X-ray Binary-Star Cluster Connection in Late-type Galaxies

The work in this chapter was originally published in the Astrophysical Journal (vol. 953, pg. 126) under the title "The X-Ray Binary-star Cluster Connection in Late-type Galaxies." The results of that work — produced in collaboration with Rupali Chandar, Elena Gallo, Matthew Floyd, Thomas J. Maccarone, and David A. Thilker — are introduced here. For a complete reading, please see Hunt et al. (2023a).

4.1 Abstract

Here, I conduct one of the largest systematic investigations of bright XRBs in both young star clusters and ancient GCs using a sample of six nearby, star-forming galaxies. Combining complete *Chandra* X-ray source catalogs with optical PHANGS-HST cluster catalogs, I identify a population of 33 XRBs within or near their parent clusters. I find that GCs that host XRBs in spiral galaxies appear to be brighter, more compact, denser, and more massive than the general GC population. However, these XRB hosts do not appear preferentially redder or more metal-rich, pointing to a possible absence of the metallicity-boosted formation of LMXBs that is observed in the GCs of older galaxies. I also find that a smaller fraction of LMXBs is found in spiral GC systems when compared with those in early-type galaxies: between 8 and 50%, or an average of 20% across galaxies in our sample. Although there is a non-negligible probability of a chance superposition between an XRB and an unrelated young cluster, I find that among clusters younger than 10 Myr, which most likely host high-mass XRBs, the fraction of clusters associated with an XRB increases at higher cluster masses and densities. The X-ray luminosity of XRBs appears to increase with the mass of the cluster host for clusters younger than ~ 400 Myr, while the inverse relation is found for XRBs in GCs.

4.2 Introduction

Whereas Chapters 2 and 3 focus on the XRB populations of two individual galaxies, this study instead considers the populations of XRBs within a sample of galaxies, specifically seeking those that are associated with star clusters. Star clusters are excellent targets in the search for XRBs in external galaxies. Not only are clusters optically brighter than the average extragalactic star, but they are effective factories for XRB formation: they boost the masses of already massive stars, harden already hard binaries, and promote the formation of new binaries through increased dynamical interactions (Fabian et al., 1975; Hills, 1976; Verbunt, 1987; Kundu et al., 2007; Garofali et al., 2012; Ivanova, 2013).

Observations of LMXBs indicate they form hundreds of times more efficiently in GCs than in the field (Clark & Parkinson, 1975; Katz, 1975; Grindlay, 1988; Hut et al., 1992), with between 20% and 70% of bright ($L_X \gtrsim 5 \times 10^{37}$ erg s^{-1}) LMXBs in massive elliptical galaxies currently residing in GCs (e.g. Angelini et al., 2001; Kundu et al., 2002; Jordán et al., 2004; Brassington et al., 2010; Fabbiano et al., 2010). A near constant 4–10% of GCs in ellipticals host bright LMXBs, on the other hand (Maccarone et al., 2003; Jordán et al., 2007; Mineo et al., 2014; Luan et al., 2018). These high efficiencies suggest that some fraction of field LMXBs may have formed in GCs that subsequently dissolved, or were dynamically ejected (e.g. Grindlay, 1984; White et al., 2002), though the impact these ejected sources have on the total LMXB population is a subject of debate (Piro & Bildsten, 2002; Kundu et al., 2002; Kundu et al., 2007; Peacock & Zepf, 2016; Kremer et al., 2018; Lehmer et al., 2020).

Studies also show that, in ellipticals, LMXBs are preferentially found in GCs that are brighter (i.e. more massive; e.g. Sivakoff et al., 2007; Brassington et al., 2010; Fabbiano et al., 2010; Riccio et al., 2022), more compact (i.e. smaller effective radii and higher densities; e.g. Kundu et al., 2002; Pooley et al., 2003; Jordán et al., 2007; Sivakoff et al., 2007; Paolillo et al., 2011; Riccio et al., 2022), and redder (i.e. metal-rich; e.g Bellazzini et al., 1995; Kundu et al., 2002, 2003; Jordán et al., 2007; Kundu et al., 2008; Sivakoff et al., 2007; Luan et al., 2018; Riccio et al., 2022). These surveys have gone a long way towards helping us understand the mechanism by which XRBs form within dense stellar environments. However, our understanding of the connection between XRBs and star clusters in *spiral galaxies* is comparatively inferior. The complex morphologies, ongoing star formation, and significant dust content of spirals make it extremely challenging to identify clusters in general, let alone to separate ancient GCs — within which LMXBs are produced — from reddened young clusters, which may host higher-mass XRBs (Chandar et al., 2004).

It is not obvious whether a comparably high fraction of the LMXB population is expected to be found in GCs of star-forming galaxies. While ellipticals appear to host more GCs per unit halo mass than star forming galaxies (Harris et al., 2015), the LMXB production efficiency likely decreases at higher redshift (Fragos et al., 2013). Tentatively, a smaller fraction of LMXBs are found in GCs across late-type galaxies that have been observed so far — between 2% and 13% for extragalactic LMXBs (Chandar et al., 2020; Hunt et al., 2021, 2023b), though as much as 20% of the Galactic LMXB population is located within GCs (Bahramian & Degenaar, 2023). The number of these galaxies explored remains too small to definitively prove that this is universally the case, and the depth of recent X-ray observations of these galaxies compared to prior observations of early-type galaxies could play a significant role in these discrepancies.

Furthermore, there is the issue of HMXBs. Although HMXBs are believed to form in young clusters, most of them are expected to be expelled into the general field population by supernova explosions (Kaaret et al., 2004; Sepinsky et al., 2005; Kalogera et al., 2007; Zuo & Li, 2010; Poutanen et al., 2013). If the natal kick velocities from black holes are smaller than those from neutron stars, then HMXBs with black hole accretors may be more likely to stay within their parent cluster than neutron star XRBs (Portegies Zwart et al., 2007), though recent work posits the kick velocities of black holes can rival those of neutron stars (Repetto et al., 2017; Atri et al., 2019). On the other hand, tight binary systems may theoretically survive kick velocities well in excess of the cluster escape velocity (Sippel & Hurley, 2013), and the ejection of black holes from clusters may not be as efficient as previously predicted, as indicated by both simulations and the identification of multiple black holes within compact star clusters (Strader et al., 2012; Morscher et al., 2015). Therefore, binaries with accreting black holes can be reasonably expected to be found both outside their birth clusters and within them.

Establishing the ratio of HMXBs in clusters versus HMXBs in the field may help illuminate the formation mechanisms and evolutionary histories of compact objects in external spiral galaxies. To date, relatively few papers have looked at XRBs in young clusters, with only a few late-type galaxies examined so far. Current observations suggest between 2% and 19% of HMXBs reside within young clusters (Rangelov et al., 2012; Chandar et al., 2020; Hunt et al., 2021, 2023b). An examination of young cluster populations by Mulia et al. (2019) find that XRBs in the Antennae galaxies and NGC 4449 prefer more massive and denser clusters among clusters with ages between 10 and 400 Myr, but there does not seem to be a similar preference for HMXBs formed in very young (< 10 Myr) clusters. Why and whether these patterns hold true for most late-type galaxies remains unknown.

In this chapter, I undertake the first systematic study of the association between bright XRBs and dense star clusters in a sample of six nearby face-on spiral galaxies that were observed by both the *Chandra* and the *HST*. I make use of the PHANGS-HST survey[1], which produced high-fidelity star cluster catalogs (Maschmann et al. in prep.; Lee et al., 2022; Thilker et al., 2022). I

---

[1] `https://phangs.stsci.edu/`

cross-match these catalogs with complete compact X-ray source catalogs based on deep Chandra observations, as compiled by L19. The paper is organized as follows: in §4.3, I describe the X-ray source and optical cluster catalogs, their astrometric alignment, and the positional uncertainties of the observations; in §4.4, I describe the cluster properties considered and how they are calculated; in §4.5, I discuss the population of clusters that I determined host XRBs and the properties of those clusters compared to the general cluster population; finally, in §4.6, I compare these findings to cluster XRBs found in previous studies, particularly in early-type galaxies.

4.3 Catalogs

4.3.1 X-ray source catalog

A comprehensive catalog of more than 4000 X-ray sources across 38 nearby galaxies was compiled by L19 from 5.8 Ms of *Chandra* ACIS data. *Chandra* has an excellent angular resolution of $0.''3$ at its aim-point, which allows us to view nearby XRBs as point-like sources (Grimm et al., 2008). The galaxies in the sample are all within 30 Mpc and have inclinations $\lesssim 70^\circ$ to our line of sight, which ensures a low degree of local absorption. Because the galaxy selection was based mainly on those covered by both *Chandra* and the *Spitzer* Infrared Nearby Galaxies Survey (SINGS; Kennicutt et al., 2003), the sample brackets a diverse range of properties, including stellar mass and star formation rate. L19 also provides a careful assessment of the X-ray completeness for each target galaxy: roughly 3500 X-ray sources are above the 90% X-ray completeness limits of their respective galaxies.

Additionally, L19 presents a model for estimating the expected contributions from LMXBs, HMXBs and cosmic X-ray background sources (CXBs) to the total X-ray luminosity function within the footprint of each galaxy. The galactic footprints are defined by the isophotal ellipse tracing the $K_s \approx 20$ mag arcsec^{-2} galactic surface brightness of each galaxy (L19; Jarrett et al., 2003). Specifically, L19 provides a functional relationship to estimate the number of LMXBs and HMXBs in each galaxy based on the total stellar mass and star formation rates, respectively, within the isophotal ellipses, as mapped from combined K-band Two Micron All Sky Survey (2MASS) and optical Sloan Digital Sky Survey (SDSS), and combined FUV GALEX and 24μm *Spitzer* observations. The results of L19's sub-galactic XRB population modeling yield a useful framework for comparing the field vs. cluster XRB populations that I aim to identify with this analysis.

4.3.2 Cluster catalog

The Physics at High Angular Resolution in Nearby Galaxies (PHANGS[2]) program is a high-resolution, multi-wavelength survey that utilizes Atacama Large Millimeter/Submillimeter Array (ALMA), HST and Very Large Telescope (VLT) observations to probe spiral galaxies within ~ 20 Mpc (Kreckel et al., 2019, 2021; Leroy et al., 2021; Lee et al., 2022). Of particular interest to this chapter is the sample of tens of thousands of compact star clusters identified by the PHANGS-HST[3] survey (Deger et al., 2021; Turner et al., 2021; Whitmore et al., 2021). These span 38 nearby galaxies with five-band (NUV, U, B, V, and I), high-resolution HST imaging data taken with the WFC3 camera. The sample is purposefully chosen to ensure that the cluster radii are broader than the PSF, thereby minimizing the limitations of instrument resolution. Clusters are identified via a combination of manual and machine-learning classification techniques using a Multiple Concentration Index scheme to select cluster candidates (Whitmore et al., 2021; Lee et al., 2022; Thilker et al., 2022).

In this work, I only use centrally concentrated clusters (class 1 and 2), which span all ages. A separate effort by Floyd et al. (2024) has distinguished ancient GCs from their younger counterparts, based on color selection followed by a careful visual examination. The PHANGS data were obtained from the Mikulski Archive for Space Telescopes (MAST) at the Space Telescope Science Institute and can be accessed via DOI: 10.17909/t9-r08f-dq31.

4.3.3 Galaxy Selection

This paper considers the six spiral galaxies that constitute the intersection between the L19 X-ray source catalogs and the PHANGS-HST cluster catalogs: NGC 628, NGC 3351, NGC 3627, NGC 4321, NGC 4569, and NGC 4826. The target galaxies, which are located between 4–16 Mpc, are shown in Figure 4.1. The L19 X-ray sources are plotted in red, where the radii of each red circle represents the 2σ positional uncertainties of the X-ray data. These are calculated, in part, using the 68% and 95% positional uncertainty equations of Kim et al. (2007), which incorporates the X-ray counts and off-axis angles of each source provided by L19. The final 2σ positional uncertainties include astrometric uncertainties, discussed in §4.3.4 below, added in quadrature to the positional uncertainties. In addition, the magenta contours represent the outermost distribution of the star clusters within the PHANGS-HST field of view (Lee et al., 2022). The basic properties of each galaxy, along with the number of X-ray point sources and optically selected clusters, are given in Table 4.1. For each galaxy, I utilize the updated distances that were used to identify and estimate

---

[2] `https://sites.google.com/view/phangs/home`

[3] `https://archive.stsci.edu/hlsp/phangs-hst`; `https:/archive.stsci.edu/hlsps/phangs-cat/`

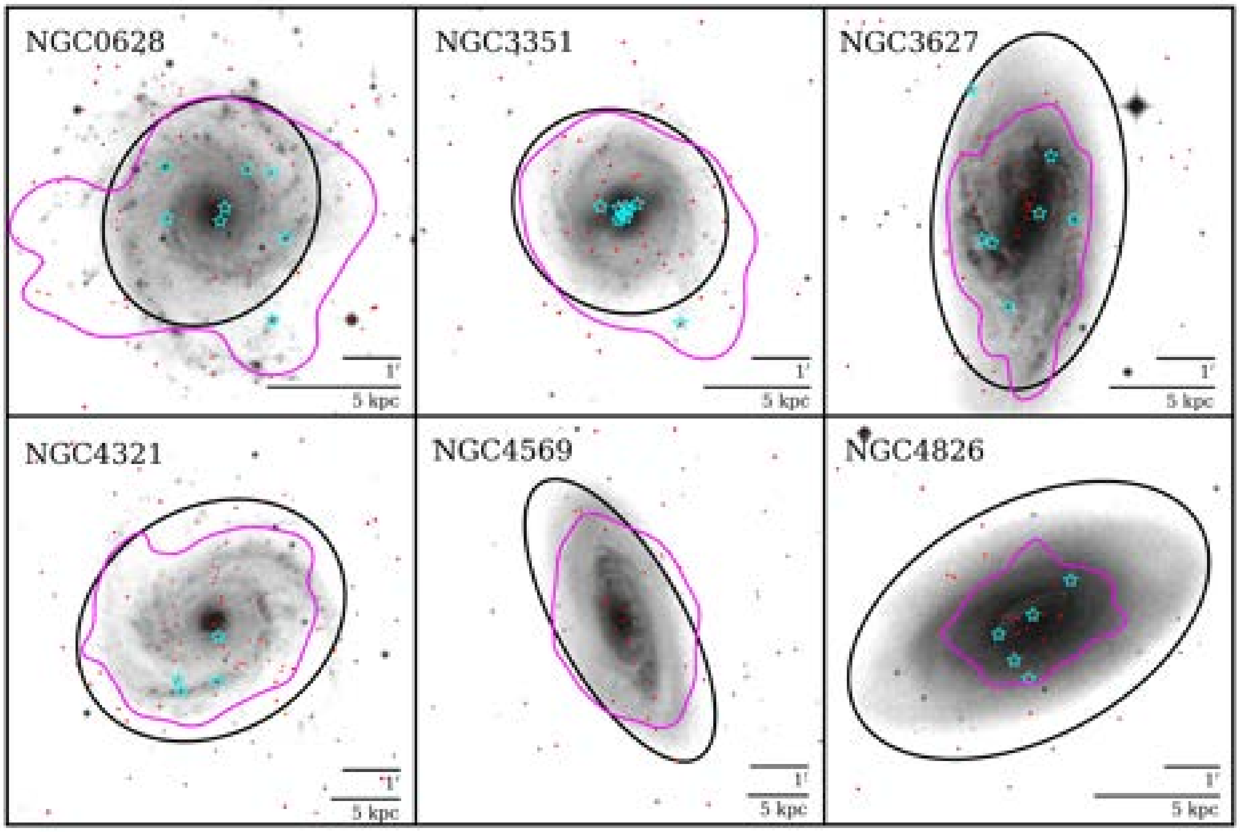

Figure 4.1 Our galaxy sample, as imaged by the Digitized Sky Survey. Small red circles represent the coordinates and 2σ radii of X-ray sources from Lehmer et al. (2019), while magenta contours show the outermost density contour of class 1 and 2 clusters in the PHANGS catalog, which I use to denote the PHANGS cluster distribution. Outlined in black are the isophotal ellipses that trace the $K_s \approx 20$ mag arcsec^{-2} galactic surface brightness of each galaxy (Jarrett et al., 2003; Lehmer et al., 2019). Cyan stars represent XRBs that I have identified as having at least one cluster association.

cluster properties (see Lee et al., 2022), and I adjust the X-ray completeness limit and luminosities of the sample accordingly. The two catalogs capture a total of 549 X-ray sources and 3919 optical clusters across the six galaxies, 271 and 3715 of which fall within the K_s-band isophotal ellipses.

4.3.4 Astrometric corrections

To identify candidate PHANGS-HST cluster counterparts to X-ray sources, I first perform the standard astrometric correction (see Chapter 2). HST images obtained from the HLA are used as the base coordinates against which to shift the L19 X-ray source coordinates. The PHANGS-HST catalogs are generated using large mosaics of HST observations, so the catalog positions of PHANGS clusters are also shifted slightly when compared to individual HST fields.

For each galaxy in our sample, I select one HST field from the HLA that was imaged in at least

Table 4.1. Galaxy Sample for Cluster XRBs

Galaxy	$\alpha_{\rm J2000}$	$\delta_{\rm J2000}$	Dist. (Mpc)	log $L_{\rm X,90\%}$ (erg s^{-1})	Limits[b] (m_V)	(M_V)	Number of sources X-ray[a]	Clusters[b]
NGC 0628	03 36 41.8	+15 47 00.5	9.84 ± 0.63	36.9	24.9	-5.1	155 (47)	750 (598)
NGC 3351	10 43 57.7	+11 42 13.0	9.96 ± 0.33	37.0	25.3	-4.7	65 (39)	335 (313)
NGC 3627	11 20 15.0	+12 59 28.6	11.32 ± 0.48	37.5	24.7	-5.6	105 (64)	1251 (1236)
NGC 4321	12 22 54.9	+15 49 20.6	15.12 ± 0.49	37.4	24.8	-6.1	109 (61)	868 (866)
NGC 4569	12 36 49.8	+13 09 46.3	15.76 ± 2.36	37.8	24.0	-7.0	66 (27)	540 (527)
NGC 4826	12 56 43.7	+21 40 57.6	4.41 ± 0.19	36.7	23.9	-4.3	49 (33)	175 (175)

Note. — Distances are from the PHANGS-HST pipeline (Lee et al., 2022), and the 90% X-ray luminosity completeness limits ($L_{\rm X,90\%}$) are adjusted from the L19 values accordingly. The limiting optical magnitude of the PHANGS ($V_{\rm PHANGS,lim.}$) is taken as the optical V-band magnitude of the dimmest cluster identified by PHANGS. The number of X-ray sources and clusters within each galaxy is given, where numbers in parentheses represent the number of sources that fall within the K_s-band isophotal ellipses, as described in L19. [a]Lehmer et al. (2019); [b]Whitmore et al. (2021); Lee et al. (2022); Thilker et al. (2022)

three filters (BVI) and that overlaps with as much of the area enclosed by the K_s-band ellipses as possible. A handful of sources with visibly identifiable counterparts in the HST field are selected as reference sources for the astrometric calculations of each catalog: background AGN, foreground stars, and isolated GCs in clear proximity to X-ray sources are used for the X-ray catalog, while isolated GCs are used for PHANGS. Ideally, at least 15 reference sources are used per catalog per galaxy, but in some cases (particularly for the L19 catalog), there are fewer than 10 reference sources suitable for use.

The sources in each catalog are then shifted by the median offsets in right ascension and declination ($\Delta_{\rm RA}$ and $\Delta_{\rm Dec}$) between the HST image and the catalog coordinates of the select reference sources. For PHANGS, a simple translational shift is sufficient to properly align cluster coordinates onto the HST image. For the X-ray sources, there is an additional positional uncertainty introduced when combining Chandra and HST observations (e.g. by rotation, instrumental resolution, etc.). These are reflected in the standard deviations of the right ascension and declination correction ($\sigma_{\rm RA}$ and $\sigma_{\rm Dec}$) and are factored into the 2σ positional uncertainty of each X-ray source as described in §4.3.3. The final astrometric corrections are listed in Table 4.2. After corrections, 95% of the new 2σ positional uncertainties of the L19 sources fall between $0.''21$ to $1.''96$, with a median of $1.''07$ across all sources. Within the K_s-band ellipses — a region that inherently limits the off-axis angle of each X-ray source and thus the degradation of the Chandra PSF — the

Table 4.2. Astrometric Corrections

Galaxy	L19 X-ray sources Δ_{RA} (arcsec)	 Δ_{Dec} (arcsec)	 σ_{RA} (arcsec)	 σ_{Dec} (arcsec)	PHANGS clusters Δ_{RA} (arcsec)	 Δ_{Dec} (arcsec)
NGC 0628	-0.03	-0.18	0.04	0.11	-0.06	-0.13
NGC 3351	-0.21	0.29	0.48	0.45	0.01	-0.01
NGC 3627	-0.18	-0.08	0.05	0.04	-0.33	-0.18
NGC 4321	-0.40	-0.19	0.06	0.08	-0.65	-0.65
NGC 4569	0.23	-0.07	0.06	0.05	0.01	-0.02
NGC 4826	-0.27	0.06	0.16	0.29	0.01	0.02

Note. — The astrometric corrections on the L19 (Chandra) X-ray sources and PHANGS (HST) clusters are given as translational shifts Δ along right ascension and declination. For the X-ray sources, the standard deviation of the shifts between the L19 reference source coordinates and their optical counterparts on the HST image, σ, are used to calculate the positional uncertainties of the X-ray sources, which are included in the 2σ positional uncertainty calculations.

maximum 2σ uncertainty is $2.''15$.

In the following sections, I use the L19 X-ray source catalog as the basis of our investigation, which will allow me to estimate the expected LMXB and HMXB populations. I search for clusters associated with each XRB, where a cluster is determined to be associated with an X-ray source if it falls within a radius equal to the 2σ positional uncertainty of said source. I explore the properties of these XRB clusters compared to both the total cluster population and the field XRBs within these spiral galaxies in §4.5. I compare these results to previous studies of XRBs within elliptical and spiral galaxies in §4.6.

4.4 Star Cluster Properties

The basic properties of the stellar clusters were determined from multi-band HST images of our sample galaxies taken as part of PHANGS-HST (Turner et al., 2021; Lee et al., 2022; Floyd et al., 2024). The cluster selection methodology is briefly summarized in Section §4.3; here I describe estimates of the age, mass, and effective radius of each cluster within the galaxy sample.

4.4.1 Age

The PHANGS-HST survey estimates the age and reddening of each cluster by comparing the measured photometry with predictions from population synthesis models. Because PHANGS galaxies have formed stars continuously over their lifetimes, they contain clusters spanning a wide age range, from very recently formed clusters with ages $\approx$ 1 Myr to ancient GCs with ages of $\approx$ 12 Gyr. The significant interstellar medium (ISM) in PHANGS galaxies means that breaking the well-known age-reddening degeneracy, where red colors for clusters are either due to older ages or because they are affected by dust, is critical for correctly age-dating clusters.

Details of the method used to estimate the age and reddening for each cluster are described in Turner et al. (2021). The fluxes measured in five broad-band filters (equivalent to NUV, U, B, V, and I bands) are compared with predictions from the solar-metallicity model for cluster ages between 1 Myr and 12 Gyr (Bruzual & Charlot, 2003). Age and reddening are the two free parameters in the fit, and reddening is allowed to vary from an E(B-V) of 0.0 to 1.5 mag. The software *Cigale* (Boquien et al., 2019) fits the photometry for a cluster to each age-reddening combination in the grid and finds the combination that minimizes χ^2.

While the PHANGS-HST study estimates ages correctly for many clusters, incorrect determinations have been found to disproportionately affect the ancient GC populations. Whitmore et al. (2023) and Floyd et al. (2024) have found that $\sim 80\%$ of ancient globular clusters, which comprise ≈ 5–10% of the PHANGS cluster catalogs, have been incorrectly age-dated, with both too young ages and too high reddening. For our sample, I assign an age of 10 Gyr to any GC that is coincident with an XRB, regardless of the age estimated in the PHANGS-HST pipeline. We similarly correct the ages of any intermediate-age (10–400 Myr) clusters which have incorrectly been assigned too young of an age from the PHANGS-HST pipeline if a visual inspection indicates they are not heavily affected by dust, using the best-fit age where a low maximum extinction of E(B-V) < 0.1 mag is allowed. For the rest of the clusters, I adopt the age (and reddening) determined by the default PHANGS-HST pipeline.

4.4.2 Mass

To estimate cluster mass, PHANGS-HST adopts a mass-to-light ratio predicted by the evolutionary model of solar metallicity clusters by Bruzual & Charlot (2003) at the best-fit age obtained in §4.4.1. The mass is then calculated using the extinction-corrected luminosity.

I adopt these default pipeline masses for all clusters where the PHANGS-HST pipeline gives good age estimates, which includes most non-GC clusters. For non-GCs which have incorrect age-dating, a revised mass is calculated by using the M/L_V ratio predicted for the new best fit age. To estimate the masses of GCs, I adopt a mass-luminosity ratio of 1.5 $\mathrm{M}_\odot/L_\odot$, as given in

Chandar et al. (2007), where the V-band luminosity of each GC is calculated from the HST V-band magnitude: $L_V \equiv 10^{0.4(M_{V,\odot}-M_V)}$. The absolute V-band Vega magnitude of the Sun ($M_{V,\odot}$) is given by Willmer (2018) as 4.91 for the WFC3 F555W filter. The mass estimates are typically uncertain to within a factor of 2 (e.g. see Chandar et al., 2010).

4.4.3 Effective Radius and Density

Floyd et al. (2024) measures the effective radius R_{eff} of each cluster in the PHANGS-HST catalog using the Ishape routine in BAOlab (Larsen, 1999), a standard software package used to estimate the half-light radii of clusters. Ishape convolves a series of model clusters having King profiles (with an assumed tidal-to-core radius ratio of 30) with a user-provided PSF. These convolved models are then fitted to the V-band image of each cluster, and the fits are converted to effective radius using the appropriate pixel scale for the WFC3 or ACS camera. A number of checks were performed to verify the size results, including reproducing the size measurements of clusters published in M51 by Chandar et al. (2016) and verifying that the Ishape measurements track other size estimates, such as the concentration index (the magnitude difference measured in aperture radii of 1 and 3 pixels). The distribution of effective (and half-light) radii for ancient globular clusters is consistent with those reported in prior studies (e.g. Jordán, 2004; Jordán et al., 2007; Puzia et al., 2014).

With the sizes and masses of the clusters, I estimate the density of each cluster by defining the internal half-mass density as $\rho_h \equiv 3M/8\pi R_h^3$, where M is the mass of the cluster, and the 3-dimensional half-mass radius R_h is calculated from the 2-dimensional effective radius using $R_h = (4/3)R_{\text{eff}}$ (e.g. see Chandar et al., 2007; McLaughlin & Fall, 2008).

4.5 X-ray Binary Host Clusters

Within the fields of view captured by the PHANGS cluster catalog (see Figure 4.1, magenta contours), there are 33 X-ray point sources that are spatially coincident with at least one cluster. Depending on the galaxy distance and physical size, a non-negligible fraction of the X-ray point source population may be background AGN, even within the K_s-band ellipses (see Figure 10 in L19). The contamination by CXBs to the total X-ray emission of the galaxy is estimated by L19; it is likely that unseen CXBs are embedded within the field X-ray source population, which are described and corrected in §4.6.2.

Observation-based simulations show that the likelihood of a randomly-distributed X-ray source coinciding with an unassociated cluster is small (Rangelov et al., 2012; Hunt et al., 2023b). I further demonstrate the unlikelihood of chance superpositions by performing a similar simulation: for each galaxy in our sample, I randomly scatter N simulated X-ray sources, where N is equivalent to the number of XRBs expected to fall within some area based on the enclosed SFR and $\mathrm{M}_\star$ (see §4.3.1, §4.6.2 and L19 for details). The chosen area in each galaxy is the region covered by both the K_s-band isophotal ellipse and the PHANGS cluster distribution (the intersection of the black ellipses and magenta contours in Figure 4.1). Each simulated source is restricted to this area and assigned a positional uncertainty equal to the median 2σ of the L19 sources above the 90% X-ray completeness limit and within the region. The sources are scattered 1000 times per galaxy, yielding a statistical measure of the number of chance superpositions with a cluster. I find that across all galaxies, the mean and median number of chance superpositions between an XRB and cluster per simulation run is approximately zero, except in the case of NGC 3351, which averaged a single superposition per simulation run (equivalent to 5% of the simulated XRB population). Thus, we conclude that the probability of a randomly distributed X-ray source intersecting with a cluster is negligible, consistent with previous estimates (Rangelov et al., 2012; Riccio et al., 2022; Hunt et al., 2023b).

However, this might not necessarily be the case for non-random distributions, such as that which may be expected for HMXBs. In a secondary test, I find that shifting the positions of our real X-ray sources by $4''$ (a separation sufficiently greater than the 2σ positional uncertainty of any source but smaller than the typical distance over which the properties of the target galaxies change significantly) in any direction yields a fairly high probability of the X-ray sources coinciding with at least one cluster: the number of XRB-cluster associations when shifting in any direction decreases by an average of 57%, and in some cases (e.g. NGC 4321) there is no change. The chance superpositions are mostly driven by younger clusters, largely due to the dense distribution of these sources and HMXBs within active star-forming regions, such as the spiral arms of their host galaxy. Because LMXBs and GCs tend to follow the underlying, radial stellar mass distributions and are generally more isolated and more uniformly distributed than higher-mass XRBs and younger clusters, I consider any X-ray source that has a GC within 2σ to be truly associated with a cluster, while I approach the population of XRBs associated with clusters younger that 400 Myr with more caution. This approach to the GC population is independently supported by prior works (e.g. see Riccio et al., 2022).

XRBs associated with GCs are almost certainly LMXBs, since only low-mass stars remain in these ancient stellar systems. The nature of the donor star is less certain for clusters younger than a few hundred million years. Because the most massive stars tend to sink towards the centers of clusters due to dynamical friction and have been found to be the most active in forming binaries (e.g. Trenti, 2006; Kaczmarek et al., 2011; Wu & Zhao, 2021), very young clusters ($<$ 10 Myr) are quite likely to host HMXBs. Clusters with ages between 10 and a few 100 Myr contain both intermediate and low-mass stars. The masses of XRB donor stars in these intermediate-age clusters are currently not well understood. For neutron star accretors (i.e., the majority of the population), intermediate-mass donors quickly evolve into low-mass stars through a short-lived thermal mass transfer phase (Podsiadlowski et al., 2002; Pfahl et al., 2003; Chen & Podsiadlowski, 2016). This likely results in a population of abnormally luminous LMXBs with intermediate-mass donor progenitors. For these reasons, I analyze intermediate-age clusters as a separate population from both GCs and very young clusters.

In total, 25 of the 33 point-like X-ray sources are coincident with a single cluster. Of these, 16 are associated with an ancient GC, 5 are associated with a very young cluster, and 4 are associated with an intermediate-age cluster. Eight additional X-ray sources are coincident with more than one cluster within 2σ. This is particularly common in bright, crowded, actively star-forming regions, as stated above. In these cases, it can be challenging to determine the specific cluster host of an XRB. An inspection of X-ray sources with multiple cluster candidates indicates that clusters within 2σ of an X-ray source generally have similar ages: 1 X-ray source is associated with 2 GCs, while 7 are each associated with more than 1 cluster younger than ~ 400 Myr. There are 2 XRBs that are associated with both young *and* intermediate-age clusters: L19X032 and L19X033 in NGC 3351. I also find that clusters associated with the same X-ray source can have drastically different masses, effective radii, and densities. Through this analysis, I explicitly indicate which clusters are confirmed XRB hosts (i.e. the only cluster within 2σ of a singly-associated XRB) and which are candidate hosts (i.e. one of several clusters within 2σ of a multiply-associated XRB). All singly-associated and multiply-associated XRBs and the properties of their (candidate) host clusters are listed in Tables D.1 and D.2 in the Apppendix.

One of the galaxies in our sample, NGC 4569, has zero clusters that host XRBs. This may, in part, be due to the fact that NGC 4569 has the brightest X-ray completeness limit of all galaxies in our sample, at 37.8 log L_X. Indeed, an inspection of X-ray sources with log $L_X \geq 37.8$ yields far fewer sources that are spatially coincident with a cluster: only 12 of the 33 XRB clusters have X-ray luminosities brighter than the completeness limit of NGC 4569, with NGC 4826 having none. For this reason, I exclude the clusters from NGC 4569 from the remainder of our analysis, particularly where I calculate statistics using the full star cluster population.

4.5.1 Magnitude and color distribution

The PHANGS cluster catalog includes measurements of cluster magnitudes in 5 HST bands, allowing us to compare the colors and brightness of XRB-host clusters to the general cluster population. Figure 4.2a shows the V vs. $B - V$ color-magnitude diagram (CMD) of all clusters, in grey, where the V-band magnitudes were calculated using the apparent magnitudes reported by PHANGS at the galactic distances from Lee et al. (2022). The distribution of the GC and young cluster populations

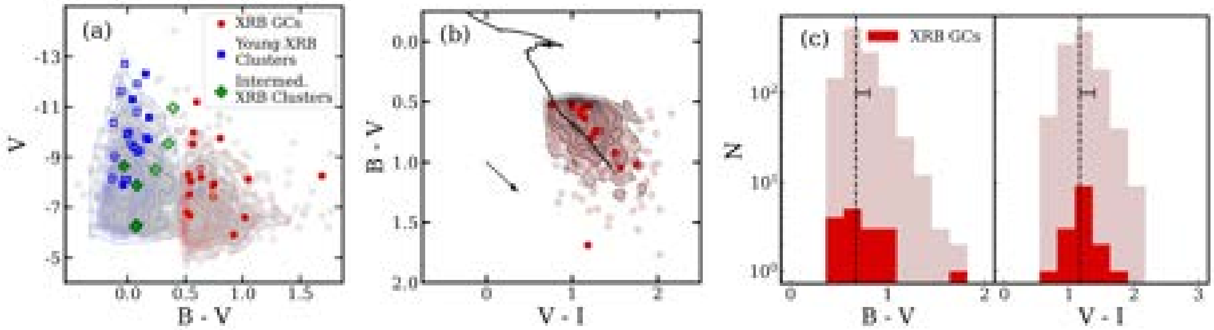

Figure 4.2 (a) A CMD of all clusters (grey, excluding clusters from NGC 4569) compared to the X-ray emitting GCs, very young clusters, and intermediate-age clusters. The 25 filled symbols represent clusters that are the sole candidate host of an XRB, whereas the 22 open symbols represent clusters that are associated with XRBs with multiple cluster counterparts (1 LMXB and 7 non-GC XRBs). The density contours of the very young cluster and GC populations are shown in blue and red, respectively. (b) The color-color diagram of the GC population, where the evolutionary model for solar-metallicity clusters (Bruzual & Charlot, 2003) is shown in black, and the arrow represents the direction of reddening. (c) The histograms of the $B-V$ and $V-I$ colors of GCs. The black dashed line and horizontal bar represent the mean and standard deviation of a Gaussian fit to the total GC population.

are respectively mapped by red and blue contours. The CMD shows that XRBs are more common in brighter GCs and very young clusters, compared to the general cluster population in each age group. However, no such preference is apparent among intermediate-age clusters.

For ancient GCs, we are interested in establishing whether XRBs are more likely to be found in redder (and thus presumably more metal-rich) GCs over blue (metal-poor) ones, as has consistently been found in elliptical galaxies (Kundu et al., 2003, 2008; Sivakoff et al., 2007; Luan et al., 2018). Figure 4.2b shows the $B-V$ vs. $V-I$ colors of XRB-hosting GCs, compared to the full GC population. For reference, the evolutionary model for solar-metallicity clusters (Bruzual & Charlot, 2003) is plotted in black, and the direction that the clusters may shift due to reddening is indicated by the arrow. To determine whether the XRB GCs are statistically redder than the general GC population, I perform a two-sample independent Wilcoxon test on the $B-V$ and $V-I$ distributions of the two populations using `ranksum` from the SciPy statistical Python package (see Jordán et al., 2007). The $B-V$ and $V-I$ distributions are plotted in Figure 4.2c. I find that XRB GCs show no color preference in any way that is inconsistent with the underlying GC population. The same test performed on the younger clusters indicates a possible tendency towards bluer colors (and thus presumably younger, more metal-poor systems) for the intermediate-age XRB clusters, although our sample size is too small to determine at this time, and there is a non-negligible chance that at least some of these clusters are spurious associations (as discussed at the beginning of §4.5).

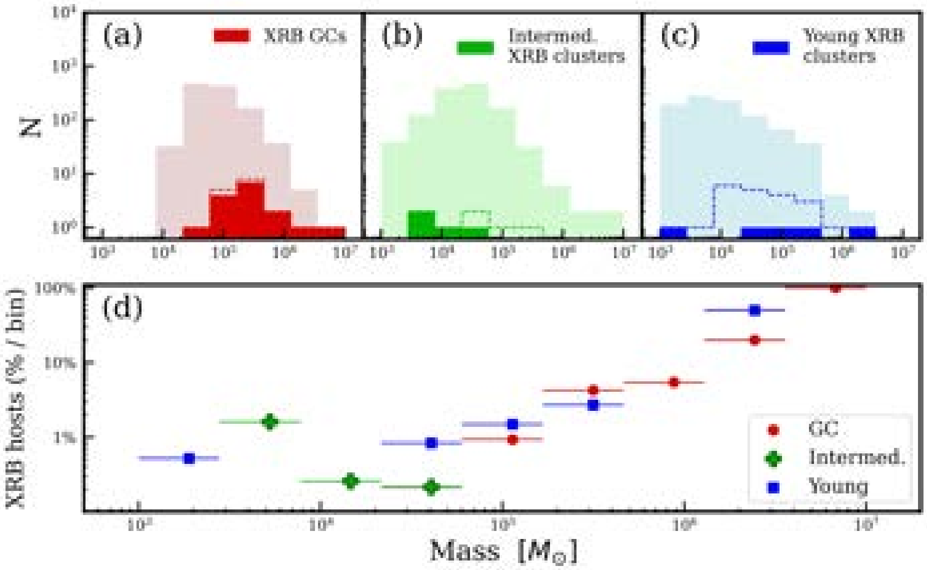

Figure 4.3 The histograms of cluster masses, separated into (a) GCs, (b) intermediate-age clusters, and (c) young clusters, excluding clusters from NGC 4569. Dashed lines indicate the bins containing the 22 candidate hosts with XRBs that have multiple cluster associations. In panel (d), the fraction of clusters that hosts at least one XRB is given as a percentage of the total clusters per age population per mass bin. The horizontal lines show the boundaries of each bin.

4.5.2 XRB cluster masses

While the connection between star cluster mass and XRBs has been explored extensively for GCs in elliptical galaxies, little work has been done to date to characterize XRB-hosting clusters in late-type galaxies. The top panel of Figure 4.3 shows histograms of the masses of PHANGS clusters, separated by (a) GC, (b) intermediate-age cluster, and (c) very young cluster populations, where the XRB hosts are highlighted. The bottom panel (Figure 4.3d) illustrates the percentage of clusters that host an XRB as a function of cluster mass.

It is clear from Figure 4.3a that XRB-hosting clusters occupy the more massive end of the GC mass distribution; that is, bright LMXBs are preferentially found in more massive GCs. In addition, in Figure 4.3d we see that the fraction of GCs that host XRBs increases significantly at higher mass bins. This is true globally and on a galaxy-by-galaxy basis. The fraction of very young clusters that host XRBs also increases with increasing mass, with a nearly 2 order of magnitude difference over the range plotted in Figure 4.3d. The statistics for intermediate-age XRB host clusters are quite poor, and these XRBs do not show any evidence of preferentially forming in higher-mass clusters.

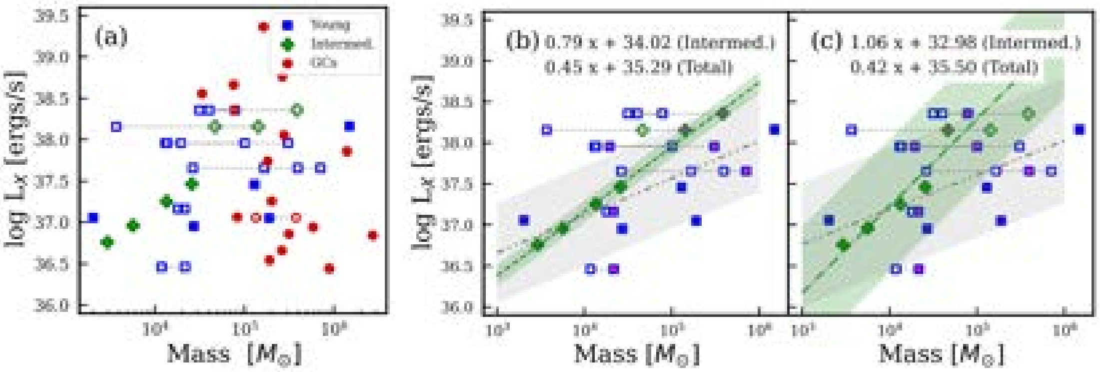

Figure 4.4 The X-ray luminosities of XRB-hosting clusters as a function of cluster mass. Open symbols represent the 22 candidate clusters of the 8 XRBs with multiple cluster associations. Clusters associated with the same XRB are connected by a dotted line. Panels (b) and (c) represent population sets (i) and (ii) respectively, for which the assumed parent cluster of multiply-associated XRBs are indicated in magenta. The best-fit line for the populations with a statistically significant $M_\star$–L_X correlation — i.e. the intermediate-age XRB cluster and the total non-GC cluster populations — is given (green dashed and grey dash-dotted lines, respectively), where $x = \log M_\star$ in solar units. The linear fits to set (i) for GCs (not shown) is $-0.82x + 42.01$.

Table 4.3 Most significant correlations per population set

	Set i	Set ii	Set iii
Very Young	0.59^a (0.07)	0.49^a (0.12)	0.17^a (0.59)
Intermediate-age	0.99^a (< 0.01)	0.95^a (0.01)	0.99^a (<0.01)
Total non-GCs	0.69^a (< 0.01)	0.57^a (0.02)	0.34^b (0.19)
GCs	-0.53^b (0.03)	—	-0.49^b (0.05)

Note. — For each cluster set as described in §4.5.3, the weighted ranks and p-values (in parentheses) for the correlation method that shows the most statistically significant $M_\star$–L_X correlation are shown (excluding results with p-values of 0), where the method from which the statistics are obtained are marked as (a) Pearson or (b) Spearman. Any rank with an absolute value greater than 0.5 is considered a strong correlation. The sign of the rank represents whether the correlation is positive (increasing) or negative (decreasing). A correlation is statistically significant if it has a p-value $\leq$ 0.05.

4.5.3 X-ray luminosity vs. cluster mass

The environment within dense star clusters is conducive to efficient XRB formation, but whether more massive clusters should be expected to retain multiple XRBs at a time is difficult to determine. Observational studies suggest that the brightest metal-rich GCs likely host multiple LMXBs (Angelini et al., 2001; Kundu et al., 2007); also, multiple LMXBs have been confirmed within

Galactic GCs, such as the metal-poor M15 (White & Angelini, 2001; Arnason et al., 2015). Mulia et al. (2019) approached the question of XRBs in *younger* clusters by comparing the X-ray luminosities to cluster mass, but found no evidence of a correlation for HMXBs. I adopt a similar analysis here.

To quantify any possible correlation between X-ray luminosity and host cluster mass, I run two correlation analyses from the SciPy statistical library: the Pearson correlation, and the Spearman correlation (Zwillinger & Kokoska, 2000; Virtanen et al., 2020). The Pearson correlation measures the degree to which two variables are linearly related, while the Spearman correlation measures for nonlinear, monotonic dependence or association. A correlation is considered statistically significant if it has a p-value ≤ 0.05, and the strength of the correlation is measured on a scale from 0 (uncorrelated) to 1 (perfect correlation). I analyze the XRB-hosting clusters in each age population (GCs, intermediate-age, and young). I also analyze the combined non-GC population, since the young and intermediate-age populations are spatially intertwined and the physical distinction between them is unclear.

The total cluster sample is shown in Figure 4.4a, including all candidate hosts of multiply-associated XRBs. Because 8 of the 33 XRBs have multiple cluster associations spanning a wide range of masses, the results of our correlation analysis depends heavily on the true parent clusters of multiply-associated XRBs. In total, there are 2304 unique combinations of cluster counterparts on which the analyses are run.

Since there is only 1 multiply-associated GC XRB, which has only 2 candidate GC counterparts, the $\mathrm{M}_{\star}$–L_{X} analysis of the GC population is simple: there are only 2 unique combinations of GC counterparts, and both show, for the first time, a statistically significant $\mathrm{M}_{\star}$–L_{X} anticorrelation. This is in contrast to the analysis of GCs within M81, which demonstrated the lack of a clear relation (Hunt et al., 2023b), and within NGC 4278, which indicated a weak positive correlation between L_{X} and brighter magnitudes (i.e. higher cluster mass; Fabbiano et al., 2010). More complicated are the non-GC cluster populations, which include 7 multiply-associated XRBs with 20 cluster candidates. Young and intermediate-age clusters tend to share similar environments, leading to 2 of the multiply-associated XRBs having both young and intermediate-age candidate counterparts. Between young and intermediate-age clusters, there is a total of 1152 unique counterpart combinations. Of these, 62% yield statistically significant $\mathrm{M}_{\star}$–L_{X} correlations among the combined (total) young and intermediate-age XRB cluster population. In analyzing these populations independently, I find that *only 6 cluster combinations* (0.5%) yield a statistically significant $\mathrm{M}_{\star}$–L_{X} correlation for young clusters alone. *All* combinations of intermediate-age XRB clusters show a nearly perfect linear $\mathrm{M}_{\star}$–L_{X} correlation, though it must be noted that there are relatively few intermediate-age XRB clusters, and the 1152 combinations yield only 6 unique intermediate-age configurations. A larger cluster analysis is required to determine the robustness of this trend.

To better assess how the combination of cluster candidates impacts the correlation models, I highlight the analysis of 3 sets of clusters, for which the parent cluster of each multiply-associated XRB is assumed to be: (i) the most massive candidate cluster; (ii) the median mass candidate cluster, with preference given to the more massive of two clusters if no single median is available; and (iii) the least massive candidate cluster. The results of the correlation analysis on each of these sets is summarized in Table 4.3. Interestingly, the trials that include either the highest mass clusters or the median mass clusters (sets i and ii) show strong positive $\mathrm{M}_{\star}$–L_{X} correlations at a statistically significant level for both the intermediate-age cluster and the total non-GC populations. The linear fits to the non-GC populations of sets (i) and (ii) are shown in Figure 4.4b and 4.4c, respectively, with the assumed hosts highlighted in magenta. It is clear that, of the three cluster sets, the high-mass trial provides the strongest correlation to the highest statistical significance, followed by the median-mass set. The set which assumes the least massive cluster is the XRB host, set (iii), gives the lowest statistical significance nearly across the board.

There is no definitive way of knowing which of the 2304 cluster combinations describe the true parent cluster population with the data used in this study. Since we find in §4.4.2 that the fraction of clusters that host XRBs appears to increase with increasing mass bins, and because clusters with a greater number of stars (i.e. greater mass) provide more opportunities for the formation of an XRB, it is reasonable to presume that the true host clusters for at least some of the 8 multiply-associated XRBs are likely higher mass. If this is the case, then based on the results from the correlation analyses on set (i) and (ii) in Figure 4.4, there is likely a strong correlation between X-ray luminosity and mass among the total non-GC X-ray clusters population. However, this correlation does not appear to hold among the very young host cluster subsample. For GCs, the $\mathrm{M}_{\star}$–L_{X} anticorrelation is strongest for the higher-mass candidate host, but is statistically significant either way.

While, for non-GC XRB hosts, these correlations *may* indicate the presence of multiple XRBs within more massive clusters, there is no indication that these clusters have higher luminosity than the general field XRB population. Furthermore, the correlation for GCs is *negative*, despite being more massive than the non-GC population. Therefore, we conclude that the $\mathrm{M}_{\star}$–L_{X} correlation for clusters younger than 400 Myr may not be due to the presence of multiple XRBs within X-ray emitting clusters, though the possibility cannot be precluded. This result assumes all XRBs included are indeed found within or near their parent clusters, and the presence of spurious cluster associations may further complicate this relation.

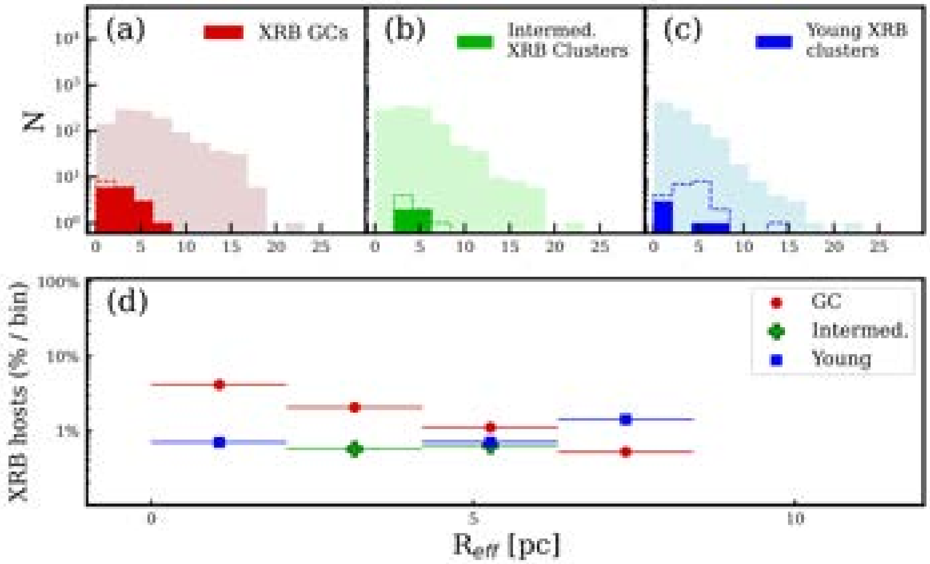

Figure 4.5 The histograms of cluster effective radii, separated into (a) GCs, (b) intermediate-age clusters, and (c) very young clusters, excluding clusters from NGC 4569. Dashed lines represent candidate hosts for multiply-associated XRBs. In panel (d), the fraction of clusters that hosts at least one XRB is given as a percentage of the total clusters per age population per bin. The horizontal lines show the boundaries of each bin.

4.5.4 XRB cluster radii

The size distribution of clusters in late-type galaxies remains poorly understood. It has been proposed that star clusters undergo rapid expansion within their first 10 Myr (Bastian et al., 2012; Chandar et al., 2016; Mulia et al., 2019). Indeed, there appears to be a preference for XRBs to form in young clusters with smaller radii, a correlation that flattens from intermediate-age clusters to GCs, although this might not necessarily be a consequence of rapid expansion. Generally, young clusters tend to be more compact than older ones (Mulia et al., 2019). Nevertheless, the size distribution of XRB hosts appears dependent on cluster age.

Figure 4.5 shows the size distribution of PHANGS clusters, binned by radius and divided into (a) GC, (b) intermediate-age cluster, and (c) very young cluster populations. As with Figure 3, panel (d) shows the percentage of clusters that host an XRB per age group per radius bin. In all cases, XRBs are preferentially seen in clusters with smaller radii — although a Wilcoxon test performed on these populations imply only XRB-hosting GCs are statistically smaller than their general cluster population. While the percentage of GCs that host XRBs decreases with increasing radius bin (affirming a strong dependence on cluster size), the same is not seen for intermediate-age and very young clusters. In particular, the fraction of very young clusters that host an XRB appears to *increase*, albeit slightly, with increasing radius bin. If these sources are indeed XRB-hosting clusters and not spurious associations, then this result, in conjunction with the results from

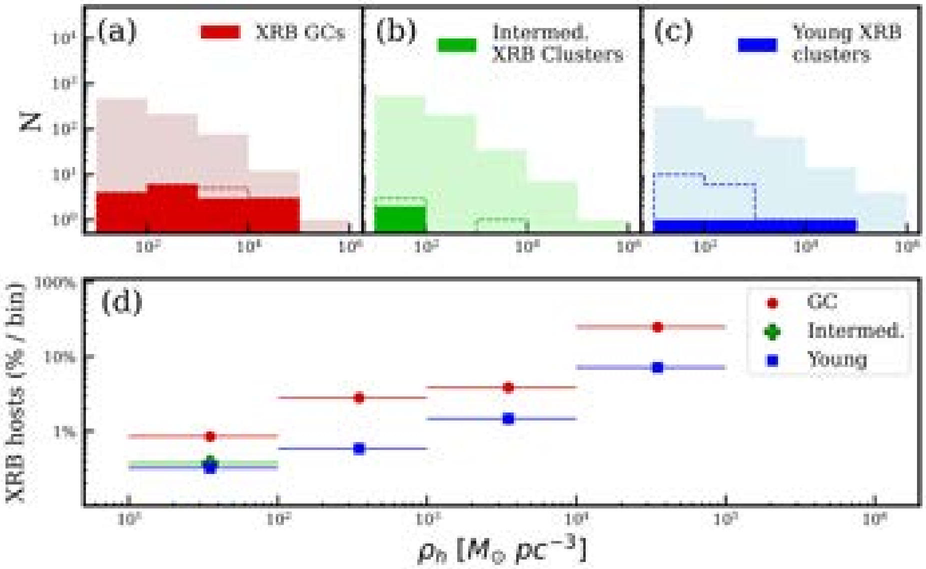

Figure 4.6 The histograms of cluster densities, separated into (a) GCs, (b) intermediate-age clusters, and (c) very young clusters, excluding clusters from NGC 4569. Dashed lines represent candidate hosts for multiply-associated XRBs. In panel (d), the fraction of clusters that hosts at least one XRB is given as a percentage of the total clusters per age population per bin. The horizontal lines show the boundaries of each bin.

§4.5.2, suggests that cluster mass is more important for XRB formation in young clusters than radius, whereas both cluster mass *and* radius appear to play a strong role in XRB formation in GCs, as seen in early-type galaxies (e.g. Paolillo et al., 2011).

4.5.5 XRB cluster densities

Figure 4.6 is a histogram of the densities of (a) GC, (b) intermediate-age cluster, and (c) very young cluster populations, where, as before, panel (d) shows the percentage of clusters that host an XRB per age group per density bin.

The number of XRB-hosting clusters remains relatively flat over increasing density bins for GCs and young clusters, with all of the singly-associated XRBs appearing in the lowest-density bin for intermediate-age clusters (panels a, b, and c). When observed as a percentage of the total population, however, we see that the fraction of clusters that host XRBs increases drastically with increasing density for both GCs and very young clusters (panel d). The fraction of very young clusters that host XRBs in the highest density bin is a factor of 22 times higher than that of the lowest density bin. For GCs, the difference between the two bins is a factor of 15.

There are a couple of interesting conclusions that can be drawn from Figure 4.6d. First, the number of GCs and very young clusters that host XRBs is strongly dependent on cluster densities. This may be due to more frequent dynamical interactions in denser clusters, which could enhance the number of tight binaries that can form in a system (Jordán et al., 2004; Peacock et al., 2009). Second, across the total galaxy sample, the fraction of GCs that host XRBs is at least twice that of young clusters for a given density bin. On a galaxy-by-galaxy basis, the difference between age populations is much less dramatic, but is generally consistent with GCs being more likely to host XRBs per density bin. This difference becomes greater if some of the younger clusters are determined to be spurious associations due to the chance superpositon on an XRB with a young cluster in star-forming regions.

4.6 XRB-hosting star clusters in late vs. early type galaxies

The majority of studies regarding XRBs within star clusters focus on the GCs of elliptical galaxies (e.g. Angelini et al., 2001; Jordán et al., 2004; Smits et al., 2006; Peacock & Zepf, 2016; Lehmer et al., 2020; Ferrell et al., 2021; Riccio et al., 2022). A few, more recent papers report on XRB associations with GCs in late-type galaxies (e.g. Pfahl et al., 2003; Peacock et al., 2009; Generozov et al., 2018; Hailey et al., 2018; Hixenbaugh et al., 2022), and fewer still include XRBs in younger clusters (e.g. Rangelov et al., 2012; Mulia et al., 2019; Hunt et al., 2023b; Avdan et al., 2022) In this section, I take the first step towards (i) assessing the fraction of star clusters — both old and young — that host XRBs in late-type galaxies, and (ii) comparing the fraction of field vs. cluster XRBs in late-type vs. early-type galaxies.

For each galaxy in the sample, the sky area over which the full X-ray source catalog extends is always larger than the sky area encompassing the PHANGS cluster catalog (i.e., the magenta contours in Figure 4.1). However, the number of XRBs expected to be observed above the completeness limit, corrected for the CXB, is estimated using models for the XRB X-ray luminosity functions of late-type galaxies generated by L19. These models rely on measurements of $\mathrm{M}_\star$ and SFR, which are confined to the K_s-band isophotal ellipses. To compare the field-to-cluster XRB ratios of each galaxy, we must restrict our analysis to the region covered by both the PHANGS-HST catalog and the corrected XRB estimates — i.e. the intersection of the isophotal ellipses and the PHANGS contours in Figure 4.1. For the sake of consistency, I also use this region for our analysis of XRB clusters vs. the total cluster population. The K_s-band isophotal ellipses are reasonably well-covered by the cluster catalogs for most of the galaxies; in total, only 2 of the 33 XRB-hosting clusters fall outside of the K_s-band ellipses. Out of the remaining XRB clusters, 22 exceed the X-ray completeness limit of their respective host galaxies.

4.6.1 Properties of XRB-hosting clusters

In elliptical galaxies, between 4 and 10% of GCs host LMXBs (e.g. Maccarone et al., 2003; Jordán et al., 2007; Brassington et al., 2010; Mineo et al., 2014; Luan et al., 2018). Analyses of these XRB hosts suggest they are more massive, more luminous, radially smaller, denser, and redder than the general GC population (e.g. Kundu et al., 2002; Sivakoff et al., 2007; Peacock et al., 2009; Brassington et al., 2010; Paolillo et al., 2011; Riccio et al., 2019). Further investigations suggest that metallicity — more so than cluster age — plays a role in the production of LMXBs (Kundu et al., 2003, 2008; Sivakoff et al., 2007; Fabbiano, 2006; Peacock et al., 2010; D´Ago, G. et al., 2014; Luan et al., 2018; Riccio et al., 2022).

In late-type galaxies, the percentage of GCs that host LMXBs is still an unsettled matter, though a recent study of M81 suggest a fraction consistent with that of elliptical galaxies — around 4% (Hunt et al., 2023b). Similarly, XRB-hosting GCs in M81 tend to be more compact, denser, and more massive than the rest of the GC population (Hunt et al., 2023b, see also Bregman et al. 2006 in the context of the Milky Way galaxy). As far as young clusters go, a study of XRB-hosting clusters younger than 400 Myr in the Antennae galaxies and NGC 4449 suggests that more massive and denser intermediate-age clusters may be more likely to host XRBs, but that this preference is not reflected in the the population of clusters younger than 10 Myr (Mulia et al., 2019).

The total number of clusters and the percent that host XRBs in each galaxy is given in Table 4.4. Among these late-type galaxies, the percentage of clusters that host bright XRBs above the completeness limits of their host galaxy varies between 0.5–7% for GCs, 0.2–2.5% for intermediate-age clusters, and 0.5–1.3% for young clusters, excluding NGC 4569 (for which no XRB-hosting clusters were identified). Combining all clusters within our galaxy sample (excluding NGC 4569), the percentage of XRB hosts among GCs, intermediate-age clusters, and young clusters is 1.2%, and $0.1^{+0.1}$%, $0.5^{+0.2}$%, respectively. Tentatively, a total of 0.7% of all compact star clusters within the PHANGS catalog, irrespective of age, host XRBs. As a word of caution, we note again that the statistics for clusters younger than 400 Myr may be inflated due to the high probability of a chance superposition with an unrelated cluster in densely populated, active regions, as determined in §4.5.

XRBs in late-type galaxies appear to prefer smaller, denser, brighter, and more massive GCs, just as they do in elliptical galaxies (see Figures 4.3, 4.5, and 4.6d). This is consistent with the notion that clusters with more stars (that is, more massive and brighter) that are in closer proximity to each other (denser and smaller) provide ample opportunities for the formation of a close binary (Smits et al., 2006; Jordán et al., 2007; Peacock et al., 2009, 2010).

In contrast to elliptical galaxies, we find that XRB-hosting GCs in the star-forming galaxies under consideration are *not* redder than the general GC population — rather, their colors are consistent with those of the full population (see Figure 4.2c). For early-type galaxies, it is believed that metallicity plays a large role in this correlation, possibly due to enhanced tidal capture rates and core concentrations (smaller radii) in higher-metallicity GCs, which in turn facilitates the formation of LMXBs (Jordán, 2004; Schulman et al., 2012; Ivanova, 2013; Vulic et al., 2018; Hixenbaugh et al., 2022). It is interesting to note that, while GCs typically display bimodal colors corresponding to metal-rich and metal-poor populations (e.g. Peacock & Zepf, 2016; Hixenbaugh et al., 2022), the GCs in our sample lack a clear distinction between red and blue GCs (Figure 4.2b and 4.2c). This could be due to the fact that (i) the metal poor "mode" becomes very broad when different late type galaxies (each with different star forming histories) are added together, and (ii) the metal rich mode may be triggered by mergers, which are rarer in spirals (Muratov & Gnedin, 2010; Pfeffer et al., 2023).

Regarding younger clusters, there is than 10 Myr are more likely to host XRBs than other clusters of similar ages (see Figures 4.2, 4.3d, and 4.6d). The sample of intermediate-age XRB-hosting clusters (younger than 400 Myr) is too small to draw a solid conclusion, but their properties appear consistent with the broader intermediate-age population. This is possibly in contrast to NGC 4449 and the Antennae galaxies, which show a tentative correlation between XRB formation and mass and density in intermediate-age clusters, but no such correlation in young clusters (Mulia et al., 2019). Larger statistics are needed to definitively confirm whether a trend exists, as only 11 intermediate-age and 17 young XRB-hosting clusters were observed in the NGC 4449 and the Antennae galaxies, compared to the 17 non-GC XRBs I analyze here. Furthermore, the likelihood of chance superpositions with unrelated clusters causing spurious associations to be included in this analysis may further complicate matters. It is interesting that such strong correlations between the presence of an XRB and cluster mass and density are identified; however, this could point to the associations of singly-associated XRBs, at the very least, being real, and that the background contamination is minimal.

4.6.2 Cluster XRBs vs. field XRBs

Studies of elliptical galaxies have shown that roughly 25–70% of LMXBs are found within GCs, while the rest are found in the field (e.g. Sarazin et al., 2000; Angelini et al., 2001; Kundu et al., 2002, 2003; Maccarone et al., 2003; Fabbiano et al., 2010; Luan et al., 2018). A growing body of work identifying LMXBs in late-type galaxies suggests that the ratio of GC LMXBs to field LMXBs may be smaller in spiral galaxies: an analysis of XRBs in M101 revealed only 2% of LMXBs are found in GCs (Chandar et al., 2020), while 12% of LMXBs in M81 are found in GCs (Hunt et al., 2023b). On the other hand, around 10% of XRBs appear in clusters younger than 400 Myr in the handful of late-type galaxies studied so far (Chandar et al., 2020; Palmore et al., 2022),

Table 4.4 Statistics of X-ray sources inside the isophotal ellipse and PHANGS footprints

	$M_{\star,\mathrm{encl}}$	$\mathrm{SFR}_{\mathrm{encl}}$	X-ray	Estimated XRBs		Observed XRB clusters (w/ % of total)		
	(10^9 $M_\odot$)	($M_\odot$ yr^{-1})	Sources	LMXBs	HMXBs	GCs	≥ 10 Myrs	< 10 Myrs
NGC 0628	2.64	0.24	33	6	7	3 (50)	1 (14)	1 (14)
NGC 3351	7.07	0.50	30	9	8	3 (33.3)	0^{+2} (0^{+25})	3^{+2} (38^{+25})
NGC 3627	19.4	1.81	48	15	14	3 (20)	1 (7)	1 (7)
NGC 4321	14.3	1.65	45	12	15	1 (8)	0	0
NGC 4569	*26.4*	*1.02*	*17*	*10*	*4*	*0*	*0*	*0*
NGC 4826	19.2	0.39	20	15	4	3 (20)	0	0
		Total*	176	67	52	13 (19)	2^{+2} (4^{+4})	5^{+2} (10^{+4})

Note. — The number of LMXBs and HMXBs in each galaxy are estimated using the global X-ray luminosity function fits from Lehmer et al. (2019), which are a function of the total stellar mass and star formation rate enclosed within the region of interest — that is, the area within the K_s-band ellipses and covered by PHANGS. The observed cluster counts here reflect the number of XRB-hosting clusters in the region of interest, with the error indicating the most that the population could increase if the true host cluster of multiply-associated XRBs were determined, if applicable. The estimated number LMXBs and HMXBs is used to calculate the percent (in parentheses, rounded to the nearest percent) of XRBs that appear in GCs and younger clusters, respectively. The percentages for clusters younger than 400 Myr may be inflated due to the non-negligible likelihood of a chance superposition of an XRB and young cluster in densely population regions (e.g. spiral arms). All numbers represent sources above the completeness limit of each galaxy.

*The total values exclude XRBs and clusters from NGC 4569, which may be significantly affected by the high X-ray completeness limit of observations.

with a fraction of at least 25% observed in NGC 4449 and the Antennae galaxies (Mulia et al., 2019). Tentatively, this may suggest the fraction of HMXBs in young clusters is higher than the fraction of LMXBs in GCs in late-type galaxies.

While I do not directly classify the XRBs in this study on the basis of their donor mass, we can estimate the relative number of LMXBs and HMXBs in the target galaxies using the best-fit X-ray luminosity function of L19. Table 4.4 shows the total number of X-ray sources within the region over which the K_s-band isophotal ellipses intersects the PHANGS region, the number of XRBs above the 90% X-ray completeness limits in that region, and the estimated number of LMXBs and HMXBs. The XRB estimates take into account possible CXB contamination, so the sum of expected LMXBs and HMXBs is always lower than the total number of X-ray sources actually contained by the region. I compare the expected number of LMXBs and HMXBs to the number that we observe within GCs and clusters younger than ~ 400 Myr over the same region and above the 90% completeness limit of their respective galaxies. I also calculate the percentages (in parentheses) of LMXBs found in GCs and HMXBs found in non-GCs.

There are a few conclusions that may be drawn from the results presented in Table 4.4. First, the fraction of LMXBs within GCs is on the low end of the estimates from elliptical galaxies; while in early-type galaxies anywhere between 25–70% of LMXBs are found in GCs, the number is between $\sim$ 8–50% within our sample of late-type galaxies, or 19.4% over all galaxies, excluding NGC4569. This is tentatively consistent with previous studies of cluster XRBs in spiral galaxies (Chandar et al., 2020; Hunt et al., 2023b), but spans a broader range of values.

One possible cause for this apparent suppression of GC-LMXBs could be an inherent difference in the metallicity distribution of GCs in certain late-type galaxies, since the presence of XRBs in GCs is correlated with higher metallicities (e.g. Kundu et al., 2008; Luan et al., 2018). The (often bimodal) metallicity distribution of GCs is thought to arise from galaxy mergers and/or GC disruption, the former of which is unlikely in spiral galaxies (Muratov & Gnedin, 2010; Pfeffer et al., 2023). Another explanation may be related to the difference in star formation rate. Since new star formation is essentially negligible in early-type galaxies, the growth of the XRB field population may slow significantly — particularly because intermediate-mass donor stars are at least a factor of 5 times more likely to form an XRB than low-mass stars in the disk of a galaxy (Pfahl et al., 2003), and elliptical galaxies are dominated exclusively by low-mass stars. Meanwhile, LMXBs can continue to efficiently form within GCs through dynamical interactions. This 'stagnation' effect may be mitigated if GCs are responsible for seeding a significant fraction of the field LMXB population (e.g. Lehmer et al., 2020). The difference in field-to-cluster LMXB ratios between early-type and late-type galaxies may provide further evidence that ejection from GCs has limited impact on the total LMXB population (see, e.g., Piro & Bildsten, 2002; Kundu et al., 2007; Peacock & Zepf, 2016; Kremer et al., 2018).

The second conclusion that may be drawn from Table 4.4 is that the fraction of (presumably high-mass) XRBs that appear in non-GCs is almost consistently smaller than the fraction of LMXBs that appear in GCs across nearly all galaxies (except NGC 3351). These fractions do not appear directly correlated to the total $\mathrm{M}_\star$ or SFR of the host galaxy. This is inconsistent with results from M101 — for which $\sim 2\%$ of LMXBs are in GCs and $\sim 5\%$ of HMXBs are in very young clusters — but *does* match findings from M83 ($\sim$ 13% vs. $\sim$ 3%; Hunt et al., 2021) and M81 ($\sim$ 12% vs. $\sim$ 2%; Hunt et al., 2023b). Furthermore, while we do not measure metallicity directly in our cluster sample, it is interesting to note that there is no indication of a color (ergo metallicity) bias among GC LMXBs in our sample of late-type galaxies. These results are, of course, contingent on our population of clusters that host singly-associated XRBs being positively identified. As there is a non-negligible probability of an XRB within an active star-forming region being associated with an unrelated cluster (see §4.5), our results must be broached with caution, though previous studies must also suffer from this issue. Ultimately, there appear to be variations between galaxies that requires more exploration to fully understand.

4.7 Summary

This study represents one of the largest systematic investigation of XRBs in both GCs and young clusters in late-type galaxies to date. I analyze the properties of clusters that host XRBs, broken into three distinct populations: ancient GCs, intermediate-age clusters between ~ 10 and 400 Myr old, and very young clusters younger than 10 Myr. The analysis of the clusters in this sample of late-type galaxies yields a number of interesting results:

- While we confirm that the chance of an XRB being wrongly associated with an unrelated, nearby GC is low (in agreement with the simulations from Hunt et al. 2023b), I find there is a non-negligible probability of a chance superposition between an XRB and an unrelated cluster in densely populated, actively star-forming regions such as the spiral arms, which may inflate the statistics for clusters younger than ~ 400 Myr. Therefore, the following results for XRBs with non-GC counterparts should be approached with caution.

- Clusters that host X-ray sources tend to be brighter than the general population for both the very young clusters and GCs. This may not necessarily be the case for intermediate-age clusters.

- GCs in these late-type galaxies do not appear to prefer redder clusters, contrary to what has been repeatedly found for elliptical galaxies. On the other hand, there is marginal evidence that XRBs preferentially form in bluer intermediate-age clusters, though better statistics are required.

- As found in previous studies, X-ray emitting GCs tend to be more massive, denser, and have smaller effective radii than the general GC population. Among young cluster populations, there is a higher fraction of very young clusters that host XRBs in denser, more massive populations.

- There may be a strong positive correlation between cluster mass and X-ray luminosity in both intermediate-age X-ray emitting clusters and the cumulative non-GC cluster population, though a greater sample of XRBs with known cluster hosts is needed. This *could* indicate the presence of multiple XRBs, though these clusters are not more X-ray luminous than the general field XRB population. On the other hand, there is a statistically significant $\mathrm{M}_{\star}$–L_{X} *anticorrelation* for GCs.

- The percentage of GCs that host XRBs in late-type galaxies varies widely between galaxies (0.5–7%). This is compared to the 4–10% seen in early-type galaxies. On the other hand, these percentages are 0.2–2.5% for intermediate-age clusters and 0.5–1.3% for young clusters, depending on the true parent clusters.

- Whereas up to 70% of LMXBs in early-type galaxies are found within their parent GCs, I find that a potentially smaller percentage ($\sim$ 8–50%) are found in GCs in late-type galaxies, in agreement with statistics from previous late-type galaxy studies.

Throughout our analysis, we note that our ability to gain insight into the population of XRBs within intermediate-age clusters is hindered by the small number of such sources in our sample. Whether this is an inherent property of cluster XRBs or a matter of insufficient data can only be addressed by a larger study of XRBs in nearby, late-type galaxies. Such a study would benefit from deeper X-ray observations (including a revisit of NGC 4569), optical observations covering a larger sky area, X-ray and optical spectroscopy, and metallicity measurements of compact star clusters. This type of data would give us a clearer picture of these sources by allowing us to identify black hole vs. neutron star XRBs within and around clusters, constrain the cluster-to-field ratios, and study the cluster metallicity dependence of XRBs in late-type galaxies.

CHAPTER 5

Characterizing the Optical Counterparts of Ultraluminous X-ray Sources

The work in this chapter represents research currently under preparation for publication. We expect the full results — produced in collaboration with Elena Gallo, Rupali Chandar, and Dominic Walton — to be submitted to the Astrophysical Journal later this year.

5.1 Introduction

As defined in Chapter 1, ULXs are defined as off-nuclear, point-like sources that exceed the X-ray Eddington limit for accretion onto a $\sim$10 $\mathrm{M}_{\odot}$ stellar remnant black hole, or roughly $L_X \gtrsim 10^{39}$ erg s^{-1} (Kaaret et al., 2017; Fornasini et al., 2023). While there has been much debate as to how ULXs produce such high-energy emission — with super-Eddington accretors now generally accepted as the cause of the majority of ULXs — the detection of > 100 $\mathrm{M}_{\odot}$ black holes by ALIGO (e.g. Abbott et al., 2020) has rekindled the idea that some of these systems may contain intermediate-mass black holes after all (e.g. Finke & Razzaque, 2017).

To date, no extragalactic ULX has been found to definitively contain a black hole accretor (Walton et al., 2022). One means for identifying black hole XRBs is by measuring the dynamical interactions between the donor star and the compact object, from which the accretor mass can be estimated (Casares & Jonker, 2014). However, so far this has only been done with limited success; only ~ 30 black hole XRBs have been dynamically confirmed in the Milky Way, and the only known Galactic ULX has not been dynamically confirmed to contain a black hole (Eikenberry et al., 2001; Corral-Santana et al., 2016; Middleton et al., 2021). Nevertheless, in order to confirm the nature of the accretor in extragalactic ULXs, we must first identify their optical counterparts and estimate the masses of the donor star.

In this chapter, I conduct a systematic review of 46 ULXs within 28 nearby galaxies. Using the aggregated observations from HST WFC3/UVIS and ACS/WFC and archival Chandra observations of extragalactic ULXs compiled by Walton et al. (2022), I apply the methodology used in

Chapter 2 and 3 to identify the optical counterparts of each ULX. Further, I employ a new SED-fitting scheme, based on familiar stellar evolutionary models (Bertelli et al., 1994; Girardi et al., 2010; Marigo et al., 2017), to estimate the likely spectral types of each donor star. Of the 46 ULXs, the optical counterparts of 8 are presented here for the first time.

5.2 Sample selection

A comprehensive catalog containing 1843 ULXs across 951 galaxies was compiled by Walton et al. (2022, hereafter W22), representing one of the single largest ULX compilations to date. The catalog was generated by cross-referencing observations by SWIFT, XMM-Newton, and Chandra — in particular, 4XMM-DR10, 2SXPS, and CSC2. The typical 3σ positional errors of X-ray sources are estimated to be $10''$ for SWIFT (Evans et al., 2020), $5''$ for XMM-Newton (Webb et al., 2020), and $3''$ for Chandra (Walton et al., 2022), respectively. Since the goal of this study is to identify the optical counterparts to ULXs, it is important to restrict the initial ULX catalog to those with relatively small positional errors to reduce the number of potential counterparts found from the HST image. Furthermore, poor instrumental spatial resolution can mistake the cumulative emission of several sub-luminous X-ray sources for a ULX in crowded regions. For these reasons, I restrict this sample to only include ULXs observed by Chandra. The W22 catalog includes only X-ray sources that are not flagged in the Chandra source catalog (CSC) as marginal, extended, or streaked. Furthermore, sources with large off-axis angles are susceptible to erroneous flux readings, as the increase in PSF far off the Chandra pointing can artificially inflate the $\mathrm{L_X}$ of an object. Such sources are removed in the W22 catalog on a case-by-case basis.

I further narrow the selection of Chandra-observed ULXs to only include those within 15 Mpc. At farther distances, the number of optical counterparts contained within the average 2σ radius increases, as does the minimum stellar mass detectable by HST. (i.e. we are only able to identify HMXBs with stars $> 8\ \mathrm{M_\odot}$ farther than 15 Mpc). Furthermore, we require HST coverage in at least 2 bandpasses with either ACS/WFC or WFC3/UVIS, to allow proper photometric analysis. With these guidelines, our final sample contains 28 galaxies with distances between 3 and 15 Mpc. These host a total of 46 ULXs with sufficient HST coverage. These are given in Figure 5.1 and Table 5.1. The ULX number corresponds to the order in which they are listed in the table in Appendix E.

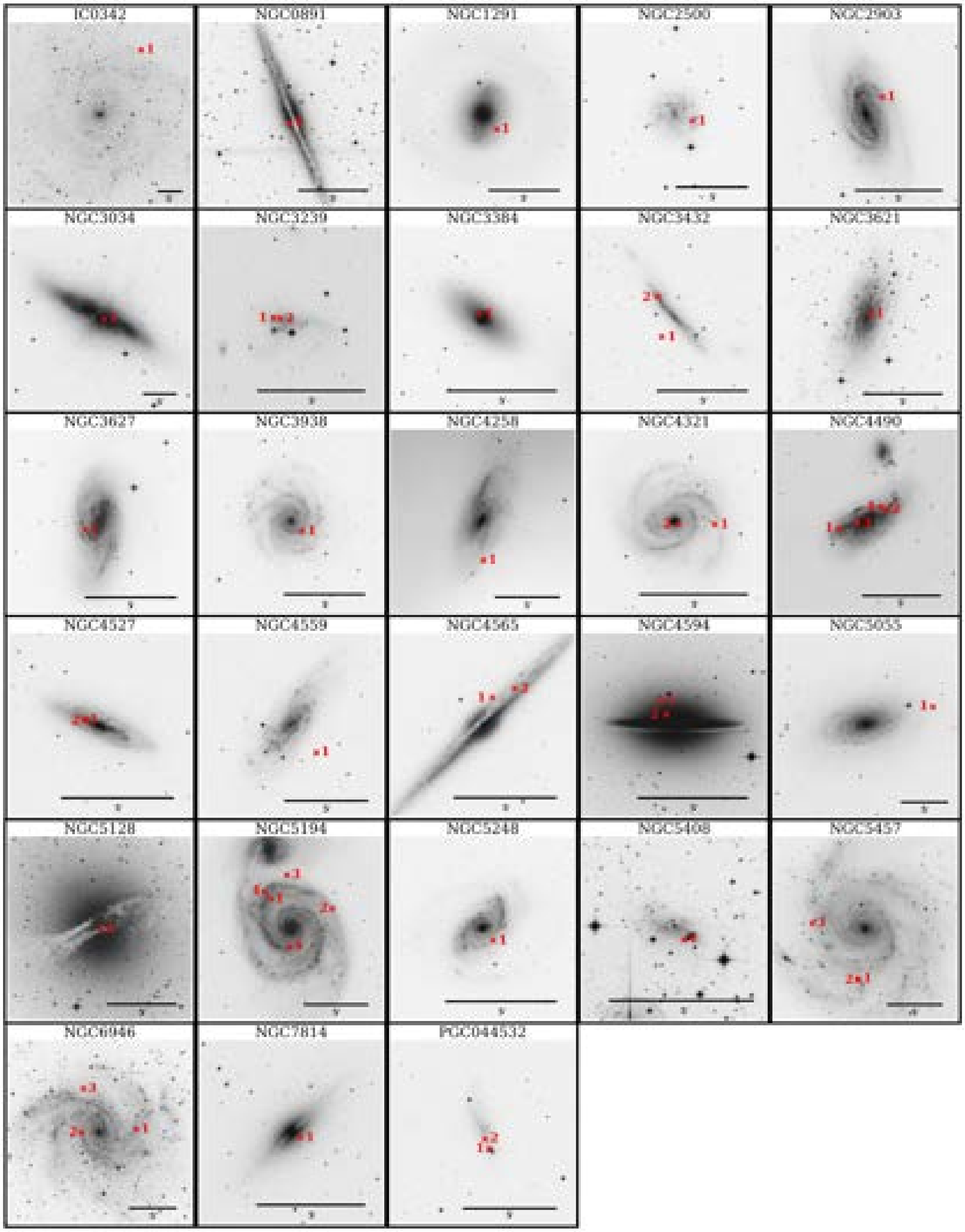

Figure 5.1 Galaxies within 15 Mpc, as imaged by the Digitized Sky Survey, with adequate HST coverage for the analysis of ULX donor stars. The positions and distances of each galaxy, and the HST detector used to observe each ULX, are given in Table 5.1. Red X's represent the ULXs that meet the three criteria outlined in §5.2. The ULXs in each galaxy are numbered in the order in which they appear in Table 5.1.

Table 5.1. Galaxy Sample and Astrometric Corrections

Galaxy	α_{J2000}	δ_{J2000}	Dist. (Mpc)	Instrument	Field no.	ULX no.	Δ_{RA} (arcsec)	Δ_{Dec} (arcsec)	σ_{RA} (arcsec)	σ_{Dec} (arcsec)
IC 342	56.702	68.096	3.4	ACS/WFC	1	1	—	—	—	—
NGC 891	35.640	42.348	9.1	ACS/WFC	1	1	0.10	0.29	0.02	0.01
NGC 1291	49.327	−41.108	9.1	ACS/WFC	1	1	-0.16	-0.01	0.29	0.58
NGC 2500	120.472	50.737	12.4	WFC3/UVIS	1	1	0.13	−0.10	0.07	0.02
NGC 2903	143.042	21.502	9.3	ACS/WFC	1	1	-0.01	0.04	0.30	0.45
				WFC3/UVIS	1	1	0.03	0.03	0.30	0.45
NGC 3034	148.970	69.679	3.5	ACS/WFC	1	1	0.77	1.0	0.73	0.30
NGC 3239	156.270	17.164	10.2	WFC3/UVIS	1	1,2	−0.20	0.19	0.04	0.02
NGC 3384	162.070	12.629	10.0	ACS/WFC	1	1	−0.33	−0.17	0.07	0.06
NGC 3432	163.129	36.619	13.9	ACS/WFC	1	1,2	0	0	0	0
NGC 3621	169.569	−32.814	6.7	WFC3/UVIS	1	1	0	0	0	0
NGC 3627	170.063	12.992	9.0	ACS/WFC	1	1	0	0	0	0
				WFC3/UVIS	1	1	0	0	0	0
NGC 3938	178.206	44.121	14.9	WFC3/UVIS	1	1	0.15	0.11	0.07	0.05
NGC 4258	184.740	47.304	7.3	ACS/WFC	1	1	0.40	0.38	—	—
NGC 4321	185.729	15.822	13.9	WFC3/UVIS	1	1	0	0	0	0
					2	2	0.41	−0.35	0.05	0.02
NGC 4490	187.651	41.644	8.9	WFC3/UVIS	1	1,2,3,4	0	0	0	0
NGC 4527	188.535	2.654	13.4	WFC3/UVIS	1	1,2	—	—	—	—
NGC 4559	188.990	27.960	7.4	ACS/WFC	1	1	-0.27	-0.01	0.25	0.16
				WFC3/UVIS	1	1	-0.08	-0.12	0.12	0.09
NGC 4565	189.087	25.988	13.4	ACS/WFC	1	1	−0.41	0.24	0.28	0.03
					2	2	−0.10	−0.38	0.55	0.37
NGC 4594	189.998	−11.623	11.3	ACS/WFC	1	1,2	1.77	−0.01	0.14	0.15
NGC 5055	198.955	42.029	9.0	ACS/WFC	1	1	0	0	0	0
NGC 5128	201.367	−43.018	3.7	WFC3/UVIS	1	1	0.11	0.14	0.13	0.07
NGC 5194	202.470	47.195	8.4	ACS/WFC	1	1,4	−0.19	−0.15	0.04	0.03
					2	2	−0.12	−0.09	0.61	0.19
					3	3	−0.48	−0.14	0.45	0.29
					4	5	−0.28	0	0.16	0.12
				WFC3/UVIS	1	1,3,4	0	0	0	0
					2	5	0	0	0	0
NGC 5248	204.383	8.885	13.6	WFC3/UVIS	1	1	0.12	−0.40	0.02	0.04
NGC 5408	210.838	−41.377	5.3	WFC3/UVIS	1	1	—	—	—	—
NGC 5457 (M101)	210.802	54.349	7.0	ACS/WFC	1	1,2	−0.10	0.07	0.08	0.07
					2	3	0.24	0.27	0.97	0.31
NGC 6946	308.718	60.154	7.7	ACS/WFC	1	1	0.36	−0.37	0.20	0.10
					2	2	−0.01	0.01	0.07	0.11
					3	3	0.16	−0.36	0.02	0.08
				WFC3/UVIS	1	1	0.45	−0.38	0.29	0.04
					2	2	0.03	−0.16	0.06	0.36
					3	3	0	0	0	0
NGC 7814	0.813	16.146	14.5	ACS/WFC	1	1	−0.56	0.16	0.13	0.05
PGC 44532 (NGC 4861)	194.758	34.861	10.0	ACS/WFC	1	1,2	−0.89	−0.20	0.31	0.02
				WFC3/UVIS	1	1,2	−0.56	−0.54	0.22	0.03

Note. — For each galaxy, the galactocentric coordinates and distance are taken from W22. For each HST field, the astrometric corrections on the X-ray source coordinates and their standard deviations are given as Δ and σ, respectively, where applicable (see §5.3 for details). In the event that there are not enough suitable reference sources against which an astrometric correction may be made (indicated with "—"), we set the 2σ of affected ULXs to $2''$, as described in §5.3. The ULXs visible in each field are listed by the number as they appear in Figure 5.1.

5.3 Astrometric corrections

To perform the necessary astrometric corrections, I collect the full X-ray point source catalogs for each galaxy from CSC2 and identify any foreground stars, background galaxies, and isolated star clusters with optical counterparts in the HST field of interest. The median offsets between the X-ray and optical coordinates are calculated and applied as astrometric corrections to the positions of the ULXs that fall within the HST field. The standard deviation of the calculated offsets are integrated in quadrature to the 1 and 2σ positional uncertainties reported in W22 for each ULX. For some HST fields, I find only one or no sufficient optical counterpart to X-ray point sources through which an astrometric correction may be obtained. If a single reference source exists, the offset between the X-ray and optical coordinates of that source is used to shift all ULXs that fall within that HST field. In either case, I assign a 2σ positional uncertainty of $2''$, derived from the median positional uncertainty of CSC-observed ULXs as described by W22.

For some ULXs, HST observations were made by both ACS/WFC and WFC3/UVIS, and a separate astrometric correction may be obtained for both fields. These observations are useful for determining whether we obtain the same candidate point sources around a single ULX using our astrometry correction methods independent of the instrument used, and how sensitively our donor star classification system depends on the depth and quality of the observations.

5.4 Photometry

The optical source identification and photometry were performed using the Python `photutils` package. Optical point sources are identified in each HST image using the `DaoFind` function. The median background is estimated using `Background2D`, and the photometry is performed on the background-subtracted image using `aperture_photometry` with a 3 pixel aperture. The errors used to generate the aperture photometry are calculated using `calc_total_error` from the same package, which estimates the total per-pixel error across the HST image by combining the background error with the Poisson noise of point sources. The zero-point magnitudes for each filter are from Calamida et al. (2022) for WFC3 observations, or are determined using `acszpt` from the Python `acstools` package, which finds the zero point for a specific filter and observation date for ACS observations.

I calculate the aperture correction required for photometric measurements of each HST image by selecting several 'ideal' stars with smooth radial brightness profiles that flatten towards the background at increasing aperture radius. A sample of 20 such stars were selected for the majority of fields, though only 10–15 were used for 5 fields, and 1 field only had 5 ideal stars available. For each field, the aperture correction is taken to be the median difference in magnitude between a 3 pixel and a 10 pixel aperture around the selected stars. I apply a further adjustment to take into account the flux missing from 10 pixels to infinity using the encircled energy fractions[1][2] for the appropriate HST instrument (Bohlin et al., 2020; Medina et al., 2022). In addition to the aperture corrections, I apply an extinction correction using values obtained from the NED extinction correction calculator at the position of each ULX[3].

For each ULX, I identify any star that falls within 2σ that is bright enough to be detected in at least two HST filters. Collectively, these represent the candidate donor stars for each ULX system.

5.5 Spectroscopic Analysis

In cases where the optical counterpart to a ULX is a point source observed in at least two filters, one is able to fit its spectral energy distribution (SED) to model stellar spectra in order to determine the most likely spectral type of the star. I adopt the newest stellar isochrone models from CMD 3.7[4] based on PARSEC release v1.2S and COLIBRI S_37 + S_35 + PR16 (Bressan et al., 2012; Marigo et al., 2013; Rosenfield et al., 2016; Pastorelli et al., 2020). The stellar tracks are modeled independently for HST ACS/WFC (with the 2021 updated filters and zeropoints) and

---

[1] `https://www.stsci.edu/hst/instrumentation/acs/data-analysis/aperture-corrections`

[2] `https://www.stsci.edu/hst/instrumentation/wfc3/data-analysis/photometric-calibration/uvis-encircled-energy`

[3] `https://ned.ipac.caltech.edu/forms/calculator.html`

[4] `http://stev.oapd.inaf.it/cmd`

updated WFC3/UVIS wide and medium filters. I use the OBC version of bolometric corrections (Girardi et al., 2002; Marigo et al., 2017), default dust compositions (Groenewegen, 2006), and a Kroupa initial mass function (Kroupa, 2002).

To fit the observed stellar spectra to theoretical stellar templates, I perform a reduced χ^2 analysis between the filters in which the observations were obtained and the corresponding model SEDs. The best-fit model is defined as that which produces a reduced χ^2 closest to unity (see Andrae et al., 2010). Because in most cases there are only a couple of data points to which to fit the models and the errors are often large, I also take into consideration at least 3 of the next best fit models, which in most cases have reduced χ^2 that are less than 0.05 from unity (for example, see Figure E.1 in Appendix E). This gives a range of possible masses. The best fit model also provides the best-fit stellar luminosity and effective temperature, which can be used to interpret the likely spectral type of the candidate donor star. I further validate the best fit models by comparing the colors and magnitudes of the candidate donors to stellar evolutionary tracks of solar-metallicity stars with known masses on a color-magnitude diagram (e.g., see Hunt et al., 2021).

5.6 Preliminary Results

Following the photometric methods described in §5.4, of the 46 ULXs in this sample, I identify 7 ULXs ($\sim 15\%$) within compact star clusters: 1 associated with a GC ($\gtrsim 400$ Myr), 5 associated with young massive clusters ($\lesssim 10$ Myr), and 1 associated with an intermediate-age cluster. An additional 5 ULXs ($\sim 11\%$) are found within OB associations, loosely bound collections of high-mass stars. Only 1 source in this sample is associated with a background AGN, and is therefore not technically considered a ULX. I determined that 6 of the ULXs could not be reliably classified, either because they appear in regions that are too bright or too dust-obscured, or because they are associated with features (e.g. point sources, haze) that are only detected in a single HST filter. The remaining 27 ULXs are classified as field XRBs: 20 HMXBs, 1 IMXB, and 6 LMXBs for which no optical counterpart is detectable. It should also be noted that at these distances, some of the sources I identify here as LMXBs would likely be classified as IMXBs with donor stars emitting

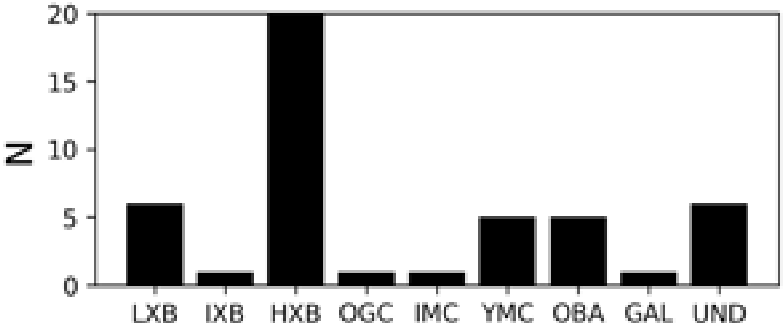

Figure 5.2 The final classifications of ULXs in our study based on the photometric analysis of their optical counterparts, where the three-letter codes represent: low-mass X-ray binary (LXB); intermediate-mass X-ray binary (IXB); high-mass X-ray binary (HXB); old globular cluster (OGC); intermediate-age massive cluster (IMC); young massive cluster (YMC); OB association (OBA); galaxy (GAL); and undetermined (UND). In total, there are 6 LXB, 1 IXB, 20 HXB, 1 OGC, 1 IMC, 5 YMC, 5 OBA, 1 GAL, and 6 UND.

below the luminosity threshold observable with HST. However, as discussed in Chapter 3, the rapid evolution of most IMXBs into bright LMXBs complicates the distinction between these two classes. The breakdown of these classifications are presented in Figure 5.2. HST images of each ULX and their best-fit masses and spectral types are given in Appendix E.

5.6.1 Contribution of accretion disk to optical emission

The spectroscopic analysis of candidate donor stars in this study assumes the optical emission of point sources associated with ULXs is dominated by the companion star. However, prior studies suggest that the SEDs of many ULXs are consistent with emission from super-Eddington accretion disks rather than the donor star alone (e.g. Tao et al., 2011; Fabrika et al., 2015). If indeed the optical emission of a ULX is dominated by the accretion disk, as is the case for most LMXBs, it becomes impossible to determine the true mass or spectral type of the donor star solely from optical photometry.

SEDs that are dominated by X-ray reprocessing in the accretion disk are expected to follow a power-law spectrum with a spectral index of $-1 \leq \alpha \leq 2$, where the flux F_ν of the point source at a given pivot frequency ν is given by $F_\nu \propto \nu^\alpha$ in units erg cm^{-2} s^{-1} Hz^{-1} (Gierliński et al., 2009; Tao et al., 2011). If the spectral index is $\alpha = 1/3$, then the emission is likely dominated by a multi-color disk blackbody (Tao et al., 2011). To explore the impact of accretion disks within our sample, I select a sample of ULXs that are: (a) associated with a single optical counterpart; and (b) observed in at least 3 wide filter bandpasses, excluding narrow and medium filters that may be emission line dominated. There are 3 ULXs that meet these criteria: J133730.1+085233 in NGC 5248, J140314.3+541806 in NGC 5457, and J203436.5+600930 in NGC 6846. In order to increase the number of data points and improve our ability to perform a fit, both WFC3/UVIS and ACS/WFC observations were used to generate a composite spectrum for each ULX, where applicable. As a result, however, some of the observations (for the ULX in NGC 6946 in particular) were taken asynchronously and may thus be affected by optical variability. The effect of variability on these ULXs will be explored at a later date.

Mirroring the process from Tao et al. (2011), I convert the photometry of each of the 3 ULXs to a dereddened F_ν and fit the spectrum to a simple power law such that $F_\nu \propto \nu^\alpha$. The resulting spectral indices are shown in Figure 5.3. Within the errors, J140314.3+541806 in NGC 5457 is consistent with a multi-color disk blackbody, while J203436.5+600930 in NGC 6846 is marginally consistent with emission dominated by X-ray reprocessing. On the other hand, J133730.1+085233 in NGC 5248, which was observed with the greatest number of bandpasses, has a best-fit spectral index well outside that of accretion disk emission. In fact, the spectra of J133730.1+085233 is well-modeled by a blackbody with an effective temperature around 8000 K, further supporting the conclusion that the emission from this ULX comes primarily from the donor star (Figure 5.3). Ultimately, without deeper contemporary observations in a wider range of filters it is difficult to determine the effect disk reprocessing has on the full ULX population presented here, so the spectral types of their donor stars should be regarded with caution.

5.6.2 Discussion and next steps

ULXs are primarily seen in young elliptical galaxies or in regions of high SFR. Their association with high SFR environments — as well as their XLFs, direct observations of their donor stars, and association with younger stellar populations — once motivated the idea that most ULXs are bright

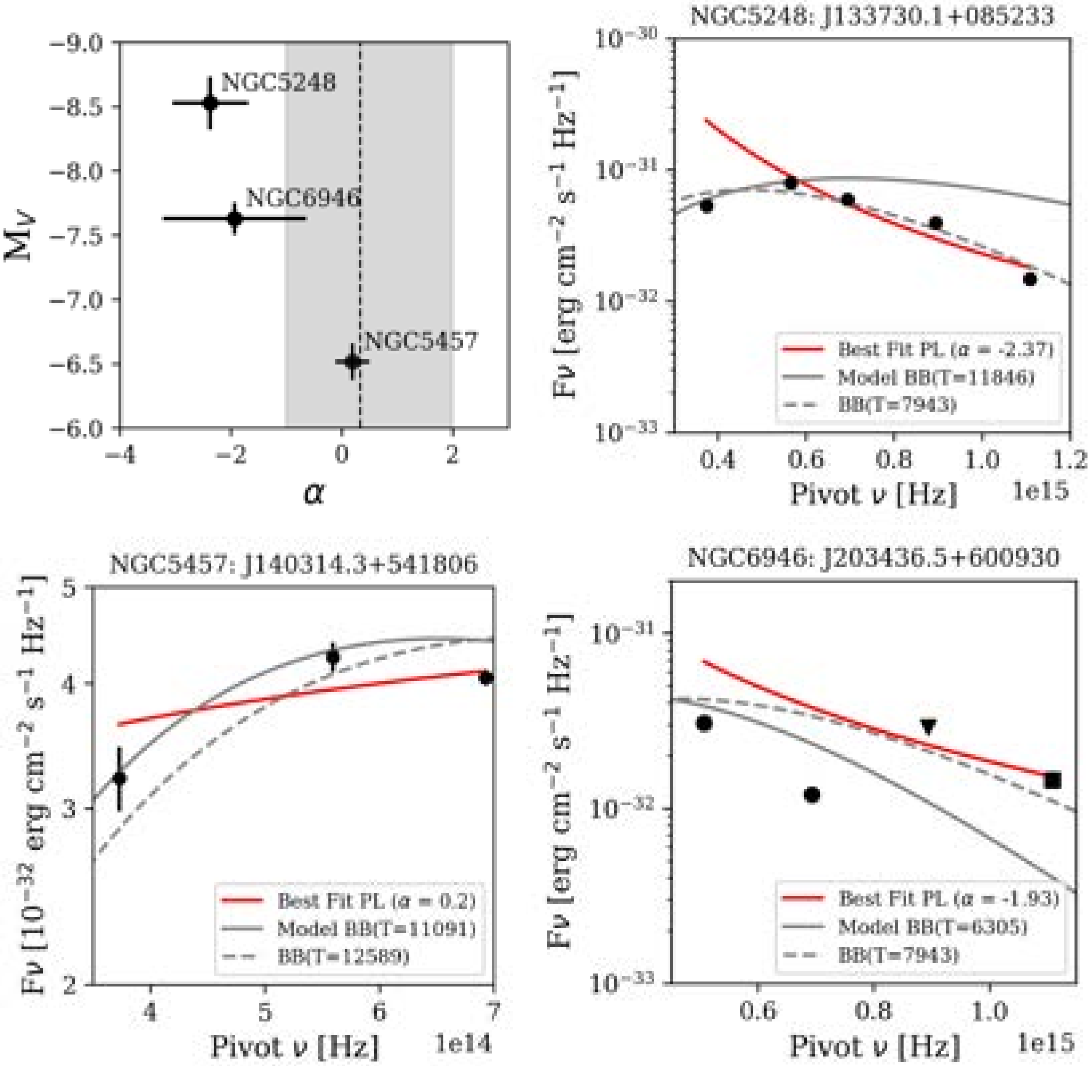

Figure 5.3 (Top left) V-band magnitudes vs. best fit power law index of the optical counterparts of 3 selected ULXs from the galaxies as labeled. The grey region represents the region within which the α is consistent with emission from X-ray reprocessing in the outer accretion disk, while the dashed vertical line indicates $\alpha = 1/3$, for which the optical photometry is dominated by direct emission from a multi-color disk. (Top right and bottom) The spectra of each ULX, compared the best fit power law (red), a blackbody with an effective temperature of the best fit SED model obtained in §5.5 (gray solid), and a blackbody of an arbitrary effective temperature (dashed gray). For each galaxy, the marker shapes indicate contemporary observations.

HMXBs (e.g. King et al., 2001; Motch et al., 2014; Wang et al., 2016). Though the discovery of pulsating ULXs has open the possibility some ULXs being powered by other means, it is no surprise that $\sim$ 43% of the ULXs in this sample are identified as field HMXBs, while another $\sim$ 22% are HMXBs within young massive clusters or OB associations.

What is surprising is the discovery of a ULX in a GC: J112018.3+125900 in NGC 3627. This source was previously reported in Weżgowiec et al. (2012) and López et al. (2020), which respectively classified it as a massive super-Eddington XRB in a star cluster or a candidate red supergiant. To the contrary, because this ULX is found in a GC, it *must* have a low-mass stellar component, while the compact component is likely a black hole. Only 20 GC ULXs have been discovered to date (Dage et al., 2021), making this a rare and exciting find.

Another $\sim 15\%$ of this ULX sample are LMXBs and IMXBs. Binary evolution models suggest neutron star ULXs likely originate from these lower-mass XRBs (Misra et al., 2020), with the orbital period evolution of IMXBs making them more likely to form neutron star ULXs than HMXBs (Tauris et al., 2017). Since the nature of the compact accretors of ULXs is still a matter of great concern (see, e.g., Lehmer et al., 2021), further inquiry into the nature of these ULX vs. the field HMXB population may help determine whether neutron star or black hole accretion is the primary driver of the ULX population. In particular, 11 of the 46 ULXs have a single optical counterpart. These sources would be ideal for future follow-up observations, particularly for spectroscopic observations that may better constrain the nature of the compact component.

Moving forward, I am working on a source-by-source analysis of the 46 ULXs in this study. I will compare the estimated masses and spectral types of the donor stars obtained here to those in the literature. This publication (expected to be submitted later this year) will represent the first donor star classification for 8 of these ULXs.

CHAPTER 6

Conclusions and Future Work

The exploration of XRBs in late-type, spiral galaxies by means of direct reconnaissance yields many interesting insights. From my analysis of LMXB and HMXB populations in M83 and M81, I conclude that, although the bulges of both galaxies do contain the highest density of LMXBs while the HMXBs tend to trace the spiral arms, there is a mix of XRB populations throughout both galaxies that may be skewing the XLFs of prior studies (e.g. Gilfanov et al., 2004; Mineo et al., 2012). There is also a significant population of XRBs that appear to have intermediate-mass donor stars, although from my analysis of M81, it is clear at least some of these stars may be unassociated with the nearby XRB (see Figure 3.6). On the other hand, simulations suggest IMXBs rapidly evolve into LMXBs over the course of a few thousand years (e.g. van den Heuvel, 1975; Kalogera & Webbink, 1996; Podsiadlowski et al., 2002), so some of these sources may simply be abnormally luminous LMXBs (e.g. Podsiadlowski & Rappaport, 2000). If either of these scenarios is the case, then the presence of LMXBs in the disk of these galaxies is even larger than previously expected. In both galaxies, there is also a population of SNRs that is largely unaccounted for in model XLFs (e.g. Lehmer et al., 2019). This issue is more severe in the galaxy with higher SFR, M83; future studies of a greater sample of galaxies may help establish whether this contamination can be modeled as a simple scaling relation.

The HMXB XLFs in both M83 and M81 indicate a statistically-significant downturn at high luminosities, which is absent from the HMXB XLF in M101 (Chandar et al., 2020) and those from Lehmer et al. (2019). I posit that the removal of SNRs from the lower L_X end may explain this difference in shape, since prior studies did not employ a similar SNR-removal technique.

This may also explain the steeper power-law slopes Lehmer et al. (2019) obtains, both for the individual XLFs for M83 and M81 and the global XLF, compared to the best fit power-law indices we obtain. I identify more than twice as many HMXBs as expected from the newest global XLF given the low SFR of M81, but less than half the number expected in M83 (Lehmer et al., 2019). These values suggest our understanding of how the XRB populations in late-type galaxies scale with SFR and $\mathrm{M}_{\star}$ is incomplete. These discrepancies are likely driven by our weaker understanding of the LMXB populations in these galaxies — compared to the decades of research conducted in elliptical galaxies — including the nature of the enigmatic population of seemingly intermediate-mass XRBs that was revealed here. Future exploration of a greater galaxy sample will, hopefully, close this gap.

Furthermore, the work in this thesis represents one of the first comprehensive studies of XRBs in clusters of all ages in late-type galaxies. From an analysis of 6 late-type galaxies containing nearly 550 X-ray sources and 4000 identified compact star clusters, we see that LMXB-hosting GCs share many of the characteristics of those in elliptical galaxies: LMXBs are preferentially found within GCs that are more massive, radially smaller, and denser. However, unlike in elliptical galaxies, I find no evidence of a color correlation that would indicate a preference for higher metallicity clusters. Young clusters, on the other hand, are shown for the first time to follow similar general trends of XRB-hosting GCs, but with a weaker correlation: HMXBs are correlated with more massive and denser clusters. These trends are not surprising, since clusters with more stars in closer proximity drive higher interaction rates, amplifying the chances of forming an XRB.

On a galaxy-by-galaxy basis, the fraction of young clusters that host HMXBs is consistently lower than the fraction of GCs that host LMXBs. Likewise, the fraction of the total HMXB population found in star clusters tends to be smaller than that of LMXBs in GCs, in agreement with the XRB populations of M83 and M81 but contrary to the population in M101 (Chandar et al., 2020). It appears that, compared to elliptical galaxies, a smaller fraction of the total LMXB population is found is clusters, which may suggest that seeding from GCs makes a limited contribution to the total field LMXB population. HMXBs, on the other hand, are more efficient at forming in the field than LMXBs.

In this work, I also show for the first time that there is a statistically significant correlation between the masses of clusters younger than ~ 400 Myr and their $\mathrm{L_X}$ (see also Mulia et al., 2019), but that there is a statistically significant (albeit weaker) *anti*correlation among GCs. While the negative slope of the $\mathrm{L_X}$-$\mathrm{M_\star}$ relation for GCs *and* the fact that the $\mathrm{L_X}$ of these young clusters is consistent with the $\mathrm{L_X}$ of field XRBs both suggest these correlations are unrelated to higher mass clusters hosting more XRBs, we cannot definitively preclude this explanation for the positive relation in young clusters.

Finally, I conducted a search for the optical counterparts of nearby ULXs, encapsulating 46 ULXs in 28 galaxies. I find that more than half of all ULXs in the sample are associated with HMXBs, either in the field, in a compact star cluster, or in an OB association. Another $\sim 15\%$ are positively associated with LMXBs or IMXBs, which may represent a population of neutron star ULXs worth further investigation. Most interesting is the new classification of 1 source as a GC ULX; only 20 other ULXs have been found within GCs to date, and the nature of the accretion physics involved in these systems is still a mystery (Dage et al., 2021). Another 8 ULXs in this sample are classified for the first time in this study, which will be submitted for publication later this year.

The research presented in this thesis is at the forefront of an effort to disentangle XRB populations that reside in star-forming galaxies, a goal that has proven difficult to accomplish until recently. Ultimately, the discoveries born from this endeavor help us understand the formation, evolution, and prevalence of compact objects in the Universe, and may allow us to more accurately tune the newest generation of population synthesis models. XRBs are also useful tools for studying the properties and evolution of galaxies, since the presence of LMXBs and HMXBs are correlated with the $\mathrm{M_\star}$ and SFRs of galaxies — albeit in complex ways. Future research dedicated to expanding this work to include a greater sample of late-type galaxies has the potential to refine our model XLFs, better understand the nature of the newly identified non-negligible “IMXB” population, and quantify the role of clusters in the formation of extragalactic XRBs.

APPENDIX A

XRB sample in M83

This appendix contains a table with the properties and classifications of all M83 X-ray sources identified in Lehmer et al. (2019) that fall within the footprint of the HST image, followed by postage stamps of each XRB from HST WFC3/UVIS imaging.

For each source in the table, the ID indicates the ID number assigned in Lehmer et al. (2019), while Long ID gives the ID for the source from Long et al. (2014), where applicable. X-ray luminosities are in units log erg s^{-1}, and magnitudes are absolute mags estimated at a distance of 4.61 Mpc. The classification for each source is given, with italics representing SNRs identified using our HR–L_X criterion or XRBs associated with clusters. Classifications in parentheses are objects with uncertain “candidate” classifications, as reported in Long et al. (2014) or as found by our methods. Sources that were identified as candidate quasars for falling red-ward of the stellar evolutionary models (see §2.3.4) are labeled ‘Gal.’ A confidence flag (CF) is assigned to each source based on the “strength” of the identification of the X-ray emitter: a CF of 1 represents the most certain classifications (those determined in other studies, or XRBs with a clear donor, with multiple candidates of similar mass, or a clear absence of a donor); CF ratings of 2 or 3 may indicate that a source is in a dust-obscured region, such as near the nucleus or along a dust lane (since the presence of heavy dust could potentially mask high-mass stars, background galaxies, and clusters, leading to possible mis-identifications), that there are multiple sources of different masses within the 2σ radius, or that the most likely optical counterpart falls just outside the 2σ radius (owing to positional uncertainties). For XRBs in clusters, the cluster ages are given in the final column in units log years.

Table A.1. Properties and Classifications of M83 X-ray Sources

ID	CSC ID (2CXO)	Long ID	R.A. (deg)	Dec (deg)	L_X	V (Mag)	B-V (Mag)	V-I (Mag)	Class	CF	Cluster Age
L19X048	J133648.3-295244	X046	204.2013	-29.8790	36.4	-6.32	-0.04	0.22	SNR	2	—
L19X049	J133648.2-295136	X047	204.2014	-29.8605	36.0	-2.31	2.26	1.13	IM	2	—
L19X050	J133648.7-295229	X048	204.2033	-29.8748	37.1	-6.02	0.01	0.22	HM	1	—
L19X051	J133649.1-295258	X049	204.2047	-29.8828	37.6	-5.00	0.25	0.73	HM	3	—
L19X052	J133649.1-295125	X050	204.2050	-29.8570	36.3	—	—	—	LM	1	—
L19X053	J133649.2-295303	X051	204.2051	-29.8842	37.5	-2.85	-0.144	0.49	*SNR*	2	—
L19X055	J133649.4-295014	X052	204.2059	-29.8374	36.7	—	—	—	LM	1	—
L19X056	J133649.7-295217	X053	204.2075	-29.8715	37.0	-3.49	-0.34	0.05	SNR	1	—
L19X057	J133649.9-295513	X055	204.2081	-29.9203	37.0	—	—	—	LM	1	—
L19X058	J133649.9-295259	X054	204.2081	-29.8832	36.8	-4.58	0.94	1.64	*LM*	1	10.3
L19X059	J133650.1-295308	X057	204.2089	-29.8857	36.2	—	—	—	SNR	1	—
L19X060	J133650.1-295320	X058	204.2089	-29.8888	36.2	-4.43	0.01	1.51	*SNR*	2	—
L19X061	—	—	204.2094	-29.8760	36.4	-1.73	1.50	1.50	LM	1	—
L19X062	J133650.5-295304	X061	204.2108	-29.8845	36.2	-2.97	0.84	2.68	SNR	1	—
L19X064	—	—	204.2114	-29.8707	36.0	-4.99	1.80	2.06	HM	2	—
L19X065	J133650.7-295041	—	204.2116	-29.8450	36.0	-4.90	0.80	1.10	HM	1	—
L19X066	J133650.8-295240	X063	204.2121	-29.8778	36.7	-5.89	0.37	1.34	SNR	1	—
L19X067	—	X064	204.2124	-29.8833	36.5	-4.97	-0.19	0.06	(SNR)	1	—
L19X068	J133650.9-295226	X065	204.2124	-29.8738	36.7	-4.48	0.40	0.5	SNR	1	—
L19X069	J133651.1-295042	X067	204.2134	-29.8451	36.8	-3.01	0.36	1.15	SNR	2	—
L19X070	—	—	204.2139	-29.8354	35.7	-3.48	0.08	0.62	IM	2	—
L19X072	J133651.4-295043	X071	204.2145	-29.8454	36.0	-2.93	2.63	2.14	IM	2	—
L19X073	J133651.5-295143	X072	204.2148	-29.8620	37.1	-1.04	-1.18	—	IM	3	—
L19X075	J133651.6-295025	X074	204.2153	-29.8402	36.6	-2.99	0.37	0.86	*SNR*	2	—
L19X076	J133651.6-295335	X073	204.2153	-29.8930	37.7	-7.11	0.18	0.97	HM	1	—
L19X077	J133651.7-295431	X076	204.2158	-29.9085	36.7	-3.04	0.71	1.62	IM	2	—
L19X078	J133651.7-295302	X078	204.2160	-29.8838	36.3	-3.80	0.20	0.06	SNR	2	—
L19X079	—	X079	204.2162	-29.8860	36.2	-4.69	0.06	0.60	HM	2	—
L19X081	—	—	204.2175	-29.8270	35.9	-4.82	0.15	0.40	HM	2	—
L19X083	J133652.2-294920	X084	204.2179	-29.8221	36.2	-5.09	0.40	0.99	HM	2	—
L19X084	J133652.3-295046	X085	204.2181	-29.8462	37.7	—	—	—	LM	1	—
L19X085	—	—	204.2182	-29.8837	36.7	-3.88	2.14	2.48	HM	2	—
L19X086	—	X087	204.2184	-29.8810	36.8	-4.15	0.03	0.32	IM	1	—
L19X087	J133652.4-295142	X088	204.2185	-29.8617	36.4	-2.06	-0.89	—	IM	3	—
L19X088	J133652.4-295107	—	204.2190	-29.8513	35.8	-7.46	-0.034	0.11	HM	2	—

Table A.1 (cont'd)

ID	CSC ID (2CXO)	Long ID	R.A. (deg)	Dec (deg)	L_X	V (Mag)	B-V (Mag)	V-I (Mag)	Class	CF	Cluster Age
L19X089	J133652.5-295531	X090	204.2192	-29.9253	36.5	-4.33	1.74	1.81	HM	2	—
L19X090	J133652.5-295147	X091	204.2192	-29.8632	36.5	-8.25	0.11	0.29	*HM*	2	6.7
L19X091	—	X093	204.2199	-29.8781	36.6	-4.73	0.33	1.20	SNR		—
L19X092	—	—	204.2200	-29.8933	36.0	-2.62	-0.05	3.34	IM	2	—
L19X093	J133652.7-295328	X094	204.2202	-29.8911	36.0	-4.52	0.22	0.80	HM	2	—
L19X094	J133652.8-295231	X097	204.2202	-29.87540	36.7	-2.22	0.31	1.99	SNR	2	—
L19X095	J133652.8-295110	X095	204.2202	-29.8531	36.7	-9.19	0.52	0.79	SNR	2	—
L19X096	J133652.8-295316	X099	204.2204	-29.8878	37.3	-3.28	-0.42	—	HM	2	—
L19X097	J133652.9-295144	—	204.2205	-29.8621	36.6	-5.99	-0.01	0.09	*SNR*	2	—
L19X098	J133652.8-295137	X098	204.2205	-29.8604	36.7	-4.56	0.21	0.40	*SNR*	2	—
L19X099	J133652.9-295309	X101	204.2210	-29.8861	36.5	—	—	—	*SNR*	2	—
L19X100	—	X100	204.2210	-29.8711	36.0	—	—	—	SNR	1	—
L19X101	J133653.1-295002	X102	204.2213	-29.8340	36.3	-3.13	0.13	1.73	IM	2	—
L19X102	J133653.1-295430	X103	204.2215	-29.9084	37.1	—	—	—	*LM*	1	10.3
L19X103	J133653.2-295247	X106	204.2217	-29.8799	36.7	-6.35	-0.03	0.12	SNR	1	—
L19X104	—	—	204.2218	-29.8658	36.0	-4.67	0.33	0.95	HM	2	—
L19X105	J133653.2-295325	X105	204.2219	-29.8903	37.0	-4.63	0.05	-0.08	SNR	1	—
L19X106	J133653.2-295133	X104	204.2219	-29.8594	36.4	-6.24	-0.15	0.79	SNR	1	—
L19X107	J133653.2-295242	X107	204.2221	-29.8785	36.9	-4.30	0.09	0.86	SNR	1	—
L19X108	—	—	204.2222	-29.8832	35.9	-4.62	0.22	0.57	HM	1	—
L19X110	J133653.4-294822	X109	204.2230	-29.8060	36.3	—	—	—	LM	1	—
L19X112	J133653.6-295336	X111	204.2234	-29.8934	37.7	-3.00	—	2.66	IM	1	—
L19X113	J133653.6-295154	X112	204.2236	-29.8651	36.1	—	—	—	LM	1	—
L19X114	J133653.6-295448	X113	204.2237	-29.9133	36.0	-3.55	1.02	1.75	IM	1	—
L19X115	J133653.8-295308	X114	204.2241	-29.8856	36.5	-2.26	-0.601	-0.64	*SNR*	2	—
L19X116	J133653.8-294848	X116	204.2245	-29.8135	36.8	-6.25	0.13	0.31	SNR	1	—
L19X117	J133653.8-295101	X115	204.2245	-29.8502	36.0	-6.46	0.32	0.48	*SNR*	2	—
L19X118	J133653.9-295114	X117	204.2247	-29.8541	37.3	-4.16	0.82	2.54	HM	1	—
L19X119	J133654.0-294933	X118	204.2254	-29.8258	36.3	-5.46	-0.09	-0.02	HM	2	—
L19X120	J133654.1-295308	X120	204.2257	-29.8852	36.2	-5.12	-0.17	0.18	*SNR*	2	—
L19X121	J133654.1-295209	X119	204.2257	-29.8693	35.9	-3.19	0.91	1.26	SNR	1	—
L19X122	—	—	204.2258	-29.8906	36.2	-5.09	1.73	2.46	HM	1	—
L19X123	J133654.2-295028	X121	204.2261	-29.8411	36.5	-4.52	1.22	2.71	SNR	2	—
L19X124	J133654.3-295144	X122	204.2264	-29.8622	36.3	-1.58	-1.16	1.19	IM	1	—
L19X125	J133654.4-295258	—	204.2269	-29.8828	36.5	-3.99	0.38	1.40	HM	1	—

Table A.1 (cont'd)

ID	CSC ID (2CXO)	Long ID	R.A. (deg)	Dec (deg)	L_X	V (Mag)	B-V (Mag)	V-I (Mag)	Class	CF	Cluster Age
L19X126	J133654.4-295026	X124	204.2272	-29.8408	36.2	-6.47	0.33	0.45	*SNR*	2	—
L19X127	—	—	204.2274	-29.8472	35.5	-6.10	0.15	0.43	HM	2	—
L19X128	—	—	204.2278	-29.9223	36.3	-0.69	—	0.78	IM	2	—
L19X129	J133654.7-295300	X127	204.2284	-29.8832	36.4	-3.29	0.55	0.65	SNR	2	—
L19X130	—	—	204.2285	-29.8859	36.4	-5.09	0.36	2.15	HM	1	—
L19X131	J133654.8-295018	X128	204.2287	-29.8385	36.3	-3.62	0.25	0.55	SNR	1	—
L19X132	J133655.0-29523	X129	204.2294	-29.8776	36.7	-3.56	0.82	1.75	SNR	2	—
L19X133	—	—	204.2294	-29.8801	35.5	-2.85	0.53	0.84	IM	1	—
L19X134	J133655.0-295304	X131	204.2295	-29.8846	37.0	—	—	—	SNR	1	—
L19X135	J133655.1-295040	X134	204.2298	-29.8445	36.2	-4.13	0.15	0.36	SNR	2	—
L19X137	J133655.2-295403	X135	204.2301	-29.9008	36.6	-5.00	0.27	0.40	*(IMXB)*	2	8.4
L19X138	—	—	204.2306	-29.8271	35.6	-1.12	0.08	0.66	IM	1	—
L19X139	—	—	204.2306	-29.8814	35.6	-4.17	0.09	0.20	IM	1	—
L19X140	—	X136	204.2307	-29.8481	35.8	-5.84	0.50	1.02	SNR	1	—
L19X141	J133655.4-294840	X137	204.2308	-29.8113	36.2	—	—	—	LM	2	—
L19X143	J133655.4-295510	X138	204.231268	-29.919348	38.0	-3.97	0.06	0.51	IM	2	—
L19X144	J133655.5-295303	X139	204.2316	-29.8843	37.0	-3.94	1.64	3.16	SNR	1	—
L19X145	—	—	204.2327	-29.8814	36.0	-4.48	0.14	0.65	HM	2	—
L19X146	—	—	204.2335	-29.8746	36.0	-1.97	1.13	1.85	LM	1	—
L19X148	—	—	204.2345	-29.8650	35.5	-4.55	0.20	0.37	IM	1	—
L19X149	J133656.2-295255	X141	204.2344	-29.8820	36.9	-3.50	0.61	2.06	SNR	2	—
L19X152	J133656.6-294819	X146	204.2350	-29.8049	36.9	-5.26	—	1.88	HM	1	—
L19X153	—	—	204.2351	-29.8408	35.9	-7.27	1.07	1.15	HM	2	—
L19X154	—	—	204.2359	-29.8325	35.8	-3.68	1.68	2.20	IM	2	—
L19X155	J133656.6-294912	X145	204.2360	-29.8201	38.2	-3.56	0.02	0.90	IM	1	—
L19X157	J133656.6-294819	X146	204.2361	-29.8053	36.3	-2.26	0.49	1.80	IM	2	—
L19X158	J133656.6-295321	X147	204.2363	-29.8892	36.4	-3.43	1.40	1.44	IM	3	—
L19X159	J133656.7-295316	X148	204.2368	-29.8879	36.0	-3.00	0.61	0.70	IM	3	—
L19X160	—	—	204.2383	-29.8843	36.0	-2.57	-0.63	—	LM	2	—
L19X161	J133657.2-295147	X150	204.2386	-29.8631	36.6	-1.88	1.54	2.57	LM	2	—
L19X162	J133657.2-295339	X152	204.2387	-29.8943	38.2	-4.25	1.75	2.18	HM	1	—
L19X163	J133657.2-295032	X153	204.2388	-29.8422	36.5	-1.14	1.39	2.16	LM	2	—
L19X165	J133657.3-295035	X154	204.2391	-29.8432	36.4	-4.33	0.32	0.68	IM	2	—
L19X167	J133657.7-295039	X157	204.2404	-29.8442	36.7	—	—	—	LM	2	—
L19X169	J133657.8-295042	X158	204.2409	-29.8451	36.8	-4.03	1.58	2.09	HM	1	—

Table A.1 (cont'd)

ID	CSC ID (2CXO)	Long ID	R.A. (deg)	Dec (deg)	L_X	V (Mag)	B-V (Mag)	V-I (Mag)	Class	CF	Cluster Age
L19X170	J133657.8-295335	—	204.2412	-29.8930	35.7	-3.85	2.27	3.68	Gal	2	—
L19X171	J133657.8-295303	X159	204.2412	-29.8841	37.1	-5.60	0.59	0.79	SNR	1	—
L19X172	J133657.9-294923	X160	204.2413	-29.8231	37.5	-3.61	1.05	1.93	IM	1	—
L19X173	—	—	204.2418	-29.8600	36.6	-2.95	2.15	2.74	IM	1	—
L19X174	J133658.2-295124	X161	204.2426	-29.8567	36.9	—	—	—	LM	1	—
L19X175	J133658.2-294833	X163	204.2429	-29.8092	37.8	-5.71	0.36	0.60	HM	3	—
L19X176	—	—	204.2431	-29.8575	35.6	-2.56	-0.55	2.8	IM	2	—
L19X177	—	—	204.2432	-29.8632	35.9	-1.00	0.30	3.36	LM	1	—
L19X178	J133658.3-295104	X165	204.2433	-29.8513	37.8	—	—	—	Gal	1	—
L19X179	—	—	204.2441	-29.8603	35.8	-2.67	0.89	1.98	LM	2	—
L19X180	J133658.5-294819	X166	204.2441	-29.8055	36.3	-3.19	-0.03	-0.10	SNR	2	—
L19X181	—	—	204.2443	-29.8658	36.3	-0.07	0.27	4.48	Gal	2	—
L19X182	J133658.6-295237	X169	204.2444	-29.8769	36.2	—	—	—	SNR	1	—
L19X183	J133658.6-295246	X168	204.2444	-29.8795	38.0	-3.42	0.15	1.30	LM	2	—
L19X184	J133658.6-295106	X170	204.2445	-29.8518	36.1	-2.61	—	2.02	LM	1	—
L19X185	J133658.7-295100	X172	204.2447	-29.8501	36.4	—	—	—	SNR	1	—
L19X186	J133658.8-294831	X173	204.2451	-29.8088	36.2	-3.32	0.83	2.26	IM	1	—
L19X188	J133658.9-295038	X175	204.2456	-29.8440	35.9	-3.13	-0.02	1.97	IM	2	—
L19X189	J133658.9-295024	X177	204.2457	-29.8402	35.9	-3.61	0.21	0.81	*SNR*	2	—
L19X190	J133658.9-295218	—	204.2458	-29.8718	35.8	-2.89	0.66	1.19	LM	2	—
L19X191	—	—	204.2463	-29.8678	36.6	—	—	—	LM	2	—
L19X192	J133659.0-295336	X178	204.2463	-29.8934	36.6	-2.26	3.55	3.02	*SNR*	2	—
L19X193	—	—	204.2464	-29.8658	36.7	-3.33	0.20	1.86	LM	1	—
L19X194	—	X181	204.2467	-29.8633	36.1	—	—	—	SNR	1	—
L19X195	J133659.3-295508	X183	204.2473	-29.9190	36.6	-2.60	1.53	1.47	SNR	1	—
L19X196	J133659.3-294837	X184	204.2475	-29.8103	36.2	-4.20	1.07	1.38	SNR	2	—
L19X197	J133659.4-295429	—	204.2475	-29.9074	36.0	-3.95	0.16	0.09	*SNR*	2	—
L19X198	—	—	204.2476	-29.8640	36.2	—	—	—	LM	1	—
L19X199	J133659.4-294959	X185	204.2478	-29.8331	38.7	-2.15	2.19	2.82	LM	3	—
L19X200	—	—	204.2478	-29.8981	35.8	-2.54	-0.17	-0.57	HM	2	—
L19X201	J133659.5-295204	X186	204.2479	-29.8677	36.8	—	—	—	SNR	1	—
L19X202	J133659.5-295414	X187	204.2484	-29.9038	37.7	-2.90	0.13	2.32	IM	3	—
L19X203	—	—	204.2487	-29.8728	36.0	-5.91	0.21	0.40	HM	1	—
L19X204	J133659.6-295108	X190	204.2486	-29.8524	36.9	—	—	—	LM	1	—
L19X205	—	—	204.2488	-29.8656	36.7	-4.73	0.51	1.27	HM	1	—

Table A.1 (cont'd)

ID	CSC ID (2CXO)	Long ID	R.A. (deg)	Dec (deg)	L_X	V (Mag)	B-V (Mag)	V-I (Mag)	Class	CF	Cluster Age
L19X206	—	—	204.2489	-29.8178	34.9	-2.97	2.48	1.74	IM	1	—
L19X207	J133659.7-295205	X193	204.2491	-29.8681	38.2	-4.94	0.90	1.25	HM	2	—
L19X208	J133659.8-295202	X194	204.2493	-29.8673	36.9	-5.43	0.83	2.04	*SNR*	2	—
L19X209	J133659.8-295526	X195	204.2494	-29.9238	36.7	-5.07	0.0019	0.24	SNR	1	—
L19X210	J133659.9-295150	X198	204.2500	-29.8639	38.0	-5.61	0.14	1.48	HM	1	—
L19X211	J133659.9-295157	X197	204.2501	-29.8659	36.7	—	—	—	LM	3	—
L19X212	J133700.0-295417	X199	204.2501	-29.9047	36.2	-2.63	-0.32	0.65	SNR	2	—
L19X213	J133700.0-295219	X200	204.2502	-29.8721	36.6	—	—	—	HM	3	—
L19X214	J133700.0-295201	X202	204.2502	-29.8671	36.9	-7.13	0.20	0.74	SNR	3	—
L19X215	J133700.0-295137	X201	204.2504	-29.8605	36.8	—	—	—	HM	3	—
L19X216	J133700.0-295329	X203	204.2505	-29.8915	37.4	—	—	—	LM	1	—
L19X217	J133700.1-295145	X204	204.2505	-29.8626	37.0	-5.46	0.47	0.98	*SNR*	3	—
L19X218	J133700.2-29515	X206	204.2508	-29.8646	37.0	-6.10	0.359	0.86	HM	2	—
L19X219	J133700.1-294810	X205	204.2508	-29.8028	36.1	-5.36	0.47	0.66	SNR	1	—
L19X220	J133700.2-295206	X207	204.2509	-29.8684	37.5	-8.135	0.18	0.41	SNR	1	—
L19X221	J133700.2-295150	X209	204.2512	-29.8636	37.1	-5.97	0.47	0.37	LM	3	—
L19X222	J133700.3-295219	X211	204.2513	-29.8719	36.0	—	—	—	*SNR*	2	—
L19X223	J133700.3-295205	X212	204.2515	-29.8681	37.3	-5.70	0.88	1.90	SNR	1	—
L19X224	—	—	204.2516	-29.8623	36.6	-4.33	0.97	1.65	HM	1	
L19X225	J133700.4-295323	X215	204.2516	-29.8897	36.2	—	—	—	SNR	1	—
L19X226	—	—	204.2518	-29.8696	37.5	-4.52	0.28	0.16	IM	1	—
L19X227	J133700.4-295054	X217	204.2519	-29.8484	36.2	-3.43	2.07	2.12	*SNR*	2	—
L19X229	J133700.4-295155	X220	204.2521	-29.8654	37.5	-10.95	0.23	0.24	*HM*	1	6.1
L19X230	J133700.5-295159	X223	204.2524	-29.8663	37.5	-8.95	0.62	0.70	HM	1	—
L19X231	J133700.6-295146	X225	204.2526	-29.8630	37.5	—	—	—	LM	2	—
L19X232	J133700.6-295200	X229	204.2527	-29.8667	37.3	-8.63	-0.03	0.01	HM	1	—
L19X233	—	—	204.2527	-29.8678	37.1	-5.71	0.17	0.79	HM	1	—
L19X234	J133700.6-295319	X227	204.2527	-29.8888	38.3	-4.50	0.41	0.51	IM	1	—
L19X235	J133700.6-295206	X228	204.2529	-29.8683	37.8	-6.444	0.53	0.83	LM	2	—
L19X236	—	—	204.2531	-29.8659	37.6	-9.73	0.12	0.31	HM	1	—
L19X237	—	—	204.2531	-29.8729	35.5	-5.25	0.48	0.86	HM	1	—
L19X238	—	—	204.2531	-29.8926	35.6	-5.92	1.92	2.22	AGN	1	—
L19X239	—	—	204.2536	-29.9069	36.0	-3.67	0.23	0.00	IM	1	—
L19X240	—	—	204.2537	-29.8761	35.6	—	—	—	LM	1	—
L19X241	J133700.8-295156	X233	204.2538	-29.8656	38.5	-11.47	0.80	1.61	Nucleus	1	—

Table A.1 (cont'd)

ID	CSC ID (2CXO)	Long ID	R.A. (deg)	Dec (deg)	L_X	V (Mag)	B-V (Mag)	V-I (Mag)	Class	CF	Cluster Age
L19X242	—	—	204.2538	-29.8665	37.4	-7.26	0.29	0.15	HM	1	—
L19X243	J133700.9-295202	X234	204.2540	-29.8674	38.2	-8.49	0.15	0.98	HM	1	—
L19X244	—	—	204.2540	-29.8603	34.9	-3.78	0.83	1.13	IM	2	—
L19X245	J133701.0-295056	X235	204.2544	-29.8490	36.4	—	—	—	SNR	1	—
L19X246	J133701.0-295245	X236	204.2545	-29.8793	37.9	—	—	—	LM	1	—
L19X247	—	—	204.2546	-29.8409	35.3	—	—	—	LM	1	—
L19X248	J133701.1-295152	X237	204.2547	-29.8644	37.5	—	—	—	LM	2	—
L19X249	J133701.1-295156	X241	204.2549	-29.8658	38.1	-8.08	0.25	0.35	(SNR)	1	—
L19X250	J133701.2-295202	X242	204.2553	-29.8671	37.2	—	—	—	LM	3	—
L19X251	J133701.2-295200	X243	204.2553	-29.8667	37.2	-5.37	0.90	1.84	SNR	3	—
L19X252	J133701.3-295139	—	204.2555	-29.8609	36.6	—	—	—	LM	1	—
L19X253	J133701.3-295136	X244	204.2555	-29.8601	37.9	—	—	—	LM	1	—
L19X254	—	—	204.2562	-29.8649	36.3	-6.35	0.50	1.35	LM	2	—
L19X255	J133701.4-295326	X248	204.2562	-29.8907	38.4	—	—	—	LM	1	—
L19X256	—	X249	204.2566	-29.8330	35.8	-8.07	0.40	0.42	SNR	1	—
L19X257	J133701.6-295202	X250	204.2568	-29.8672	36.5	—	—	—	SNR	1	—
L19X259	J133701.6-295410	X253	204.2569	-29.9026	35.9	-4.34	0.08	0.54	SNR	2	—
L19X260	J133701.6-295128	X251	204.2569	-29.8578	38.3	-6.30	0.04	0.05	HM	1	—
L19X261	—	—	204.2571	-29.8696	35.1	-4.98	0.03	0.30	HM	2	—
L19X262	J133701.7-295113	X256	204.2573	-29.8537	36.6	-3.95	1.08	1.32	SNR	1	—
L19X263	—	—	204.2574	-29.8656	35.6	-4.10	0.55	1.68	HM	2	—
L19X264	—	—	204.2577	-29.8555	35.8	-4.26	0.05	0.09	IM	1	—
L19X265	J133702.0-295518	X258	204.2585	-29.9216	38.2	-5.25	0.38	0.64	HM	2	—
L19X266	—	—	204.2589	-29.8586	34.8	-6.39	0.46	0.55	HM	2	—
L19X267	J133702.1-295506	X259	204.2591	-29.9183	37.1	—	—	—	LM	1	—
L19X268	J133702.1-295144	X260	204.2592	-29.8623	36.5	—	—	—	LM	1	—
L19X269	J133702.2-294952	X261	204.2593	-29.8312	36.7	-3.33	0.50	1.90	SNR	2	—
L19X270	—	—	204.2594	-29.8090	35.9	—	—	—	LM	2	—
L19X271	—	X262	204.2597	-29.8352	35.9	-3.88	0.22	0.35	SNR	2	—
L19X272	—	—	204.2598	-29.8651	35.2	—	—	—	LM	1	—
L19X274	J133702.3-295206	X264	204.2600	-29.8685	35.6	-3.815	1.62	1.70	IM	2	—
L19X275	J133702.4-295126	X265	204.2601	-29.8572	37.1	-6.96	1.13	1.10	SNR	2	—
L19X276	—	—	204.2602	-29.8557	35.5	-3.73	0.22	—	IM	2	—
L19X277	—	—	204.2603	-29.8499	35.9	-4.74	0.10	0.65	HM	2	—
L19X278	J133702.4-295319	X267	204.2603	-29.8886	37.6	-3.913	1.25	2.32	IM	2	—

Table A.1 (cont'd)

ID	CSC ID (2CXO)	Long ID	R.A. (deg)	Dec (deg)	L_X	V (Mag)	B-V (Mag)	V-I (Mag)	Class	CF	Cluster Age
L19X279	J133702.5-295345	X268	204.2606	-29.8958	36.6	-5.95	1.79	2.09	AGN	1	—
L19X280	—	—	204.2611	-29.8605	35.8	—	—	—	LM	1	—
L19X281	J133702.6-294824	X269	204.2611	-29.8067	36.3	—	—	—	LM	2	—
L19X282	—	—	204.2618	-29.8618	36.1	-7.13	0.53	0.5	HM	1	—
L19X284	—	—	204.2622	-29.8503	35.8	—	—	—	LM	1	—
L19X285	J133703.0-294945	X272	204.2626	-29.8292	36.7	-3.56	1.57	2.28	SNR	1	—
L19X286	—	—	204.2627	-29.8638	35.6	-4.89	0.35	0.60	HM	2	—
L19X287	J133703.1-295531	X273	204.2633	-29.9255	36.1	-2.69	-0.21	-0.33	HM	2	—
L19X288	J133703.2-295226	X274	204.2638	-29.8741	37.3	-5.58	1.44	1.51	HM	1	—
L19X289	J133703.4-295401	X275	204.2644	-29.9006	36.0	-6.24	0.51	1.90	SNR	1	—
L19X290	J133703.5-295331	X277	204.2647	-29.8920	36.3	—	—	—	LM	1	—
L19X291	J133703.5-295320	X278	204.2649	-29.8888	36.1	1.07	-2.61	1.67	LM	1	—
L19X292	J133703.5-294940	X279	204.2650	-29.8280	37.1	-4.49	0.20	0.94	SNR	1	—
L19X293	J133703.8-294930	X281	204.2662	-29.8251	38.1	-4.17	0.04	0.26	IM	2	—
L19X294	J133703.9-295322	X282	204.2664	-29.8894	35.6	-2.81	5.11	2.42	IM	2	—
L19X295	J133704.0-294915	—	204.2669	-29.8209	35.7	-5.28	0.44	0.51	*SNR*	2	—
L19X296	J133704.1-295312	X283	204.2675	-29.8867	36.1	-3.82	0.28	0.25	IM	1	—
L19X297	—	—	204.2679	-29.8495	35.9	—	—	—	LM	2	—
L19X298	J133704.2-295403	X284	204.2679	-29.9010	38.4	-5.35	1.80	1.93	HM	1	—
L19X299	J133704.3-295138	—	204.2680	-29.8608	35.8	-3.66	-0.011	-0.98	HM	2	—
L19X300	J133704.3-295130	X285	204.2683	-29.8585	37.4	—	—	—	LM	1	—
L19X301	J133704.3-295121	X286	204.2683	-29.8559	38.7	-4.27	0.13	0.50	IM	2	—
L19X302	J133704.4-294938	X287	204.2684	-29.8274	36.5	-5.90	0.13	0.19	SNR	1	—
L19X303	J133704.5-294935	X288	204.2689	-29.8265	36.1	-5.16	0.14	0.32	SNR	1	—
L19X304	J133704.6-295120	X290	204.2695	-29.8556	36.7	-7.66	0.83	1.23	*LM*	1	6.2
L19X305	J133704.6-295054	X291	204.2695	-29.8485	36.3	—	—	—	LM	1	—
L19X306	J133704.7-295040	X293	204.2696	-29.8445	36.0	-4.22	-0.05	-0.16	HM	2	—
L19X308	J133704.7-294851	X295	204.2699	-29.8144	37.3	-2.44	-0.14	-0.10	IM	1	—
L19X309	J133704.8-295107	X296	204.2700	-29.8520	36.1	-3.75	-0.09	—	*SNR*	2	—
L19X310	—	—	204.2702	-29.8497	36.0	-6.02	0.24	0.42	HM	2	—
L19X311	J133704.9-295339	X298	204.2705	-29.8943	36.0	-2.46	0.89	4.40	Gal	1	—
L19X313	—	—	204.2710	-29.8459	35.9	—	—	—	LM	1	—
L19X314	J133705.1-295207	X299	204.2715	-29.8686	39.5	—	—	—	LM	1	—
L19X315	J133705.2-295122	X301	204.2720	-29.8560	36.3	—	—	—	LM	1	—
L19X316	J133705.4-295234	X303	204.2729	-29.8761	37.7	—	—	—	LM	1	—

Table A.1 (cont'd)

ID	CSC ID (2CXO)	Long ID	R.A. (deg)	Dec (deg)	L_X	V (Mag)	B-V (Mag)	V-I (Mag)	Class	CF	Cluster Age
L19X317	J133705.5-295032	X304	204.2732	-29.8423	35.7	—	—	—	*SNR*	2	—
L19X318	—	—	204.2733	-29.8960	36.1	-3.54	-0.06	—	IM	2	—
L19X321	J133705.7-294923	X307	204.2740	-29.8231	35.8	—	—	—	LM	1	—
L19X322	—	—	204.2742	-29.8842	35.4	-5.11	0.14	0.59	HM	2	—
L19X323	J133705.8-294822	X308	204.2744	-29.8061	36.1	-2.64	0.34	0.67	IM	3	—
L19X324	—	—	204.2745	-29.8459	35.7	-5.62	0.99	1.22	HM	1	—
L19X325	J133705.9-295159	X309	204.2750	-29.8664	36.8	—	—	—	LM	1	—
L19X326	J133706.0-295514	X310	204.2752	-29.9206	37.0	-2.98	0.27	1.63	SNR	2	—
L19X327	J133706.1-295444	X311	204.2759	-29.9123	36.6	-3.51	0.19	1.08	SNR	1	—
L19X328	J133706.4-295025	X313	204.2771	-29.8405	36.2	—	—	—	SNR	1	—
L19X329	J133706.6-294944	X314	204.2776	-29.8290	36.0	-6.82	0.12	0.08	HM	1	—
L19X330	J133706.6-295332	X316	204.2778	-29.8924	36.8	-3.81	0.02	1.36	SNR	1	—
L19X331	J133706.7-294947	—	204.2782	-29.8299	35.8	-3.715	1.39	2.01	IM	2	—
L19X332	J133706.7-295057	X317	204.2783	-29.8494	36.4	—	—	—	*SNR*	2	—
L19X333	J133706.9-294934	X318	204.2789	-29.8261	36.1	-3.37	0.49	0.16	IM	1	—
L19X334	—	X319	204.2792	-29.8189	36.1	-6.97	0.19	0.36	SNR	1	—
L19X335	J133707.0-295321	X320	204.2796	-29.8891	35.9	-2.51	0.87	2.18	SNR	1	—
L19X336	—	—	204.2796	-29.8242	35.4	-5.39	0.49	0.60	Gal	1	—
L19X337	J133707.1-295101	X321	204.2797	-29.8504	38.7	-5.03	-0.01	0.02	HM	2	—
L19X338	J133707.1-295202	X322	204.2797	-29.8672	36.5	-6.38	0.85	1.33	*SNR*	2	—
L19X339	—	—	204.2800	-29.8523	36.1	-5.87	1.58	3.02	HM	2	—
L19X341	J133707.4-295133	X326	204.2812	-29.8592	36.4	—	—	—	LM	1	—
L19X342	J133707.5-294859	X327	204.2814	-29.8164	36.7	-5.49	0.14	0.07	*SNR*	2	—
L19X343	J133707.5-294918	X328	204.2816	-29.8219	36.4	—	—	—	*SNR*	2	—
L19X344	—	—	204.2821	-29.8541	35.9	-4.35	0.03	0.09	IM	2	—
L19X345	J133707.6-295056	X329	204.2822	-29.8492	35.9	-6.65	0.02	0.14	HM	2	—
L19X346	—	—	204.2828	-29.8526	36.1	-6.08	0.05	-0.12	HM	1	—
L19X347	—	—	204.2830	-29.8863	35.9	-6.37	0.36	0.55	HM	2	—
L19X348	J133708.1-294916	X332	204.2831	-29.8222	36.1	-3.35	0.98	1.40	IM	2	—
L19X349	—	—	204.2832	-29.8708	35.7	-5.32	0.31	0.76	HM	2	—
L19X350	—	—	204.2836	-29.8933	36.0	-3.05	-0.10	1.34	IM	2	—
L19X351	J133708.1-294916	X332	204.2842	-29.8213	36.5	-5.50	0.33	0.52	*IM*	1	8.1
L19X352	—	—	204.2844	-29.8569	36.4	-3.99	0.19	0.21	IM	2	—
L19X353	—	—	204.2847	-29.8147	35.4	-5.48	1.45	1.18	HM	2	—
L19X354	J133708.3-295056	X336	204.2848	-29.8490	36.0	-5.79	-0.01	-0.19	SNR	1	—

Table A.1 (cont'd)

ID	CSC ID (2CXO)	Long ID	R.A. (deg)	Dec (deg)	L_X	V (Mag)	B-V (Mag)	V-I (Mag)	Class	CF	Cluster Age
L19X355	—	—	204.2850	-29.8821	35.9	-6.84	0.03	0.70	*HM*	1	6.9
L19X356	—	—	204.2852	-29.8703	36.1	-4.175	0.15	-0.06	*IM*	1	8.9
L19X357	J133708.4-295201	X338	204.2855	-29.8672	36.1	-4.78	0.523	0.75	SNR	2	—
L19X358	J133708.5-295135	X339	204.2858	-29.8597	36.2	-4.26	1.30	1.79	SNR	2	—
L19X360	—	X341	204.2862	-29.8786	35.9	-3.96	0.15	0.74	SNR	2	—
L19X361	J133708.7-295137	X342	204.2866	-29.8604	36.3	—	—	—	SNR	2	—
L19X362	J133708.7-295334	X344	204.2867	-29.8929	36.4	-1.67	1.93	2.49	LM	2	—
L19X363	—	—	204.2867	-29.8683	35.7	—	—	—	LM	2	—
L19X364	—	—	204.2876	-29.8527	35.8	-3.17	0.29	0.18	IM	3	—
L19X365	J133709.0-294938	X345	204.2878	-29.8273	37.1	-3.73	0.46	0.76	IM	2	—
L19X366	J133709.0-295125	X346	204.2879	-29.8570	36.0	—	—	—	LM	3	—
L19X367	J133709.2-294924	X347	204.2885	-29.8235	35.9	-6.04	1.91	2.55	*SNR*	2	—
L19X368	—	—	204.2885	-29.8724	35.1	-6.87	0.33	0.71	*HM*	2	6.1
L19X369	J133709.2-295133	X348	204.2886	-29.8593	36.0	-6.27	0.29	0.51	SNR	1	—
L19X370	J133709.2-295343	—	204.2887	-29.8950	36.2	-4.33	1.80	2.08	HM	1	—
L19X372	—	—	204.2913	-29.8494	35.7	-5.13	0.24	0.83	HM	1	—
L19X373	J133710.0-295128	X350	204.2920	-29.8578	36.2	-6.07	0.01	0.24	SNR	2	—
L19X374	J133710.3-294918	X351	204.2930	-29.8218	36.2	-3.97	-0.14	-0.26	HM	2	—
L19X375	—	—	204.2938	-29.8521	35.6	-3.37	0.64	1.53	IM	1	—
L19X376	—	—	204.2941	-29.8290	35.6	-5.47	0.34	0.29	HM	2	—
L19X377	—	—	204.2957	-29.8315	35.9	-3.67	-0.10	-0.46	HM	2	—
L19X378	J133710.9-295046	X353	204.2958	-29.8462	36.1	-2.73	1.89	2.02	SNR	2	—
L19X381	J133711.4-295141	X356	204.2981	-29.8614	36.0	—	—	—	SNR	1	—
L19X383	J133711.8-295215	X358	204.2996	-29.8710	36.8	-3.13	-0.12	1.81	SNR	3	—
L19X385	J133712.0-295056	X360	204.3003	-29.8491	36.5	—	—	—	SNR	2	—
L19X387	—	—	204.3011	-29.9212	36.1	-2.57	0.02	0.87	IM	3	—
L19X388	—	—	204.3012	-29.8425	35.5	-2.89	2.3	2.00	IM	2	—
L19X390	J133712.4-295140	X363	204.3019	-29.8611	36.8	-3.95	0.79	1.21	*SNR*	2	—
L19X393	J133712.5-295154	X366	204.3023	-29.8652	37.9	—	—	—	LM	1	—
L19X397	—	—	204.3045	-29.8607	35.8	-8.97	0.72	0.87	HM	1	—
L19X398	J133713.1-295238	X370	204.3048	-29.8773	37.1	-2.91	0.18	0.56	IM	2	—
L19X399	J133713.6-295200	X371	204.3068	-29.8666	35.8	-2.97	1.45	0.95	IM	1	—
L19X404	J133714.4-295130	X377	204.3101	-29.8584	36.3	-3.19	0.199	1.52	IM	1	—
L19X405	J133714.4-295148	X378	204.3103	-29.8635	37.5	-6.75	0.89	1.60	HM	1	—
L19X408	J133715.0-295138	X381	204.3126	-29.8608	36.4	-3.28	0.06	1.54	IM	1	—

Table A.1 (cont'd)

ID	CSC ID (2CXO)	Long ID	R.A. (deg)	Dec (deg)	L_X	V (Mag)	B-V (Mag)	V-I (Mag)	Class	CF	Cluster Age
L19X411	J133716.2-295202	X384	204.3176	-29.8673	37.1	—	—	—	LM	1	—
L19X416	J133717.2-295153	X389	204.3218	-29.8648	37.2	-4.53	0.00	0.86	SNR	1	—
L19X418	J133717.2-295153	X389	204.3227	-29.8650	36.7	-2.12	1.45	2.32	*SNR*	3	—
L19X421	J133718.3-295118	X395	204.3267	-29.8551	36.2	-2.33	1.13	1.94	LM	2	—
L19X422	J133718.8-295013	X397	204.3288	-29.8371	36.6	-4.16	0.81	1.30	HM	1	—
L19X426	J133719.6-295131	X402	204.3319	-29.8588	37.2	-6.34	1.58	1.78	AGN	1	—
L19X430	J133720.8-295035	—	204.3364	-29.8430	36.3	-2.54	0.89	1.49	IM	3	—
L19X432	J133721.1-295242	X408	204.3380	-29.8785	36.1	-1.84	1.61	1.79	LM	3	—
L19X433	J133721.4-295121	X409	204.3394	-29.8560	36.4	—	—	—	LM	1	—
L19X434	J133722.1-295208	X412	204.3424	-29.8689	37.0	-5.08	—	3.09	AGN	2	—

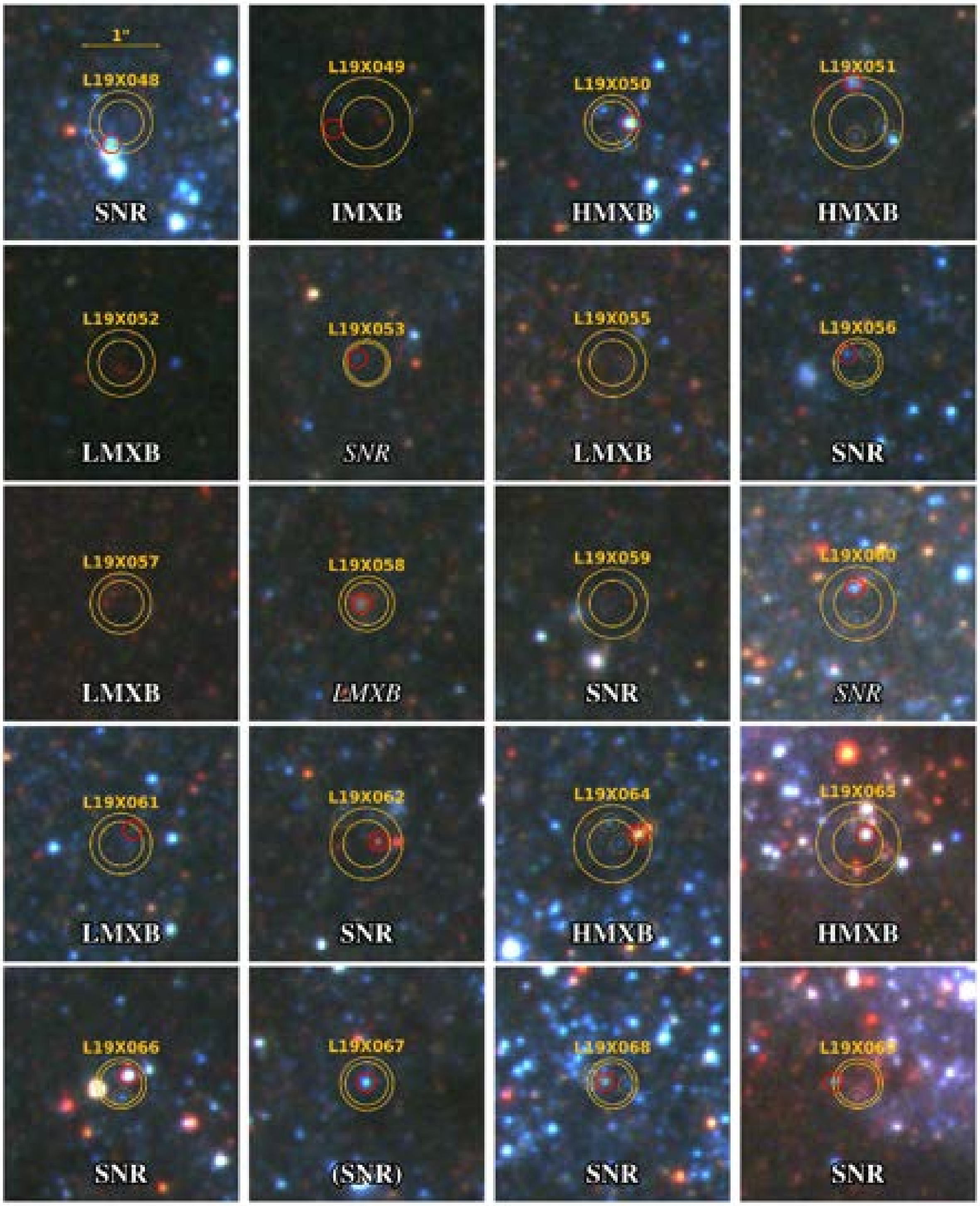

Figure A.1 Optical counterparts within the 1- and 2-σ radii for each X-ray source, with the most likely donor circled in red. Classifications in italics represent SNRs identified using our HR–L_X criterion or XRBs associated with clusters. Parentheses indicate objects with uncertain "candidate" classifications, as reported in Long et al. (2014) or as found by our methods.

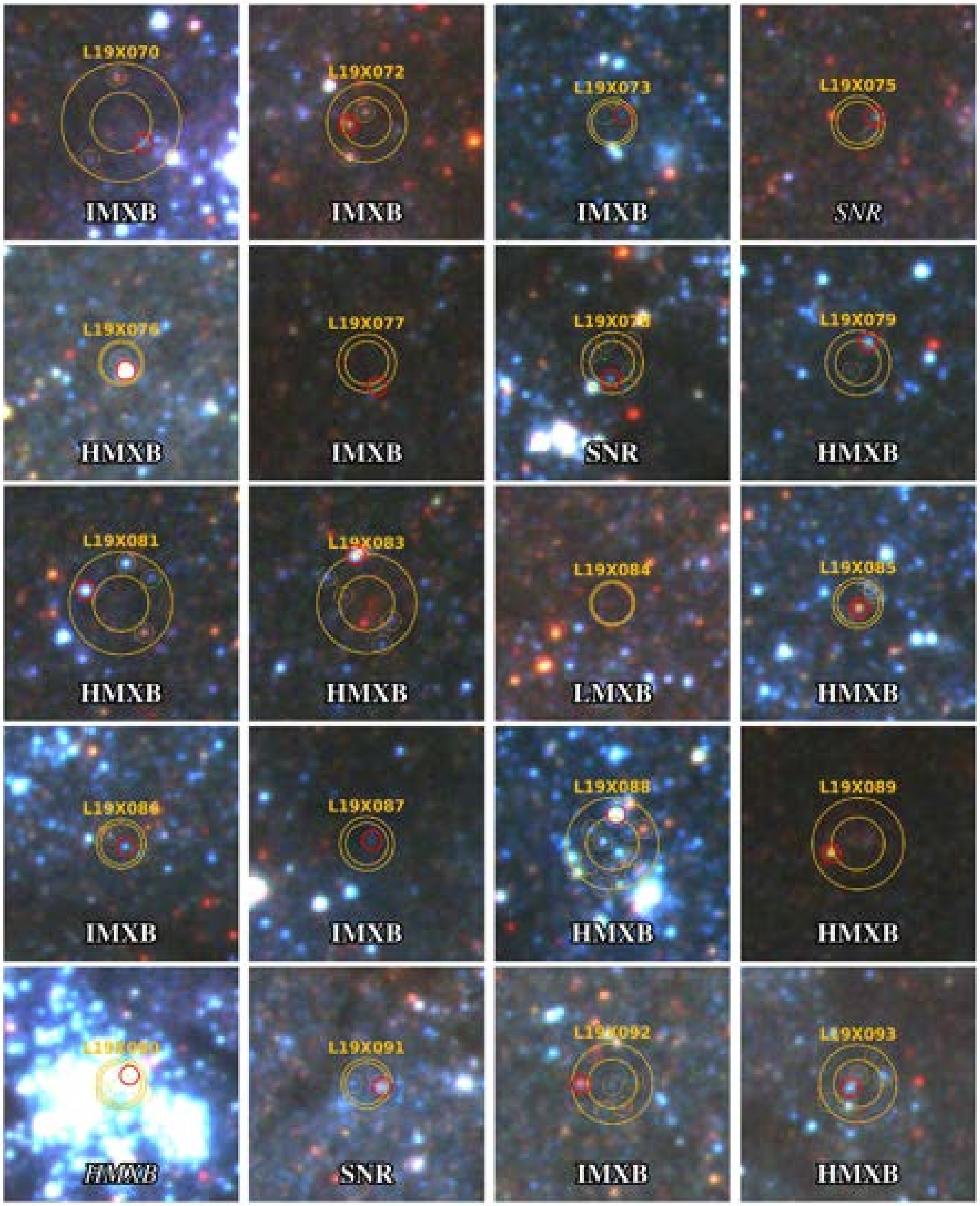

Figure A.1 *(continued)*

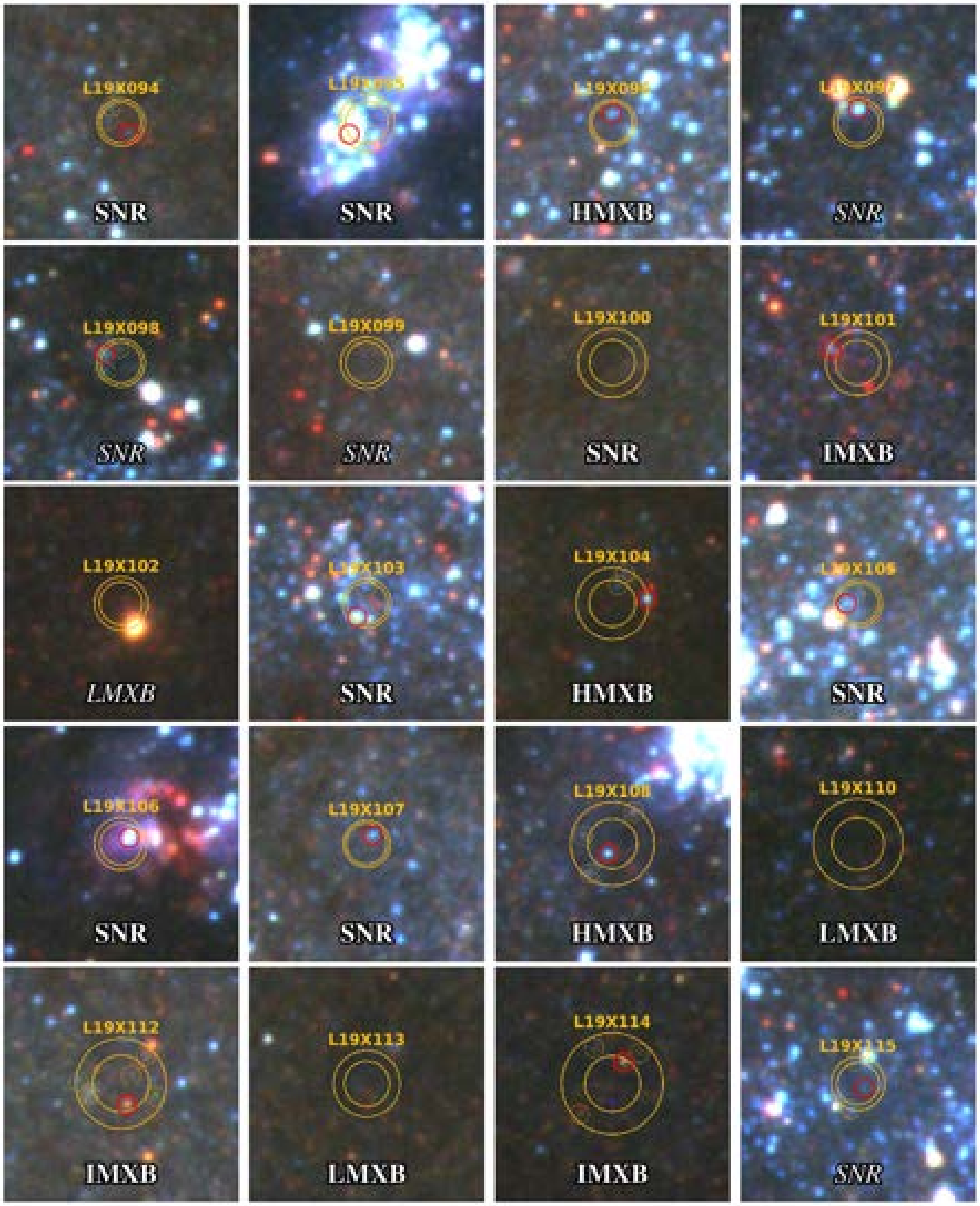

Figure A.1 *(continued)*

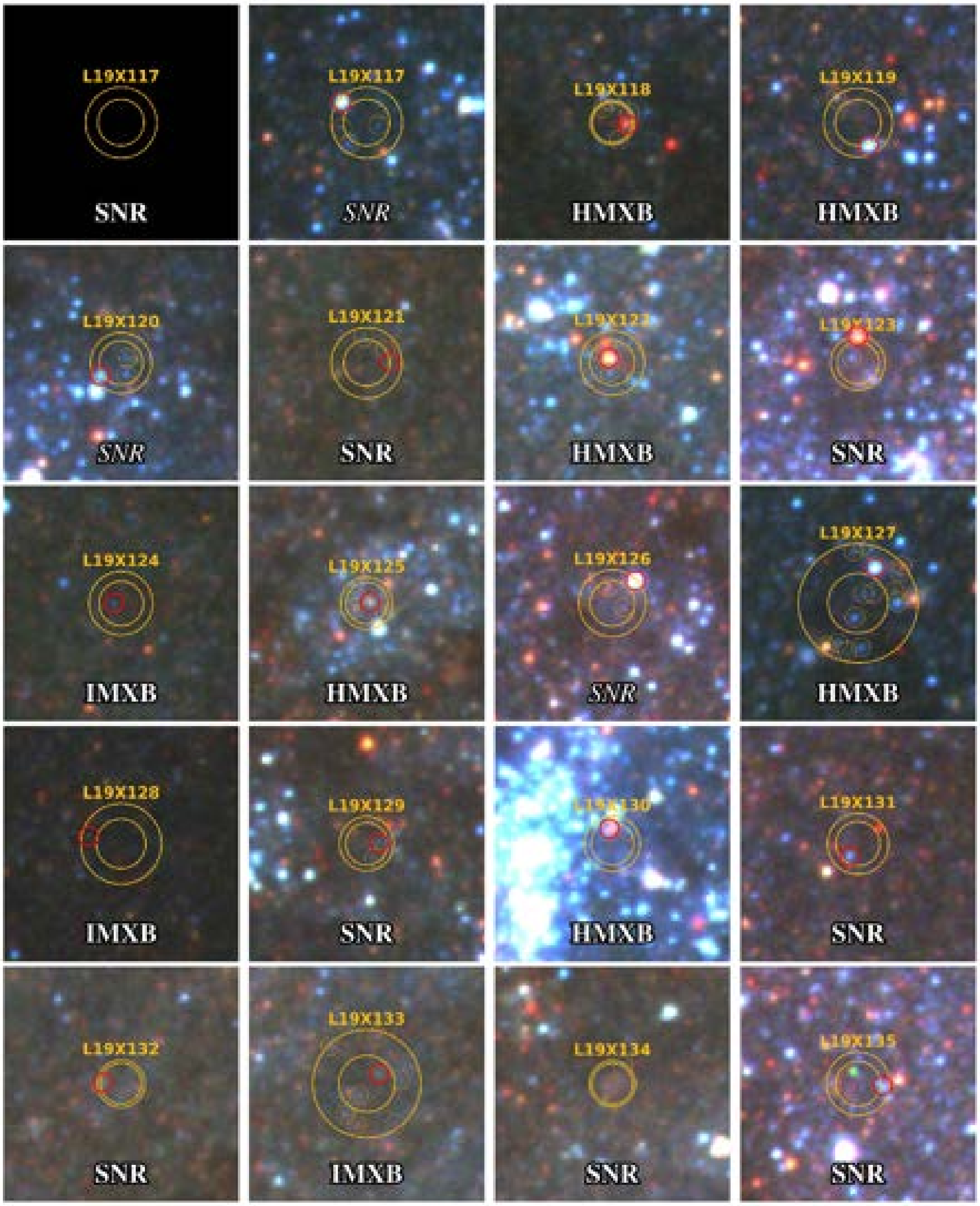

Figure A.1 *(continued)*

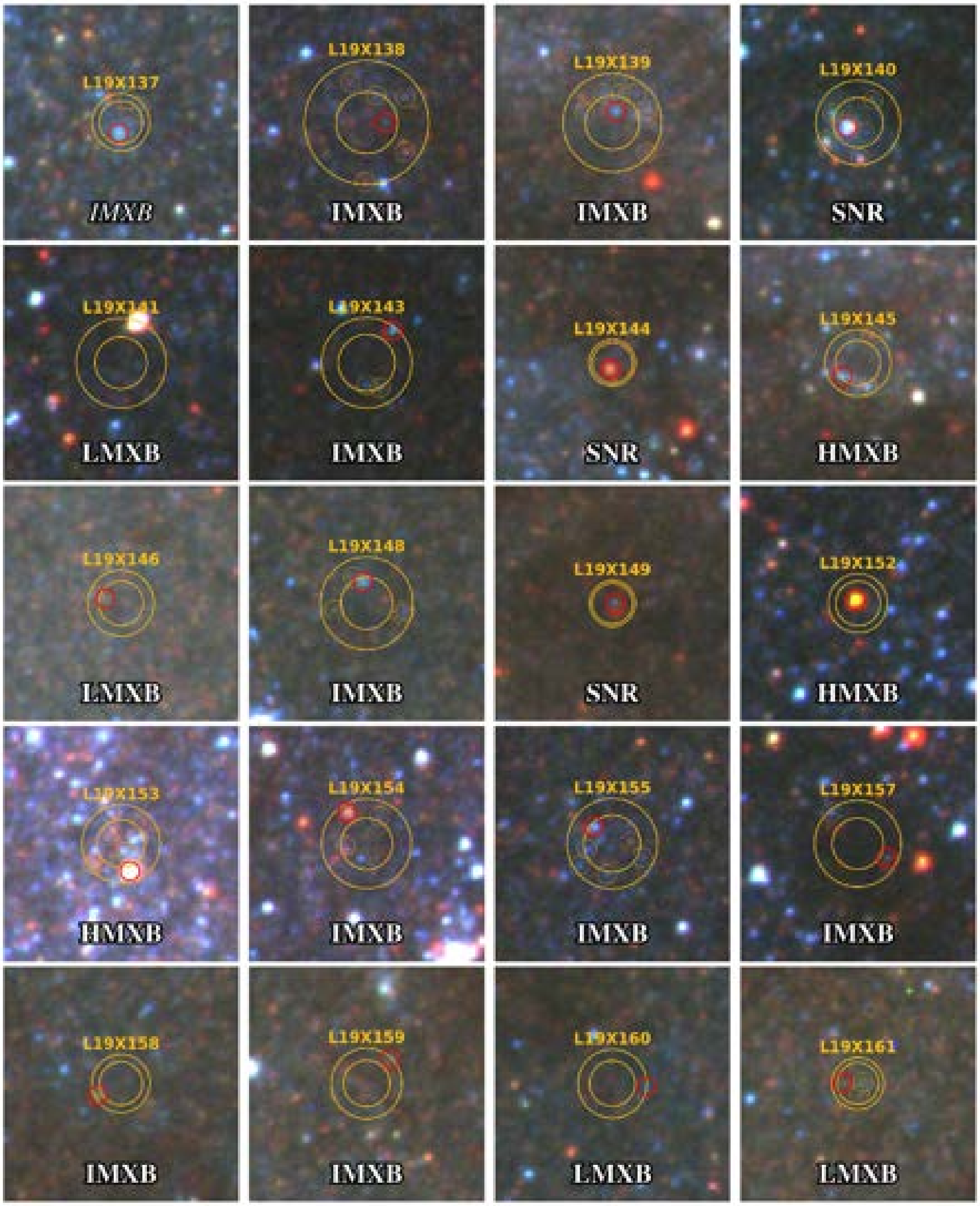

Figure A.1 *(continued)*

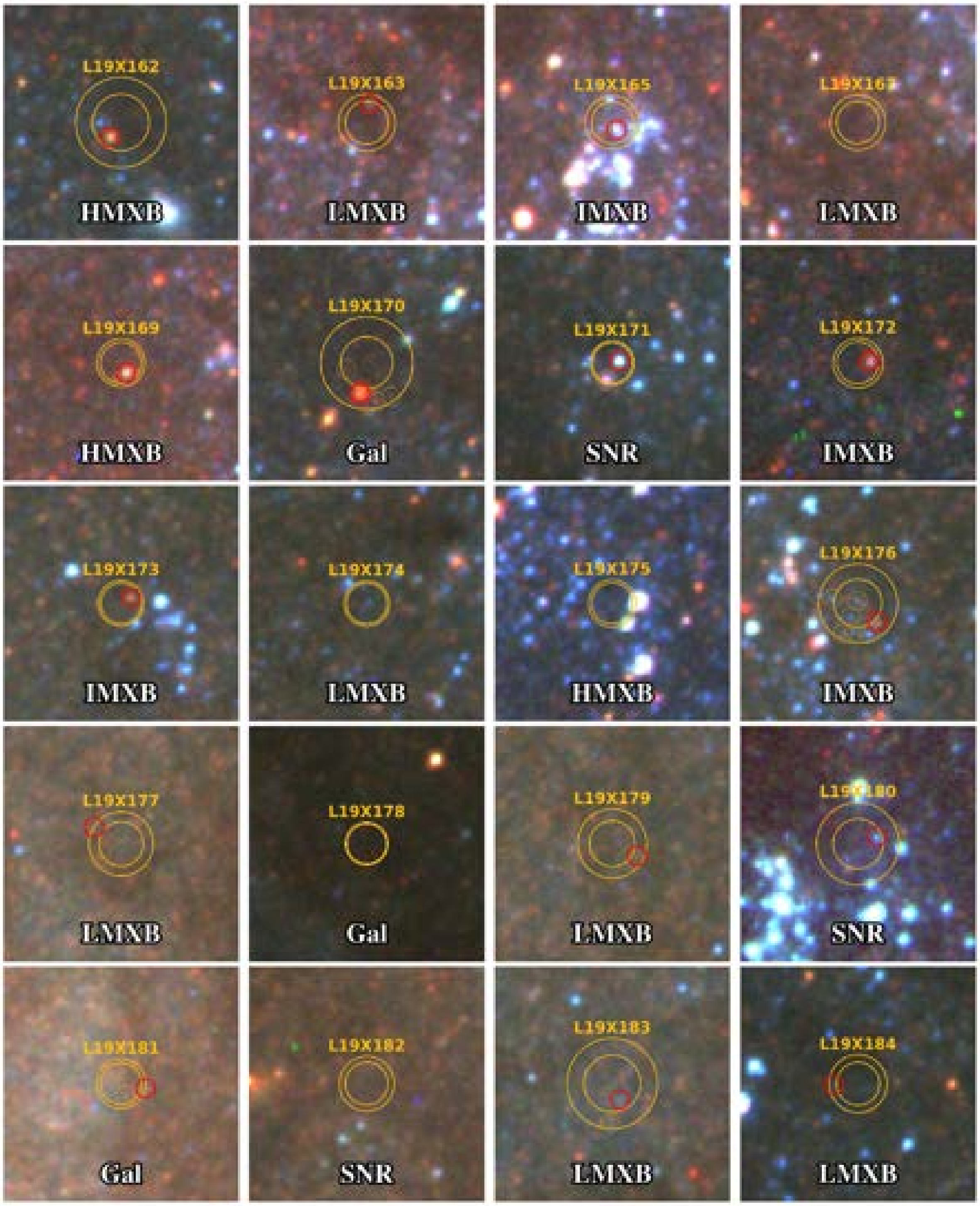

Figure A.1 *(continued)*

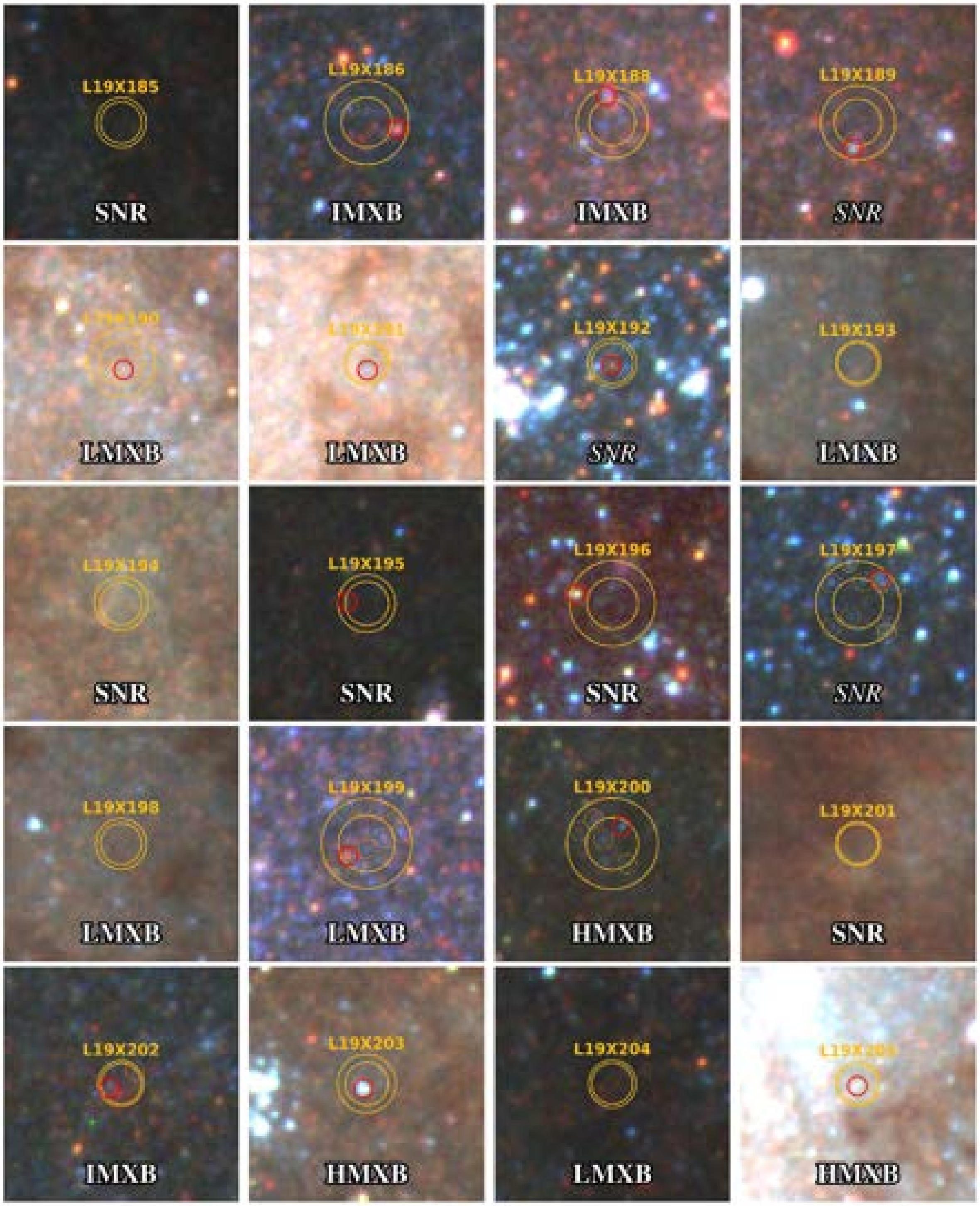

Figure A.1 *(continued)*

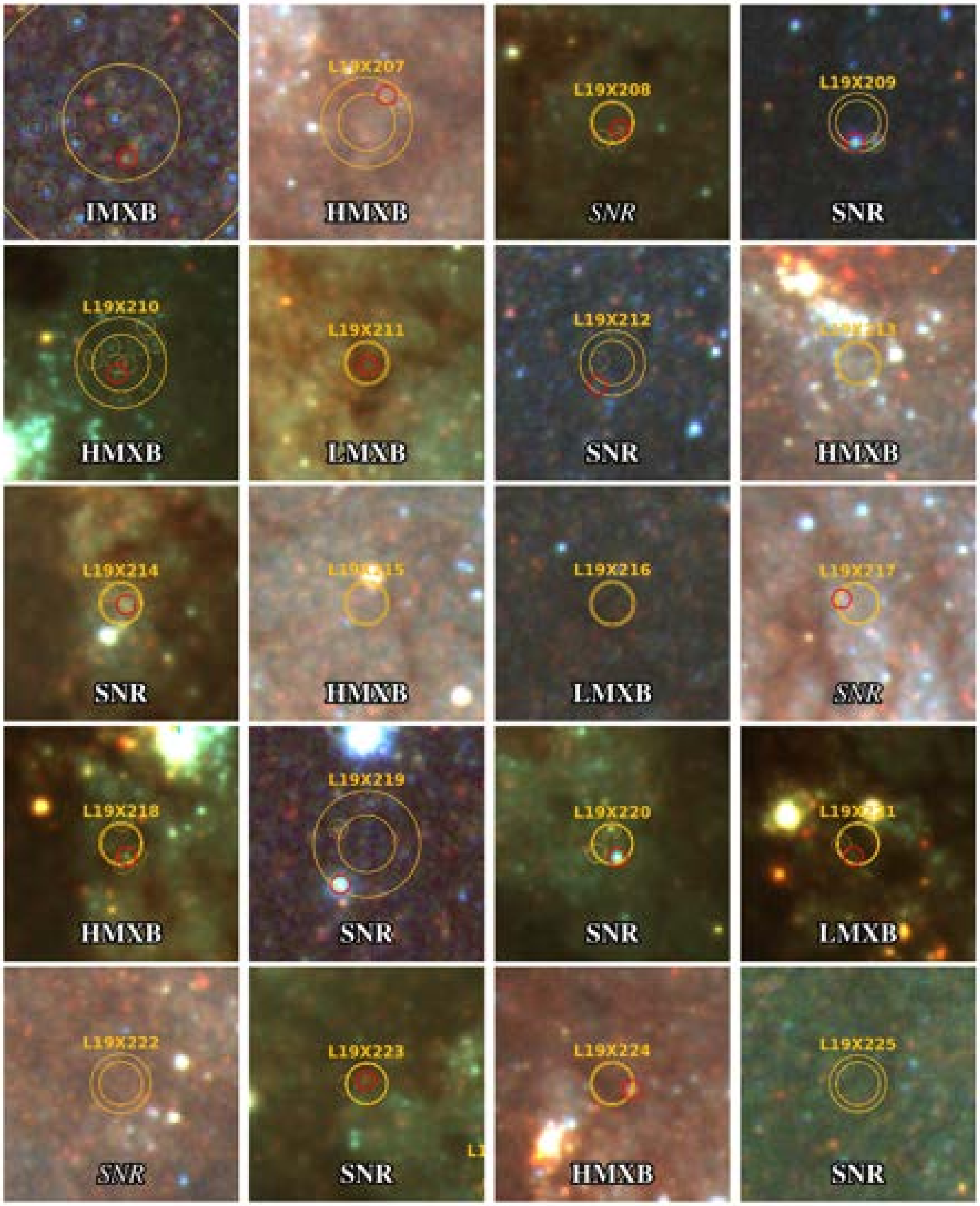

Figure A.1 *(continued)*

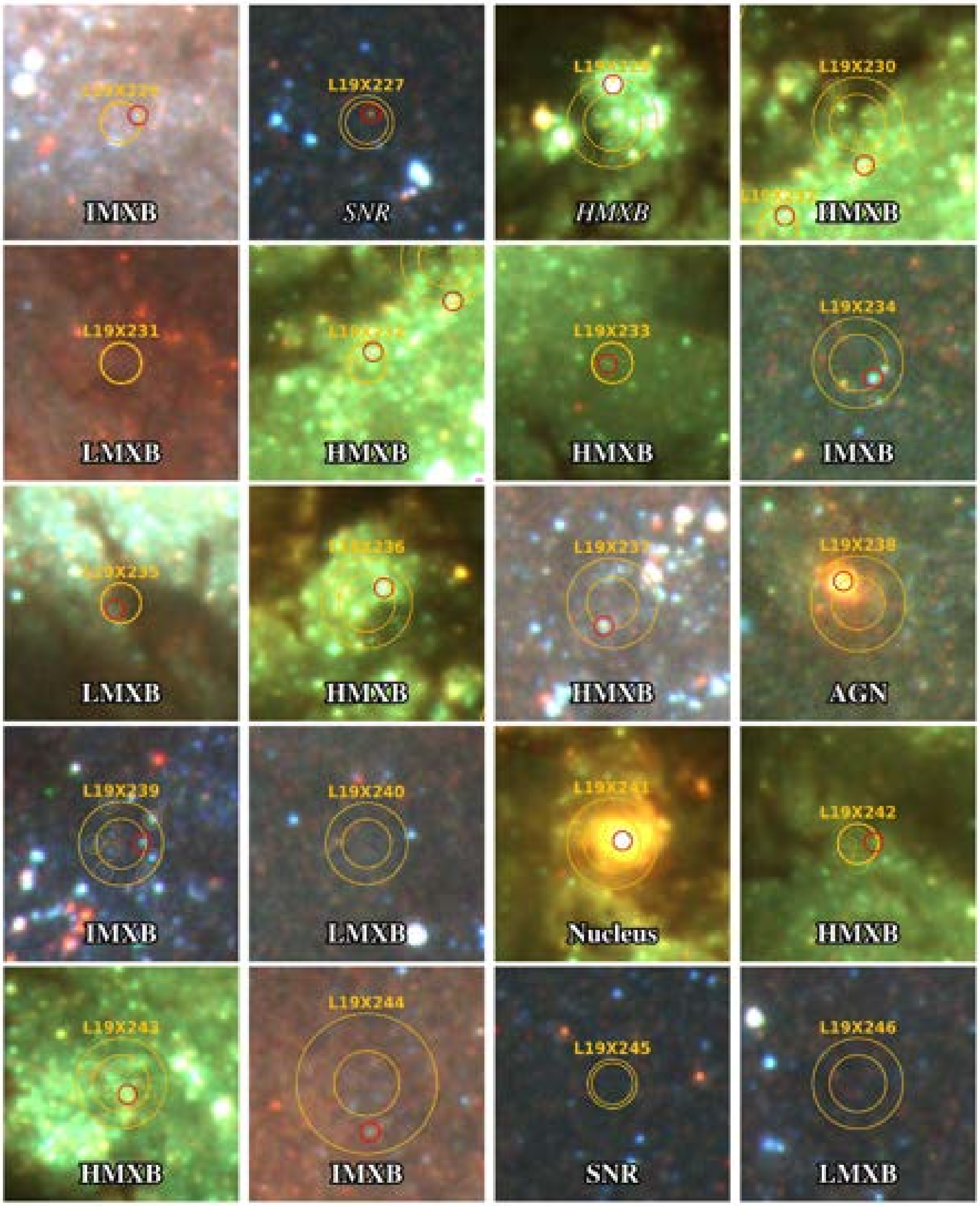

Figure A.1 *(continued)*

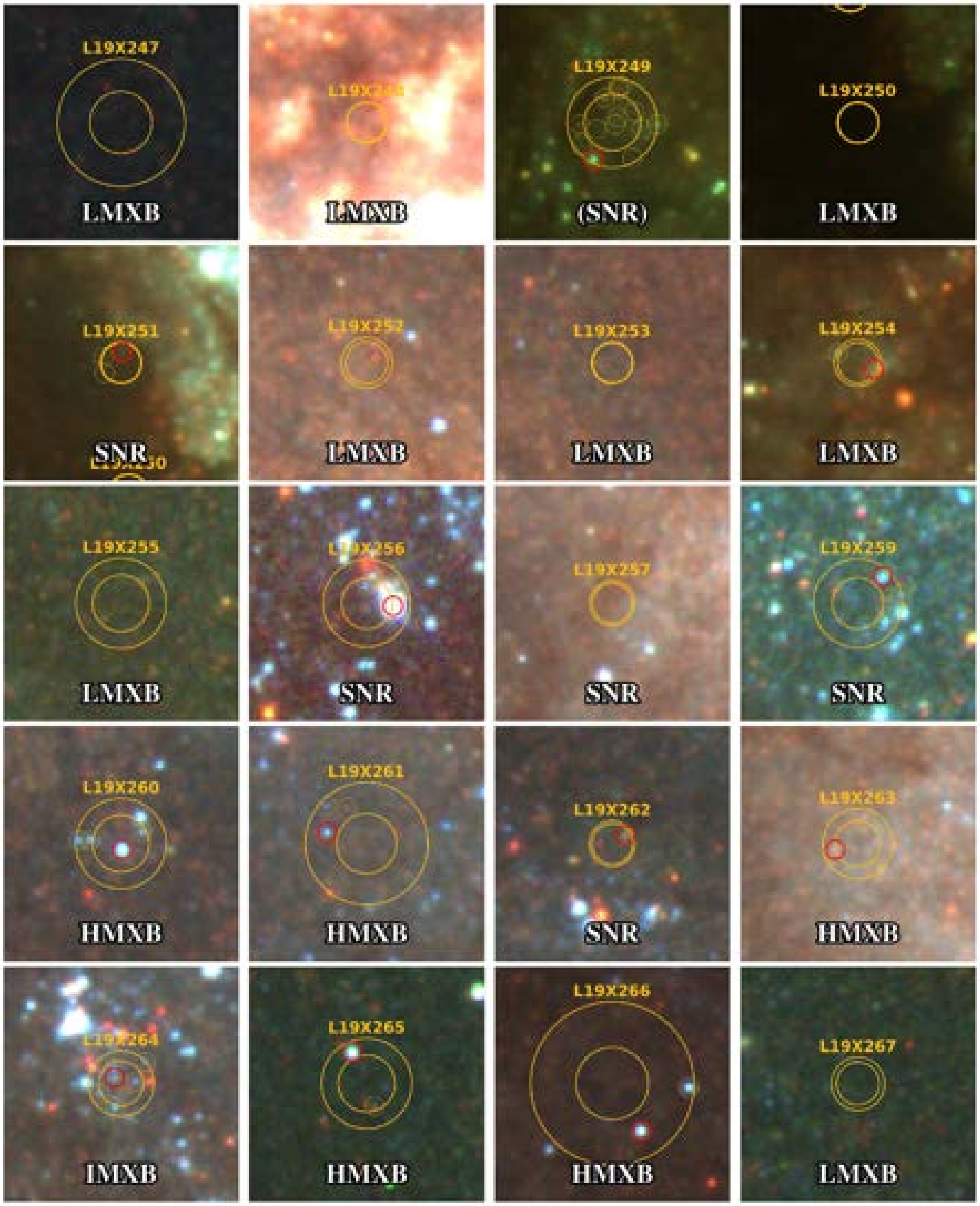

Figure A.1 *(continued)*

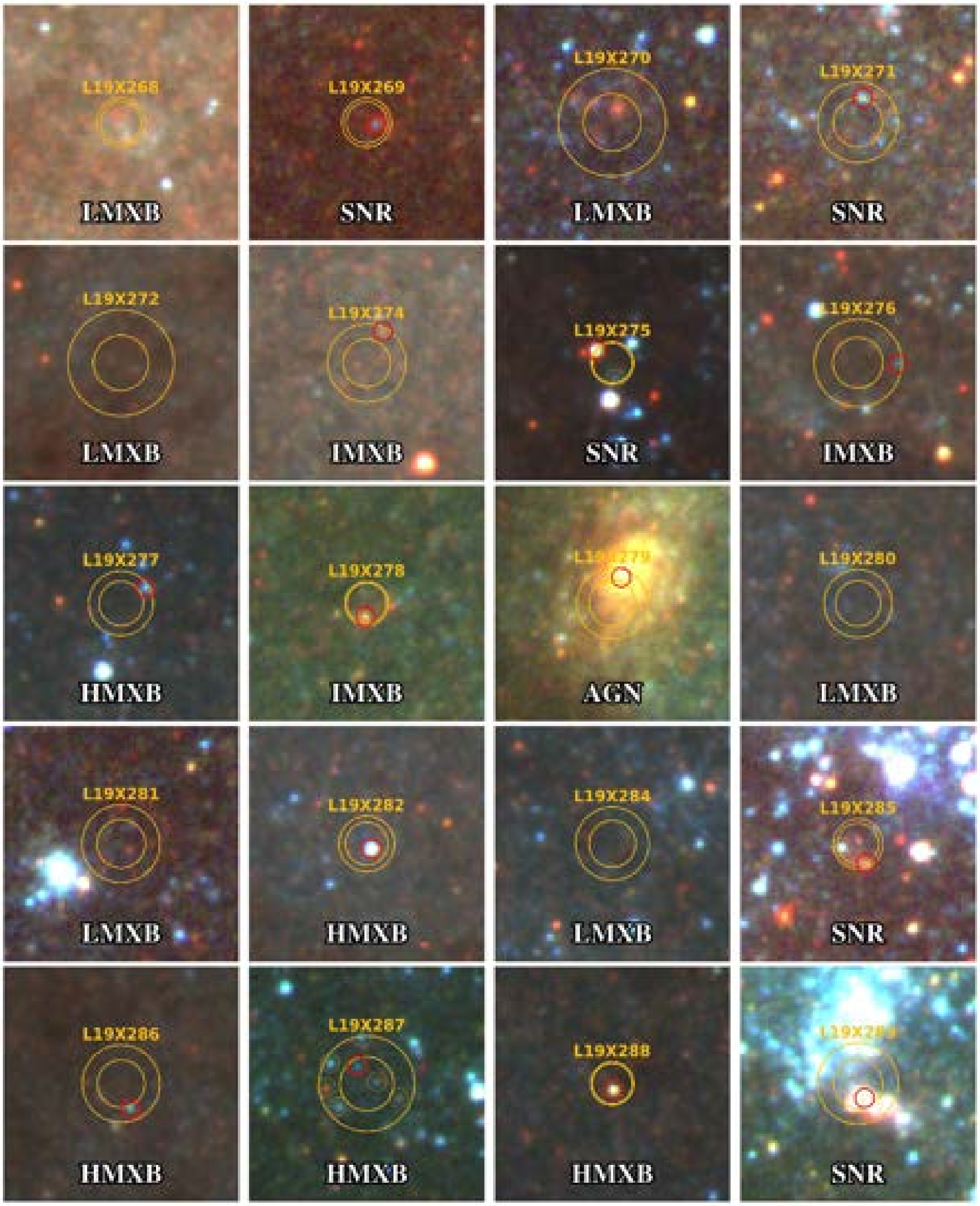

Figure A.1 *(continued)*

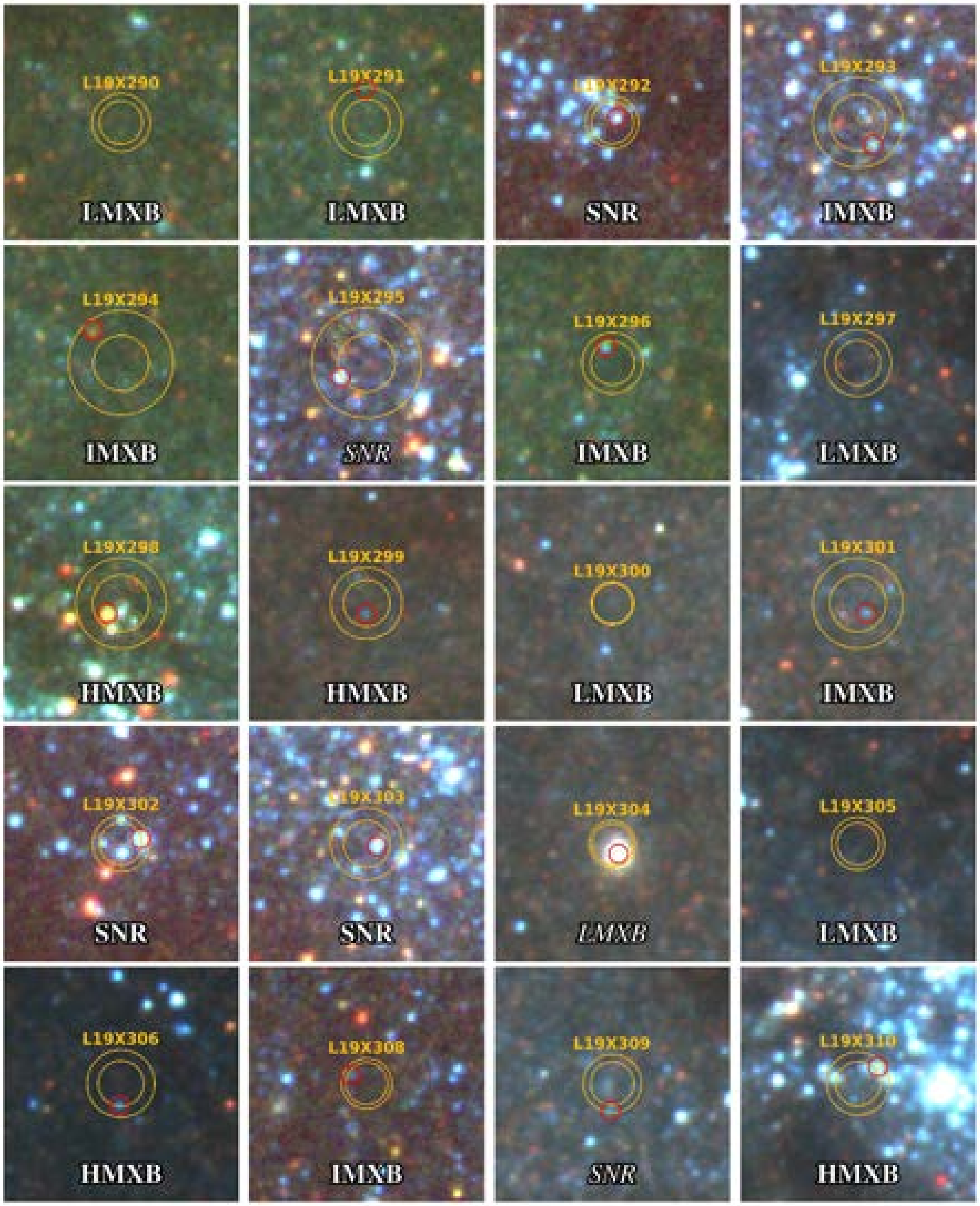

Figure A.1 *(continued)*

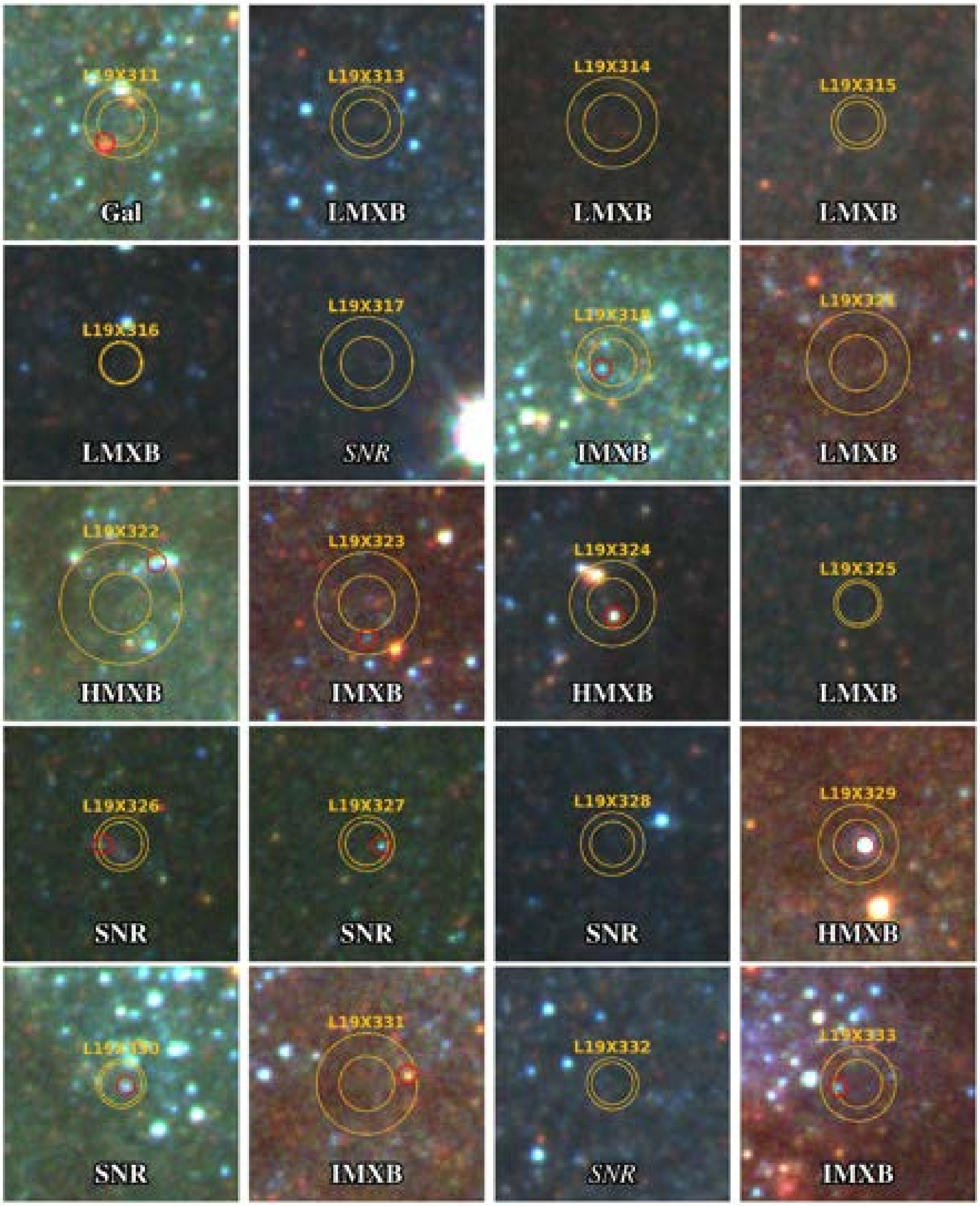

Figure A.1 *(continued)*

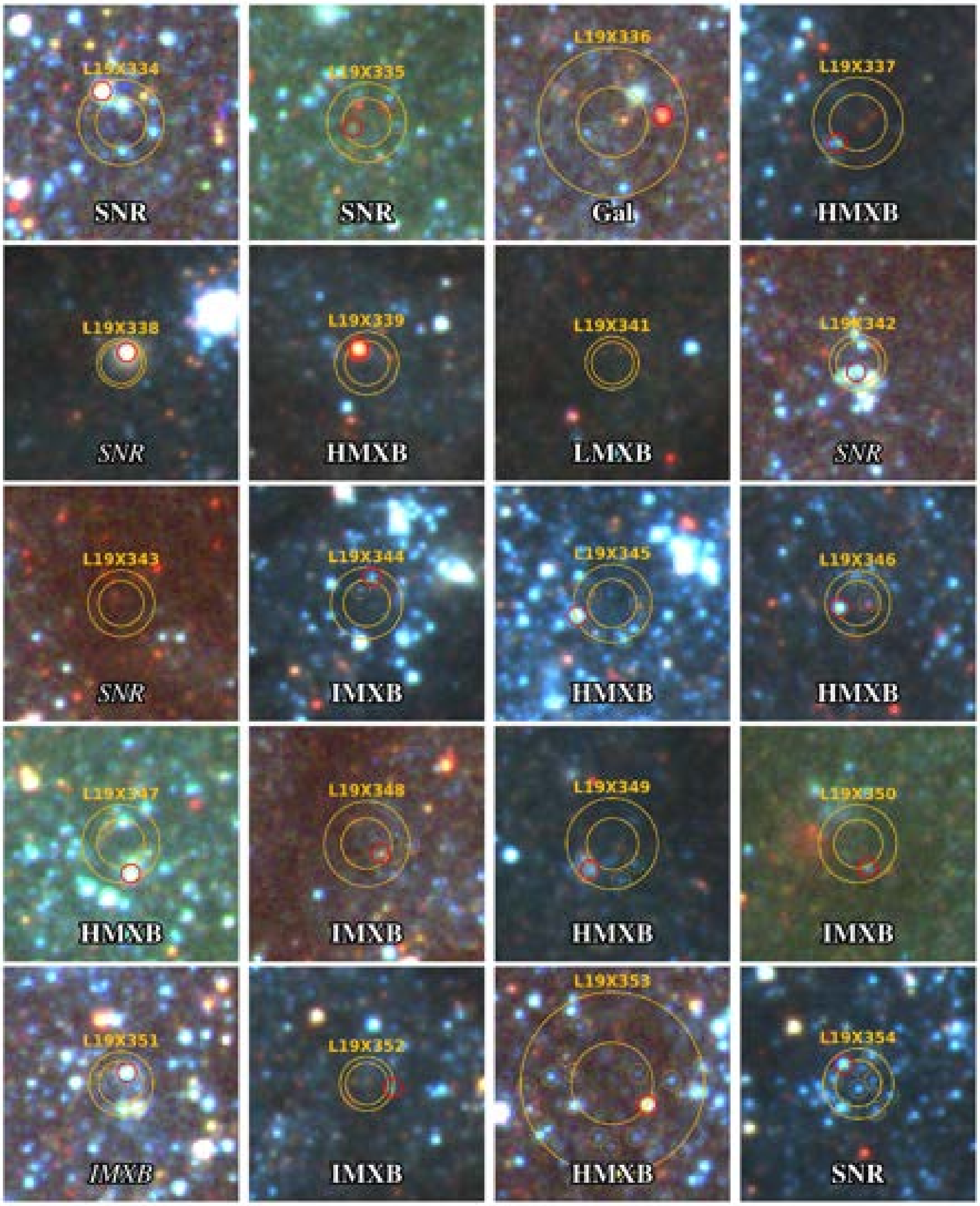

Figure A.1 *(continued)*

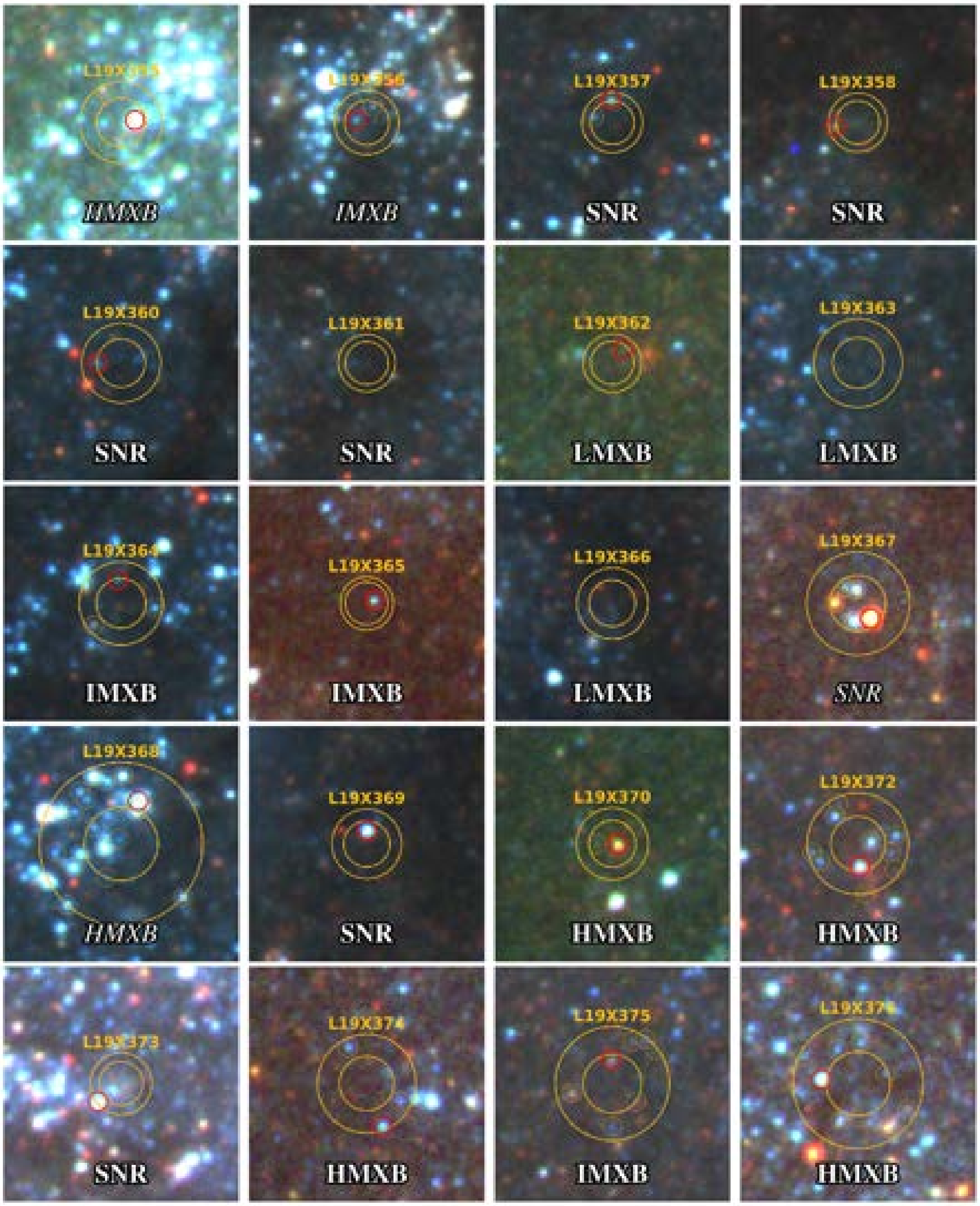

Figure A.1 *(continued)*

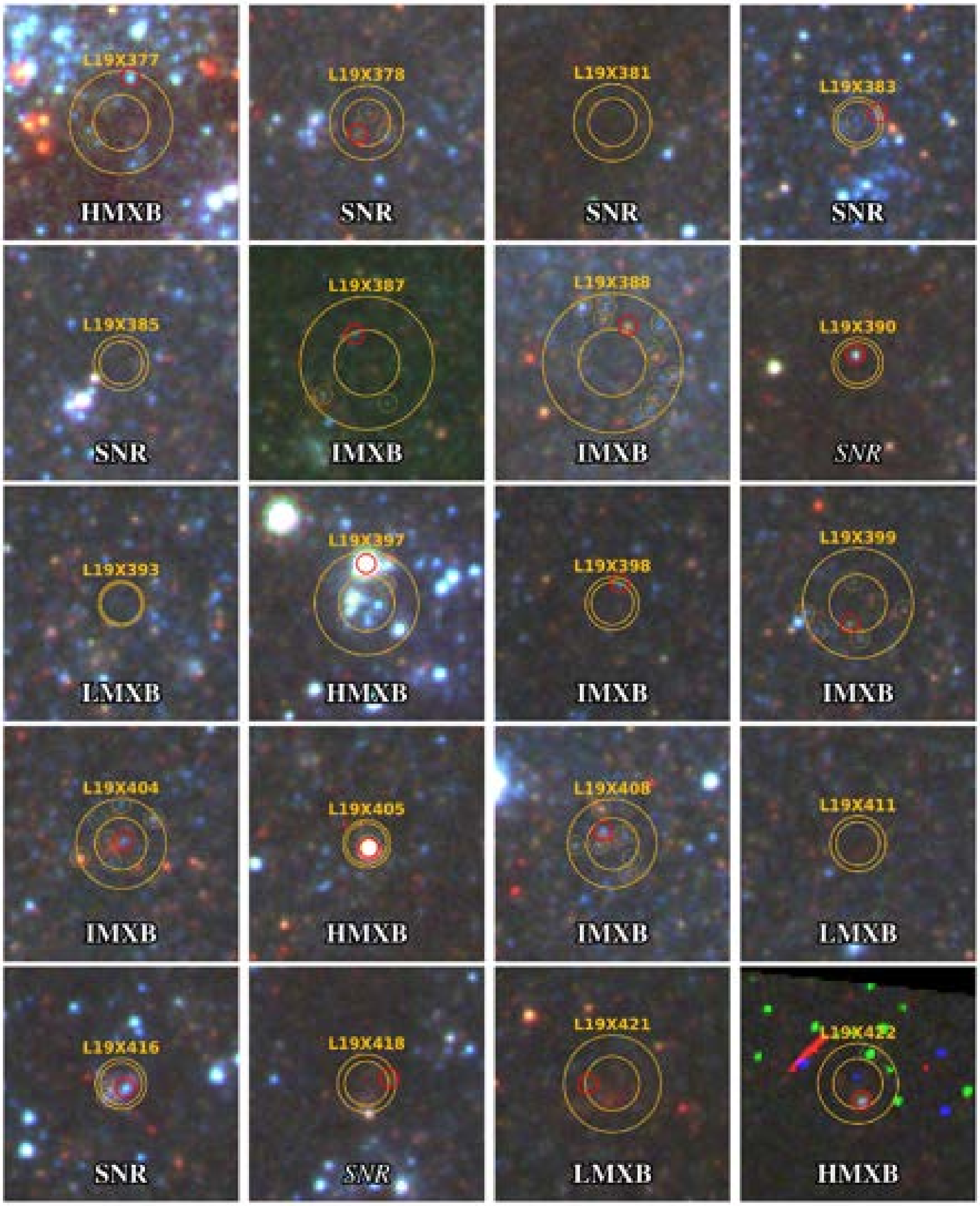

Figure A.1 *(continued)*

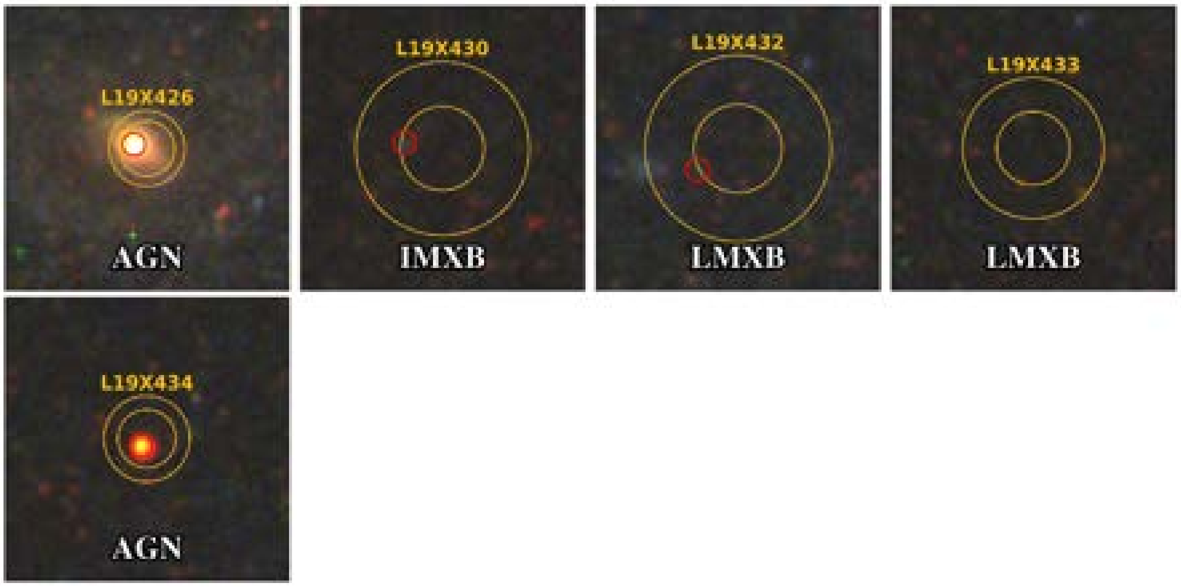

Figure A.1 *(continued)*

APPENDIX B

Single vs. Broken Power-law fits of M83 XRBs

To facilitate a direct comparison with the literature, where the XRB XLFs are typically fit with single or broken power-laws (PLs and BPLs), here I approximate M83's XRB luminosity distribution as follows:

$$N(>L)_{\rm PL} = K_{\rm PL} L^{-(\alpha-1)} \tag{B.1}$$

$$N(>L)_{\rm BPL} = \begin{cases} K_{\rm BP1} L^{-(\alpha_1-1)}, & (L \leq L_{\rm b}) \\ K_{\rm BP2} L^{-(\alpha_2-1)}, & (L > L_{\rm b}) \end{cases} \tag{B.2}$$

where $N(>L)$ is the cumulative XLF, $L_{\rm b}$ is the break luminosity of the broken power-law (BPL), and the K values are normalization constants. I choose to fit cumulative distributions, as they tend to be more sensitive to the presence of a downturn at high luminosities; at the same time, the choice to represent the power-law indices as $(\alpha - 1)$ is meant to facilitate a direct comparison to those studies that adopt a differential, rather than cumulative, form of the XLF. Apart from the break luminosity, which is fixed to $\ell_b = 38.0$ for consistency with L19, all variables are fitted for, using the Python `scipy.curve_fit` function.

I am interested primarily in comparing these fits to the results reported by L19. However, since previous studies do not take into account the SNR contamination to the compact X-ray source population, I also examine the effects of removing (secure and candidate) SNRs to the shape of the XLF. For completeness, I also report the results of fitting the HMXB, LMXB, and IMXB samples separately. Table B and Figure B.1 summarize the results of our fits.

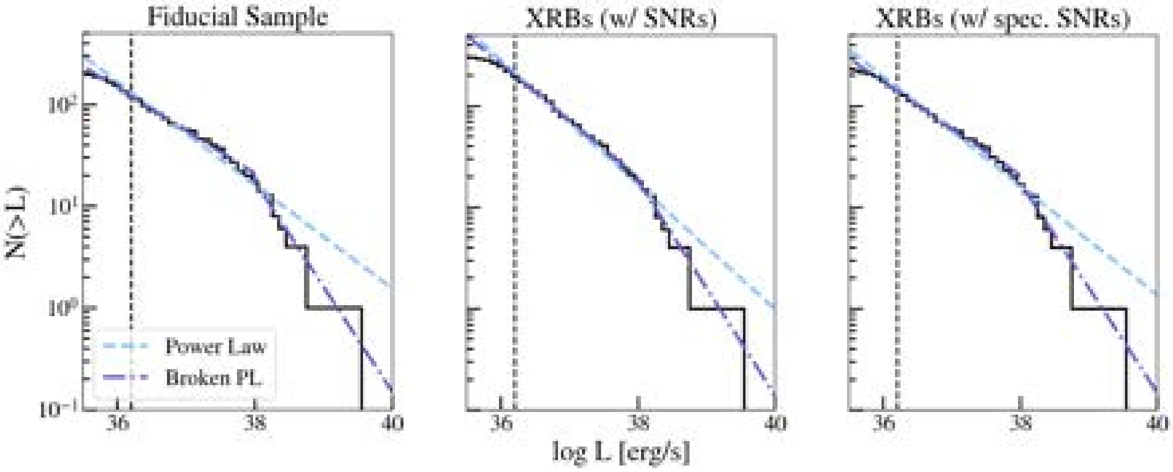

Figure B.1 Single and broken power-law function fits to the composite XRB XLFs in M83 (i.e., the "All XRBs" rows) of the fiducial sample containing all XRBs with luminosities above the 90% completeness limit (left), sources including XRBs and all SNR (center), and sources with only SNRs identified in Long et al. (2014) removed (right). See Table B for the corresponding best-fit parameters.

The "Fiducial Sample" (from the Chapter 2) includes a total 120 sources above the 90% completeness limit of $\ell = 36.2$. This excludes 103 sources identified as SNRs either by Long et al. (2014) (76 in total) or by their X-ray properties (27 additional sources), as described in §2.3.4. For this sample, I find a PL index of 1.51 ± 0.02, and BPL indices of 1.42 ± 0.01 and 2.03 ± 0.07, respectively below and above the break. This is to be compared with the values inferred by L19, i.e., a PL index of $1.56^{+0.05}_{-0.04}$, and BPL indices of $1.47^{+0.06}_{-0.05}$ and $1.93^{+0.22}_{-0.18}$ below and above the break, all of which are formally consistent with our best-fit values, within the errors.

Including the SNRs to the sample ("With SNRs") yields a single PL index 1.61 ± 0.02, whereas the BPL indices are 1.56 ± 0.01 and 2.06 ± 0.07. Not surprisingly, the inclusion of these low-luminosity sources slightly steepens the inferred PL slope, as well as the BPL slope below the break. The X-ray based diagnostics I developed to identify and reject SNR candidates (see §2.3.4) may be too aggressive, in that it may lead to the rejection of faint, X-ray soft XRBs. To fully illustrate the effects of our rejection criteria, I present the results of the fits to a sample in which *only the 76* X-ray sources that were directly identified by Long et al. (2014) are removed ("With spec. SNRs"), while the additional 27 SNR candidates that I reject from the fiducial sample on the

Table B.1. XRB XLF fit parameters

	POWER LAW		BROKEN POWER LAW†			
XLF (1)	$K_{\rm PL}$ (2)	α (3)	$K_{\rm BP1}$ (4)	$K_{\rm BP2}$ (5)	α_1 (6)	α_2 (7)
(a) Fiducial Sample						
All XRBs	60.90 ± 0.86	1.51 ± 0.02	58.45 ± 0.40	79.74 ± 2.70	1.42 ± 0.01	2.03 ± 0.07
HMXBs	57.16 ± 1.03	1.43 ± 0.03	55.51 ± 0.69	96.63 ± 8.90	1.37 ± 0.02	2.50 ± 0.23
IMXBs	57.93 ± 0.90	1.47 ± 0.02	56.36 ± 0.82	85.37 ± 5.05	1.42 ± 0.02	2.21 ± 0.13
LMXBs	60.74 ± 0.51	1.54 ± 0.01	58.73 ± 0.32	57.70 ± 1.67	1.48 ± 0.01	1.47 ± 0.04
(b) With SNRs						
All XRBs	64.57 ± 0.63	1.61 ± 0.02	62.85 ± 0.28	80.67 ± 2.70	1.56 ± 0.01	2.06 ± 0.07
HMXBs	61.39 ± 0.85	1.55 ± 0.02	60.15 ± 0.57	100.52 ± 8.19	1.51 ± 0.02	2.60 ± 0.21
IMXBs	63.33 ± 0.63	1.62 ± 0.02	62.70 ± 0.68	85.37 ± 5.05	1.61 ± 0.02	2.21 ± 0.13
LMXBs	63.52 ± 0.37	1.62 ± 0.01	62.54 ± 0.30	57.70 ± 1.67	1.59 ± 0.01	1.47 ± 0.04
(c) With Spec. SNRs						
All XRBs	61.95 ± 0.79	1.54 ± 0.02	59.68 ± 0.36	79.74 ± 2.70	1.46 ± 0.01	2.03 ± 0.07
HMXBs	58.41 ± 0.95	1.46 ± 0.03	56.84 ± 0.59	96.63 ± 8.90	1.41 ± 0.02	2.50 ± 0.23
IMXBs	59.05 ± 0.90	1.50 ± 0.02	57.56 ± 0.88	85.37 ± 5.05	1.45 ± 0.02	2.21 ± 0.13
LMXBs	61.79 ± 0.45	1.57 ± 0.01	60.22 ± 0.34	57.70 ± 1.67	1.52 ± 0.01	1.47 ± 0.04

Note. — The best-fit parameters inferred by approximating the XLFs with the functional shapes given in Equations B.1 and B.2. †For the broken power-law fits, the break luminosity is fixed at $\ell_b = 38$, to facilitate comparison with Lehmer et al. (2019). Three subsamples are examined: (a) the fiducial sample of XRBs identified in the main Paper; (b) the fiducial sample plus *all* SNRs; and (c) the fiducial sample plus *only* SNRs identified in §2.3.4, with all SNRs identified in Long et al. (2014) removed.

Columns (1)-(10) describe:

(1) the population of XRBs fit by each function; (2) the normalization of the power-law; (3) the index of the power-law;

(4) the normalization of the power-law fit to the XLF below ℓ_b; (5) the normalization of the power-law fit to the XLF above ℓ_b;

(6) the index of the power-law fit to the XLF below ℓ_b; (7) the index of the power-law fit to the XLF above ℓ_b.

basis of the X-ray color are included. However, it should be noted that, in terms of the inferred slopes, all three fits are consistent with the values reported by L19, within 2σ. This suggests that, though strict, our SNR filtering method does not drastically alter the overall shape of the XLF. It does, however, alter the normalization.

APPENDIX C

XRB sample in M81

This appendix contains a table with the properties and classifications of all M81 X-ray sources identified in Lehmer et al. (2019) that fall within the footprint of the HST image, followed by postage stamps of each XRB from HST ACS/WFC imaging.

For each source in the table, the ID is the galaxy name and the ID number assigned in Lehmer et al. (2019). X-ray luminosities are in units log erg s^{-1}, and magnitudes are absolute mags estimated at a distance of 3.63 Mpc. The classification for each source is given, with (SNR) representing SNRs identified using our HR–L_X criterion, and italics indicating XRBs associated with clusters. A confidence flag (CF) is assigned to each source based on the "strength" of the identification of the X-ray emitter: a CF of 1 represents the most certain classifications (i.e. those determined in other studies, or XRBs with a clear donor, with multiple candidates of similar mass, or a clear absence of a donor); CF ratings of 2 or 3 may indicate that a source is in a dust-obscured region, such as near the nucleus or along a dust lane, since the presence of heavy dust could potentially mask high-mass stars, background galaxies, and clusters, leading to possible misidentifications.

Table C.1. Properties and Classifications of M81 X-ray Sources

ID	CSC ID (2CXO)	R.A.	Dec	L_X	V	B-V	V-I	Class	CF
M81X003	—	148.579	69.07	36.5	-2.393	—	1.199	LM	1
M81X006	J095422.6+690346	148.595	69.063	37.1	-0.552	—	2.552	LM	1
M81X007	—	148.618	69.099	36.6	-4.616	0.382	0.694	Gal	1
M81X008	J095431.1+690506	148.629	69.085	36.6	-1.636	—	1.497	LM	1
M81X009	J095434.5+690452	148.644	69.081	36.7	-5.612	1.194	1.045	(SNR)	1
M81X010	J095436.0+690856	148.651	69.149	37.0	-2.934	—	1.389	(SNR)	1
M81X011	—	148.654	69.078	36.4	-8.706	1.875	0.520	Star	1
M81X013	—	148.669	69.038	36.2	-4.473	2.054	0.976	HM	1
M81X014	J095440.8+690548	148.67	69.097	36.4	-3.081	1.997	1.263	LM	2
M81X015	J095442.0+690244	148.675	69.046	37.0	-1.591	—	1.552	LM	1
M81X016	J095444.3+690454	148.685	69.082	37.0	-2.633	—	1.636	LM	1
M81X018	J095446.4+690513	148.694	69.087	37.0	-2.5	—	1.650	LM	1
M81X019	J095446.7+691123	148.695	69.19	37.1	-2.169	—	1.135	LM	1
M81X020	J095447.2+690101	148.697	69.017	36.8	-2.712	1.421	2.017	LM	1
M81X021	J095447.4+690322	148.698	69.056	36.2	-8.6	-0.009	0.658	*HM*	1
M81X022	J095449.2+690538	148.705	69.094	36.5	-5.155	0.362	0.365	HM	1
M81X023	—	148.708	69.194	37.2	-3.142	—	1.816	IM	1
M81X024	J095452.0+690455	148.717	69.082	36.4	-3.703	—	1.954	IM	1
M81X025	J095455.0+690419	148.73	69.072	36.2	-3.349	—	1.826	IM	1
M81X026	J095455.8+690517	148.733	69.088	36.3	-4.379	0.423	0.256	(SNR)	1
M81X027	—	148.738	69.149	36.5	-5.269	-0.067	-0.168	HM	1
M81X028	J095457.6+690241	148.74	69.045	37.5	-3.578	—	0.281	IM	1
M81X029	J095458.4+685922	148.744	68.99	36.2	-2.986	0.158	0.169	IM	1
M81X030	J095458.8+690521	148.745	69.089	36.1	—	—	—	LM	1
M81X031	J095458.8+690438	148.745	69.077	36.5	—	—	—	LM	1
M81X032	J095459.8+685817	148.75	68.972	36.2	-5.095	0.268	0.101	HM	1
M81X033	J095500.0+690745	148.75	69.129	38.3	-2.514	2.16	—	LM	1
M81X034	J095500.1+690437	148.751	69.077	36.5	—	—	—	LM	1
M81X035	J095500.3+690148	148.752	69.03	37.1	-4.37	0.841	1.937	Gal	1
M81X036	J095501.0+690726	148.754	69.124	38.3	-3.293	—	2.512	Gal	1
M81X037	J095501.0+685622	148.754	68.939	37.5	—	—	—	Star	1

Table C.1 (cont'd)

ID	CSC ID (2CXO)	R.A.	Dec	L_X	V	B-V	V-I	Class	CF
M81X038	J095501.7+691040	148.757	69.178	37.3	-6.276	0.685	0.157	HM	1
M81X039	J095502.6+685621	148.761	68.939	37.2	—	—	—	Star	1
M81X040	J095505.6+685852	148.774	68.981	36.8	-4.358	1.842	0.942	HM	1
M81X041	J095506.3+690405	148.777	69.068	36.8	—	—	—	LM	2
M81X042	J095507.2+690314	148.78	69.054	35.9	-4.06	0.939	1.029	SNR	1
M81X043	J095507.5+690713	148.781	69.12	35.9	-7.397	0.206	0.266	*IM*	1
M81X044	J095508.8+685722	148.787	68.956	36.9	—	—	—	Star	1
M81X045	—	148.79	69.071	35.8	—	—	—	SNR	1
M81X046	J095509.6+690743	148.79	69.129	37.4	-4.855	1.267	0.819	HM	1
M81X047	J095509.7+690407	148.791	69.069	37.1	-10.368	0.94	0.526	*LM*	1
M81X048	J095509.6+690832	148.791	69.142	37.2	-5.145	1.008	0.920	HM	2
M81X049	J095510.2+690502	148.793	69.084	38.5	-3.411	—	1.713	LM	2
M81X050	—	148.793	68.99	35.6	-4.884	0.058	0.011	HM	1
M81X051	J095510.6+690843	148.795	69.145	37.3	-5.372	0.515	0.411	HM	1
M81X052	J095511.8+685748	148.799	68.963	36.9	-1.538	—	2.194	LM	1
M81X053	J095512.2+690344	148.801	69.062	36.2	—	—	—	LM	2
M81X054	J095512.4+690411	148.802	69.07	35.9	-2.529	—	2.212	LM	1
M81X055	J095512.4+690121	148.802	69.023	36.7	—	—	—	LM	1
M81X056	J095512.6+690141	148.803	69.028	36.0	-6.722	0.408	0.252	Gal	1
M81X057	J095514.1+690740	148.809	69.128	36.3	-4.388	0.216	0.282	IM	1
M81X058	J095514.5+690641	148.811	69.111	36.4	-3.462	0.625	0.799	IM	1
M81X059	J095515.2+690230	148.813	69.042	36.6	-2.752	—	1.415	LM	1
M81X060	J095515.2+690537	148.814	69.094	36.5	—	—	—	LM	2
M81X061	J095516.6+690512	148.819	69.087	36.4	—	—	—	LM	2
M81X062	J095518.0+685820	148.825	68.972	36.0	-2.277	—	1.801	LM	1
M81X063	J095518.2+685930	148.826	68.992	36.4	-5.193	0.615	0.860	HM	1
M81X064	J095519.6+690732	148.832	69.126	36.3	-4.12	0.65	0.799	SNR	1
M81X065	J095519.9+690351	148.833	69.064	36.5	—	—	—	LM	2
M81X066	J095521.0+690313	148.838	69.054	36.1	—	—	—	LM	2
M81X067	J095521.1+685855	148.838	68.982	36.4	-2.802	—	1.394	LM	1
M81X068	J095521.4+690831	148.84	69.142	36.6	-5.571	1.543	0.924	SNR	1

Table C.1 (cont'd)

ID	CSC ID (2CXO)	R.A.	Dec	L_X	V	B-V	V-I	Class	CF
M81X069	J095521.7+690345	148.841	69.062	36.6	—	—	—	LM	2
M81X070	J095521.8+690522	148.841	69.09	37.4	—	—	—	LM	2
M81X071	J095521.8+690637	148.841	69.11	37.7	-10.613	0.92	0.864	*LM*	1
M81X072	J095521.9+690228	148.842	69.041	36.0	-3.296	—	1.397	LM	2
M81X073	J095522.0+690518	148.842	69.089	36.7	-9.921	1.234	0.775	*LM*	1
M81X074	J095522.1+690510	148.842	69.086	38.2	—	—	—	LM	2
M81X075	J095522.7+690237	148.845	69.044	35.8	-3.98	—	1.438	IM	2
M81X076	J095523.7+685849	148.849	68.98	37.2	-2.347	—	2.225	LM	1
M81X077	J095524.2+690957	148.851	69.166	38.8	-2.534	—	1.242	LM	1
M81X078	J095524.2+690439	148.851	69.078	36.7	—	—	—	LM	2
M81X079	J095524.7+690113	148.853	69.02	38.2	-7.485	1.003	0.601	HM	1
M81X080	J095525.6+690458	148.857	69.083	36.1	—	—	—	(SNR)	2
M81X081	—	148.86	69.067	36.6	—	—	—	LM	2
M81X082	J095526.6+690523	148.861	69.09	36.2	—	—	—	LM	2
M81X083	J095526.9+690541	148.863	69.095	36.5	—	—	—	LM	3
M81X084	J095527.2+690247	148.864	69.047	37.3	—	—	—	LM	2
M81X085	J095527.2+690250	148.864	69.047	36.3	—	—	—	LM	3
M81X086	J095527.5+690631	148.865	69.109	36.0	-1.982	—	2.010	LM	2
M81X087	J095527.7+690704	148.866	69.118	36.3	-3.491	-0.087	0.323	IM	1
M81X088	J095527.7+690400	148.866	69.067	37.1	—	—	—	LM	2
M81X089	J095528.2+690541	148.867	69.095	35.9	—	—	—	LM	2
M81X090	J095528.4+690244	148.869	69.046	36.7	—	—	—	(SNR)	2
M81X091	J095528.8+690613	148.87	69.104	37.2	-2.861	—	0.422	LM	2
M81X092	J095529.1+690320	148.871	69.056	36.8	—	—	—	LM	2
M81X093	—	148.873	69.047	35.8	—	—	—	LM	2
M81X094	J095530.1+690318	148.876	69.055	36.9	—	—	—	LM	2
M81X095	J095530.2+690246	148.876	69.046	36.5	—	—	—	LM	2
M81X096	J095530.3+690039	148.877	69.011	35.9	-2.849	—	1.372	IM	1
M81X097	—	148.877	69.071	36.5	—	—	—	LM	2
M81X098	—	148.878	69.062	35.9	—	—	—	LM	2
M81X099	—	148.878	69.062	36.2	—	—	—	LM	2

Table C.1 (cont'd)

ID	CSC ID (2CXO)	R.A.	Dec	L_X	V	B-V	V-I	Class	CF
M81X100	J095531.0+690055	148.879	69.015	35.8	-4.512	0.092	0.006	(SNR)	1
M81X101	J095531.1+690144	148.88	69.029	35.9	-4.377	—	1.695	Gal	1
M81X102	J095531.2+690418	148.881	69.072	37.6	—	—	—	LM	2
M81X103	—	148.885	69.069	36.3	—	—	—	LM	2
M81X104	J095532.6+690231	148.886	69.042	37.1	-3.244	—	2.022	IM	1
M81X105	J095532.6+690352	148.886	69.065	37.8	—	—	—	LM	2
M81X106	J095532.6+690513	148.886	69.087	36.3	—	—	—	(SNR)	2
M81X107	—	148.886	69.073	36.1	—	—	—	LM	2
M81X108	J095532.8+690639	148.887	69.111	35.9	-9.241	1.173	0.874	*LM*	1
M81X110	J095532.9+690033	148.887	69.009	39.2	-4.326	0.066	-0.025	IM	1
M81X111	—	148.888	69.067	36.9	—	—	—	LM	2
M81X112	—	148.888	69.068	36.8	—	—	—	LM	2
M81X113	J095533.1+690354	148.888	69.065	39.4	—	—	—	Nucleus	1
M81X117	J095533.7+690124	148.891	69.023	36.3	—	—	—	LM	1
M81X118	—	148.892	69.065	36.8	—	—	—	LM	2
M81X119	J095534.0+690713	148.892	69.12	37.1	-6.572	0.297	0.267	HM	1
M81X120	J095534.1+690618	148.892	69.105	35.9	-3.622	0.695	0.146	IM	1
M81X121	J095534.3+690350	148.893	69.064	37.5	—	—	—	LM	2
M81X122	—	148.893	69.063	37.0	—	—	—	LM	2
M81X123	—	148.894	69.061	36.6	-8.698	1.319	0.983	*LM*	1
M81X124	J095534.5+690250	148.894	69.047	37.4	—	—	—	LM	2
M81X125	J095534.6+690453	148.894	69.082	37.5	—	—	—	LM	2
M81X126	J095534.7+690351	148.895	69.064	37.8	—	—	—	LM	2
M81X127	J095534.8+690408	148.895	69.069	37.5	—	—	—	LM	2
M81X128	J095534.9+690342	148.896	69.062	38.2	—	—	—	LM	2
M81X129	J095535.2+690316	148.897	69.054	37.8	—	—	—	LM	2
M81X130	J095535.3+690352	148.897	69.065	37.7	—	—	—	LM	2
M81X131	J095535.3+690638	148.898	69.111	37.2	-4.819	0.88	1.699	HM	1
M81X132	J095535.4+690557	148.898	69.099	36.8	—	—	—	LM	2
M81X133	J095536.2+690245	148.901	69.046	36.5	—	—	—	(SNR)	2
M81X134	J095536.6+690632	148.903	69.109	37.2	-7.988	1.351	1.010	*LM*	1

Table C.1 (cont'd)

ID	CSC ID (2CXO)	R.A.	Dec	L_X	V	B-V	V-I	Class	CF
M81X135	J095536.9+685656	148.904	68.949	36.9	-2.325	0.508	1.195	LM	1
M81X136	J095536.9+690439	148.904	69.078	37.0	—	—	—	LM	2
M81X137	J095536.9+690433	148.904	69.076	37.5	—	—	—	LM	2
M81X138	J095537.2+690207	148.905	69.035	36.1	-9.593	1.304	1.006	*LM*	1
M81X139	J095537.5+690457	148.907	69.083	36.9	—	—	—	LM	2
M81X140	J095537.6+685833	148.907	68.976	36.6	-4.106	0.853	0.945	HM	1
M81X141	J095537.7+690327	148.907	69.058	36.1	-9.272	1.016	0.758	*LM*	1
M81X142	—	148.91	68.943	36.5	-2.544	—	1.228	LM	2
M81X143	J095538.9+690423	148.912	69.073	36.4	—	—	—	LM	2
M81X144	J095539.9+690348	148.916	69.064	36.5	—	—	—	LM	2
M81X145	J095540.3+690314	148.918	69.054	36.4	—	—	—	LM	2
M81X146	J095540.6+690105	148.92	69.018	36.1	—	—	—	LM	3
M81X147	J095540.7+690258	148.92	69.05	36.1	—	—	—	LM	2
M81X148	J095541.8+690301	148.925	69.051	35.9	—	—	—	LM	2
M81X149	J095541.9+690504	148.925	69.085	36.2	—	—	—	LM	3
M81X150	J095542.1+690336	148.926	69.06	38.0	-6.606	0.307	0.364	HM	1
M81X151	—	148.926	69.116	36.2	-2.067	—	1.567	SNR	1
M81X152	J095542.5+690320	148.927	69.056	37.1	—	—	—	LM	2
M81X153	J095542.5+691127	148.928	69.191	36.8	-4.71	1.782	0.899	(SNR)	1
M81X154	J095542.9+690522	148.929	69.09	36.0	—	—	—	LM	1
M81X155	J095543.1+690445	148.93	69.079	36.6	—	—	—	LM	2
M81X156	J095543.2+690423	148.93	69.073	36.5	—	—	—	LM	2
M81X157	J095543.5+690355	148.932	69.065	36.3	—	—	—	LM	2
M81X158	J095543.8+690551	148.932	69.098	36.5	-4.485	2.117	1.364	IM	1
M81X159	J095543.7+685905	148.932	68.985	37.4	—	—	—	LM	1
M81X160	J095544.5+690534	148.936	69.093	36.8	-5.657	0.723	1.113	HM	1
M81X161	J095544.6+691003	148.936	69.168	36.9	-6.616	0.128	0.049	HM	1
M81X162	J095545.3+690253	148.939	69.048	36.1	-4.253	0.58	0.838	(SNR)	3
M81X163	—	148.939	69.038	35.9	—	—	—	Gal	1
M81X164	J095545.8+690300	148.941	69.05	37.4	-10.078	1.154	0.829	*LM*	1
M81X165	J095547.0+690551	148.946	69.098	37.9	-9.11	1.519	1.164	*LM*	1

Table C.1 (cont'd)

ID	CSC ID (2CXO)	R.A.	Dec	L_X	V	B-V	V-I	Class	CF
M81X166	J095546.9+690536	148.946	69.093	36.3	-3.238	—	1.865	IM	1
M81X167	J095547.9+685928	148.95	68.991	36.3	-5.454	0.433	0.016	SNR	1
M81X168	J095548.2+685915	148.951	68.988	36.4	-3.217	—	1.696	IM	2
M81X169	J095548.7+690140	148.953	69.028	36.2	-2.954	—	2.318	IM	2
M81X170	J095549.3+685836	148.956	68.977	37.6	-6.873	0.694	0.438	HM	1
M81X171	J095549.4+690811	148.956	69.137	38.0	-2.223	—	1.808	LM	1
M81X172	J095549.7+690531	148.958	69.092	38.7	-7.053	1.218	0.915	*LM*	1
M81X173	J095549.8+690300	148.958	69.05	36.1	-3.744	—	0.797	IM	2
M81X174	J095550.0+690714	148.959	69.121	36.5	-5.162	0.162	0.104	HM	2
M81X175	J095550.1+690540	148.959	69.095	36.3	—	—	—	LM	1
M81X176	J095550.5+685832	148.961	68.976	36.7	-2.688	—	1.234	LM	1
M81X177	J095551.0+690512	148.963	69.087	36.4	—	—	—	(SNR)	2
M81X178	J095551.5+691104	148.964	69.185	36.7	-2.902	2.969	1.241	IM	1
M81X179	J095551.5+685910	148.965	68.986	36.0	-5.353	0.356	0.416	HM	2
M81X180	J095551.8+690739	148.966	69.128	36.7	-9.302	1.285	0.951	*LM*	1
M81X181	J095552.4+685625	148.968	68.94	36.5	-2.508	-2.176	2.398	IM	1
M81X182	J095552.4+690306	148.969	69.052	38.2	—	—	—	LM	2
M81X183	J095553.1+685926	148.971	68.991	37.8	-3.545	-0.28	-0.302	HM	1
M81X184	J095553.2+690207	148.972	69.035	36.9	-5.731	1.087	1.019	HM	1
M81X185	J095553.3+690446	148.972	69.08	36.1	-4.86	1.256	0.993	(SNR)	1
M81X186	J095553.6+690434	148.973	69.076	37.1	—	—	—	LM	1
M81X187	J095554.2+690346	148.976	69.063	36.3	—	—	—	(SNR)	1
M81X188	J095554.9+690055	148.979	69.016	37.5	-9.38	1.376	1.098	*LM*	1
M81X189	J095554.9+690239	148.979	69.044	36.9	-5.432	1.408	1.348	Gal	2
M81X190	J095555.5+691007	148.981	69.169	36.7	-4.442	0.875	0.815	HM	1
M81X191	J095555.3+685859	148.981	68.983	36.1	-4.784	0.355	0.353	(SNR)	2
M81X192	J095555.6+690814	148.982	69.137	36.9	-2.299	—	1.085	LM	1
M81X193	J095555.7+690901	148.982	69.15	36.4	-3.554	0.545	0.422	IM	1
M81X194	J095555.9+690515	148.983	69.088	36.3	-2.578	—	1.946	LM	2
M81X195	J095556.0+690358	148.984	69.066	36.1	—	—	—	(SNR)	2
M81X196	J095556.0+690312	148.984	69.053	36.6	—	—	—	(SNR)	1

Table C.1 (cont'd)

ID	CSC ID (2CXO)	R.A.	Dec	L_X	V	B-V	V-I	Class	CF
M81X197	J095556.5+690802	148.986	69.134	37.8	-5.53	1.17	1.417	*LM*	2
M81X198	J095557.6+690436	148.99	69.077	37.8	-4.561	0.024	—	IM	1
M81X199	J095558.5+690525	148.994	69.091	37.6	—	—	—	LM	1
M81X200	J095559.1+690617	148.997	69.105	37.2	-3.48	—	1.190	IM	1
M81X201	—	149.0	69.093	36.2	-6.115	2.352	1.376	Gal	1
M81X202	J095600.1+690418	149.001	69.072	36.5	-3.374	-0.105	—	(SNR)	1
M81X203	—	149.001	69.021	35.6	-4.979	2.101	1.158	HM	2
M81X204	—	149.007	69.005	35.8	-5.234	-0.184	0.055	HM	1
M81X205	J095601.9+685859	149.008	68.983	37.0	-6.296	0.283	0.324	HM	1
M81X206	J095602.6+685935	149.011	68.993	37.6	-4.437	0.137	0.810	HM	2
M81X207	J095602.7+685844	149.011	68.979	37.1	-5.699	1.976	-0.487	HM	1
M81X208	J095602.6+690547	149.011	69.096	36.6	-2.912	—	1.610	IM	1
M81X209	J095602.9+690217	149.013	69.038	36.7	-3.485	1.138	1.664	IM	2
M81X210	J095603.2+690107	149.013	69.019	36.4	-1.603	—	2.348	LM	1
M81X211	—	149.014	69.001	36.2	-6.076	0.629	0.506	HM	1
M81X212	J095604.0+690726	149.017	69.124	36.3	-2.56	—	2.097	LM	1
M81X213	J095604.8+690344	149.02	69.062	36.3	-8.314	0.044	0.120	(SNR)	1
M81X214	J095604.7+685840	149.02	68.978	36.9	-3.822	3.515	1.616	IM	1
M81X215	—	149.023	69.112	36.2	-8.904	1.192	0.918	*LM*	1
M81X216	J095606.0+685941	149.025	68.995	37.0	-4.358	1.851	1.720	Gal	1
M81X217	J095606.0+690833	149.025	69.143	36.8	-5.335	0.712	0.606	HM	1
M81X218	J095607.7+690325	149.032	69.057	37.0	-4.637	0.74	1.172	HM	1
M81X219	J095608.1+690142	149.034	69.029	36.0	-3.381	1.961	1.163	IM	1
M81X220	J095608.9+690106	149.037	69.019	37.6	-5.432	-0.141	0.149	HM	1
M81X221	—	149.038	68.993	36.0	-3.922	-0.058	-0.181	HM	2
M81X222	—	149.052	69.104	36.4	-2.258	—	1.823	LM	2
M81X223	J095613.6+690631	149.056	69.109	37.3	-2.259	0.716	1.094	LM	1
M81X224	J095613.7+685724	149.057	68.957	37.4	—	—	—	Star	1
M81X225	J095614.3+690248	149.06	69.047	37.1	—	—	—	LM	1
M81X226	J095614.6+690339	149.061	69.061	36.8	-4.918	1.272	1.047	Gal	1
M81X227	J095614.9+685732	149.062	68.959	37.3	-5.357	0.913	0.523	HM	1

Table C.1 (cont'd)

ID	CSC ID (2CXO)	R.A.	Dec	L_X	V	B-V	V-I	Class	CF
M81X228	J095616.3+690119	149.068	69.022	36.4	-2.977	—	1.805	IM	1
M81X229	J095616.5+685649	149.069	68.947	37.1	-3.034	0.886	0.936	IM	1
M81X230	J095617.0+685820	149.071	68.972	37.5	-5.536	0.901	0.374	HM	1
M81X231	—	149.076	69.052	36.8	-2.407	—	2.423	LM	1
M81X232	J095619.7+690201	149.083	69.034	36.9	-3.746	0.79	0.482	IM	1
M81X233	J095622.2+690220	149.092	69.039	36.5	-3.226	—	1.395	IM	1
M81X234	J095622.3+690446	149.093	69.08	36.6	-2.734	—	1.652	(SNR)	2
M81X235	—	149.098	69.03	36.1	-2.855	1.09	2.473	IM	1
M81X236	J095624.0+690009	149.1	69.003	36.6	-4.584	0.512	0.778	HM	1
M81X237	J095628.0+690102	149.117	69.017	37.4	-5.536	0.273	0.599	HM	1
M81X238	J095630.8+690222	149.128	69.04	36.8	-2.48	—	1.762	LM	1
M81X239	J095631.0+685837	149.129	68.977	37.0	-2.224	1.037	2.038	LM	1
M81X240	J095632.5+685714	149.135	68.954	36.9	—	—	—	LM	1
M81X241	J095633.4+690035	149.139	69.01	36.5	-2.098	—	1.464	LM	2
M81X242	J095633.5+690331	149.14	69.059	37.3	-1.704	1.187	1.972	LM	1
M81X243	J095636.4+690028	149.152	69.008	37.9	-8.657	1.029	0.779	HM	1
M81X244	J095642.0+685858	149.174	68.983	36.7	-4.448	-0.224	-0.081	HM	1
M81X245	J095645.2+690108	149.189	69.019	36.7	-2.038	-0.169	1.207	LM	1
M81X246	—	149.198	69.064	36.9	-2.889	1.17	0.746	IM	1
M81X248	—	149.214	68.977	36.6	-4.075	0.378	0.588	IM	1
M81X249	J095651.4+685606	149.214	68.935	37.8	-2.469	—	1.652	LM	1
M81X250	—	149.227	69.032	36.9	-2.051	—	1.344	LM	1
M81X251	J095658.2+690046	149.243	69.013	37.5	-7.659	0.517	0.760	HM	1.0

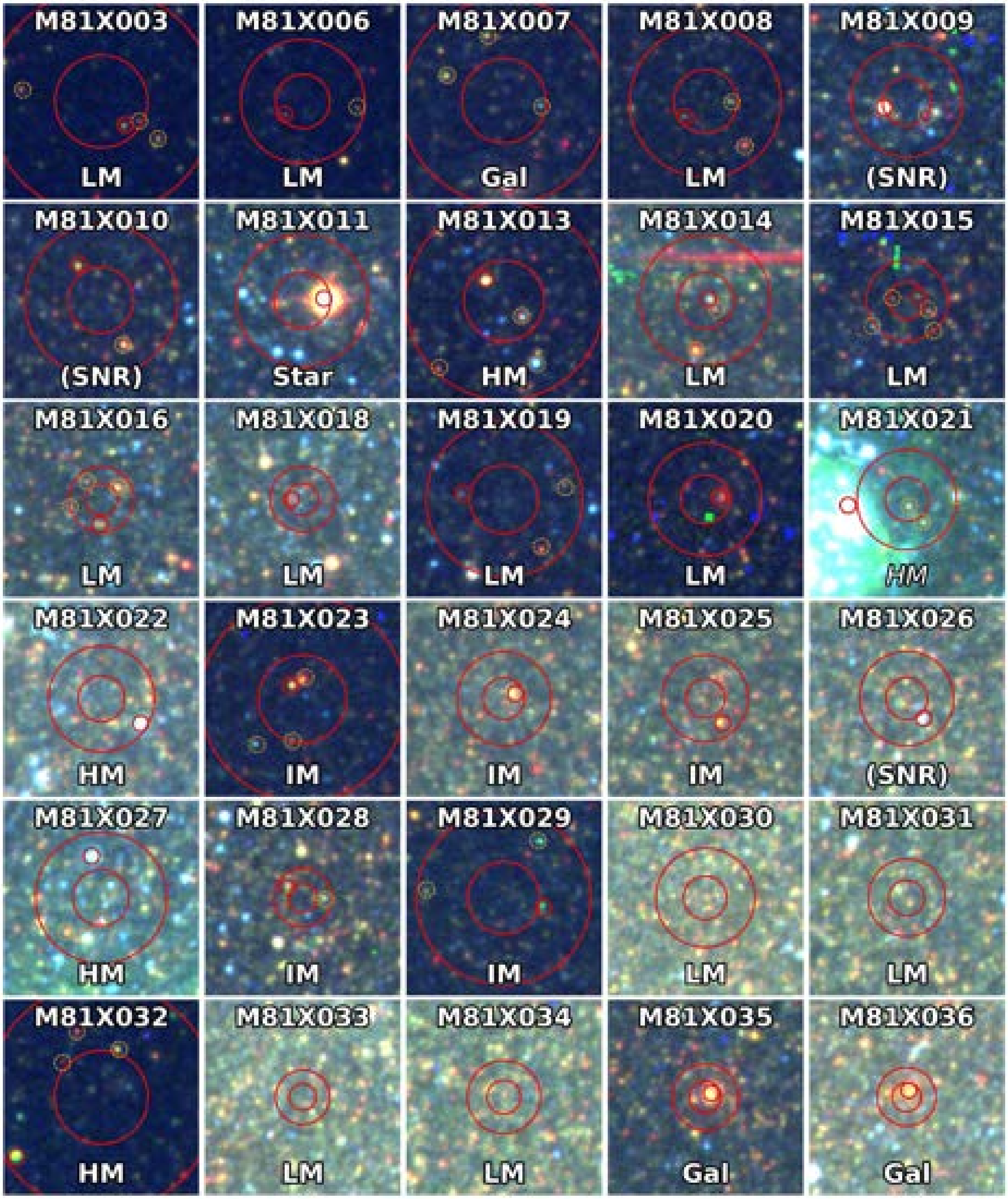

Figure C.1 Optical counterparts within the 1- and 2-σ radii for each X-ray source, with the most likely donor circled in red. The classifications of each source are also given, with LM, IM, and HM representing our LMXBs, IMXBs, and HMXBs, respectively, and those in italics represent cluster XRBs. Sources classified as (SNR) represent SNRs identified using our HR–L_X criterion; all other SNRs are identified within published catalogs (Nantais et al., 2010, 2011; Santiago-Cortés et al., 2010, see §3.4.1). The size of each image is roughly $3.''7\times3.''7$.

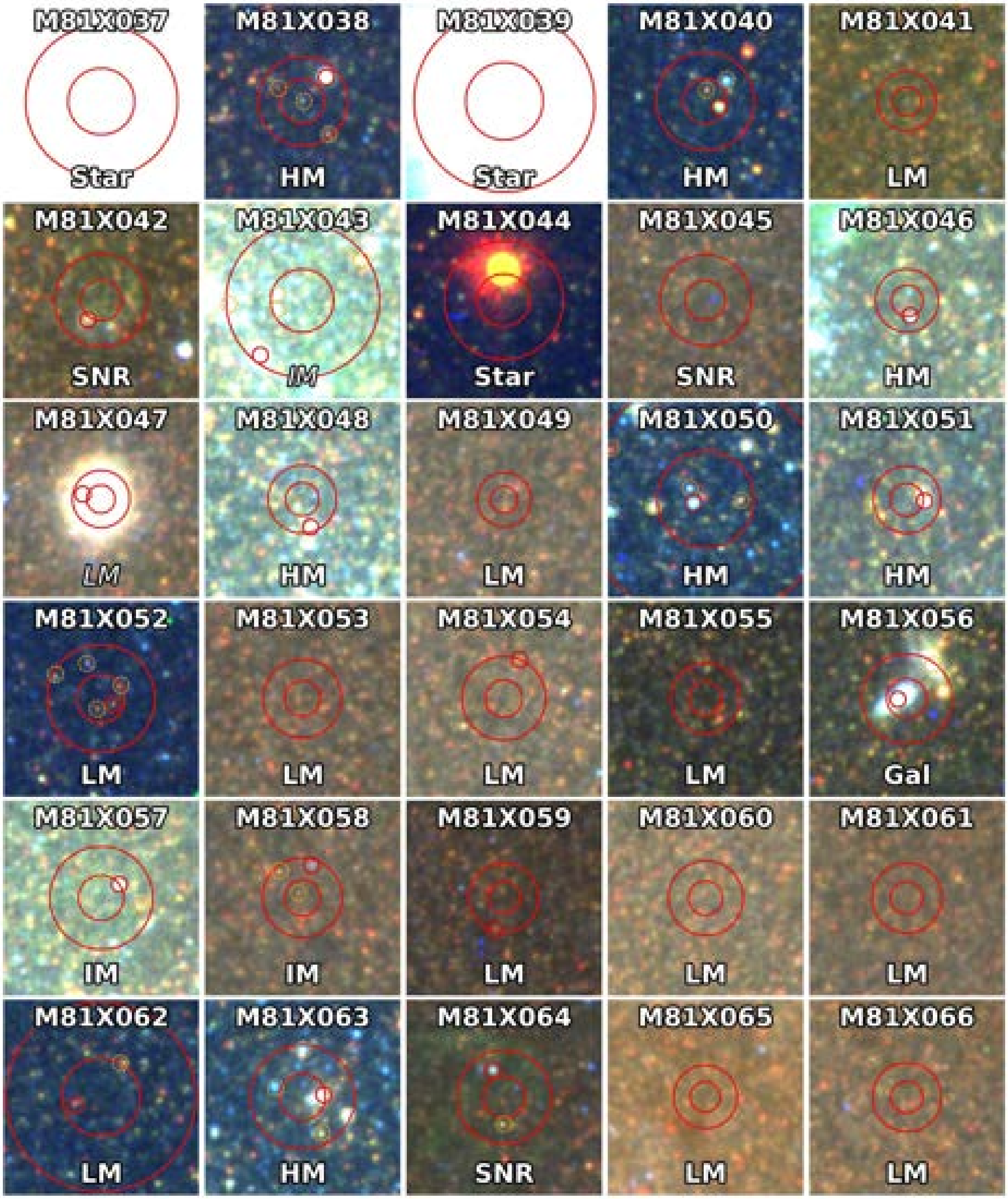

Figure C.1 *(continued)*

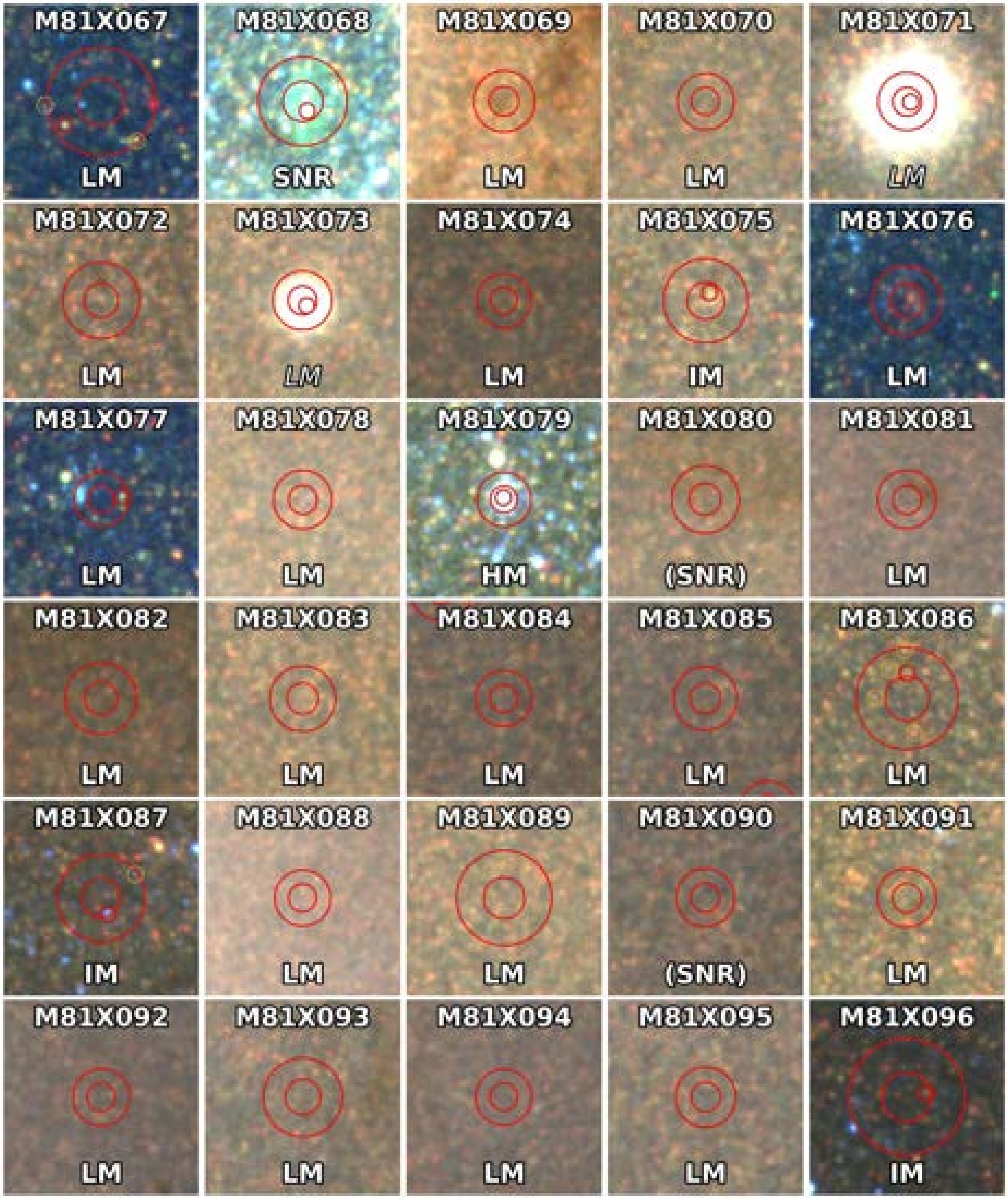

Figure C.1 *(continued)*

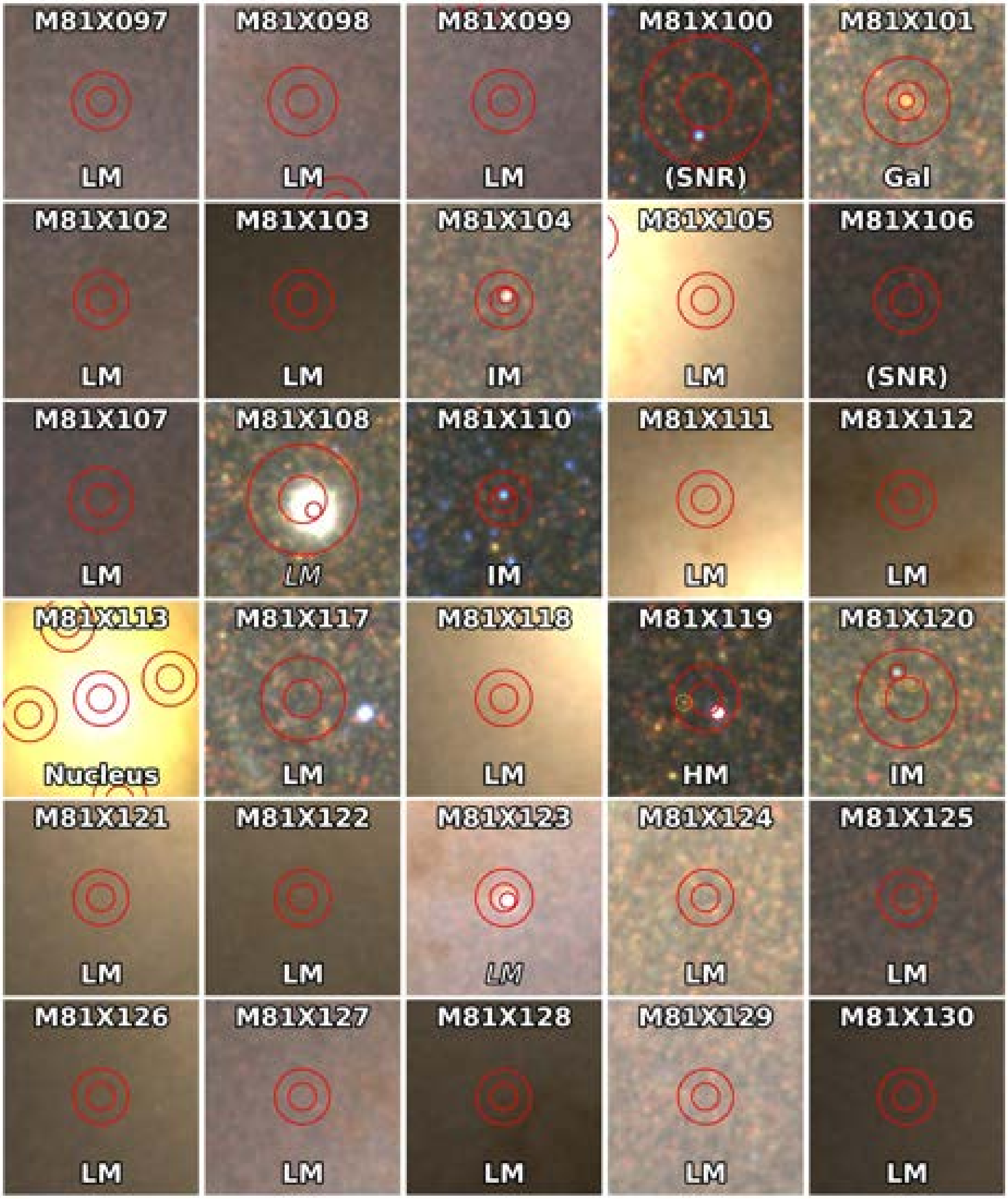

Figure C.1 *(continued)*

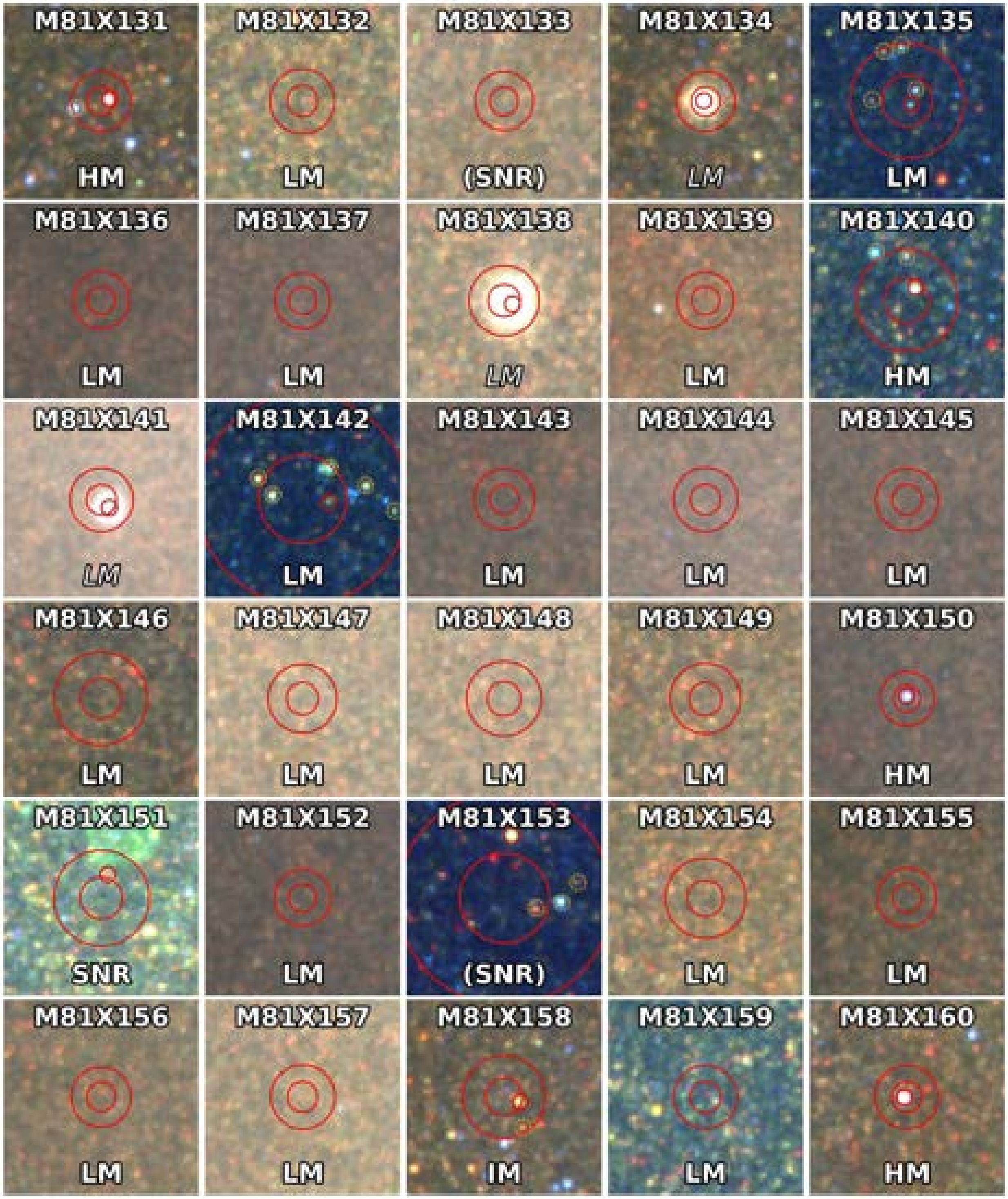

Figure C.1 *(continued)*

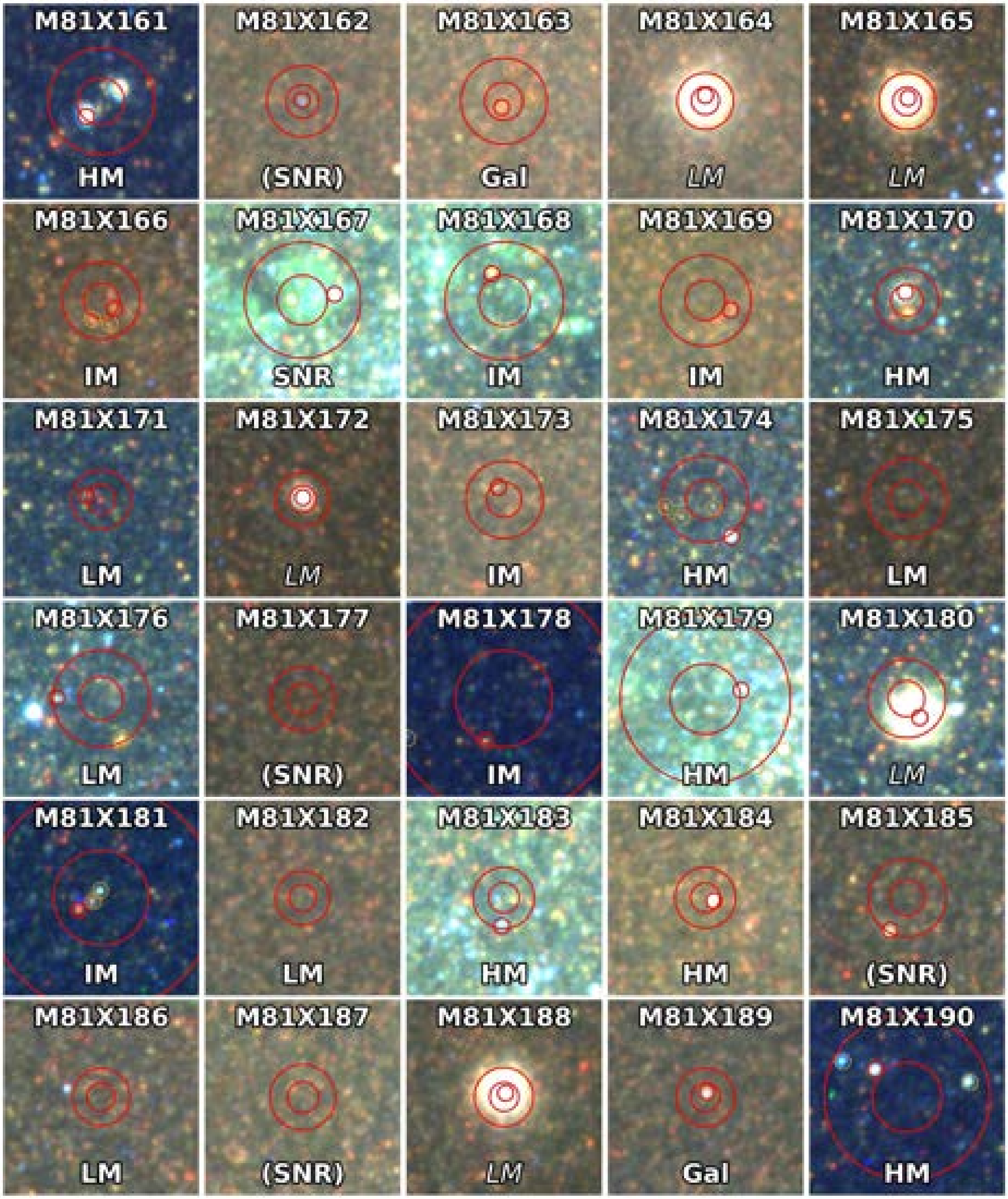

Figure C.1 *(continued)*

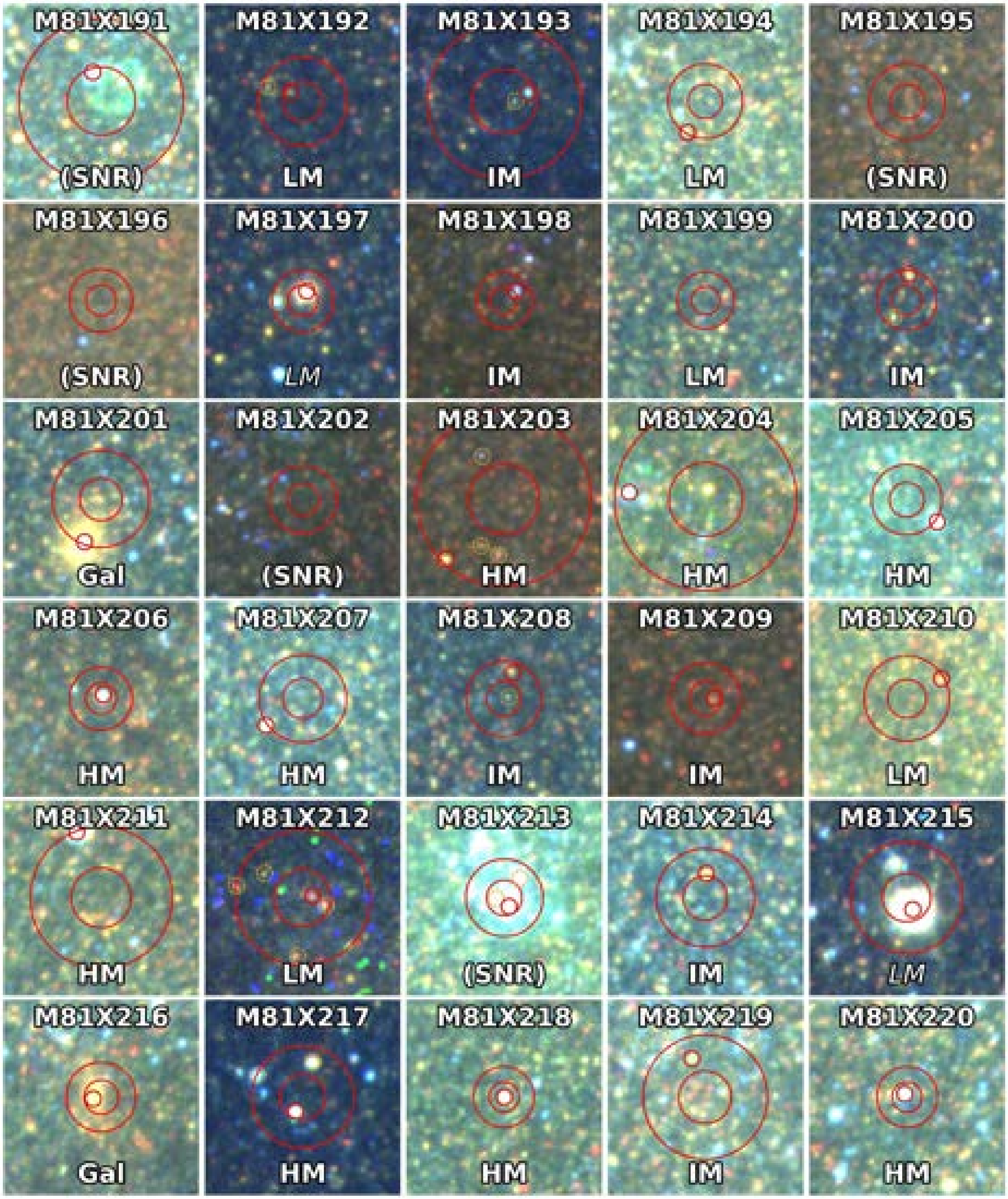

Figure C.1 *(continued)*

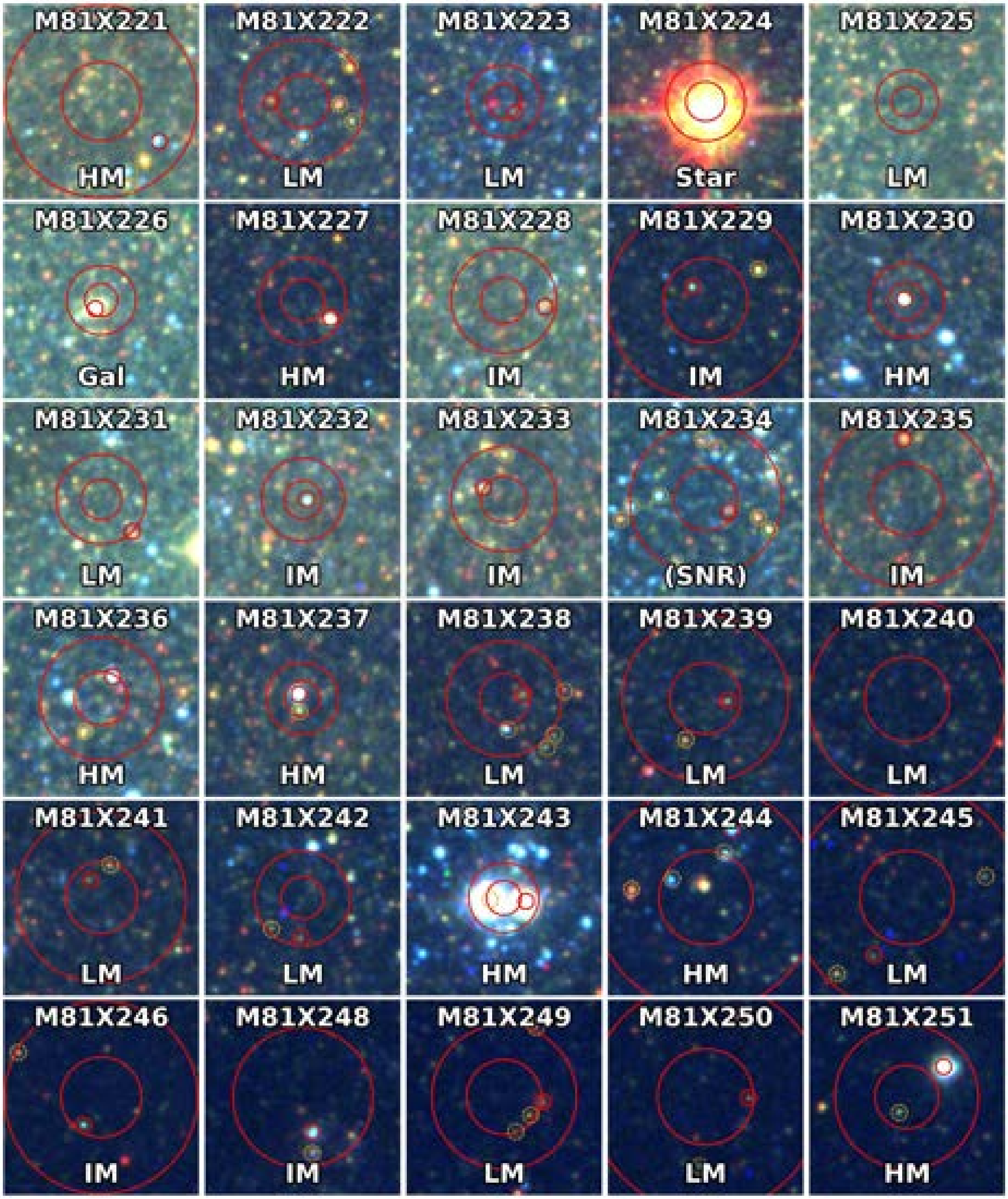

Figure C.1 *(continued)*

APPENDIX D

The Host Clusters of XRBs

Compiled below are the X-ray and optically-derived properties of the clusters within 2σ of single-associated (Table D.1) and multiply-associated (Table D.2) XRBs. Colors and magnitudes are taken from the values reported in the PHANGS-HST catalog. Age (log yrs), mass (log $M_\odot$), effective radius (pc), and density (log $M_\odot$ pc^{-3}) are obtained as described in Chapter 4, §4.4. The L_X of each source are in units log CGS, as reported by Lehmer et al. (2019).

Table D.1. Properties of singly-associated XRBs and clusters

Galaxy	L19 ID	log L_X	PHANGS ID	V	U-B	V-I	Age	Mass	R_{eff}	Density
NGC 0628	L19X038	36.8	481	-6.30	-1.38	0.51	7.28	3.47	4.80	0.13
	L19X039	37.9	7257	-9.75	0.20	1.22	10.00*	6.04	4.65	2.74
	L19X048	38.4	7375	-6.60	-0.01	1.75	10.00*	4.78	3.38	1.90
	L19X059	37.0	5558	-6.21	-0.67	0.43	7.88	3.75	4.27	0.56
	L19X060	36.9	4602	-8.13	0.49	1.57	10.00*	5.39	4.16	2.24
	L19X086	36.7	4841	-7.94	-0.01	1.27	10.00*	5.31	3.38	2.43
	L19X087	37.5	7497	-11.30	—	0.23	6.70	5.11	4.56	1.84
NGC 3351	L19X014	37.1	151	-7.88	-0.81	-0.20	6.70	3.31	7.49	-0.61
	L19X026	38.6	3845	-5.91	—	1.50	10.00*	4.5	1.37	2.79
	L19X040	37.3	2881	-7.85	0.24	1.26	10.00*	5.28	2.20	2.96
NGC 3627	L19X032	38.2	9731	-12.32	-1.10	0.49	6.00	6.17	1.95	4.00
	L19X040	38.8	7367	-8.04	-0.05	1.13	10.00*	5.36	1.26	3.75
	L19X063	37.1	1421	-6.78	-0.50	0.99	10.00*	4.85	4.28	1.66
	L19X074	37.5	5530	-8.65	-1.04	0.62	7.51	4.41	3.20	1.60
	L19X078	39.4	5876	-7.51	0.44	1.20	10.00*	5.15	6.94	1.32
	L19X083	38.7	10673	-6.69	0.39	1.01	10.00*	4.81	5.03	1.41
NGC 4321	L19X055	38.1	2466	-8.21	0.13	1.14	10.00*	5.42	1.70	3.43
	L19X056	37.0	831	-9.70	-0.94	0.83	6.90	4.43	1.98	2.24
	L19X070	37.1	368	-10.58	-1.19	0.48	6.00	5.28	2.05	3.05
	L19X071	37.3	878	-7.88	-0.77	0.72	7.66	4.13	2.12	1.85
NGC 4826	L19X011	36.5	1885	-8.31	0.07	0.76	10.00*	5.46	3.16	2.67
	L19X021	37.7	876	-8.26	0.53	1.18	10.00*	5.44	1.49	3.62
	L19X023	36.8	10	-11.19	-0.12	1.09	10.00*	6.62	2.70	4.02
	L19X028	36.4	33	-9.98	-0.18	1.09	10.00*	6.13	1.49	4.31
	L19X034	36.9	287	-9.53	-0.10	1.12	10.00*	5.95	1.21	4.40

Note. — * XRBs associated with GCs are assigned an age of 10 log yrs due to complications in estimating the ages of GCs (see §4.4.1).
** Some intermediate-age clusters are assigned manually-corrected ages, as the PHANGS-HST pipeline provides inaccurate age estimates for certain young clusters.

Table D.2. Properties of multiply-associated XRBs and clusters

Galaxy	L19 ID	log L_X	PHANGS ID	V	U-B	V-I	Age	Mass	R_{eff}	Density
NGC 0628	L19X033	36.5	3546	-8.15	-1.48	-0.07	6.00	4.07	2.64	1.51
		36.5	3557	-8.12	-1.20	0.17	6.00	4.33	2.21	2.00
NGC 3351	L19X032	38.2	3382	-8.12	-0.99	0.08	6.70	3.57	2.71	0.97
		38.2	3399	-9.54	-0.51	1.06	8.21**	5.15	4.15	2.00
		38.2	3499	-8.50	-0.64	0.58	8.06**	4.67	7.17	0.80
	L19X033	38.4	3627	-10.96	-0.85	0.74	7.96**	5.59	2.35	3.18
		38.4	3660	-9.90	-0.98	0.46	6.60	4.5	6.08	0.85
		38.4	3673	-9.98	-1.39	0.36	6.00	4.89	6.12	1.24
		38.4	3705	-9.36	-1.09	0.37	6.48	4.61	3.28	1.76
	L19X034	37.7	3000	-12.72	-1.31	0.17	6.30	5.85	4.70	2.54
		37.7	3009	-11.92	-1.16	0.36	6.48	5.6	4.60	2.31
		37.7	3017	-10.81	-1.29	0.19	6.00	5.22	6.80	1.43
		37.7	3028	-9.77	-1.07	0.85	6.90	4.42	4.58	1.14
	L19X037	38.0	3081	-9.54	-0.96	0.77	6.90	4.29	4.45	1.05
		38.0	3159	-9.27	-1.07	0.67	6.90	4.11	13.09	-0.54
	L19X039	38.0	3624	-11.60	-1.35	0.23	6.00	5.49	3.03	2.75
		38.0	3631	-9.40	-1.13	0.15	6.60	4.14	1.72	2.14
		38.0	3650	-10.36	-1.31	0.27	6.00	5.0	4.72	1.68
	L19X044	37.1	3630	-7.41	0.43	1.33	10.00*	5.11	1.37	3.40
		37.1	3712	-8.53	0.01	1.15	10.00*	5.55	1.37	3.84
NGC 3627	L19X020	37.2	7021	-9.01	-1.31	0.12	6.48	4.33	2.62	1.78
		37.2	7031	-9.19	-1.00	0.71	6.90	4.26	3.88	1.19

Note. — * XRBs associated with GCs are assigned an age of 10 log yrs due to complications in estimating the ages of GCs (see §4.4.1).

** Some intermediate-age clusters are assigned manually-corrected ages, as the PHANGS-HST pipeline provides inaccurate age estimates for certain young clusters.

APPENDIX E

Optical observations of ULXs

Here, I present the results of my photometric analysis of ULXs, including the best fit masses from the SED fitting methods (§5.4), and the spectral types inferred from the best fit effective temperatures and stellar luminosities. The mass range represents the lowest and highest mass of all stars within 2σ of the corresponding ULX from the top 3 best-fit SED models (as an example, see Figure E.1below). Multi-color images of each ULX, as observed with the instrument and filters indicated, are also shown. The three-letter codes in both Table E.1 and Figure E.2 represent: low-mass X-ray binary (LXB); intermediate-mass X-ray binary (IXB); high-mass X-ray binary (HXB); old globular cluster (OGC); intermediate-age massive cluster (IMC); young massive cluster (YMC); OB association (OBA); galaxy (GAL); and undetermined (UND).

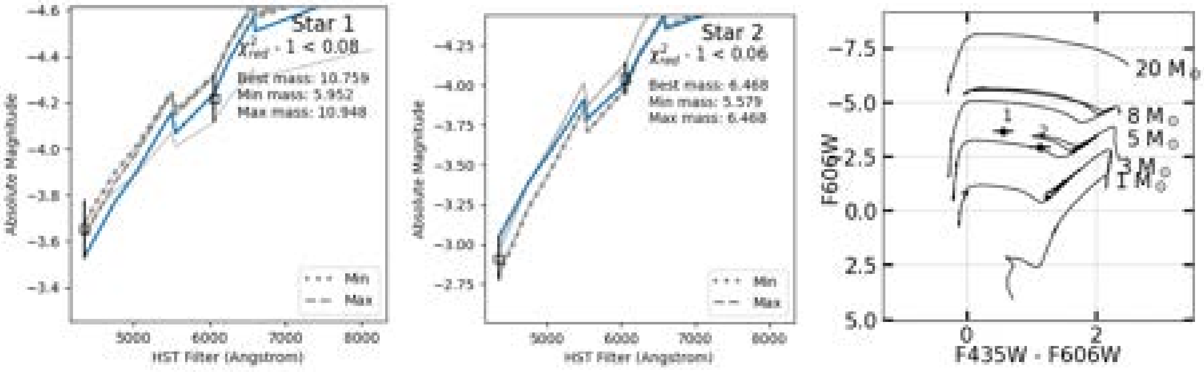

Figure E.1 An example of the SED fitting scheme (IC 342), in which the best-fit stellar model (blue) is that which minimizes $\chi^2_{\text{red}} - 1$ between the observed photometry and the model. The best-fit mass is verified on a CMD (right).

Table E.1. Results of photometric analysis of ULX optical counterparts

Galaxy	2CXO ID	RA	Dec	Instr.	HST filters	Class	Mass Range [$M_\odot$]	Best Mass [$M_\odot$]	Spectral type
IC0342	J034615.7+681112	03 46 15.8	+68 11 12.9	ACS	2	IXB	5.58–10.95	10.76	F,G
NGC0891	J022233.4+422026	02 22 33.5	+42 20 27.1	ACS	2	HXB	8.58–15.44	8.85	G,K
NGC1291	J031714.3-410717	03 17 14.4	−41 07 17.3	ACS	2	UND	—	—	—
NGC2500	J080148.0+504354	08 01 48.1	+50 43 54.6	WFC3	5	LXB	—	—	—
NGC2903	J093206.1+213058	09 32 06.2	+21 30 58.8	ACS	2	HXB	8.1–229.36	118.94	O
		09 32 06.2	+21 30 58.8	WFC3	2		8.82–10.64	10.64	M
NGC3034	J095550.1+694043	09 55 50.2	+69 40 44.7	ACS	3	UND	—	—	—
NGC3239	J102508.2+170948	10 25 08.2	+17 09 48.2	WFC3	2	UND	—	—	—
NGC3239	J102506.9+170947	10 25 07.0	+17 09 47.1	WFC3	2	HXB	5.95–79.81	8.56	K,M
NGC3384	J104817.5+123756	10 48 17.5	+12 37 55.9	ACS	3	UND	—	—	—
NGC3432	J105233.8+363615	10 52 33.9	+36 36 15.7	ACS	3	GAL	—	—	—
NGC3432	J105234.7+363803	10 52 34.8	+36 38 03.0	ACS	3	YMC	—	—	—

Table E.1 (cont'd)

Galaxy	2CXO ID	RA	Dec	Instr.	HST filters	Class	Mass Range [$M_\odot$]	Best Mass [$M_\odot$]	Spectral type
NGC3621	J111815.1-324840	11 18 15.2	−32 48 40.6	WFC3	2	HXB	8.55–29.59	—	B
NGC3627	J112018.3+125900	11 20 18.3	+12 59 00.8	ACS	2	OGC	—	—	—
		11 20 18.3	+12 59 00.8	WFC3	3		—	—	—
NGC3938	J115246.6+440648	11 52 46.7	+44 06 48.6	WFC3	2	HXB	13.17–204.99	—	O,A,G,K
NGC4258	J121857.8+471607	12 18 57.9	+47 16 07.9	ACS	3	OBA	8.81–57.43	—	A,F,G,K,M
NGC4321	J122247.3+154911	12 22 47.4	+15 49 11.5	WFC3	2	LXB	—	—	—
NGC4321	J122254.1+154912	12 22 54.2	+15 49 12.0	WFC3	2	HXB	14.32–180.07	22.23	A,F
NGC4490	J123043.1+413818	12 30 43.2	+41 38 18.7	WFC3	5	HXB	6.15–66.41	—	B,A,F
NGC4490	J123030.7+413911	12 30 30.7	+41 39 11.7	WFC3	5	HXB	0.84–79.8	—	B,A,F
NGC4490	J123038.4+413831	12 30 38.4	+41 38 31.9	WFC3	5	HXB	5.6–31.13	—	B,A,F
NGC4490	J123032.1+413918	12 30 32.2	+41 39 18.3	WFC3	5	HXB	9.66–21.98	—	B
NGC4527	J123411.4+023928	12 34 11.4	+02 39 28.8	WFC3	2	YMC	—	—	—
NGC4527	J123410.9+023925	12 34 10.9	+02 39 25.2	WFC3	2	YMC	—	—	—

Table E.1 (cont'd)

Galaxy	2CXO ID	RA	Dec	Instr.	HST filters	Class	Mass Range [M$_\odot$]	Best Mass [M$_\odot$]	Spectral type
NGC4559	J123551.7+275604	12 35 51.7	+27 56 04.3	ACS	2	OBA	6.17–116.35	—	O,B,G,K
		12 35 51.7	+27 56 04.1	WFC3	2		6.48–34.98	—	A,F,G,K,M
NGC4565	J123619.0+260026	12 36 19.0	+26 00 27.2	ACS	2	LXB	—	—	—
NGC4565	J123614.5+260053	12 36 14.6	+2600 52.6	ACS	2	OBA	12.72–16.94	—	B,A
NGC4594	J124001.8-113615	12 40 01.0	−11 36 15.8	ACS	3	LXB	—	—	—
NGC4594	J124000.9-113654	12 40 01.0	−11 36 54.5	ACS	3	UND	—	—	—
NGC5055	J131519.5+420301	13 15 19.5	+42 03 02.0	ACS	2	HXB	7.12–55.17	—	O,A
NGC5128	J132527.0–430110	13 25 27.0	−43 01 10.6	WFC3	3	HXB	9.24–13.03	—	K,M
NGC5194	J132959.0+471318	13 29 59.1	+47 13 18.4	ACS	4	LXB	—	—	—
		13 29 59.1	+47 13 18.5	WFC3	3		—	—	—
NGC5194	J132939.4+471243	13 29 39.5	+47 12 43.6	ACS	3	HXB	14.46–172.5	—	O,B
NGC5194	J132953.7+471435	13 29 53.7	+47 14 36.0	ACS	3	LXB	—	—	—
		13 29 53.7	+47 14 35.8	WFC3	3		—	—	—
NGC5194	J133001.0+471343	13 30 01.0	+47 13 43.8	ACS	4	OBA	14.46–26.1	—	B,A,F
		13 30 01.0	+47 13 44.0	WFC3	3		16.25–43.42	—	A,B,F
NGC5194	J132953.3+471042	13 29 53.3	+47 10 42.7	ACS	4	YMC	—	—	—

Table E.1 (cont'd)

Galaxy	2CXO ID	RA	Dec	Instr.	HST filters	Class	Mass Range [$M_\odot$]	Best Mass [$M_\odot$]	Spectral type
		13 29 53.3	+47 10 42.7	WFC3	3		—	—	—
NGC5248	J133730.1+085233	13 37 30.1	+08 52 33.0	WFC3	5	HXB	20.15–31.52	20.15	B
NGC5408	J140319.6-412258	14 03 19.6	−41 22 58.7	WFC3	4	HXB	12.42–82.88	—	O,B,A
NGC5457	J140313.9+541810	14 03 14.0	+54 18 10.2	ACS	3	UND	—	—	—
NGC5457	J140314.3+541806	14 03 14.3	+54 18 06.2	ACS	3	HXB	12.49–15.45	14.94	B
NGC5457	J140332.3+542102	14 03 32.4	+54 21 03.1	ACS	3	HXB	7.29–59.94	—	B,A,F
NGC6946	J203436.5+600930	20 34 36.5	+60 09 30.1	ACS	2	HXB	31.02–196.01	195.95	O
		20 34 36.5	+60 09 30.1	WFC3	3		27.81–29.05	28.42	B
NGC6946	J203500.1+600908	20 35 00.1	+60 09 08.1	ACS	3	HXB	9.32–119.37	—	O,F,G,K
		20 35 00.1	+60 09 08.0s	WFC3	3		18.05–59.94	—	B
NGC6946	J203500.7+601130	20 35 00.8	+60 11 30.4	ACS	4	YMC	—	—	—
		20 35 00.7	+60 11 30.8	WFC3	4		—	—	—
NGC7814	J000313.3+160827	00 03 13.3	+16 08 28.0	ACS	2	IMC	—	—	—
PGC044532	J125900.8+345047	12 59 00.8	+34 50 47.6	ACS	2	OBA	7.83–297.23	—	O,B,F,K
		12 59 00.8	+34 50 47.2	WFC3	2		5.28–347.94	—	O,B,A,F,K,M

Table E.1 (cont'd)

Galaxy	2CXO ID	RA	Dec	Instr.	HST filters	Class	Mass Range [$M_\odot$]	Best Mass [$M_\odot$]	Spectral type
PGC044532	J125901.8+345114	12 59 01.8	+34 51 14.5	ACS	2	HXB	20.11–318.59	—	O,B
		12 59 01.8	+34 51 14.1	WFC3	2		15.32–248.87	—	B,A

Note. — The RA and Dec coordinates listed here include the astrometric corrections. The number of HST filters is given; sources covered by fewer HST filters are expected to give poorer SED fits. Sources with a listed best-fit mass are those with a single stellar counterpart.

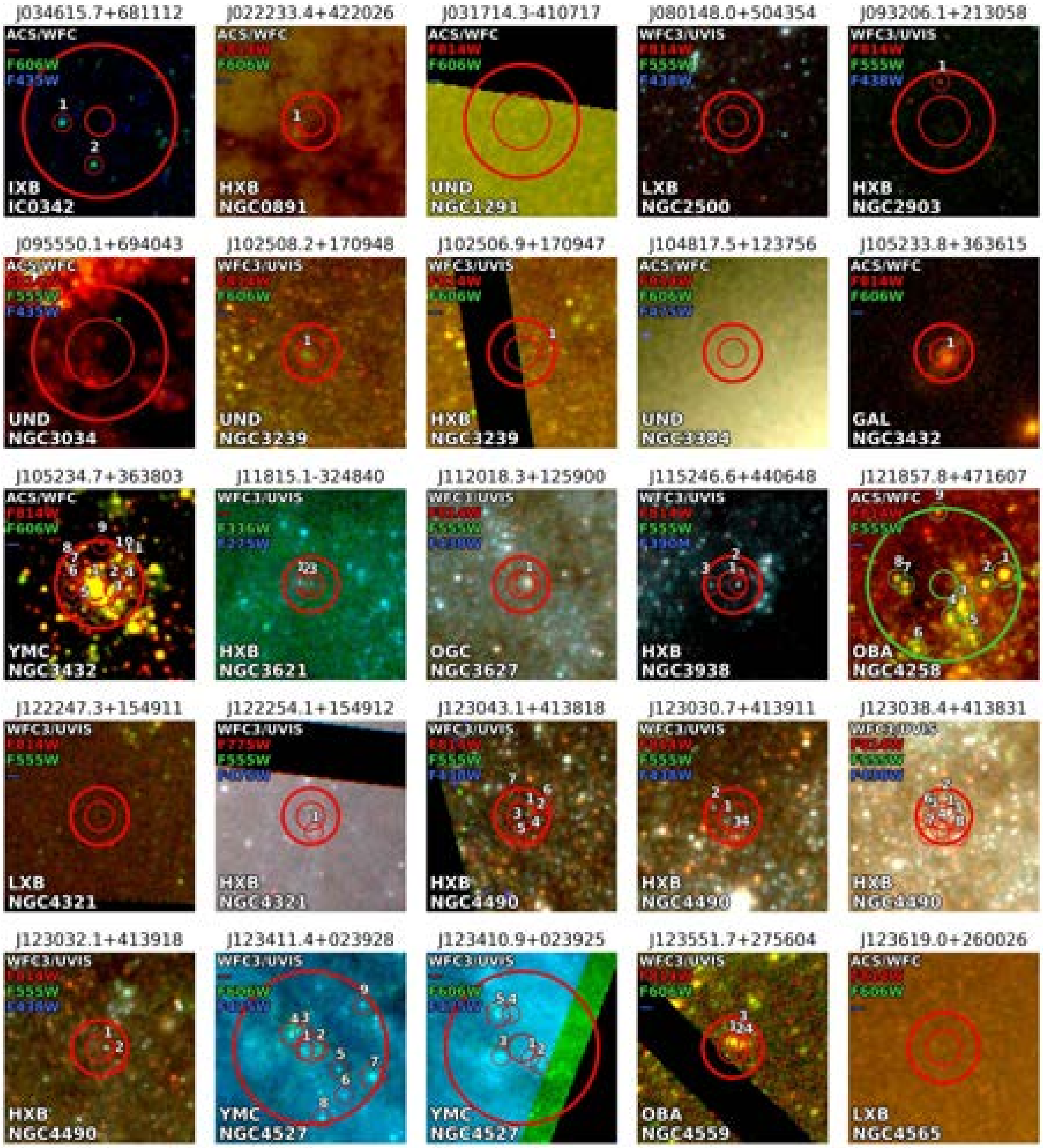

Figure E.2 Color images of each ULX, as observed by *HST*. Where available, the filters used are given in the order of red, green, and blue. The large concentric circles represent the 1- and 2-σ positional uncertainties calculated for each ULX. Each square is $5'' \times 5''$.

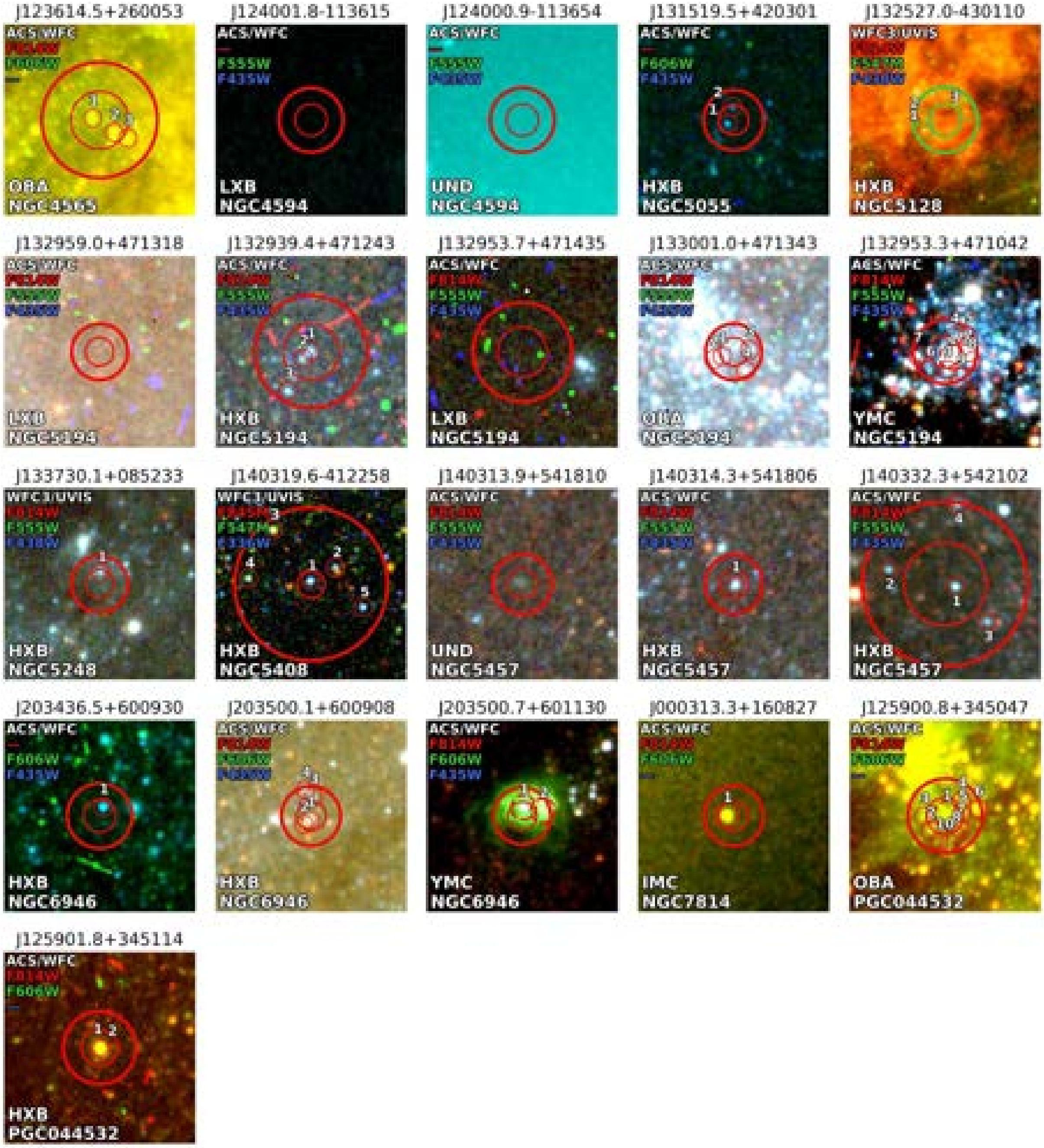

Figure E.2 *(continued)*

BIBLIOGRAPHY

Abbott, B. P., Abbott, R., Abbott, T. D., & Abernathy, M. R. e. a. 2016, Phys. Rev. Lett., 116, 061102, doi: 10.1103/PhysRevLett.116.061102

Abbott, R., Abbott, T. D., Abraham, S., et al. 2020, Phys. Rev. Lett., 125, 101102, doi: 10.1103/PhysRevLett.125.101102

Aird, J., Coil, A. L., & Georgakakis, A. 2017, MNRAS, 465, 3390, doi: 10.1093/mnras/stw2932

Allak, S. 2023, Monthly Notices of the Royal Astronomical Society, 527, 2599–2611, doi: 10.1093/mnras/stad3332

Anders, P., Gieles, M., & de Grijs, R. 2006, Astronomy & Astrophysics - ASTRON ASTROPHYS, 451, doi: 10.1051/0004-6361:20054175

Andrae, R., Schulze-Hartung, T., & Melchior, P. 2010, Dos and don'ts of reduced chi-squared. https://arxiv.org/abs/1012.3754

Angelini, L., Loewenstein, M., & Mushotzky, R. F. 2001, The Astrophysical Journal, 557, doi: 10.1086/323026

Antoniou, V., Zezas, A., Drake, J. J., et al. 2019, ApJ, 887, 20, doi: 10.3847/1538-4357/ab4a7a

Arnason, R. M., Sivakoff, G. R., Heinke, C. O., Cohn, H. N., & Lugger, P. M. 2015, The Astrophysical Journal, 807, 52, doi: 10.1088/0004-637X/807/1/52

Atri, P., Miller-Jones, J. C. A., Bahramian, A., et al. 2019, MNRAS, 489, 3116, doi: 10.1093/mnras/stz2335

Avdan, S., Akyuz, A., Acar, S., et al. 2022, Monthly Notices of the Royal Astronomical Society, 519, 4826, doi: 10.1093/mnras/stac3811

Avdan, S., Akyuz, A., Vinokurov, A., et al. 2019, The Astrophysical Journal, 875, 68, doi: 10.3847/1538-4357/ab10d9

Bachetti, M., Harrison, F. A., Walton, D. J., et al. 2014, Nature, 514, 202, doi: 10.1038/nature13791

Bahramian, A., & Degenaar, N. 2023, Low-Mass X-ray Binaries (Springer Nature Singapore), 1–62, doi: 10.1007/978-981-16-4544-0_94-1

Bastian, N., Adamo, A., Gieles, M., et al. 2012, MNRAS, 419, 2606, doi: 10.1111/j.1365-2966.2011.19909.x

Basu-Zych, A. R., Lehmer, B., Fragos, T., et al. 2016, ApJ, 818, 140, doi: 10.3847/0004-637X/818/2/140

Belczynski, K., Kalogera, V., Rasio, F. A., et al. 2008, ApJS, 174, 223, doi: 10.1086/521026

Bellazzini, M., Pasquali, A., Federici, L., Ferraro, F. R., & Pecci, F. F. 1995, The Astrophysical Journal, 439, 687, doi: 10.1086/175208

Bertelli, G., Bressan, A., Chiosi, C., Fagotto, F., & Nasi, E. 1994, A&AS, 106, 275

Blair, W. P., Winkler, P. F., & Long, K. S. 2012, The Astrophysical Journal Supplement Series, 203, 8, doi: 10.1088/0067-0049/203/1/8

Blair, W. P., Chandar, R., Dopita, M. A., et al. 2014, ApJ, 788, 55, doi: 10.1088/0004-637X/788/1/55

Bohlin, R. C., Ryon, J. E., & Anderson, J. 2020, Update of the Photometric Calibration of the ACS CCD Cameras, Instrument Science Report ACS 2020-8

Bonnell, I. A., & Bate, M. R. 2005, MNRAS, 362, 915, doi: 10.1111/j.1365-2966.2005.09360.x

Boquien, M., Burgarella, D., Roehlly, Y., et al. 2019, A&A, 622, A103, doi: 10.1051/0004-6361/201834156

Boroson, B., Kim, D.-W., & Fabbiano, G. 2011, ApJ, 729, 12, doi: 10.1088/0004-637X/729/1/12

Brassington, N. J., Fabbiano, G., Blake, S., et al. 2010, The Astrophysical Journal, 725, 1805, doi: 10.1088/0004-637X/725/2/1805

Bregman, J. N., Irwin, J. A., Seitzer, P., & Flores, M. 2006, The Astrophysical Journal, 640, 282, doi: 10.1086/500037

Bressan, A., Marigo, P., Girardi, L., et al. 2012, MNRAS, 427, 127, doi: 10.1111/j.1365-2966.2012.21948.x

Bruzual, G., & Charlot, S. 2003, MNRAS, 344, 1000, doi: 10.1046/j.1365-8711.2003.06897.x

Bykov, S. D., Gilfanov, M. R., & Sunyaev, R. A. 2024, MNRAS, 527, 1962, doi: 10.1093/mnras/stad3355

Calamida, A., Bajaj, V., Mack, J., et al. 2022, AJ, 164, 32, doi: 10.3847/1538-3881/ac73f0

Carbone, D., & Wijnands, R. 2019, MNRAS, 488, 2767, doi: 10.1093/mnras/stz1645

Casares, J., & Jonker, P. G. 2014, Space Sci. Rev., 183, 223, doi: 10.1007/s11214-013-0030-6

Chandar, R., Fall, S. M., & McLaughlin, D. E. 2007, Astrophys. J. Lett., 668, L119, doi: 10.1086/523040

Chandar, R., Johns, P., Mok, A., et al. 2020, ApJ, 890, 150, doi: 10.3847/1538-4357/ab6b27

Chandar, R., Whitmore, B., & Lee, M. G. 2004, ApJ, 611, 220, doi: 10.1086/421934

Chandar, R., Whitmore, B. C., Calzetti, D., & O'Connell, R. 2014, The Astrophysical Journal, 787, 17, doi: 10.1088/0004-637x/787/1/17

Chandar, R., Whitmore, B. C., Dinino, D., et al. 2016, ApJ, 824, 71, doi: 10.3847/0004-637X/824/2/71

Chandar, R., Whitmore, B. C., Kim, H., et al. 2010, ApJ, 719, 966, doi: 10.1088/0004-637X/719/1/966

Chen, W.-C., & Podsiadlowski, P. 2016, The Astrophysical Journal, 830, 131, doi: 10.3847/0004-637X/830/2/131

Chen, X., Wang, W., & Tong, H. 2021, Journal of High Energy Astrophysics, 31, 1, doi: 10.1016/j.jheap.2021.04.002

Clark, D. H., & Parkinson, J. H. 1975, Nature, 258, 408, doi: 10.1038/258408a0

Colbert, E. J. M., Heckman, T. M., Ptak, A. F., Strickland, D. K., & Weaver, K. A. 2004, ApJ, 602, 231, doi: 10.1086/380899

Coleiro, A., & Chaty, S. 2013, The Astrophysical Journal, 764, 185, doi: 10.1088/0004-637X/764/2/185

Corral-Santana, J. M., Casares, J., Muñoz-Darias, T., et al. 2016, A&A, 587, A61, doi: 10.1051/0004-6361/201527130

Crowther, P. 2012, Astronomy Geophysics, 53, 4.30, doi: 10.1111/j.1468-4004.2012.53430.x

Dage, K. C., Kundu, A., Thygesen, E., et al. 2021, Monthly Notices of the Royal Astronomical Society, 504, 1545–1554, doi: 10.1093/mnras/stab943

Dage, K. C., Bahramian, A., Naoz, S., et al. 2024, MNRAS, 529, 1347, doi: 10.1093/mnras/stae578

D´Ago, G., Paolillo, M., Fabbiano, G., et al. 2014, A&A, 567, A2, doi: 10.1051/0004-6361/201322722

David, L. P., Jones, C., & Forman, W. 1992, ApJ, 388, 82, doi: 10.1086/171131

Deger, S., Lee, J. C., Whitmore, B. C., et al. 2021, Monthly Notices of the Royal Astronomical Society, 510, 32, doi: 10.1093/mnras/stab3213

Deustua, S. E., Mack, J., Bajaj, V., & Khandrika, H. 2017, WFC3/UVIS Updated 2017 Chip-Dependent Inverse Sensitivity Values, Tech. rep., STScI

Dopita, M. A., Blair, W. P., Long, K. S., et al. 2010, ApJ, 710, 964, doi: 10.1088/0004-637X/710/2/964

Dottori, H., Diaz, R. J., Agüero, M. P., Mast, D., & Rodrigues, I. 2008, in IAU Symposium, Vol. 245, Formation and Evolution of Galaxy Bulges, ed. M. Bureau, E. Athanassoula, & B. Barbuy, 297–300, doi: 10.1017/S174392130801795X

Ducci, L., Sasaki, M., Haberl, F., & Pietsch, W. 2013, Astronomy & Astrophysics, 553, A7, doi: 10.1051/0004-6361/201321035

Eikenberry, S. S., Cameron, P. B., Fierce, B. W., et al. 2001, ApJ, 561, 1027, doi: 10.1086/323380

Evans, I. N., Primini, F. A., Miller, J. B., et al. 2020, in American Astronomical Society Meeting Abstracts, American Astronomical Society Meeting Abstracts, 154.05

Fabbiano, G. 1989, ARA&A, 27, 87, doi: 10.1146/annurev.aa.27.090189.000511

—. 2006, ARA&A, 44, 323, doi: 10.1146/annurev.astro.44.051905.092519

Fabbiano, G., Feigelson, E., & Zamorani, G. 1982, ApJ, 256, 397, doi: 10.1086/159917

Fabbiano, G., & Shapley, A. 2002, ApJ, 565, 908, doi: 10.1086/324780

Fabbiano, G., Brassington, N. J., Lentati, L., et al. 2010, The Astrophysical Journal, 725, 1824, doi: 10.1088/0004-637x/725/2/1824

Fabian, A. C., Pringle, J. E., & Rees, M. J. 1975, MNRAS, 172, 15, doi: 10.1093/mnras/172.1.15P

Fabricius, M., Saglia, R., Bender, R., et al. 2012, Astrophysical Journal, 754, doi: 10.1088/0004-637X/754/1/67

Fabrika, S., Ueda, Y., Vinokurov, A., Sholukhova, O., & Shidatsu, M. 2015, Nature Physics, 11, 551, doi: 10.1038/nphys3348

Ferrell, A. P., Lehmer, B. D., Doore, K., et al. 2021, in American Astronomical Society Meeting Abstracts, Vol. 53, American Astronomical Society Meeting Abstracts, 308.05

Finke, J. D., & Razzaque, S. 2017, MNRAS, 472, 3683, doi: 10.1093/mnras/stx2248

Floyd, M., Chandar, R., Whitmore, B. C., et al. 2024, AJ, 167, 95, doi: 10.3847/1538-3881/ad1889

Fornasini, F. M., Antoniou, V., & Dubus, G. 2023, arXiv e-prints, arXiv:2308.02645, doi: 10.48550/arXiv.2308.02645

Fortin, F., García, F., & Chaty, S. 2022, A&A, 665, A69, doi: 10.1051/0004-6361/202244048

Fortin, F., García, F., Simaz Bunzel, A., & Chaty, S. 2023, A&A, 671, A149, doi: 10.1051/0004-6361/202245236

Fortin, F., Kalsi, A., García, F., & Chaty, S. 2024, arXiv e-prints, arXiv:2401.11931, doi: 10.48550/arXiv.2401.11931

Fragos, T., Lehmer, B. D., Naoz, S., Zezas, A., & Basu-Zych, A. 2013, ApJ, 776, L31, doi: 10.1088/2041-8205/776/2/L31

Galiullin, I., & Gilfanov, M. 2021, Astronomy and Astrophysics, 646, A85, doi: 10.1051/0004-6361/202039522

Garofali, K., Converse, J. M., Chandar, R., & Rangelov, B. 2012, ApJ, 755, 49, doi: 10.1088/0004-637X/755/1/49

Generozov, A., Stone, N. C., Metzger, B. D., & Ostriker, J. P. 2018, Monthly Notices of the Royal Astronomical Society, 478, 4030, doi: 10.1093/mnras/sty1262

Gierliński, M., Done, C., & Page, K. 2009, Monthly Notices of the Royal Astronomical Society, 392, 1106, doi: 10.1111/j.1365-2966.2008.14166.x

Gilfanov, M. 2004, MNRAS, 349, 146, doi: 10.1111/j.1365-2966.2004.07473.x

Gilfanov, M., Grimm, H. J., & Sunyaev, R. 2004, MNRAS, 347, L57, doi: 10.1111/j.1365-2966.2004.07450.x

Girardi, L., Bertelli, G., Bressan, A., et al. 2002, A&A, 391, 195, doi: 10.1051/0004-6361:20020612

Girardi, L., Williams, B. F., Gilbert, K. M., et al. 2010, ApJ, 724, 1030, doi: 10.1088/0004-637X/724/2/1030

Gladstone, J. C., Copperwheat, C., Heinke, C. O., et al. 2013, The Astrophysical Journal Supplement Series, 206, 14, doi: 10.1088/0067-0049/206/2/14

Grimm, H. J., Gilfanov, M., & Sunyaev, R. 2002, A&A, 391, 923, doi: 10.1051/0004-6361:20020826

—. 2003a, MNRAS, 339, 793, doi: 10.1046/j.1365-8711.2003.06224.x

Grimm, H.-J., Gilfanov, M., & Sunyaev, R. 2003b, Chinese Journal of Astronomy and Astrophysics Supplement, 3, 257, doi: 10.1088/1009-9271/3/S1/257

Grimm, H. J., Gilfanov, M., & Sunyaev, R. 2006, in Populations of High Energy Sources in Galaxies, ed. E. J. A. Meurs & G. Fabbiano, Vol. 230, 353–358, doi: 10.1017/S1743921306008660

Grimm, H.-J., McDowell, J., Fabbiano, G., & Elvis, M. 2008, The Astrophysical Journal, 690, 128, doi: 10.1088/0004-637X/690/1/128

Grindlay, J. E. 1984, Advances in Space Research, 3, 19, doi: 10.1016/0273-1177(84)90054-1

Grindlay, J. E. 1988, in The Harlow-Shapley Symposium on Globular Cluster Systems in Galaxies, ed. J. E. Grindlay & A. G. D. Philip, Vol. 126, 347–363

Grindlay, J. E., & Hertz, P. 1985, in Cataclysmic Variables and Low-Mass X-ray Binaries, ed. D. Q. Lamb & J. Patterson, 79, doi: 10.1007/978-94-009-5319-2_9

Groenewegen, M. A. T. 2006, A&A, 448, 181, doi: 10.1051/0004-6361:20054163

Grogin, N. A., Koekemoer, A. M., Schreier, E. J., et al. 2003, ApJ, 595, 685, doi: 10.1086/377450

Grogin, N. A., Conselice, C. J., Chatzichristou, E., et al. 2005, ApJ, 627, L97, doi: 10.1086/432256

Güver, T., & Özel, F. 2009, MNRAS, 400, 2050, doi: 10.1111/j.1365-2966.2009.15598.x

Hailey, C., Mori, K., Bauer, F., et al. 2018, Nature, 556, 70, doi: 10.1038/nature25029

Harris, W. E., Harris, G. L., & Hudson, M. J. 2015, The Astrophysical Journal, 806, 36, doi: 10.1088/0004-637x/806/1/36

Harris, W. E., Harris, G. L. H., & Alessi, M. 2013, The Astrophysical Journal, 772, 82, doi: 10.1088/0004-637x/772/2/82

Heida, M., Jonker, P. G., Torres, M. A. P., et al. 2014, MNRAS, 442, 1054, doi: 10.1093/mnras/stu928

Hills, J. G. 1976, MNRAS, 175, 1P, doi: 10.1093/mnras/175.1.1P

Hixenbaugh, K., Chandar, R., & Mok, A. 2022, The Astronomical Journal, 163, 271, doi: 10.3847/1538-3881/ac680d

Humphrey, P. J., & Buote, D. A. 2008, ApJ, 689, 983, doi: 10.1086/592590

Hunt, Q., Chandar, R., Gallo, E., et al. 2023a, The Astrophysical Journal, 953, 126, doi: 10.3847/1538-4357/ace162

Hunt, Q., Gallo, E., Chandar, R., et al. 2021, The Astrophysical Journal, 912, 31, doi: 10.3847/1538-4357/abe531

Hunt, Q., Gallo, E., Chandar, R., Mok, A., & Prestwich, A. 2023b, The Astrophysical Journal, 947, 31, doi: 10.3847/1538-4357/ac78da

Hut, P., McMillan, S., & Romani, R. W. 1992, ApJ, 389, 527, doi: 10.1086/171229

Inoue, Y., & Kusenko, A. 2017, Journal of Cosmology and Astroparticle Physics, 2017, 034–034, doi: 10.1088/1475-7516/2017/10/034

Irwin, J. A., Bregman, J. N., & Athey, A. E. 2004, ApJ, 601, L143, doi: 10.1086/382026

Ivanova, N. 2013, Mem. Soc. Astron. Italiana, 84, 123, doi: 10.48550/arXiv.1301.2203

Jarrett, T. H., Chester, T., Cutri, R., Schneider, S. E., & Huchra, J. P. 2003, AJ, 125, 525, doi: 10.1086/345794

Jordán, A., Côté, P., Ferrarese, L., et al. 2004, ApJ, 613, 279, doi: 10.1086/422545

Jordán, A. 2004, The Astrophysical Journal, 613, L117, doi: 10.1086/425147

Jordán, A., Sivakoff, G. R., McLaughlin, D. E., et al. 2007, The Astrophysical Journal, 671, L117, doi: 10.1086/525524

Kaaret, P., Alonso-Herrero, A., Gallagher, J. S., et al. 2004, Monthly Notices of the Royal Astronomical Society, 348, L28, doi: 10.1111/j.1365-2966.2004.07516.x

Kaaret, P., Feng, H., & Roberts, T. P. 2017, ARA&A, 55, 303, doi: 10.1146/annurev-astro-091916-055259

Kaaret, P., Schmitt, J., & Gorski, M. 2011, ApJ, 741, 10, doi: 10.1088/0004-637X/741/1/10

Kaczmarek, T., Olczak, C., & Pfalzner, S. 2011, A&A, 528, A144, doi: 10.1051/0004-6361/201015233

Kalberla, P. M. W., Burton, W. B., Hartmann, D., et al. 2005, Astronomy & Astrophysics, 440, 775–782, doi: 10.1051/0004-6361:20041864

Kalogera, V., Sepinsky, J., & Belczynski, K. 2007, in Astronomical Society of the Pacific Conference Series, Vol. 367, Massive Stars in Interactive Binaries, ed. N. St. -Louis & A. F. J. Moffat, 623

Kalogera, V., & Webbink, R. F. 1996, ApJ, 458, 301, doi: 10.1086/176813

Katz, J. I. 1975, Nature, 253, 698, doi: 10.1038/253698a0

Kennicutt, Robert C., J. 1998, ARA&A, 36, 189, doi: 10.1146/annurev.astro.36.1.189

Kennicutt, Robert C., J., Tamblyn, P., & Congdon, C. E. 1994, ApJ, 435, 22, doi: 10.1086/174790

Kennicutt, Robert C., J., Armus, L., Bendo, G., et al. 2003, PASP, 115, 928, doi: `10.1086/376941`

Kiel, P. D., & Hurley, J. R. 2006, Monthly Notices of the Royal Astronomical Society, 369, 1152, doi: `10.1111/j.1365-2966.2006.10400.x`

Kim, D.-W., & Fabbiano, G. 2004, ApJ, 611, 846, doi: `10.1086/422210`

Kim, D. W., Fabbiano, G., Ivanova, N., et al. 2013, ApJ, 764, 98, doi: `10.1088/0004-637X/764/1/98`

Kim, D. W., Cameron, R. A., Drake, J. J., et al. 2004, ApJS, 150, 19, doi: `10.1086/379819`

Kim, D. W., Fabbiano, G., Brassington, N. J., et al. 2009, ApJ, 703, 829, doi: `10.1088/0004-637X/703/1/829`

Kim, E., Kim, D.-W., Fabbiano, G., et al. 2006, ApJ, 647, 276, doi: `10.1086/505261`

Kim, M., Kim, D., Wilkes, B. J., et al. 2007, in Chandra Multiwavelength Project X-Ray Point Source Catalog

King, A., & Lasota, J.-P. 2020, MNRAS, 494, 3611, doi: `10.1093/mnras/staa930`

King, A. R., Davies, M. B., Ward, M. J., Fabbiano, G., & Elvis, M. 2001, ApJ, 552, L109, doi: `10.1086/320343`

Kochanek, C. S., Auchettl, K., & Belczynski, K. 2019, Monthly Notices of the Royal Astronomical Society, 485, 5394, doi: `10.1093/mnras/stz717`

Körding, E., Falcke, H., & Markoff, S. 2002, A&A, 382, L13, doi: `10.1051/0004-6361:20011776`

Kreckel, K., Ho, I.-T., Blanc, G. A., et al. 2019, The Astrophysical Journal, 887, 80, doi: `10.3847/1538-4357/ab5115`

—. 2021, The Astrophysical Journal, 912, 167, doi: `10.3847/1538-4357/abf7c2`

Kremer, K., Chatterjee, S., Rodriguez, C. L., & Rasio, F. A. 2018, arXiv e-prints, arXiv:1802.04895. `https://arxiv.org/abs/1802.04895`

Kretschmar, P., Fürst, F., Sidoli, L., et al. 2019, , 86, 101546, doi: `10.1016/j.newar.2020.101546`

Kroupa, P. 2002, Science, 295, 82, doi: `10.1126/science.1067524`

Kundu, A., Maccarone, T. J., & Zepf, S. E. 2002, The Astrophysical Journal, 574, L5–L9, doi: `10.1086/342353`

Kundu, A., Maccarone, T. J., & Zepf, S. E. 2007, ApJ, 662, 525, doi: `10.1086/518021`

Kundu, A., Maccarone, T. J., Zepf, S. E., & Puzia, T. H. 2003, The Astrophysical Journal, 589, L81–L84, doi: 10.1086/376493

Kundu, A., Zepf, S. E., Maccarone, T. J., et al. 2008, in AIP Conference Proceedings (AIP), doi: 10.1063/1.2945065

Larsen, S. S. 1999, A&AS, 139, 393, doi: 10.1051/aas:1999509

Lasota, J., & King, A. 2023, Monthly Notices of the Royal Astronomical Society, 526, 2506–2509, doi: 10.1093/mnras/stad2926

Lasota, J.-P. 2001, New Astronomy Reviews, 45, 449–508, doi: 10.1016/s1387-6473(01)00112-9

Lattimer, J. M. 2012, Annual Review of Nuclear and Particle Science, 62, 485

Lau, R. M., Heida, M., Walton, D. J., et al. 2019, The Astrophysical Journal, 878, 71, doi: 10.3847/1538-4357/ab1b1c

Lee, J. C., Whitmore, B. C., Thilker, D. A., et al. 2022, ApJS, 258, 10, doi: 10.3847/1538-4365/ac1fe5

Lee, M. G., Sohn, J., Lee, J. H., et al. 2015, The Astrophysical Journal, 804, 63, doi: 10.1088/0004-637x/804/1/63

Lehmer, B. D., Alexander, D. M., Bauer, F. E., et al. 2010, ApJ, 724, 559, doi: 10.1088/0004-637X/724/1/559

Lehmer, B. D., Basu-Zych, A. R., Mineo, S., et al. 2016, ApJ, 825, 7, doi: 10.3847/0004-637X/825/1/7

Lehmer, B. D., Eufrasio, R. T., Markwardt, L., et al. 2017, ApJ, 851, 11, doi: 10.3847/1538-4357/aa9578

Lehmer, B. D., Eufrasio, R. T., Tzanavaris, P., et al. 2019, ApJS, 243, 3, doi: 10.3847/1538-4365/ab22a8

Lehmer, B. D., Ferrell, A. P., Doore, K., et al. 2020, ApJS, 248, 31, doi: 10.3847/1538-4365/ab9175

Lehmer, B. D., Eufrasio, R. T., Basu-Zych, A., et al. 2021, ApJ, 907, 17, doi: 10.3847/1538-4357/abcec1

Leroy, A. K., Schinnerer, E., Hughes, A., et al. 2021, The Astrophysical Journal Supplement Series, 257, 43, doi: 10.3847/1538-4365/ac17f3

Liu, Q. Z., van Paradijs, J., & van den Heuvel, E. P. J. 2006, A&A, 455, 1165, doi: 10.1051/0004-6361:20064987

—. 2007, A&A, 469, 807, doi: 10.1051/0004-6361:20077303

Lomelí-Núñez, L., Mayya, Y. D., Rodríguez-Merino, L. H., Ovando, P. A., & Rosa-González, D. 2021, Monthly Notices of the Royal Astronomical Society, doi: `10.1093/mnras/stab2890`

Long, K., Kuntz, K., Blair, W., et al. 2014, Astrophysical Journal, Supplement Series, 212, doi: `10.1088/0067-0049/212/2/21`

Lower, S., Narayanan, D., Leja, J., et al. 2020, ApJ, 904, 33, doi: `10.3847/1538-4357/abbfa7`

Luan, L., Jones, C., Forman, W. R., et al. 2018, ApJ, 862, 73, doi: `10.3847/1538-4357/aaca94`

Luo, B., Brandt, W. N., Xue, Y. Q., et al. 2017, ApJS, 228, 2, doi: `10.3847/1538-4365/228/1/2`

Lutovinov, A. A., Revnivtsev, M. G., Tsygankov, S. S., & Krivonos, R. A. 2013, Monthly Notices of the Royal Astronomical Society, 431, 327, doi: `10.1093/mnras/stt168`

López, K. M., Heida, M., Jonker, P. G., et al. 2020, Monthly Notices of the Royal Astronomical Society, 497, 917–932, doi: `10.1093/mnras/staa1920`

Maccarone, T. J., Kundu, A., & Zepf, S. E. 2003, The Astrophysical Journal, 586, 814, doi: `10.1086/367886`

Maccarone, T. J., Kundu, A., & Zepf, S. E. 2004, ApJ, 606, 430, doi: `10.1086/382937`

Maccarone, T. J., Kundu, A., Zepf, S. E., & Rhode, K. L. 2007, Nature, 445, 183, doi: `10.1038/nature05434`

Maddox, L. A., Cowan, J. J., Kilgard, R. E., et al. 2006, The Astronomical Journal, 132, 310–320, doi: `10.1086/505024`

Marchant, P., Langer, N., Podsiadlowski, P., et al. 2017, A&A, 604, A55, doi: `10.1051/0004-6361/201630188`

Marigo, P., Bressan, A., Nanni, A., Girardi, L., & Pumo, M. L. 2013, MNRAS, 434, 488, doi: `10.1093/mnras/stt1034`

Marigo, P., Girardi, L., Bressan, A., et al. 2017, ApJ, 835, 77, doi: `10.3847/1538-4357/835/1/77`

Mathis, J. S. 1990, ARA&A, 28, 37, doi: `10.1146/annurev.aa.28.090190.000345`

McLaughlin, D. E., & Fall, S. M. 2008, The Astrophysical Journal, 679, 1272, doi: `10.1086/533485`

McSwain, M. V., Ransom, S. M., Boyajian, T. S., Grundstrom, E. D., & Roberts, M. S. E. 2007, ApJ, 660, 740, doi: `10.1086/512155`

Medina, J., Mack, J., & Calamida, A. 2022, WFC3/UVIS Encircled Energy, Instrument Science Report WFC3 2022-2, 23 pages

Middleton, M. J., Walton, D. J., Alston, W., et al. 2021, Monthly Notices of the Royal Astronomical Society, 506, 1045–1058, doi: `10.1093/mnras/stab1280`

Mineo, S., Gilfanov, M., Lehmer, B. D., Morrison, G. E., & Sunyaev, R. 2014, MNRAS, 437, 1698, doi: `10.1093/mnras/stt1999`

Mineo, S., Gilfanov, M., & Sunyaev, R. 2012, MNRAS, 419, 2095, doi: `10.1111/j.1365-2966.2011.19862.x`

Misra, D., Fragos, T., Tauris, T. M., Zapartas, E., & Aguilera-Dena, D. R. 2020, Astronomy amp; Astrophysics, 642, A174, doi: `10.1051/0004-6361/202038070`

Mok, A., Chandar, R., & Fall, S. M. 2019, ApJ, 872, 93, doi: `10.3847/1538-4357/aaf6ea`

Montero-Camacho, P., Zhang, Y., & Mao, Y. 2024, MNRAS, 529, 3666, doi: `10.1093/mnras/stae751`

Morscher, M., Pattabiraman, B., Rodriguez, C., Rasio, F. A., & Umbreit, S. 2015, ApJ, 800, 9, doi: `10.1088/0004-637X/800/1/9`

Motch, C., Pakull, M. W., Soria, R., Grisé, F., & Pietrzyński, G. 2014, Nature, 514, 198–201, doi: `10.1038/nature13730`

Mulia, P. J., Chandar, R., & Rangelov, B. 2019, The Astrophysical Journal, 871, 122, doi: `10.3847/1538-4357/aaf56a`

Muratov, A. L., & Gnedin, O. Y. 2010, The Astrophysical Journal, 718, 1266, doi: `10.1088/0004-637X/718/2/1266`

Mushtukov, A. A., Portegies Zwart, S., Tsygankov, S. S., Nagirner, D. I., & Poutanen, J. 2020, Monthly Notices of the Royal Astronomical Society, 501, 2424, doi: `10.1093/mnras/staa3809`

Nantais, J. B., & Huchra, J. P. 2010, AJ, 139, 2620, doi: `10.1088/0004-6256/139/6/2620`

Nantais, J. B., Huchra, J. P., McLeod, B., Strader, J., & Brodie, J. P. 2010, AJ, 139, 1413, doi: `10.1088/0004-6256/139/4/1413`

Nantais, J. B., Huchra, J. P., Zezas, A., Gazeas, K., & Strader, J. 2011, AJ, 142, 183, doi: `10.1088/0004-6256/142/6/183`

National Academies of Sciences, E., & Medicine. 2023, Pathways to Discovery in Astronomy and Astrophysics for the 2020s: Highlights of a Decadal Survey (Washington, DC: The National Academies Press), doi: `10.17226/26933`

Okamoto, S., Arimoto, N., Ferguson, A. M. N., et al. 2015, The Astrophysical Journal, 809, L1, doi: `10.1088/2041-8205/809/1/l1`

Pakull, M. W., & Mirioni, L. 2003, in Revista Mexicana de Astronomia y Astrofisica Conference Series, Vol. 15, Revista Mexicana de Astronomia y Astrofisica Conference Series, ed. J. Arthur & W. J. Henney, 197–199

Palmore, D., Rangelov, B., Chandar, R., & Prestwich, A. 2022, in American Astronomical Society Meeting Abstracts, Vol. 54, American Astronomical Society Meeting Abstracts, 126.05

Paolillo, M., Puzia, T. H., Goudfrooij, P., et al. 2011, The Astrophysical Journal, 736, 90, doi: 10.1088/0004-637X/736/2/90

Pastorelli, G., Marigo, P., Girardi, L., et al. 2020, MNRAS, 498, 3283, doi: 10.1093/mnras/staa2565

Peacock, M. B., Maccarone, T. J., Kundu, A., & Zepf, S. E. 2010, MNRAS, 407, 2611, doi: 10.1111/j.1365-2966.2010.17119.x

Peacock, M. B., Maccarone, T. J., Waters, C. Z., et al. 2009, MNRAS, 392, L55, doi: 10.1111/j.1745-3933.2008.00588.x

Peacock, M. B., & Zepf, S. E. 2016, ApJ, 818, 33, doi: 10.3847/0004-637X/818/1/33

Peacock, M. B., Zepf, S. E., Kundu, A., et al. 2017a, MNRAS, 466, 4021, doi: 10.1093/mnras/stw3375

—. 2017b, MNRAS, 466, 4021, doi: 10.1093/mnras/stw3375

Pfahl, E., Rappaport, S., & Podsiadlowski, P. 2003, ApJ, 597, 1036, doi: 10.1086/378632

Pfeffer, J., Kruijssen, D., Bastian, N., Crain, R., & Trujillo-Gomez, S. 2023, Monthly Notices of the Royal Astronomical Society, 519, doi: 10.1093/mnras/stad044

Piro, A. L., & Bildsten, L. 2002, The Astrophysical Journal, 571, L103, doi: 10.1086/341341

Plotkin, R. M., Gallo, E., Miller, B. P., et al. 2014, ApJ, 780, 6, doi: 10.1088/0004-637X/780/1/6

Podsiadlowski, P., & Rappaport, S. 2000, ApJ, 529, 946, doi: 10.1086/308323

Podsiadlowski, P., Rappaport, S., & Pfahl, E. D. 2002, ApJ, 565, 1107, doi: 10.1086/324686

Politakis, B., Zezas, A., Andrews, J. J., & Williams, S. J. 2020, MNRAS, 493, 5369, doi: 10.1093/mnras/staa561

Pooley, D., Lewin, W. H. G., Anderson, S. F., et al. 2003, ApJ, 591, L131, doi: 10.1086/377074

Portegies Zwart, S. F., McMillan, S. L. W., & Makino, J. 2007, MNRAS, 374, 95, doi: 10.1111/j.1365-2966.2006.11142.x

Postnov, K. A., & Yungelson, L. R. 2014, Living Reviews in Relativity, 17, 3, doi: 10.12942/lrr-2014-3

Poutanen, J., Fabrika, S., Valeev, A. F., Sholukhova, O., & Greiner, J. 2013, Monthly Notices of the Royal Astronomical Society, 432, 506, doi: 10.1093/mnras/stt487

Prestwich, A. H., Irwin, J. A., Kilgard, R. E., et al. 2003, ApJ, 595, 719, doi: 10.1086/377366

Prestwich, A. H., Tsantaki, M., Zezas, A., et al. 2013, ApJ, 769, 92, doi: 10.1088/0004-637X/769/2/92

Puzia, T. H., Paolillo, M., Goudfrooij, P., et al. 2014, ApJ, 786, 78, doi: 10.1088/0004-637X/786/2/78

Ranalli, P., Comastri, A., & Setti, G. 2003, A&A, 399, 39, doi: 10.1051/0004-6361:20021600

Rangelov, B., Chandar, R., Prestwich, A., & Whitmore, B. C. 2012, The Astrophysical Journal, 758, 99, doi: 10.1088/0004-637x/758/2/99

Rangelov, B., Prestwich, A. H., & Chandar, R. 2011, The Astrophysical Journal, 741, 86, doi: 10.1088/0004-637x/741/2/86

Rappaport, S. A., Podsiadlowski, P., & Pfahl, E. 2005, MNRAS, 356, 401, doi: 10.1111/j.1365-2966.2004.08489.x

Repetto, S., Igoshev, A. P., & Nelemans, G. 2017, Monthly Notices of the Royal Astronomical Society, stx027, doi: 10.1093/mnras/stx027

Riccio, G., Paolillo, M., D'Abrusco, R., et al. 2019, Proceedings of the International Astronomical Union, 14, 151, doi: 10.1017/s1743921319007890

Riccio, G., Paolillo, M., Cantiello, M., et al. 2022, A&A, 664, A41, doi: 10.1051/0004-6361/202142894

Rosenfield, P., Marigo, P., Girardi, L., et al. 2016, ApJ, 822, 73, doi: 10.3847/0004-637X/822/2/73

Rosolowsky, E. 2005, PASP, 117, 1403, doi: 10.1086/497582

Russell, D., Yang, Y., Gladstone, J., Wiersema, K., & Roberts, T. 2011, Astronomische Nachrichten, 332, 371–374, doi: 10.1002/asna.201011502

Saha, A., Thim, F., Tammann, G. A., Reindl, B., & Sand age, A. 2006, ApJS, 165, 108, doi: 10.1086/503800

Santiago-Cortés, M., Mayya, Y. D., & Rosa-González, D. 2010, Monthly Notices of the Royal Astronomical Society, 405, 1293, doi: 10.1111/j.1365-2966.2010.16531.x

Sarazin, C. L., Irwin, J. A., & Bregman, J. N. 2000, ApJ, 544, L101, doi: 10.1086/317308

Schechter, P. 1976, ApJ, 203, 297, doi: 10.1086/154079

Schulman, R. D., Glebbeek, v., & Sills, A. 2012, Monthly Notices of the Royal Astronomical Society, 420, 651, doi: 10.1111/j.1365-2966.2011.20079.x

Sepinsky, J., Kalogera, V., & Belczynski, K. 2005, ApJ, 621, L37, doi: 10.1086/428942

Shtykovskiy, P. E., & Gilfanov, M. R. 2007, Astronomy Letters, 33, 299, doi: 10.1134/S1063773707050039

Sippel, A. C., & Hurley, J. R. 2013, MNRAS, 430, L30, doi: 10.1093/mnrasl/sls044

Sivakoff, G. R., Jordán, A., Sarazin, C. L., et al. 2007, ApJ, 660, 1246, doi: 10.1086/513094

Smits, M., Maccarone, T. J., Kundu, A., & Zepf, S. E. 2006, A&A, 458, 477, doi: 10.1051/0004-6361:20065298

Soria, R., & Wu, K. 2003, Astronomy & Astrophysics, 410, 53–74, doi: 10.1051/0004-6361:20031074

Strader, J., Chomiuk, L., Maccarone, T. J., Miller-Jones, J. C. A., & Seth, A. C. 2012, Nature, 490, 71, doi: 10.1038/nature11490

Sutantyo, W. 1975, A&A, 44, 227

Sutton, A. D., Roberts, T. P., & Middleton, M. J. 2013, Monthly Notices of the Royal Astronomical Society, 435, 1758, doi: 10.1093/mnras/stt1419

Talbot, R. J., J., Jensen, E. B., & Dufour, R. J. 1979, ApJ, 229, 91, doi: 10.1086/156933

Tao, L., Feng, H., Grisé, F., & Kaaret, P. 2011, ApJ, 737, 81, doi: 10.1088/0004-637X/737/2/81

Tauris, T. M., & van den Heuvel, E. P. J. 2006, in Compact stellar X-ray sources, Vol. 39, 623–665, doi: 10.48550/arXiv.astro-ph/0303456

Tauris, T. M., Kramer, M., Freire, P. C. C., et al. 2017, ApJ, 846, 170, doi: 10.3847/1538-4357/aa7e89

Thilker, D. A., Whitmore, B. C., Lee, J. C., et al. 2022, MNRAS, 509, 4094, doi: 10.1093/mnras/stab3183

Trenti, M. 2006, arXiv e-prints, astro, doi: 10.48550/arXiv.astro-ph/0612040

Turner, J. A., Dale, D. A., Lee, J. C., et al. 2021, MNRAS, 502, 1366, doi: 10.1093/mnras/stab055

Tzanavaris, P., Hornschemeier, A. E., Gallagher, S. C., et al. 2016, ApJ, 817, 95, doi: 10.3847/0004-637X/817/2/95

Tzanavaris, P., Fragos, T., Tremmel, M., et al. 2013, ApJ, 774, 136, doi: 10.1088/0004-637X/774/2/136 van den Heuvel, E. P. J. 1975, ApJ, 198, L109, doi: 10.1086/181824

van den Heuvel, E. P. J., & van Paradijs, J. 1997, ApJ, 483, 399, doi: 10.1086/304249

Verbunt, F. 1987, ApJ, 312, L23, doi: 10.1086/184812

Virtanen, P., Gommers, R., Oliphant, T. E., et al. 2020, Nature Methods, 17, 261, doi: 10.1038/s41592-019-0686-2

Vulic, N., Barmby, P., & Gallagher, S. C. 2018, MNRAS, 473, 4900, doi: 10.1093/mnras/stx2626

Walton, D. J., Mackenzie, A. D. A., Gully, H., et al. 2022, MNRAS, 509, 1587, doi: 10.1093/mnras/stab3001

Wang, S., Qiu, Y., Liu, J., & Bregman, J. N. 2016, ApJ, 829, 20, doi: 10.3847/0004-637X/829/1/20

Webb, N. A., Coriat, M., Traulsen, I., et al. 2020, A&A, 641, A136, doi: 10.1051/0004-6361/201937353

Weżgowiec, M., Soida, M., & Bomans, D. J. 2012, A&A, 544, A113, doi: 10.1051/0004-6361/201118436

White, Raymond E., I., Sarazin, C. L., & Kulkarni, S. R. 2002, ApJ, 571, L23, doi: 10.1086/341122

White, N. E., & Angelini, L. 2001, ApJ, 561, L101, doi: 10.1086/324561

Whitmore, B. C., Lee, J. C., Chandar, R., et al. 2021, MNRAS, 506, 5294, doi: 10.1093/mnras/stab2087

Whitmore, B. C., Chandar, R., Lee, J. C., et al. 2023, Monthly Notices of the Royal Astronomical Society, 520, 63, doi: 10.1093/mnras/stad098

Willmer, C. N. A. 2018, The Astrophysical Journal Supplement Series, 236, 47, doi: 10.3847/1538-4365/aabfdf

Wood, R., & Andrews, P. J. 1974, Monthly Notices of the Royal Astronomical Society, 167, 13, doi: 10.1093/mnras/167.1.13

Wu, W., & Zhao, G. 2021, The Astrophysical Journal, 908, 224, doi: 10.3847/1538-4357/abd6b8

Yan, Z., & Yu, W. 2015, ApJ, 805, 87, doi: 10.1088/0004-637X/805/2/87

Zhang, Z., Gilfanov, M., & Bogdán, Á. 2012, A&A, 546, A36, doi: 10.1051/0004-6361/201219015

Zhang, Z., Gilfanov, M., & Bogdán, 2013, Astronomy amp; Astrophysics, 556, A9, doi: 10.1051/0004-6361/201220685

Zuo, Z.-Y., & Li, X.-D. 2010, Monthly Notices of the Royal Astronomical Society, 405, 2768, doi: `10.1111/j.1365-2966.2010.16658.x`

Zwillinger, D., & Kokoska, S. 2000, CRC Standard Probability and Statistics Tables and Formulae (Chapman & Hall)